Stochastic Population Dynamics in Astrochemistry and Aerosol Science

PhD thesis

Student: Christiane Maria Losert-Valiente Kroon

First Supervisor: Prof Ian J Ford

Second Supervisor: Dr Robert Thorne

Department of Physics and Astronomy,

UCL,

Gower Street

London WC1E 6BT

and

London Centre for Nanotechnology

Gordon Street

London WC1H 0AH

April 2010

I, Christiane Maria Losert-Valiente Kroon, confirm that the work presented in this thesis is my own. Where information has been derived from other sources, I confirm that this has been indicated in the thesis.

Abstract

Classical, non-equilibrium systems of diffusing species or entities undergoing depletion, evaporation and reaction processes are at the heart of many problems in Physics, Chemistry, Biology and Financial Mathematics. It is well known that fluctuations and correlations in statistical systems can have a profound influence on the macroscopic properties of the system. However, the traditional rate equations that describe the evolution of mean populations in time and space do not incorporate statistical fluctuations. This becomes an issue of great importance when population densities are low. In order to develop a stochastic description of birth-and-death processes beyond the mean field approximation I employ techniques in classical many-body Physics in a manner analogous to the treatment of quantum systems. I obtain promising results to understand and quantify the exact circumstances of the failure of the mean-field approximation in specific problems in Astrophysics, namely heterogeneous chemical reactions in interstellar clouds, and in Aerosol Science, namely heterogeneous nucleation processes, and deliver the means to manipulate the alternative stochastic framework according to the Doi-Peliti formalism. In this framework the mean population of a species is given by the average of a solution to a set of constraint equations over all realisations of the stochastic noise. The constraint equations are inhomogeneous stochastic partial differential equations with multiplicative real or complex Gaussian noise. In general, these equations cannot be solved analytically. Therefore I resort to the numerical implementation of the Doi-Peliti formalism. The main code is written in the GNU C language, some algebraic calculations are performed by means of the MapleV package. In the case of large population densities the stochastic framework renders the same results as the mean field approximation whereas for low population densities its predictions differ substantially from the calculations using the traditional model.

Acknowledgements

First and foremost I would like to thank Prof Ian Ford who introduced me to the particular topic of research that has kept me fascinated until the last page of the thesis was typed and Prof Andrew Fisher for his warm welcome to the Department of Physics and Astronomy at UCL.

This work would not have been able without the financial support by the Leverhulme Trust (grant F/07134/BV) and by the Aerosol Society (CN Davies Award).

The scientific exchanges at international conferences and workshops were invaluable to the development of my research and the financial contributions of the Institute of Physics, UCL, the Aerosol Society, Gesellschaft für Aerosolforschung and the COST programme which made possible my participation at these meetings are thankfully acknowledged.

I thouroughly enjoyed my scientific stays with Dr Herma Cuppen (Sackler Laboratory for Astrophysics, Leiden Observatory, University of Leiden, The Netherlands,) and Dr José Cañizo (Department of Mathematics, Autononomous University of Barcelona, Spain) who were kind and patient enough to put up with my many curious questions.

Also, I am very grateful to Dr Henner Busemann who agreed to the inclusion of one of his research images in my thesis.

In the course of my PhD studies I learned to appreciate more deeply the scientific foundations I obtained due to the excellent lectures given by my former teachers at the University of Vienna, Austria.

I am forever grateful for the incessant support and unremitting encouragement by my old friends in Austria and my new friends in the UK, by my loyal and caring parents and by my loving husband whose confidence in my abilities made me go all the way.

Contents

List of Tables

List of Figures

Chapter 1

Introduction

1.1 Heterogeneous Chemical Reactions in Interstellar Clouds

Heterogeneous chemical reactions are chemical reactions taking place on a pre-existing surface, the *grain* or *seed particle* onto which atoms or molecules from the surrounding gas-phase can be adsorbed onto or from which they can be evaporated. In this thesis we study heterogeneous chemical reactions taking place on the surface of grain particles that are suspended in interstellar clouds.

1.1.1 On the Classification of Interstellar Clouds

Stellar events such as, for example, massive explosions or gentler winds, result in the ejection of gaseous and particulate matter into the interstellar medium, where interstellar clouds are formed under the influence of gravity. The gaseous matter is mainly atomic in nature. Consequently, molecular synthesis must occur within the interstellar clouds themselves. This is important since molecules produced in interstellar clouds will be incorporated into solid bodies such as comets, meteors, and planets. Small portions of matter in interstellar clouds gradually collapse and heat up to the point where nuclear reaction sets in and stars are formed. In turn, the stars blow away interstellar matter surrounding them.

Interstellar clouds are regions of many light years in extent. In the 1970s [42] the interstellar medium was classified into three phases that can be thought to be in approximate pressure equilibrium with each other: the *cold neutral medium* or *interstellar clouds*, the *warm ionised medium* or *warm neutral medium*, and the

hot ionised medium or *coronal gas*. Within the cold neutral medium itself one can distinguish between the *dense clouds* or *dark clouds* or *molecular clouds* —see Figure 1.1— which are most protected from UV radiation, the *diffuse clouds* which are fully exposed to starlight, and the *translucent clouds* which are somewhere in between. In 2006 a new systematic classification was introduced in [56], namely the *diffuse atomic region*, the *diffuse molecular region*, the *translucent region*, and the *dense molecular region*.

The study of interstellar molecules requires a wide range of observational techniques since they can be identified via their electronic (detectable in the UV band or visible spectrum), vibrational (observed at IR wavelengths), and rotational spectra (radio wavelengths). Since molecular hydrogen is symmetric and homonuclear it is not possible to detect this chemical species via vibrational or rotational transitions caused by the electric dipole. The number density of molecules is not directly observable, whereas, the integral of the number density along the line of sight to stellar or non-stellar lamps is. Molecular destruction can be caused by photodissociation where photons break the molecular bond or by predissociation, where the molecule is first photoexcited to an unstable state and then dissociates. Molecules must form at rates fast enough to counterbalance the rates of destruction.

Diffuse atomic clouds are defined by the low molecular fraction in comparison to diatomic hydrogen, H_2. Hydrogen appears to be mainly in neutral atomic form. Carbon and other atoms whose ionisation potentials are less than that of hydrogen are almost fully ionised and provide abundant electrons. In diffuse atomic clouds all molecules are quickly destroyed by photodissocation since this particular region is fully exposed to the interstellar radiation field. Diffuse atomic clouds have low atomic density ($10\text{cm}^{-3} - 100\text{cm}^{-3}$) and gas temperatures of around 30K−100K.
In diffuse molecular clouds the intensity of the interstellar radiation field is lessened so that the local fraction of hydrogen in molecular form is greater than 0.1. Although molecules are observed in diffuse molecular clouds there is, nevertheless, enough interstellar radiation present to photoionise atomic carbon, or to photodissociate carbon monoxide. Atomic densities lie in the range of $100\text{cm}^{-3} - 500\text{cm}^{-3}$ and the gas phase temperature is again between 30K−100K. Hydrogen is the dominant chemical species followed by helium (10 % of hydrogen population) and C, N, O with orders of 10^{-3} to 10^{-4} of hydrogen densities.
In translucent clouds, carbon begins to transfer from ionised atomic form into neutral atomic or molecular form since this region in space is sufficiently protected

from interstellar radiation. The type of chemistry occuring in translucent clouds is qualitatively different from the chemistry in diffuse clouds due to the decreasing electron fraction and the increasing abundance of the highly reactive carbon atoms.
In dense molecular clouds, the reactive carbon atoms are replaced by the very stable carbon monoxide. Dense clouds are self-gravitating, their particle densities are at least 10^4cm^{-3}, and their temperatures are of the order of 10K−50K. The molecules are mostly organic. Gas densities can be quite inhomogeneous. In the cores, the density can be greater than 10^4cm^{-3}. It is difficult to see through denser interstellar clouds in the visible. They are usually observed at longer wavelengths: via spacebased measurements (ISO, European satellite) in the infrared and via groundbased measurements (radiotelescopes) in mm wavelength. More than 120 different molecular species have been detected with molecular hydrogen again the dominant chemical species. Concentrations of molecular hydrogen are about 10^4 times that of the second most abundant molecule CO. Molecules range in size from 2 to 13 atoms.

1.1.2 On the Nature of Grain Particles

Roughly one percent (by mass) of interstellar matter is tied up in dust particles —see Figure 1.2. Interstellar dust particles are assumed to be 98 % amorphous and only 2 % crystalline. The grains are considered to be complex entities, fractal-like and porous. Different rates of surface diffusion can occur on the same impure grain with sites of strong binding that can trap species [32]. The size distribution of grain particles ranges from tens of ångströms to several microns. The smaller grains are considered to be large carbonaceous molecules. They are considered to be non-spherical. This has been deduced from the scattering and polarisation properties of the grains and via the absorption of radiation. In diffuse clouds the grain diameter is in the range of 10^{-8}m to 5×10^{-7}m and the grain surface temperature is around 20K. It seems that there are many more smaller grains than larger ones [30]. In addition, it is likely that the grains are negatively charged unless photoelectric effects dominate since, in a thermal medium, electrons travel more quickly than heavy positive ions. Therefore, one probably does not have to consider positive ions on grain surfaces. In dense clouds, grain surface temperatures can be as low as 10K. Most of the extinction is caused by the dust particles that can scatter and adsorb radiation with an efficiency that increases with decreasing wave length. One can distinguish between three size classes: standard grains with a radius of $(0.003 - 3) \times 10^{-6}$m, small grains $2 - 10 \times 10^{-9}$m and $0.5 - 1 \times 10^{-9}$m for polycylic aromatic hydrocarbon-like species. The grain density $n(grain)$ is estimated to be smaller than the atomic hydrogen gas density $n(H)$ and

Figure 1.1: *"This composite image, combining data from NASA's Chandra X-ray Observatory and Spitzer Space Telescope shows the star-forming cloud Cepheus B, located in our Milky Way galaxy about 2,400 light years from Earth. A molecular cloud is a region containing cool interstellar gas and dust left over from the formation of the galaxy and mostly contains molecular hydrogen. The Spitzer data, in red, green and blue shows the molecular cloud (in the bottom part of the image) plus young stars in and around Cepheus B, and the Chandra data in violet shows the young stars in the field."* Image credit: NASA/CXC/JPL-Caltech/PSU/CfA

is roughly $n(grain) = 10^{-12}n(H)$ [58]. The grains can be composed of carbonaceous matter as well as of metallic silicates. Heavy elements (Si, Fe) and lighter elements (O,C) are both important types of elements. Ice mantles that can develop around dust particle cores consist mainly of water ice. This is observed through the broad absorption features. Other components of ice mantles are CO, CO_2 and methanol ices. In reality, several types of inhomogeneities can occur: mixed, composite surfaces and surfaces with imperfections such as kinks and terraces at which binding energies are significantly greater than at normal binding sites. When considering grains with ice mantles, the surface properties change during reaction processes and reactants can not only sink into pores but enter the layer where they are enclosed by the ices. Most heavy molecules formed on grains remain on the surface of the grain to form a grain mantle unless a star forms nearby and the temperature rises —as became clear from observational evidence. The appropriate temperature for cold cores in

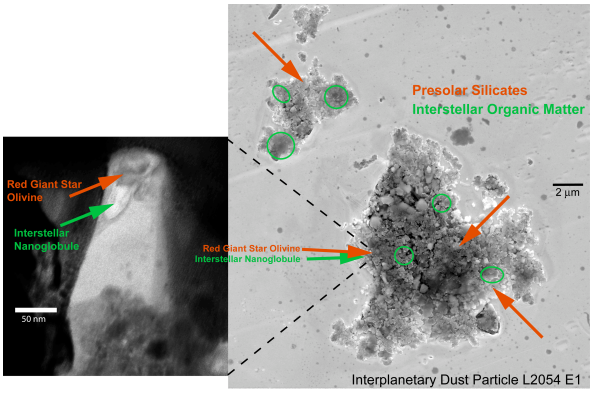

Figure 1.2: Interplanetary dust particle: such dust particles are made up by interstellar dust sticking together. Interstellar dust particles are assumed to be of the size of one tenth of the planetary dust. Image Credit: Dr. Henner Busemann, University of Manchester.

dense interstellar clouds is about $T = 10$K. Grains can heat up quickly when a cosmic ray (protons, iron nuclei) hits the grain —see [36]. One distinguishes between three different desorption mechanisms: thermal desorption including cosmic ray induced desorption, [31] photodesorption, [44] and reactive desorption [23]. Furthermore, there are two possible mechansims triggering a heterogeneous chemical reaction: firstly, a heterogeneous chemical reaction that takes place when an adsorbate lands atop another one (*Eley-Rideal mechanism*). On smaller grains a strong interaction between the adsorbate and the grain is likely to occur (*chemisorption*) which immobilises the adsorbed reactant. Chemical reactions can only take place when a gas-phase species strikes another reactant on the surface of the grain. This mechanism contributes to interstellar chemistry only when the surface of the grain is covered with reactive species. In that case, this mechanism is thought to dominate the formation of molecular hydrogen in warm regions where weakly bound species evaporate too quickly to diffuse appreciably [32]. At lower temperatures and on larger grains diffusive chemistry (*Langmuir-Hinshelwood diffusion mechanism*) dominates: the heterogeneous chemical reaction is initiated by the collision and reaction of two atoms or molecules adsorbed onto the grain and their diffusion on its surface. In this case, the temperature has to be high enough for motion to occur. Weakly bound species (*physisorbed*) —see [58]— can sweep across the grain surface by thermal hopping between the binding sites or by quantum mechanical tunnelling. Conditions where reactions occur much faster than the rate at which species accrete onto grain surfaces are also called *accretion limited* —see [58].

1.1.3 Challenges in Interstellar Surface Chemistry

The nature of the gas phase of interstellar clouds is well established. *In situ* homogeneous production within interstellar clouds is not efficient due to the low densities and low temperatures [36]. The chemistry is not rapid enough with estimated collision times of around two weeks and a mean free path of $100,000$km. Furthermore, the collisions are probably not reactive since the activation energy is too large compared to the thermal energy. If the molecules were produced elsewhere there are two possible means: the production of molecules in the huge atmospheres around old stars (*envelopes*) and their transport to interstellar clouds by strong winds from the star, and the formation in explosive events (*supernovae*) where gaseous and particulate matter are ejected into the interstellar medium and clouds can form under the influence of gravity. However, gaseous matter is mainly atomic in nature which leads to the conclusion that the synthesis must occur within the interstellar clouds. The biggest obstacle in the path of synthesis is the conversion of atoms into diatomic molecules. In order to stabilise, for example, the H_2 chemical bond the system must rid itself of sufficient energy via emission of radiation (*radiative association*) which is more efficient for larger systems with molecules. The chance of a third body striking the H_2 collision complex before the latter dissociates, in order to stabilise the complex in the interstellar cloud is essentially zero. Under interstellar conditions, it seems that it is not possible to convert atomic to molecular hydrogen. Yet, the surface of seed particles present in an interstellar cloud can provide a template for chemical reactions. The heterogeneous chemistry in interstellar clouds is, at the moment, the only alternative available, although the process does not seem to be efficient enough to fully convert atomic hydrogen into diatomic hydrogen in dense clouds within reasonable astronomical time scales (10^5y - 10^6y).

Let us quote [30] on the state of research in interstellar surface chemistry: *"Even with the results of recent experiments, surface chemistry is generally far more poorly understood than gas-phase chemistry, and in the case of interstellar dust grains, there are additional problems given our lack of a detailed knowledge of the physical nature of the surface. Among the problems faced by astrochemists are:*
(i) the detailed mechanism for the formation of molecules (Langmuir-Hinshelwood vs Eley-Rideal);
(ii) the dependence of the rate of surface reaction on grain size, the possible existence of a grain mantle, the probable fluffy nature of interstellar grains, the smoothness and roughness of the surface, and unknown energy parameters;
(iii) whether or not the rate equations used by surface chemists even apply to chemistry

on small grain particles;
(iv) and how products can desorb from grain surfaces back into the gas."

According to [58], in interstellar space, abundances of some reactants are so low that it is questionable to consider them as averages. If the mean density of the reacting atoms is small, statistical fluctuations brought about by the gain of atoms onto the surface of the seed and by the loss of atoms from the grain, and by the random diffusion of atoms on the surface of the seed particle, are important. The traditional model employed to predict the abundances of chemical species produced in heterogeneous chemical reactions does not include the treatment of such fluctuations. Several attempts have been introduced to resolve that problem; in the Astrophysics community this would comprise mainly Monte Carlo methods [9, 10, 59] and [8], the modified rate approach [7, 57], the direct master equation approach [27, 4], and the moments master equation method [1]. Analytical solutions to a master equation approach have been found for the steady state[1] case [4, 27, 40]. In the Mathematics community, related studies have been carried out with respect to the Positive P representation in [17] and the Gauge Poisson representation approach in [13, 33]. Renormalisation group analysis has been carried out in, for example, [34, 39, 52]. Experiments concerning grain surface chemistry under interstellar conditions with seeds made of olivine or amorphous carbon have been carried out in [35, 47, 46, 48].

Our work provides an alternative approach for describing the kinetics of a heterogeneous chemical reaction which can be extended to other areas in population dynamics.

1.2 Heterogeneous Nucleation of Aerosols

Nucleation is a relaxation process allowing a system to move forwards to thermodynamic stability. It plays a fundamental role in processes such as condensation, precipitation, crystallisation, sublimation, boiling and freezing. In Nucleation Theory one distinguishes between the *homogeneous nucleation*, that is, the condensation of a single chemical compound on its own and the *heterogeneous nucleation*, that is, the condensation of a compound on the surface of a pre-existing substance —the *seed particle*. Many of the seed particles for heterogeneous nucleation are anthropogenic in origin

[1] If a system is in a steady state the recently observed behaviour of the system will continue into the future. In stochastic systems, the probabilities that various different states will be repeated remains constant. A system in dynamic equilbrium is also in a steady state. The reverse might not be true.

and, in view of global climate change —see the reports of the Intergovernmental Panel on Climate Change (IPCC)[2]—, it is pertinent to better understand the effect of particulate pollutants. In this thesis we will study a general framework for nucleation kinetics which can be used to interpret experimental and observational data.

1.2.1 On the Nature of Aerosols

Aerosols are multiphase dispersed systems consisting of solid and/or liquid particles suspended in a gas. The aerosol particles can interact with thermal, acoustic and optical radiation, with gas-phase chemical species, with electric and gravitational fields. They can be transported in gas flows and be deposited onto surfaces. They range in size from the nanometer scale to the micrometer scale. The larger aerosols settle to the ground by gravity in a matter of hours; the smaller aerosol particles can stay in the atmosphere for several weeks until they are removed by precipitation. Aerosol particles have a great impact on the environment in general, and on human lives in particular; the latter can, for example, be illustrated by contemplating the effects of inhaling aerosol particles causing asthma, lung cancer, cardiovascular issues, even premature death. Aerosols also play an important role in the alteration of the energy balance of the climate system. All aerosol particles both absorb and scatter solar and terrestrial radiation, but one can distinguish particles that pre-dominantly scatter from those that predominantly absorb radiation, for example, sulphate aerosols and black carbon respectively. The reflectivity of a surface or a body is measured via the *albedo* which is defined as the ratio of the reflected electromagnetic radiation to the amount incident upon it. Aerosols are thought to contribute to an effective increase in the Earth's albedo: an overall cooling. In addition to direct scattering of radiation, sulphate aerosols in particular can have an indirect effect on climate, through serving as cloud condensation nuclei and hence affecting the size, density and lifetime of atmospheric clouds.

"Atmospheric Aerosols are the product of a complicated totality of chemical and physical processes." [38]. Aerosols can vary widely in their composition and their physical characteristics. They are either directly emitted into the atmosphere —*primary sources*— or they are products of gas-to-particle conversions —*secondary sources*. The global aerosol production is estimated to be between 2×10^{15}g a^{-1} and 3×10^{15}g a^{-1} [50]. Aerosols can be produced by humans, *anthropogenic aerosols* —see Figure 1.3—, or they can arise due to natural reasons, *natural areosols* —see Figure 1.4. Examples for anthropogenic sources of aerosols are: industrial wastes from chimneys, exhausts from

[2]See `http://www.ipcc.ch`

vehicles, fires, explosions, soil erosion in agriculture, and open mining. Among the natural aerosol sources are: sea spray evaporation, mineral dust wind, volcanic ashes, biogenic aerosols, smokes from biota burning on land. According to [38], anthropogenic sources have an input of 3×10^{14}g a^{-1} to 4×10^{14}g a^{-1} of aerosols to the atmosphere. *"The concentration of aerosol smog due to photochemical reactions with exhaust gases in industrial centres reaches* $2 \times 10^{-4} g\ m^{-3}$*, which is comparable with the consequences of dust storms."* [38].

1.2.2 Heterogeneous Nucleation

Nucleation is the initial stage of a first-order phase transition[3]. Molecular *clusters* or *embryos* —an aggregate of a small number of atoms or molecules— of a stable phase form out of a metastable phase. The transformation involves emergences of clusters of the new phase which —in a thermodynamical sense— are not necessarily more stable than the original phase. Small clusters tend to be unstable and break apart due to the high proportions of surface. Latent heat is transferred during the process of nucleation. At thermodynamic equilibrium[4] there is a non-zero surface tension between the two phases. There is a critical supersaturation, or degree of metastability of the vapour phase, required to drive nucleation forward at a chosen rate. A vapour is called *saturated* when the vapour phase is in thermodynamic equilibrium with the bulk condensate. If the vapour pressure is greater than the pressure of the saturated vapour the vapour is supersaturated. This is a necessary condition for nucleation to take place. Still the supersaturated phase can remain in a metastable state in thermodynamic equilibrium for a certain time. The system has to climb a free energy barrier before clusters become supercritical. A *critical cluster* is a cluster of such size that the free energy at constant pressure and temperature is a maximum. Clusters larger than the critical cluster are called *nuclei*. The time scale for nucleation is less than microseconds and the growth process from a nucleus to a droplet is in the millisecond range. For heterogeneous nucleation the *critical supersaturation* and *activation free energy* or *nucleation barrier* are considerably lower than for homogeneous nucleation. Typically, heterogeneous nucleation occurs soon after the saturation ratio exceeds one, at much lower vapour concentrations than

[3]A phase is a region in the parameter space of thermodynamic variables in which the free energy is analytic. Between such regions there are abrupt changes in the properties of the system, that is, the free energy is no longer analytic in such a phase transition.

[4]A system is in thermodynamic equilibrium when it is in thermal equilibrium, mechanical equilibrium and chemical equilibrium. It is characterised by the minimum of a thermodynamic potential (Helmholtz free energy, Gibbs free energy etc.). In contrast, a dynamic equilibrium occurs when two or more reversible processes occur at the same rate.

homogeneous nucleation. In the atmosphere, conditions for homogeneous nucleation are not easy to achieve, since the required vapour densities must be very much larger than the equilibrium density. Water vapour, for example, preferentially condenses on pre-existing surfaces.

Nucleation can be treated as a growth-decay ladder of molecular clusters. Molecules of the gas-phase form clusters on the surface of the seed particle which grow and decay until a critical cluster size is reached —see Figure 1.5. Henceforth, clusters with sizes larger than the critical size grow rapidly to macroscopic sizes. The *nucleation current* or *nucleation rate* is of special interest and is defined as the net number of clusters per unit time that grow past the critical cluster size. Classical Nucleation Theory is based on Gibb's description of heterogeneous systems [24] —and was further developed in [65, 21, 61, 51]— which has as a consequence that the critical clusters and the evolving macrophase are characterised by similar bulk state parameters, that is, one assigns thermodynamic properties of macroscopic systems to a microscopic entity. Direct measurements of the characteristic properties of critical clusters are usually very difficult to undertake. *"However, the description of the critical cluster properties remains the main problem of the application of any nucleation theory regardless of the approaches used to estimate the thermodynamic barrier for nucleation."* [20].

1.2.3 Introducing a Stochastic Framework to Nucleation Theory

The process of nucleation is driven by thermal fluctuations. Under certain circumstances statistical fluctuations might need to be included in the calculations. In [3] a description using master equations instead of mean population dynamics was studied. The values of the cluster concentrations on the surface of the seed differed in the two approaches. Furthermore, a nucleation rate lower than the classical equations predicted was obtained in the stochastic model. Therefore, it is important to develop a model by which we replace the standard mean-field evolution equations[5], the *Becker-Döring rate equations* [2], with a stochastic dynamical framework. Since the nucleation process can be regarded as a complex network of chemical reactions, it is natural to implement the same stochastic framework as used to study interstellar surface chemistry.

[5]In many-body systems the mean-field theory replaces all interactions to any particular body with an average interaction. This reduces a many-body problem to a one-body problem.

Figure 1.3: Open fireplace in Hampton Court Palace: an example of an anthropogenic aerosol source.

Figure 1.4: Clouds over London: an example of a natural aerosol source.

1.3 Overview

The common problem in heterogeneous chemical reactions and heterogeneous nucleation processes that we want to address in this thesis is the implementation of a formalism that takes into account statistical fluctuations in the time evolution of the systems under consideration. For the correct treatment of population fluctuations we employ methods based on the exploitation of the techniques of Quantum Field Theory applied to classical many-body systems, [15, 16] and [45], according to the Doi-Peliti formalism. These techniques have been summarised in the first sections of the review paper [60]. In *Chapter 2* we introduce the reader to the technical details of the Doi-Peliti formalism concentrating on a simple example. We start from a

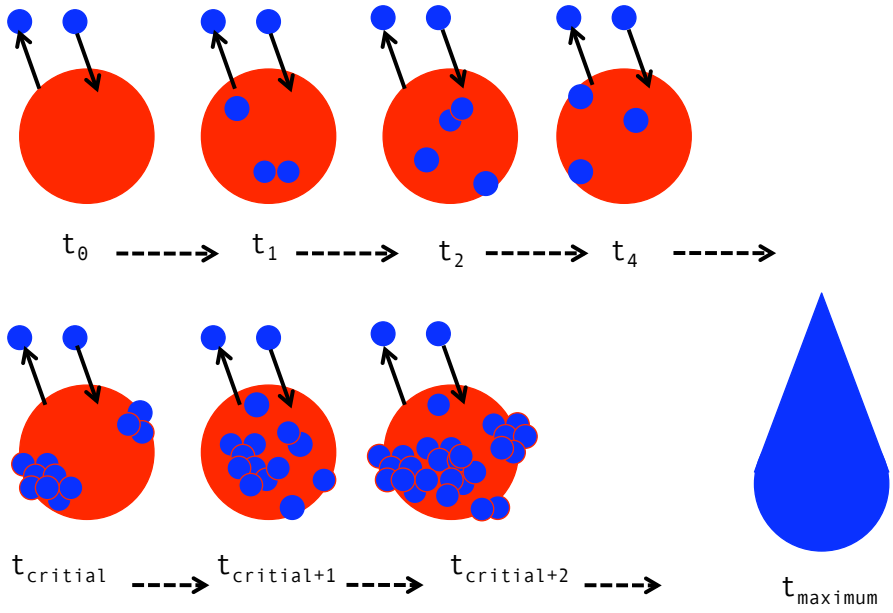

Figure 1.5: Activation of aerosol particles into cloud droplets: before a critical configuration is reached molecules from the surrounding gas-phase of the seed particle are gained and lost and the clusters grow and decay alternately. After a cluster has reached a certain critical size at time $t_{critical}$ the cluster will, on average, grow further easily and eventually form a cloud or mist droplet.

master equation[6], that is, the evolution equation of a probability distribution, for a heterogeneous chemical reaction of type $A + A \rightarrow C$. We introduce a spatial lattice where the microstates[7] of the system correspond to a set of occupation numbers at each lattice site. A Fock space is constructed using annihilation and creation operators at each lattice site. By means of this set-up it is easy to show that the master equation is equivalent to a Schrödinger-like equation. This enables us to employ techniques to a classical many-body problem that were originally developed in order to describe a quantum mechanical system where the fluctuations are due to a quantum uncertainty. We obtain the average particle population of the classical many-body system by developing a mechanism for computing expectation values of observables analogous to Feynman's path integral formulation. Introducing a stochastic variable in a Gaussian

[6]See Appendix A.

[7]A microstate describes a specific microscopic configuration of a system. A macrostate refers to the macroscopic configuration of the system and is characterised by a probability distribution on a certain ensemble of microstates.

transformation helps with the evaluation of the expression for the expectation values. The complex fluctuating solutions to a set of constraint equations, which are stochastic partial differential equations[8], are then averaged over all realisations of the stochastic noise. For numerical investigations, the solutions to the constraint equations can be generated by various numerical schemes taken from [37]. A comparison of the advantages and disadvantages between the Doi-Peliti formalism and other approaches concludes the chapter.

In *Chapter 3*, exact and numerical solutions to the full dynamical evolution equations as well as to the full stationary equations describing the evolution of the population of chemical species in time involved in heterogeneous reaction types are analysed. Furthermore, we highlight certain features of special cases where one of the rate coefficients is equal to zero. We give the exact solutions to the mean-field evolution equations of the average population of the reactants and the reaction products in zero space dimensions which we will compare later on to the respective quantities derived from the Doi-Peliti formalism. In order to verify the correct implementation and the validity of the dynamical solutions according to the stochastic framework we re-examine the steady state solution to the stationary master equation for the probability distribution of the population of chemical reactants in the single spatial site model. The latter can be obtained as an explicit solution in terms of Bessel functions derived from an Ansatz based on generating functions. We emphasise that great care has to be taken concerning the convergence of the series expansions of the generating function solution. The steady state solution that is known from the literature —see, for example, [27, 40, 5]— has to be restricted to a certain subspace of the parameter space and a novel stochastic steady state solution valid in the rest of the parameter space is presented. In the dynamical stochastic framework, the path integral average according to the Doi-Peliti formalism provides the means to derive the average density of reactants and reaction products. This average is computed for the single spatial site model using Monte Carlo methods [43]. The Code is written in the `GNU C` language. We expand on the models for the rate coefficients as employed in the community of astrochemists and discuss the numerical results for various data, especially for the heterogeneous hydrogen-hydrogen recombination and the heterogeneous oxygen-oxygen recombination in interstellar clouds. We investigate the dependence of the results on the rate with which molecules are accreted onto the grain particle as well as the dependence on the grain surface temperature and compare our

[8]Stochastic differential equations are differential equations with an additional random term with given stochastic properties.

findings in the mean-field approximation, the stochastic steady state results and the late-time value of the stochastic dynamical solution. We comment on the Stochastic Gauge representation and —after a short summary— end the chapter with some suggestions for some possible further work.

Chapter 4 is concerned with the extension of our calculations of heterogenoues chemical reactions of type $A + A \rightarrow C$ from zero space dimensions to one space dimension. We impose periodic boundary conditions and continue our analysis in the same fashion as in the previous chapter for chemical reactions taking place on the surface of a seed particle of the geometrical form of a ring. We conclude that for homogeneous surfaces and periodic boundary conditions the stochastic results are qualitatively the same as obtained in the single spatial site model. There are plenty of future projects that could expand on that basis.

The hydrogen-oxygen chemical reaction network is of particular interest since it is thought to be the main production route leading to the large abundance of water ice in dense cold sources. Therefore, we focus our attention on chemical reaction networks in *Chapter 5*. We start with the following class of heterogeneous chemical reactions, namely, $A + B \rightarrow C$. A stability analysis of the mean-field evolution equations shows that for specific special cases instabilities might occur. We derive the form of the stochastic constraint equations and the path integral average according to the Doi-Peliti formalism. Furthermore, we formulate the master equation for the hydrogen-oxygen network and obtain, by generalising the Gaussian transformation, the corresponding set of coupled stochastic partial differential equations constraining the fluctuating field associated with the density of reactants on the surface of the seed. We note that a thorough discussion with regards to the numerical evolution of the constraint equations is needed since the stochastic equations are stiff for interstellar conditions.

In *Chapter 6* we focus on nucleation processes taking place on foreign substances. After a short introduction to the Classical Nucleation Theory, we confront the predictions of the nucleation current in the Fletcher theory and in the Becker-Döring model. We employ various models concerning the form of the rate coefficients and analyse the overall behaviour of the evolution of the mean cluster concentrations and of the nucleation current according to the mean-field rate equations, namely, the Becker-Döring equations. We compare the value of the nucleation current with regards to the Fletcher theory, the kinetic Becker-Döring nucleation rate and the dynamical

Becker-Döring nucleation rate with experimental data considering the attachment of monomers from the surrounding gas-phase of the seed to clusters preciding on the surface of the seed particle. We proceed with the calculations for an effective surface tension of the vapour-liquid interface and include growth processes of clusters on the surface of the pre-existing particle that are due to diffusion on the surface of the seed in the model. In order to take statistical fluctuations in heterogeneous nucleation processes into account, we derive the constraint equations according to the Doi-Peliti formalism in analogy to Chapter 5 where we studied chemical reaction networks. A comparison between the mean-field framework and the stochastic framework is made for a simple choice of rate coefficients.

We complete the thesis in *Chapter 7* with some concluding remarks.

We want to point out that the definition of equilibrium will not be used in the sense of a thermodynamical equilibrium but rather in a broader context. We understand "equilibrium" as a sort of steady state that is the result of a late-time limit in a dynamical evolution. The words "steady state" will not be used as they convey the idea of a solution to a non-dynamical equation, that is an equation where the time derivatives are set to zero.

A list of symbols used in this thesis can be found in Appendix F.

Chapter 2

The Doi-Peliti Formalism

In this chapter we give an overview of the mathematical techniques employed to develop a dynamical stochastic framework to deal with the evolution of average densities of molecules or clusters diffusing on pre-existing surfaces. Our numerical investigations are based on the Doi-Peliti formalism —see [15, 16, 45, 60] which encorporates methods of Second Quantisation, Path Integral Calculations, Stochastic Differential Equations and the Monte Carlo Approximation Methods among others. Subindices identifying the particle type are suppressed when the context is clear. A schematic overview of the mathematical procedures is given in Figure 2.6.

2.1 Master Equation and Schrödinger-like Equation

In this chapter, we concentrate on the prototypical heterogeneous chemical reactions of type $A + A \longrightarrow C$, that is, situations in which atoms of a chemical species A are adsorbed onto grain particles where they can react with each other to produce diatomic molecules of another chemical species C —see Figure 2.1 and Figure 2.2. The probability of two reaction partners to form a particle of species C in the surrounding gas-phase of the seed is assumed to be negligible. We expect that when the number of incoming reactive species on an individual grain is small, the mean-field rate equations will fail to accurately describe the diffusive chemistry occurring on the surface of the grain particle since they do not take into account statistical fluctuations. As an alternative to the mean-field equations one can make use of a *master equation*. We start our investigations by presenting the master equation that describes the heterogeneous chemical process $A + A \longrightarrow C$. In the model to be considered one has a D-dimensional *lattice* $\mathbb{L}$ with *lattice constant* l, the microstates correspond to the

occupation numbers N_i, where i is a multi-index denoting the location in the lattice. On the lattice, we assume that particles of a certain chemical species A perform a continuous-time random walk. Molecules of species A are taken not to interact with each other except when they occupy the same lattice site and form a reaction product of chemical species C. In addition, particles of type A and C are allowed to occupy the same site.

The dynamics of this stochastic system is modelled by the following master equation:

$$\begin{aligned}
\frac{\mathrm{d}P(\{N_A\},\{N_C\};t)}{\mathrm{d}t} &= \bar{\iota}_A \sum_i \big(P(...,N_{A_i}-1,...,\{N_C\};t) - P(\{N_A\},\{N_C\};t)\big) + \\
&\bar{\iota}_C \sum_i \big(P(\{N_A\}...,N_{C_i}-1,...;t) - P(\{N_A\},\{N_C\};t)\big) + \\
&\bar{\kappa}_{AA} \sum_i \big((N_{A_i}+2)(N_{A_i}+1)P(...,N_{A_i}+2,...N_{C_i}-1,...;t) - \\
&\qquad N_{A_i}(N_{A_i}-1)P(\{N_A\},\{N_C\};t)\big) + \\
&\bar{\lambda}_A \sum_i \big((N_{A_i}+1)P(...,N_{A_i}+1,...,\{N_C\};t) - N_{A_i}P(\{N_A\},\{N_C\};t)\big) + \\
&\bar{\lambda}_C \sum_i \big((N_{C_i}+1)P(\{N_A\},...,N_{C_i}+1,...;t) - N_{C_i}P(\{N_A\},\{N_C\};t)\big) + \\
&\bar{\zeta}_A \sum_{\langle ij\rangle} \big((N_{A_i}+1)P(...,N_{A_i}+1,N_{A_j}-1,...,\{N_C\};t) - N_{A_i}P(\{N_A\}\{N_C\};t) + \\
&(N_{A_j}+1)P(...,N_{A_i}-1,N_{A_j}+1,...,\{N_C\};t) - N_{A_j}P(\{N_A\},\{N_C\};t)\big) + \\
&\bar{\zeta}_C \sum_{\langle ij\rangle} \big((N_{C_i}+1)P(\{N_A\},...,N_{C_i}+1,N_{C_j}-1,...;t) - N_{C_i}P(\{N_A\}\{N_C\};t) + \\
&(N_{C_j}+1)P(\{N_A\},...,N_{C_i}-1,N_{C_j}+1,...;t) - N_{C_j}P(\{N_A\},\{N_C\};t)\big).
\end{aligned} \tag{2.1}$$

The above equation (2.1) describes the evolution of the probability distribution $P(\{N_A\},\{N_C\};t)$ for the total number of adsorbed molecules $\{N_A\} := \{N_{A_1}, N_{A_2}, N_{A_3}, ..., N_{A_{i_{max}}}\}$ of species A where i_{max} is the maximum number of lattice sites and for the number of reaction products $\{N_C\} := \{N_{C_1}, N_{C_2}, N_{C_3}, ..., N_{C_{i_{max}}}\}$ of species C. The symbols N_{A_i} and N_{C_i} denote the number of A or C molecules at lattice site i, respectively. The rate coefficient $\bar{\iota}$ is called the *source rate* and gives the rate at which atoms from the gas-phase are adsorbed onto the grain surface. The rate

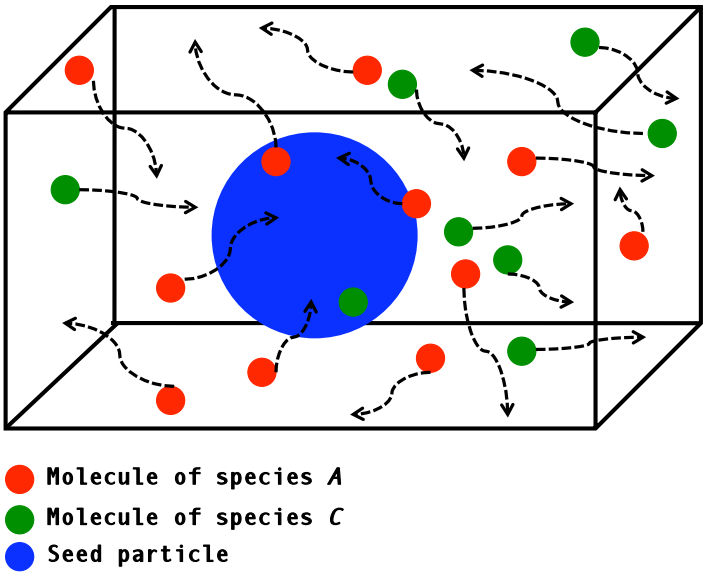

Figure 2.1: Seed particle —illustrated by the blue sphere— and several molecules of the chemical species A —represented by the red discs— and of the chemical species C —represented by the green discs— moving freely in the vicinity of the seed particle. Eventually, some particles of species A or C will impinge upon the surface of the seed particle and can, in turn, be emitted from the surface into the vicinity of the seed particle.

coefficient $\bar{\lambda}$ is called the *evaporation rate* and denotes the rate at which atoms are evaporated from the grain surface into the gas-phase. The rate coefficient $\bar{\kappa}$ is known as the *reaction rate* and gives the rate with which two atoms react at the same lattice site. The *diffusion rate constant* $\bar{\zeta}$ describes the rate at which the particles move on the lattice.

In our model, the chemical reaction is taking place on a D-dimensional lattice, allowing for multiple occupancy on each site —see Figure 2.3. This configuration is also called the *bosonic representation*. The changes in population which we consider are caused by:

1. adsorption of molecules of species A from the surrounding gas-phase of the grain particle (first line in equation (2.1)), and adsorption of molecules of species C from the surrounding gas-phase of the grain (second line in equation (2.1)),

2. binary reaction on the surface of the grain (third and fourth line in equation (2.1)),

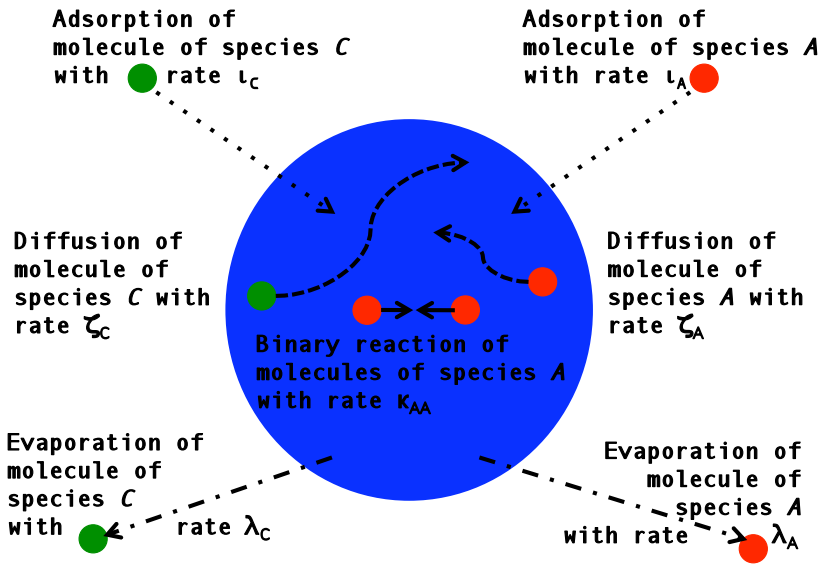

Figure 2.2: Molecules of the chemical species A and C can be adsorbed onto the surface of the seed at a rate ι and desorbed from the surface of the seed at a rate λ. The molecules of species A and C are assumed to move across the surface of the seed particle at a rate ζ. On the surface of the grain, molecules of species A can collide, react and form a particle of chemical species C at a rate κ.

3. evaporation of molecules of species A from the grain into the surrounding gas-phase (fifth line in equation (2.1)), and evaporation of molecules of species C from the grain particle into the surrounding gas-phase (sixth line in equation (2.1)),

4. particle hopping of molecules of species A from lattice site i to lattice site j (seventh line in equation (2.1)), and particle hopping of molecules of species C from site i to site j (ninth line in equation (2.1)),

5. particle hopping of molecules of species A from lattice site j to lattice site i (eighth line in equation (2.1)), and particle hopping of molecules of species C from site j to site i (last line in equation (2.1)).

In terms of the master equation (2.1) the above mentioned processes have the following consequences on the evolution of the probability distribution: for example, the probability $P(\{N_A\},\{N_C\};t)$ of finding a certain number of A or C particles at a specific lattice site increases at a rate $\bar{\iota}_A P(N_A-1,\{N_C\};t)$ when an atom of species A is adsorbed onto a grain particle that has already $\{N_A\}-1$ adsorbed atoms on the

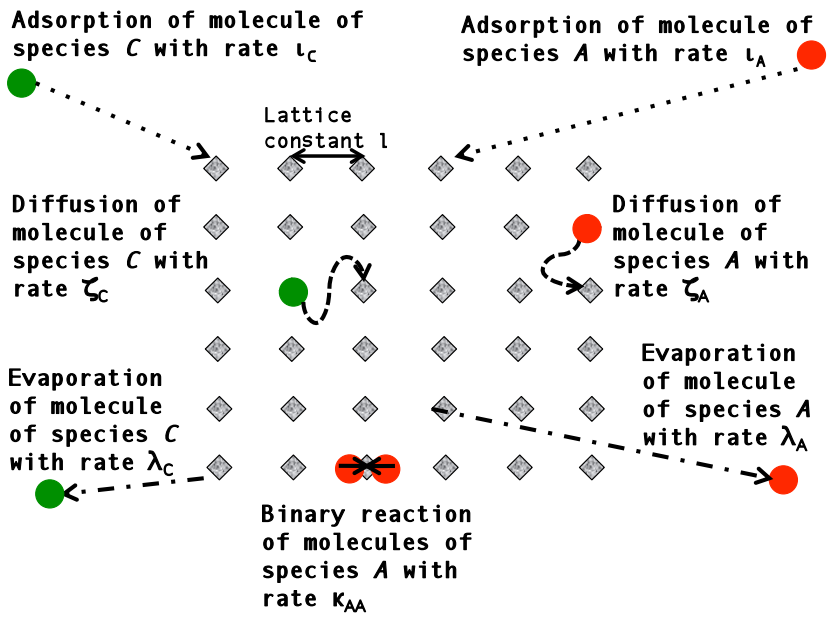

Figure 2.3: Portion of the 2-dimensional lattice on which the chemical reaction $A + A \longrightarrow C$ takes place. On each lattice site we allow multiple occupancy. The changes in population are caused by adsorption and evaporation of molecules, by hopping of molecules from site i to site j and by binary reaction between the A molecules.

surface and decreases at a rate of $\bar{\iota}_A P(\{N_A\},\{N_C\};t)$ when an A atom is adsorbed onto a grain with $\{N_A\}$ atoms on the surface. Furthermore, the probability distribution $P(\{N_A\},\{N_C\};t)$ decreases when an A atom is desorbed from a grain that has $\{N_A\}$ atoms on the surface and increases when an A atom is desorbed from a grain with $\{N_A\}+1$ adsorbed A atoms present on the surface of the grain with the respective rates of $\bar{\lambda}_A\{N_A\}P(\{N_A\},\{N_C\};t)$ and $\bar{\lambda}_A(\{N_A\}+1)P(\{N_A\}+1,\{N_C\};t)$. The remaining terms can be explained in the same fashion. The summation in equation (2.1) indicated by the symbol $\sum_{\langle ij\rangle}$ is taken over nearest neighbour sites only. The factors $(N_{X_i}+2),(N_{X_i}+1),N_{X_i},(N_{X_i}-1)$ describe the number of ways of choosing particles of species X involved in the considered process. The random initial condition is chosen corresponding to a *Poissonian distribution*[1] on each lattice site

$$P(\{N_A\},\{N_C\};t\equiv 0)=e^{-\bar{n}_A(0)-\bar{n}_C(0)}\prod_i \frac{\bar{n}_A(0)^{N_{A_i}}\bar{n}_C(0)^{N_{C_i}}}{N_{A_i}!N_{C_i}!}, \tag{2.2}$$

where $\bar{n}_A(0)$ and $\bar{n}_C(0)$ are the *initial average occupation numbers per lattice site* for

[1]See Appendix A.

the A and C particles, respectively.

Second Quantised Representation

In the next step we apply the methods of Second Quantisation according to the publications by Doi [15, 16] with the long-term goal in mind to map the framework of the dynamics of the heterogeneous chemical reaction system to a field theory. We rewrite the master equation as a *Schrödinger-like equation* for a many-body wave function[2]. This approach can be justified by noting that, first of all, the master equation is a differential equation of first order with respect to time, and also, the master equation is linear in the probability.

In order to simplify the notation we will suppress the dependence on space coordinates $\mathbf{x} = (x_1, x_2, ..., x_D)$. We work in an appropriate mathematical space, the *Fock space*. A Fock space $\mathcal{F}_\nu(\mathcal{H})$ is a Hilbert space[3] made from the direct sum of tensor products of single-particle Hilbert spaces $\mathcal{H}$

$$\mathcal{F}_\nu(\mathcal{H}) = \bigoplus_{n=0}^{\infty} S_\nu \mathcal{H}^{\otimes n}, \tag{2.3}$$

with S_ν a symmetrising (in the case of bosons) or antisymmetrising (in the case of fermions) operator. The Fock space is constructed by introducing the following operators at each lattice site i:

$$\begin{aligned} &\overset{+}{\mathsf{a}}_i,\ i \in \mathbb{L} : \textit{creation operator}, \\ &\overset{-}{\mathsf{a}}_i,\ i \in \mathbb{L} : \textit{annihilation operator}, \end{aligned}$$

which satisfy the commutation relations

$$\frac{1}{2}[\overset{+}{\mathsf{a}}_i, \overset{-}{\mathsf{a}}_j] := \frac{1}{2}(\overset{+}{\mathsf{a}}_i \overset{-}{\mathsf{a}}_j - \overset{-}{\mathsf{a}}_i \overset{+}{\mathsf{a}}_j) = \delta_{ij}. \tag{2.4}$$

The *vacuum state* $|\{0\}\rangle$ is defined by

$$\overset{-}{\mathsf{a}}_i \, |\{0\}\rangle = 0 \quad \forall i \in \mathbb{L}, \tag{2.5}$$

[2]More precisely, one obtains a Schrödinger equation with imaginary time. The substitution $t \to \mathrm{i}t$ (*Wigner rotation*) cancels out the imaginary i in the Schrödinger equation so that one is working with an equation on $\mathbb{R}$.

[3]A Hilbert space is an inner product space (vector space in which distances and angles can be measured) that is complete (the limit of a sequence of vectors is an element of the vector space).

with

$$|\{0\}\rangle := \bigotimes_j |0_j\rangle, \tag{2.6}$$

where $|0_j\rangle$ denotes the vacuum state in a single-particle Hilbert space.

It can be shown that the master equation (2.1) is equivalent to the Schrödinger-like equation

$$\frac{\mathrm{d}}{\mathrm{d}t}|\Psi(t)\rangle = -\mathtt{H}[\overset{+}{\mathtt{a}}_{A_i}, \overset{-}{\mathtt{a}}_{A_j}, \overset{+}{\mathtt{a}}_{C_k}, \overset{-}{\mathtt{a}}_{C_l}]|\Psi(t)\rangle, \tag{2.7}$$

with the *many-body wave function*

$$|\Psi(t)\rangle := \sum_{\{N_A\},\{N_C\}} P(\{N_A\},\{N_C\};t) \prod_i (\overset{+}{\mathtt{a}}_{A_i})^{N_{A_i}} (\overset{+}{\mathtt{a}}_{C_i})^{N_{C_i}} |\{0\}\rangle, \tag{2.8}$$

which is, in general, a non-Hermitian time evolution operator (*quasi-Hamiltonian*)[4]. The *Hamiltonian operator* for the heterogeneous chemical reaction of type $A + A \to C$ reads

$$\begin{aligned}\mathtt{H}[\overset{+}{\mathtt{a}}_{A_i}, \overset{-}{\mathtt{a}}_{A_j}, \overset{+}{\mathtt{a}}_{C_k}, \overset{-}{\mathtt{a}}_{C_l}] = & \sum_{M\in\{A,C\}} \sum_i (\overset{+}{\mathtt{a}}_{M_i} - \mathtt{1}_i)(\bar{\iota}_M \mathtt{1}_i - \bar{\lambda}_M \overset{-}{\mathtt{a}}_{M_i}) - \\ & \frac{\bar{\kappa}_{AA}}{V} \sum_i \left(\overset{+}{\mathtt{a}}_{C_i} - \overset{+2}{\mathtt{a}}_{A_i} \right) \overset{-2}{\mathtt{a}}_{A_i} + \\ & \sum_{M\in\{A,C\}} \bar{\zeta}_M \sum_{\langle ij\rangle} (\overset{+}{\mathtt{a}}_{M_i} - \overset{+}{\mathtt{a}}_{M_j})(\overset{-}{\mathtt{a}}_{M_i} - \overset{-}{\mathtt{a}}_{M_j}).\end{aligned} \tag{2.10}$$

The Schrödinger-like equation (2.7) is formally solved by

$$|\Psi(t)\rangle = \exp(-\mathtt{H}t)|\Psi(0)\rangle, \tag{2.11}$$

with

$$|\Psi(0)\rangle := \sum_{\{N_A\},\{N_C\}} e^{-\bar{n}_A(0)-\bar{n}_C(0)} \prod_i \frac{\bar{n}_A(0)^{N_{A_i}} \bar{n}_C(0)^{N_{C_i}}}{N_{A_i}! N_{C_i}!} (\overset{+}{\mathtt{a}}_{A_i})^{N_{A_i}} (\overset{+}{\mathtt{a}}_{C_i})^{N_{C_i}} |\{0\}\rangle. \tag{2.12}$$

For the verification of the equivalence between the master equation (2.1) and the Schrödinger equation (2.7) one has to insert the states $\prod_i (\overset{+}{\mathtt{a}}_{A_i})^{N_{A_i}} (\overset{+}{\mathtt{a}}_{C_i})^{N_{C_i}} |\{0\}\rangle$ on

[4] A Hamiltonian is the observable corresponding to the total energy of the system. A Hermitian operator H satisfies

$$\langle u|Hv\rangle = \langle Hu|v\rangle. \tag{2.9}$$

Hermitian operators have real eigenvalues and orthogonal eigenfunctions.

both sides of the master equation —equation (2.1)— and sum over the set of all occupation numbers $\{N_A\}$ and $\{N_C\}$. The form of the many-body wave function (2.8) can be made plausible when considering the *state vector* $|N_i\rangle$ at site $i \in \mathbb{L}$, namely,

$$|N_i\rangle := \overset{+}{\mathtt{a}}_i^{N_i} \, |0_i\rangle. \tag{2.13}$$

It holds that

$$\bar{\mathtt{a}}_i \, |N_i\rangle = N_i |N_i - 1\rangle, \quad \overset{+}{\mathtt{a}}_i \, |N_i\rangle = |N_i + 1\rangle. \tag{2.14}$$

2.2 Expectation Values of Observables

We are interested in obtaining the expectation values for specific observables, in particular, the average number density of the chemical reaction partners and products involved in the heterogeneous chemical reaction $A + A \rightarrow C$. With respect to the latter considerations, the *expectation values* of observables $\mathtt{O}$ are given by

$$\langle \mathtt{O} \rangle := \sum_{\{N_i\}} O(\{N_i\}) P(\{N_i\}; t). \tag{2.15}$$

We want the expectation values of the observables to be linear in the probabilities according to the classical microscopic theory. The above expression (2.15) can be rewritten in terms of projection states. A *projection state* $\langle \{\mathtt{P}\}|$ is defined as

$$\langle \{\mathtt{P}\}| := \langle \{0\}| e^{\sum_j \bar{\mathtt{a}}_j}. \tag{2.16}$$

By definition, the projection state is a left eigenstate of all creation operators with unit eigenvalue

$$\langle \{\mathtt{P}\}| \, \overset{+}{\mathtt{a}}_i = \langle \{\mathtt{P}\}| \quad \forall i \in \mathbb{L}, \tag{2.17}$$

and obeys the relation

$$\langle \{\mathtt{P}\} | \{0\} \rangle = 1. \tag{2.18}$$

Furthermore,

$$\langle \{\mathtt{P}\} | \Psi(t) \rangle = 1. \tag{2.19}$$

Conservation of probability of the master equation requires that

$$\langle \{\mathtt{P}\} | \mathtt{H} = 0. \tag{2.20}$$

From the above mentioned properties of the projection state it follows that

$$\langle \mathtt{O} \rangle = \sum_{\{N_i\}} O(\{N_i\}) P(\{N_i\};t) = \sum_{\{N_i\}} \langle \{\mathtt{P}\} | \mathtt{O}(\bar{\mathtt{a}}_i \overset{+}{\mathtt{a}}_i) \prod_i (\overset{+}{\mathtt{a}}_i)^{N_i} | \{0\} \rangle P(\{N_i\};t)$$
$$= \langle \{\mathtt{P}\} | \mathtt{O}(\bar{\mathtt{a}}_i \overset{+}{\mathtt{a}}_i) | \Psi(t) \rangle. \tag{2.21}$$

When interested in, for example, the average number of particles at a given lattice site irrespective of the number of particles elsewhere it is convenient to commute the factor of $e^{\sum_i \bar{\mathtt{a}}_i}$ through to the right in the operators $\mathtt{O}$ and $\mathtt{H}$ in equation (2.28). This has the effect of shifting $\overset{+}{\mathtt{a}} \rightarrow \overset{+}{\mathtt{a}} + 1$ using $e^{\bar{\mathtt{a}}} \overset{+}{\mathtt{a}} = (\overset{+}{\mathtt{a}} + 1) e^{\bar{\mathtt{a}}}$. The operators are then normal ordered. A similar manipulation, the *Doi shift* can be performed in the field theory by a corresponding field shift. The operator $\mathtt{O}$ and its normal ordered counterpart have the same expectation value if all creation operators occurring in the normal ordered operator are replaced by the identity operator —see for example [60]. In particular, the density operator $\overset{+}{\mathtt{a}}\bar{\mathtt{a}}$ reduces to the annihilation operator $\bar{\mathtt{a}}$. After having performed the Doi shift we assume that the operator $\mathtt{O}$ depends only on the annihilation operators.

Coherent State Representation

We divide the temporal evolution into T time slices of infinitesimal size $\triangle t = tT^{-1}$:

$$|\Psi(t)\rangle = \lim_{\triangle t \to 0} \exp\left(-\mathtt{H} \triangle t\right)^{\frac{t}{\triangle t}} |\Psi(0)\rangle. \tag{2.22}$$

Before the limit $\triangle t \to 0$ is taken, the second quantised operators are mapped onto complex numbers by inserting a complete set of coherent states $|\mathtt{C}_i(t)\rangle$ at each time slice. *Coherent states* are right eigenstates of the annihilation operator

$$\bar{\mathtt{a}}_i \, |\mathtt{C}_i(t)\rangle = \varphi_i(t) |\mathtt{C}_i(t)\rangle \quad i \in \mathbb{L}, \tag{2.23}$$

where the eigenvalue $\varphi_i(t)$ is a complex function. The duals $\langle \mathtt{C}_i(t)|$ are left eigenstates of the creation operator

$$\langle \mathtt{C}_i(t)| \, \overset{+}{\mathtt{a}}_i = \langle \mathtt{C}_i(t)| \varphi_i^*(t) \quad i \in \mathbb{L}, \tag{2.24}$$

with $\varphi_i^*(t)$ denoting the complex conjugate of the eigenvalue $\varphi_i(t)$. We have, in the basis of state vectors,

$$|\mathtt{C}_i(t)\rangle := e^{-\frac{1}{2}|\varphi_i(t)|^2 + \varphi_i(t) \overset{+}{\mathtt{a}}_i} |0_i\rangle,$$
$$\langle \mathtt{C}_i(t)| := \langle 0_i | e^{-\frac{1}{2}|\varphi_i^*(t)|^2 + \varphi_i^*(t) \bar{\mathtt{a}}_i}. \tag{2.25}$$

The coherent states are over-complete. Still, one can use them to create the identity

$$\mathtt{1} = \frac{1}{\pi}\int \mathrm{d}[\Re(\varphi_i)]\mathrm{d}[\Im(\varphi_i)]|\mathtt{C}_i(t)\rangle\langle\mathtt{C}_i(t)|, \tag{2.26}$$

for a single lattice site $i \in \mathbb{L}$, and for multiple lattice sites accordingly,

$$\mathtt{1} = \int \prod_i \left(\frac{1}{\pi}\mathrm{d}[\Re(\varphi_i)]\mathrm{d}[\Im(\varphi_i)]\right)|\{\mathtt{C}(\mathtt{t})\}\rangle\langle\{\mathtt{C}(\mathtt{t})\}|, \tag{2.27}$$

with $|\{\mathtt{C}(\mathtt{t})\}\rangle := \bigotimes_j |\mathtt{C}_j(t)\rangle$. Let us recall the formula for the expectation values of observables

$$\langle\mathtt{O}\rangle = \langle\{\mathtt{P}\}|\mathtt{O}|\Psi(t)\rangle = \langle\{0\}|e^{\sum_i \bar{\mathtt{a}}_i}\mathtt{O}e^{-\mathtt{H}t}|\Psi(0)\rangle, \tag{2.28}$$

where the initial many-body wave function takes the form —see equations (2.2) and (2.8)—

$$|\Psi(0)\rangle := e^{\bar{n}(0)\left(\sum_i \overset{+}{\mathtt{a}}_i - 1\right)}|\{0\}\rangle. \tag{2.29}$$

We observe the following proportionalities:

$$\langle\{\mathtt{P}\}| \propto \langle\{\mathtt{C}_1(t)\}|, \tag{2.30}$$

and for Poissonian initial conditions we have

$$|\Psi(0)\rangle \propto |\{\mathtt{C}_{\bar{n}(0)}(t)\}\rangle, \tag{2.31}$$

with

$$\begin{aligned}
&\langle\{\mathtt{C}_1(t)\}| := \langle\{\mathtt{C}(t)\}|_{\varphi_j^*=1} = \langle\{0\}|e^{-\frac{1}{2}+\sum_i \bar{\mathtt{a}}_i}, \\
&|\{\mathtt{C}_{\bar{n}(0)}(t)\}\rangle := |\{\mathtt{C}(t)\}\rangle_{\varphi_j=\bar{n}(0)} = e^{-\frac{1}{2}|\bar{n}(0)|^2+\bar{n}(0)\sum_i \overset{+}{\mathtt{a}}_i}|\{0\}\rangle,
\end{aligned} \tag{2.32}$$

for all admissible values of j. Therefore, one can recast the equation for the expectation values (2.28) into

$$\langle\mathtt{O}(t)\rangle \propto \langle\{\mathtt{C}_1(t)\}|\mathtt{O}e^{-\mathtt{H}t}|\{\mathtt{C}_{\bar{n}(0)}(t)\}\rangle. \tag{2.33}$$

We break the time interval $[t_0, t_T]$ into T short slices of duration $\triangle t = \frac{t_T - t_0}{T}$. We rewrite the expression

$$e^{-\mathtt{H}t} = \underbrace{e^{-\mathtt{H}\triangle t}e^{-\mathtt{H}\triangle t}\ldots.}_{\text{T times}}, \tag{2.34}$$

occurring in the equation for the expectation values (2.33) and insert the identity as defined in (2.27) between each factor [6]. As a consequence, the discrete version of the

expectation values of operators $\mathtt{O}(t)$ reads

$$\langle \mathtt{O}(t) \rangle \propto \lim_{\triangle t \to 0} \int \left(\prod_{i,\tau} \mathrm{d}[\Re(\varphi_{i,\tau})] \mathrm{d}[\Im(\varphi_{i,\tau})] \right) \langle \{\mathtt{C}_1\} | \mathtt{O} | \{\mathtt{C}\}_T \rangle \times \cdots$$
$$\cdots \times \left(\prod_{\tau=\triangle t}^{T} \langle \{\mathtt{C}\}_\tau | e^{-\mathtt{H}\triangle t} | \{\mathtt{C}\}_{\tau-\triangle t} \rangle \right) \langle \{\mathtt{C}\}_{\tau=0} | \{\mathtt{C}_{\bar{n}(0)}\} \rangle, \tag{2.35}$$

where we have labelled each time slice by a time index $\tau \in [0, \triangle t, 2\triangle t, ..., T]$. The normalisation constant will be determined later on. One has that

$$\langle \{C\}_\tau | \exp\left(-\mathtt{H}(\overset{+}{\mathtt{a}}_i \bar{\mathtt{a}}_i) \triangle t \right) | \{C\}_{\tau-\triangle t} \rangle = \langle \{C\}_\tau | \{C\}_{\tau-\triangle t} \rangle \exp\left(-H(\{\varphi^*\}_\tau, \{\varphi\}_{\tau-\triangle t}) \triangle t \right), \tag{2.36}$$

where the function H is obtained via

$$H(\{\varphi^*\}_\tau, \{\varphi\}_{\tau-\triangle t}) \propto \langle \{C\}_\tau | \mathtt{H}(\overset{+}{\mathtt{a}}_i \bar{\mathtt{a}}_i) | \{C\}_{\tau-\triangle t} \rangle, \tag{2.37}$$

and

$$\langle \{C\}_\tau | \{C\}_{\tau-\triangle t} \rangle = \prod_i \langle C_{i,\tau} | C_{i,\tau-\triangle t} \rangle$$
$$= \prod_i \exp\left(-\varphi^*_{i,\tau} \big(\varphi_{i,\tau} - \varphi_{i,\tau-\triangle t} \big) \right) \exp\left(\frac{1}{2} |\varphi_{i,\tau}|^2 - \frac{1}{2} |\varphi_{i,\tau-\triangle t}|^2 \right), \tag{2.38}$$

where we use the overlap relation for two coherent states $|C_\alpha\rangle$ and $|C_\beta\rangle$ with eigenvalues C_α and C_β between different time slices, respectively:

$$\langle C_\alpha | C_\beta \rangle = \exp\left(-\frac{1}{2} |C_\alpha|^2 - \frac{1}{2} |C_\beta|^2 + C^*_\alpha C_\beta \right). \tag{2.39}$$

The contributions of the second exponential in (2.38) cancel except for the initial and final time slice. At each time slice τ the first exponential renders

$$\exp\left(-\varphi^*_{i,\tau} \frac{\mathrm{d}\varphi_{i\tau}}{\mathrm{d}t} \triangle t + \mathcal{O}(\triangle t^2) \right), \tag{2.40}$$

since $\mathtt{O} = \mathtt{O}(\bar{\mathtt{a}}_i)$ and

$$\langle \{C_1\} | \mathtt{O}(\bar{\mathtt{a}}_i) | \{C\}_T \rangle = \langle \{C_1\} | \{C\}_T \rangle O(\{\varphi\}_T), \tag{2.41}$$

where the functional[5] $O(\{\varphi\}_T)$ is derived by replacing the annihilation operators with the complex eigenvalue functions in the operator expression $\mathtt{O}(\bar{\mathtt{a}}_i)$. The remaining factors that do not cancel, $\langle\{C_1\}|\{C\}_T\rangle\langle\{C\}_T|$, give

$$\prod_i \exp\big(-\varphi^*_{1,i}(\varphi_{1,i}-\varphi_{i,T})+\frac{1}{2}|\varphi_{1,i}|^2-\frac{1}{2}|\varphi_{i,T}|^2+\frac{1}{2}|\varphi_{i,T}|^2\big)\propto\exp\sum_i\varphi_{i,T}, \quad (2.42)$$

with $\varphi_{1,i}=1$ for all i. The factors arising from $|\{C\}_0\rangle\langle\{C\}_0|\{C_{\bar{n}(0)}\}\rangle$ are

$$\prod_i \exp\big(\varphi^*_{i,0}\bar{n}(0)-\frac{1}{2}|\varphi_{i,0}|^2-\frac{1}{2}|\varphi_{i,0}|^2-\frac{1}{2}|\bar{n}(0)|^2\big)\propto\exp\sum_i(\bar{n}(0)\varphi^*_{i,0}-|\varphi_{i,0}|^2). \quad (2.43)$$

The time ordering of the eigenvalue functions and the complex conjugate of the eigenvalue functions in the arguments of the quasi-Hamiltonian is assumed not to be an issue with the understanding of the complex conjugates to follow in time the original fields. We expand the exponential function for small $\triangle t$, neglect higher order terms in $\triangle t$ and, in the limit $\triangle t\to 0$, obtain the following expression for the expectation value of an operator $\mathtt{O}$:

$$\langle\mathtt{O}(t)\rangle\propto\int\prod_i \mathrm{D}\varphi_i\mathrm{D}\varphi^*_i O(\{\varphi\}_T)\exp\left(-S(\{\varphi^*\},\{\varphi\})\right), \quad (2.44)$$

where D denotes the *measure* of the functional integral[6] and with the action functional[7] $S(\{\varphi^*\},\{\varphi\})$

$$S(\{\varphi^*\},\{\varphi\})=\sum_i\left(-\varphi_i(T)-\bar{n}(0)\varphi^*_i(0)+|\varphi_i(0)|^2+\int_0^T \mathrm{d}t\,(\varphi^*_i(t)\partial_t\varphi_i(t)+H(\{\varphi^*\},\{\varphi\}))\right). \quad (2.45)$$

[5] A functional is a function on a function space $\mathbb{B}$ that determines uniquely a number in $\mathbb{R}$ for each element in $\mathbb{B}$.

[6] In contrast to the domain of an ordinary integral which is a region in spacetime, the domain of a functional integral is a space of functions.

[7] The evolution of a physical system corresponds to the requirement of the action being stationary for small perturbations about the true evolution.

After having performed the field theoretic Doi shift, the shifted action reads

$$\tilde{S}(\{\tilde{\varphi}\},\{\varphi\}) = \sum_i \Bigg(- \bar{n}_A(0) + \bar{n}_A(0)(\tilde{\varphi}_{A,i}(0) - \bar{n}_A(0)) - \\ \bar{n}_C(0) + \bar{n}_C(0)(\tilde{\varphi}_{C,i}(0) - \bar{n}_C(0)) + \\ \int_0^T \mathrm{d}t \left(\tilde{\varphi}_{A,i}(t)\partial_t \varphi_{A,i}(t) + \tilde{\varphi}_{C,i}(t)\partial_t \varphi_{C,i}(t) + \tilde{H}(\{\tilde{\varphi}\},\{\varphi\}) \right) \Bigg), \tag{2.46}$$

where —following the procedure of [60]— one has the shifted Hamiltonian

$$\tilde{H}[\{\varphi\},\{\tilde{\varphi}\}] = -\tilde{\varphi}_{A,i}(t)(\bar{\iota}_A - \bar{\lambda}_A \varphi_{A,i}(t)) - \tilde{\varphi}_{C,i}(t)(\bar{\iota}_C - \bar{\lambda}_C \varphi_{C,i}(t)) + \\ \bar{\kappa}_{AA}(2\tilde{\varphi}_{A,i}(t) + \tilde{\varphi}^2_{A,i}(t) - \tilde{\varphi}_{C,i}(t))\varphi^2_{A,i}(t) - \\ \tilde{\varphi}_{A,i}(t)\bar{\zeta}_A \Delta \varphi_{A,i}(t) - \tilde{\varphi}_{C,i}(t)\bar{\zeta}_C \Delta \varphi_{C,i}(t), \tag{2.47}$$

where $\Delta := \sum_{k=1}^{D} \frac{\partial^k}{\partial x^k}$ is the *Laplace operator*. The symbol $\tilde{\varphi}(t)$ is the *shifted eigenvalue* of the dual of a coherent state under the creation operator defined by $\tilde{\varphi}(t) := \varphi^*(t) - 1$. Accordingly, all fields $\mathfrak{F}$ that incorporate shifted eigenvalues instead of the original eigenvalues will be denoted by the symbol $\tilde{\mathfrak{F}}$ in the sequel. In a next step, we take the continuum limit of the lattice expectation value via

$$\sum_i \longrightarrow \int l^{-D}\, \mathrm{d}^D x. \tag{2.48}$$

The dimensions of the unknown functions and of the constants are chosen by examining the discrete Hamiltonian operator (2.10):

$$\begin{aligned} &\varphi_{A_i,C_j}(t) \to \psi_{A,C}(\mathbf{x},t) l^D, && \tilde{\varphi}_{A_i,C_j}(t) \to \tilde{\psi}_{A,C}(\mathbf{x},t), \\ &\bar{\zeta}_{A,C} \to \zeta_{A,C} l^{-2}, && \bar{\kappa}_{AA} \to \kappa_{AA} l^{-D}, \\ &\bar{\lambda}_{A,C} \to \lambda_{A,C}, && \bar{\iota}_{A,C} \to \iota_{A,C} l^D, \\ &\bar{n}_{A,C}(0) \to n_{A,C}(0) l^D. \end{aligned} \tag{2.49}$$

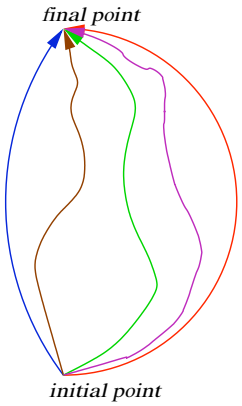

Figure 2.4: Different paths from the initial point to the final point: the path integral sums up all possible paths from the initial to the final point with a certain weight.

The object $\tilde{\psi}_{A,C}(\mathbf{x},t)$ is dimensionless and $\psi_{A,C}(\mathbf{x},t)$ scales like a density. The newly introduced quantities have the following Standard International Units:

$$\begin{aligned} &[\psi_{A,C}(\mathbf{x},t)] = \mathrm{m}^{-D}, && [\zeta_{A,C}] = \mathrm{m}^2\mathrm{s}^{-1}, \\ &[\kappa_{AA}] = \mathrm{m}^D\mathrm{s}^{-1}, && [\iota_{A,C}] = \mathrm{m}^{-D}\mathrm{s}^{-1}, \\ &[\lambda_{A,C}] = \mathrm{s}^{-1}, && [n_{A,C}(0)] = \mathrm{m}^{-D}. \end{aligned} \tag{2.50}$$

In the continuum limit, the average particle density for the A molecules in the Doi-Peliti formalism is given by the path integral average of the complex eigenvalue functions of the coherent state vectors under the annihilation operator:

$$\begin{aligned} \langle \psi_A(\mathbf{x},t)\rangle &:= \langle\{0\}|\psi_A(\mathbf{x},t)e^{-\tilde{S}[\psi,\tilde{\psi}]}|\{0\}\rangle \\ &= \frac{\int \mathrm{D}\psi_A\mathrm{D}\psi_C\mathrm{D}\tilde{\psi}_A\mathrm{D}\tilde{\psi}_C\psi_A(\mathbf{x},t)e^{-\tilde{S}[\psi,\tilde{\psi}]}}{\int \mathrm{D}\psi_A\mathrm{D}\psi_C\mathrm{D}\tilde{\psi}_A\mathrm{D}\tilde{\psi}_C e^{-\tilde{S}[\psi,\tilde{\psi}]}}. \end{aligned} \tag{2.51}$$

For an illustration of the interpretation of a path integral see Figure 2.4 and Figure 2.5. The shifted action $\tilde{S}$ for the chemical reaction $A + A \longrightarrow C$ in the continuum

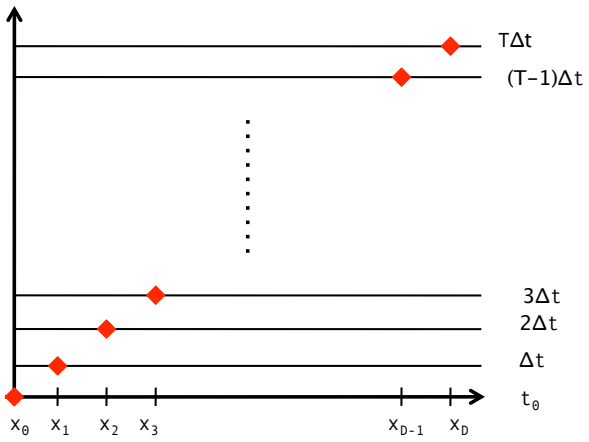

Figure 2.5: Definition of the path integral: we divide the time interval $[t_0, t_T]$ into small time slices $\triangle t = tT^{-1}$ and integrate over the coordinates x_k of each slice. In the continuum limit, $\triangle t \to 0$.

limit is given by

$$\begin{aligned}\tilde{S}[\psi_A, \tilde{\psi}_A, \psi_C, \tilde{\psi}_C] := \int \mathrm{d}^D x \Big(& - n_A(0) + n_A(0)(\tilde{\psi}_A(\mathbf{x}, 0) - n_A(0)) - \\ & n_C(0) + n_C(0)(\tilde{\psi}_C(\mathbf{x}, 0) - n_C(0)) + \\ & \int_0^{t_T} \mathrm{d}t \big(\tilde{\psi}_A(\mathbf{x}, t) \frac{\partial \psi_A(\mathbf{x}, t)}{\partial t} + \tilde{\psi}_C(\mathbf{x}, t) \frac{\partial \psi_C(\mathbf{x}, t)}{\partial t} + \\ & \tilde{H}[\psi_A(\mathbf{x}, t), \tilde{\psi}_A(\mathbf{x}, t), \psi_C(\mathbf{x}, t), \tilde{\psi}_C(\mathbf{x}, t)] \Big),\end{aligned} \tag{2.52}$$

with the *shifted Hamiltonian* $\tilde{H}$ in the continuum limit

$$\begin{aligned}\tilde{H}[\psi_A, \tilde{\psi}_A, \psi_C, \tilde{\psi}_C] = & -\tilde{\psi}_A(\mathbf{x}, t)(\iota_A - \lambda_A \psi_A(\mathbf{x}, t)) - \tilde{\psi}_C(\mathbf{x}, t)(\iota_C - \lambda_C \psi_C(\mathbf{x}, t)) + \\ & \kappa_{AA}(2\tilde{\psi}_A(\mathbf{x}, t) + \tilde{\psi}_A^2(\mathbf{x}, t) - \tilde{\psi}_C(\mathbf{x}, t))\psi_A^2(\mathbf{x}, t) - \\ & \tilde{\psi}_A(\mathbf{x}, t)\zeta_A \Delta \psi_A(\mathbf{x}, t) - \tilde{\psi}_C(\mathbf{x}, t)\zeta_C \Delta \psi_c(\mathbf{x}, t).\end{aligned} \tag{2.53}$$

Reverse Standard Field Theory Representation of a Langevin-type[8] Stochastic Partial Differential Equation

In order to obtain an action linear in the eigenvalue functions $\tilde{\psi}(\mathbf{x},t)$ we introduce an auxiliary field, $\eta(\mathbf{x},t)$. We want to untangle the quadratic term[9] $\tilde{\psi}_A^2(\mathbf{x},t)$ in the second line of the above formula (2.53). A linear expression in $\tilde{\psi}_A(\mathbf{x},t)$ can be obtained by means of a *Gaussian transformation*:

$$e^{-\kappa_{AA}\int_0^{t_T}\mathrm{d}t\int\mathrm{d}^Dx\tilde{\psi}_A^2(\mathbf{x},t)\psi_A^2(\mathbf{x},t)}\propto\int\mathrm{D}\eta\;\mathcal{P}[\eta]e^{\mathrm{i}\sqrt{2\kappa_{AA}}\int_0^{t_T}\mathrm{d}t\int\mathrm{d}^Dx\tilde{\psi}_A(\mathbf{x},t)\psi_A(\mathbf{x},t)\eta(\mathbf{x},t)},\qquad(2.54)$$

where $\mathcal{P}[\eta]$ is the *Gaussian probability distribution* for a *white noise*[10] $\eta(\mathbf{x},t)$,

$$\mathcal{P}[\eta]=e^{-\frac{1}{2}\int_0^{t_T}\mathrm{d}t\int\mathrm{d}^Dx\eta^2(\mathbf{x},t)}.\qquad(2.55)$$

The above procedure leads to the shifted action $\tilde{S}$ being linear in $\tilde{\psi}_A$. Thus, one can integrate out over $\tilde{\psi}_A(\mathbf{x},t)$ and $\tilde{\psi}_C(\mathbf{x},t)$ in (2.51) which results in the following expression:

$$\begin{aligned}\langle\mathsf{O}[\psi_A,\psi_C]\rangle&\propto\int\mathrm{D}\psi_A\mathrm{D}\psi_C\mathrm{D}\eta\;\mathsf{O}[\psi_A,\psi_C]\delta[\mathcal{F}_A]\delta[\mathcal{F}_C]\delta[\mathcal{F}_{A_0}]\delta[\mathcal{F}_{C_0}]\mathcal{P}[\eta]\\&\propto\int\mathrm{D}\eta\;\mathsf{O}[\bar{\psi}_A[\eta(\mathbf{x},t),\mathbf{x},t],\bar{\psi}_C[\eta(\mathbf{x},t),\mathbf{x},t]]\mathcal{P}[\eta],\end{aligned}\qquad(2.56)$$

where $\delta[\mathcal{F}]$ is a *functional Dirac delta distribution*[11]. In its generalised Fourier representation it is defined by

$$\delta[\mathcal{F}]:=constant\int\mathrm{D}\gamma(y)e^{\int\mathrm{d}y\gamma(y)\mathcal{F}[\mathbf{z}(y),y]},\qquad(2.58)$$

[8] See Appendix A.

[9] Note that this manipulation is only applicable for binary chemical reactions.

[10] See Appendix A.

[11] A Dirac Delta Function is, loosely speaking, a 'function' that has the value zero everywhere except if the argument is equal to zero where its value is infinitely large in such a way that its total integral is one. Mathematically more rigorous is the following definition

$$\int_{-\infty}^{\infty}f(x)\delta(dx)=f(0),\qquad(2.57)$$

for all continuous compactly supported functions f, the integral a Lesbegue integral and δ a measure. The Dirac delta function may be seen as a continuous analog of the Kronecker delta.
A Dirac Delta Functional is regarded as a generalised function of the above definition.

with $\gamma(y)$ an arbitrary function and $\mathbf{z}(y)$ being a multicomponent field satisfying the constraint

$$\mathcal{F}[\mathbf{z}(y), y] = 0. \tag{2.59}$$

Accordingly, the functions $\bar{\psi}_A[\eta(\mathbf{x},t),\mathbf{x},t]$ and $\bar{\psi}_C[\eta(\mathbf{x},t),\mathbf{x},t]$ satisfy the following constraint equations:

$$\mathcal{F}_A[\bar{\psi}_A(\mathbf{x},t),\mathbf{x},t] \equiv -\frac{\partial\bar{\psi}_A(\mathbf{x},t)}{\partial t} + \zeta_A\Delta\bar{\psi}_A(\mathbf{x},t) - 2\kappa_{AA}\bar{\psi}_A^2(\mathbf{x},t) - \lambda_A\bar{\psi}_A(\mathbf{x},t) + \iota_A + \mathrm{i}\sqrt{2\kappa_{AA}}\bar{\psi}_A(\mathbf{x},t)\eta(\mathbf{x},t) = 0, \tag{2.60}$$

$$\mathcal{F}_C[\bar{\psi}_C(\mathbf{x},t),\mathbf{x},t] \equiv -\frac{\partial\bar{\psi}_C(\mathbf{x},t)}{\partial t} + \zeta_C\Delta\bar{\psi}_C(\mathbf{x},t) + \kappa_{AA}\bar{\psi}_A^2(\mathbf{x},t) - \lambda_C\bar{\psi}_C(\mathbf{x},t) + \iota_C = 0, \tag{2.61}$$

$$\mathcal{F}_{A_0}[\bar{\psi}_A(\mathbf{x},0),\mathbf{x},0] \equiv \bar{\psi}_A(\mathbf{x},0) - n_A(0) = 0, \tag{2.62}$$

$$\mathcal{F}_{C_0}[\bar{\psi}_C(\mathbf{x},0),\mathbf{x},0] \equiv \bar{\psi}_C(\mathbf{x},0) - n_C(0) = 0, \tag{2.63}$$

The remaining term incorporating the initial conditions cancels out in the normalisation of the average. It follows from equation (2.56) that the average particle densities for the A and C molecules on the surface of the grain, respectively, are given by the path integral average (PIA)

$$\langle\psi_{A,C}(\mathbf{x},t)\rangle = \frac{\int \mathrm{D}\eta\ \bar{\psi}_{A,C}[\eta(\mathbf{x},t),\mathbf{x},t]e^{-\frac{1}{2}\int_0^{t_T}\mathrm{d}t\int\mathrm{d}^D x\eta^2(\mathbf{x},t)}}{\int \mathrm{D}\eta e^{-\frac{1}{2}\int_0^{t_T}\mathrm{d}t\int\mathrm{d}^D x\eta^2(\mathbf{x},t)}}. \tag{2.64}$$

The stochastic noise $\eta(\mathbf{x},t)$ has zero mean value

$$\langle\eta(\mathbf{x},t)\rangle_{\mathcal{P}[\eta]} = 0, \tag{2.65}$$

and unit variance, that is, an auto-correlation given by

$$\langle\eta(\mathbf{x},t)\eta(\mathbf{x}',t')\rangle_{\mathcal{P}[\eta]} = \delta^{(D)}(\mathbf{x}-\mathbf{x}')\delta(t-t'), \tag{2.66}$$

where δ denotes a Dirac Delta distribution. The above feature becomes evident when considering the Gaussian distribution (2.55). The constraint equation (2.60) is an inhomogeneous partial stochastic differential equation with multiplicative noise for a complex fluctuating unknown field. Equations (2.60) and (2.61) resemble the deterministic partial differential equations that describe the evolution of the mean particle

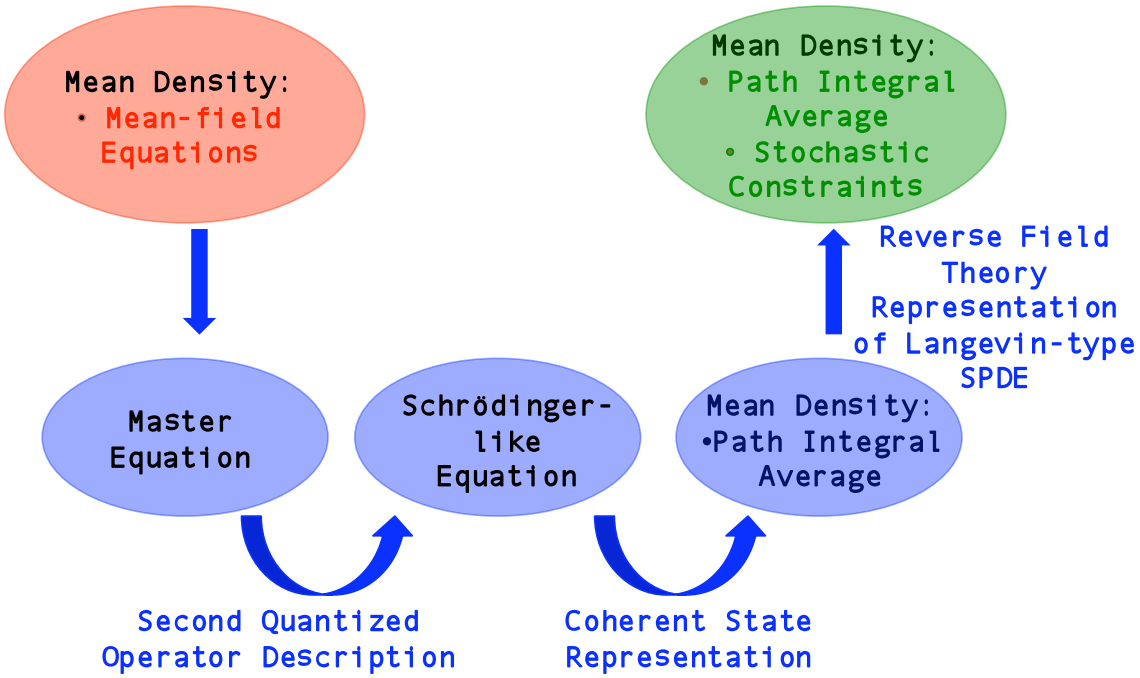

Figure 2.6: Schematic of the Doi-Peliti Formalism.

densities $\langle \mathrm{n}_A(\mathbf{x},t)\rangle$ and $\langle \mathrm{n}_C(\mathbf{x},t)\rangle$ in the mean-field theory:

$$\begin{aligned} -\frac{\partial\langle \mathrm{n}_A(\mathbf{x},t)\rangle}{\partial t} + \zeta_A\Delta\langle \mathrm{n}_A(\mathbf{x},t)\rangle - 2\kappa_{AA}\langle \mathrm{n}_A(\mathbf{x},t)\rangle^2 - \lambda_A\langle \mathrm{n}_A(\mathbf{x},t)\rangle + \iota_A = 0, \\ -\frac{\partial\langle \mathrm{n}_C(\mathbf{x},t)\rangle}{\partial t} + \zeta_C\Delta\langle \mathrm{n}_C(\mathbf{x},t)\rangle + \kappa_{AA}\langle \mathrm{n}_C(\mathbf{x},t)\rangle^2 - \lambda_C\langle \mathrm{n}_C(\mathbf{x},t)\rangle + \iota_C = 0. \end{aligned} \tag{2.67}$$

Despite this suggestive interpretation it is very important to keep in mind that in equation (2.61) we are confronted with a complex fluctuating quantity that has, as such, no physical interpretation. Only if the path integral average, equation (2.64), of a solution to the set of constraint equations (2.60), (2.61), (2.62) and (2.63) is taken over all possible realisations of the stochastic noise that appears in the constraint equations can one interpret the outcome of this computation as a mean particle density.

2.3 Comparison of the Doi-Peliti Formalism to other Approaches

2.3.1 Positive P Representation or Fokker-Planck Approach

The Positive P representation —see, for example, [25, 14]— is a tool to map the master equation for birth and death processes into more tractable stochastic differential equations. Other representations are the W, Q, P, and R representations which will not discuss here. It is an alternative method by which one derives the same set of stochastic equations and the mean density of chemical reactants as given by the Doi-Peliti formalism via a Fokker-Planck equation instead of via a Schrödinger-like equation. The latter has the advantage that at least in the case of the simple chemical reaction $A + A \to C$ the form of the noise coefficients and the nature of the noise itself arise naturally and without having to make certain assumptions beforehand. The Positive P representation results in a stochastic time evolution with a positive propagator. One uses a basis of coherent states which are not orthogonal. That allows a certain freedom of choice in the construction of the representation. Provided that certain boundary terms vanish one can generate a Fokker-Planck equation[12] from the master equation which in turn can be converted into a set of stochastic Langevin-type equations. The solutions of the latter have to be averaged over many realisations of the stochastic process. The biggest problem in the Positive P representation is the boundary terms. In the derivation of the Fokker-Planck equation it is assumed that certain boundary terms arising in the partial integration can be neglected. This is not always the case. Therefore, systematic errors in the stochastic averages can occur especially with non-integrable dynamical systems. The standard time-evolution equation is invalid when non-linear terms are large relative to the other (linear) rates. The boundary terms in the derivation of the Fokker-Planck equation become non-negligible. The so-called Gauge-Poisson techniques eliminate boundary terms to give an exact representation as a weighted rate equation with stochastic terms.

2.3.2 Direct Master Equation Approach

The basis for the Direct Master Equation Approach —cfr. [27, 4]— is the chemical master equation for the state probability distribution. The probability distribution is represented as a discrete set of many-body probabilities. Integration of the equations and suitable summation give the average abundances. The coupling to the rate equa-

[12] See Appendix A.

tions for gas-phase concentrations is easy. Yet, the biggest drawback of the Direct Master Equation Approach is that the number of equations scales with the number of molecules involved in the chemical reaction processes and not with the number of species. For example, for eleven species involved in a chemical reaction network one has to solve 6912 equations.

There is an attempt to resolve this problem in the Moments Equation Approach —see, for example, [1]— which is a modification of the Direct Master Equation Approach. However, new problems have emerged since the numerical code breaks down in the deterministic regime and gives negative abundances.

2.3.3 Monte Carlo Simulations

One way to solve the master equation is by means of macroscopic Monte Carlo techniques —see [9, 10, 59] — which are based on the Gillespie algorithm [26]. In the Continous-Time Random-Walk (CTRW) Monte Carlo simulation —for a detailed description of the method we refer to [8]— microphysical processes are considered. It determines the propagation of a microstate of a system forward in time via a Monte Carlo algorithm. This method derives linear differential equations from the master equation which yield the time dependence of a probability density. For one possible evolution of the system one defines a most likely time interval (derived from an exponential time distribution) and finds the most likely process that occurs in that interval. This calculation is undertaken by comparing relative rates functions. The procedure is repeated until a final time is reached. The initial state of the system propagates towards the final state. One repeats the procedure and averages the results. The drawback of this method is that it is not possible to couple these calculations to rate equations describing the gas phase which is highly desirable.

2.3.4 Modified Rate Approach

The Modified Rate Approach —see, for example, [7, 57]— is a semi-empirical method. In this approach one artificially forces the abundances of reactive surface species to be at least unity. In certain regions of the parameter space one modifies, for a simple system, the basic rate equations for the diffusive surface chemistry. One reproduces results of Monte Carlo treatments by slowing down the rate of diffusion of a fast-moving surface particle so that it does not exceed the larger of the rates of evaporation or accretion. In this approach one allows solutions of coupled differential equations for gas-phase and surface chemistry. But there is no guarantee that it is correct in all instances. Sometimes it can even yield worse results than the mean-field rate equations.

2.3.5 Doi-Peliti Approach

In the light of the needs of the Astrochemistry community the Doi-Peliti formalism has the advantage of the smooth tranisition between the stochastic and the deterministic regime. The number of constraint equations scales only with the number of chemical species under consideration. Furthermore, it seems possible to couple the grain-surface equations to the gas-phase equations since the former are of rate equation type. It might also be easier to consider inhomogeneities on an extended surface.

Chapter 3

Heterogeneous Chemical Reaction of Type $A + A \longrightarrow C$ in the Single Spatial Site Model

In this chapter, we concentrate on the single spatial site model for a heterogeneous chemical reaction where two reactants of the same chemical species A form a chemical reaction product of another chemical species C. In the course of our investigations, we make the following assumptions on the nature of the grain particles:

- grains have all the same size;
- grains are homogeneous;
- each binding site on the grain has the same potential barrier between the one site and its nearest neighbour (*flat surfaces*);
- grains have a constant base temperature.

We will only consider bare grains and are not concerned with the formation of ice mantles.

We allow atoms or molecules to be adsorbed onto and evaporated from the surface of the grain particle. The atoms are assumed to stick to the surface with high efficiency which means the grain temperature is low enough. In our model, we assume that the only reaction mechanism of importance is the diffusive one and consider physisorbed species only. The adsorbed molecules diffuse on the surface of the seed and eventually collide with another reactant. Consequently, they either form a temporary chemical bond that is stabilised by the loss of energy to the phonon modes

of the grain or the reaction product is immediately ejected from the surface.

The gas-phase atoms are assumed to remain at their initial concentration for the duration of the calculation as in [57]. In addition, we focus on the case of low energy barriers resulting in high inverse sweeping times, that is the time for one atom to sweep the entire surface of the grain.

In the sequel, we study the time evolution of the population of the chemical reactants on the surface of the seed particle employing various approaches: we give some analytical results concerning the mean-field solutions, the steady state stochastic solutions and, in the special case when the source rate is equal to zero, the dynamical stochastic solutions. Furthermore, we present numerical results obtained from a code written in the `GNU C` language. We compare the observations in the stochastic model with those obtained in the mean-field approach. In zero space dimensions, the rate coefficients λ [s^{-1}], κ [$\mathrm{m}^{D}\mathrm{s}^{-1}$] and ι [$\mathrm{m}^{-D}\mathrm{s}^{-1}$], reduce to L [s^{-1}], K [s^{-1}], and J [s^{-1}]. Furthermore, in the single spatial site model, we calculate an average particle population instead of an average particle density —this can be easily verified in equations (3.168) and (3.181).

3.1 Mean-Field Steady State and Mean-Field Dynamical Solutions

The implicit solution to the mean-field evolution equation for the population of the reactants of chemical species type A in zero space dimensions

$$\frac{\mathrm{d}}{\mathrm{d}t}\langle N_A(t)\rangle + 2K_{AA}\langle N_A(t)\rangle^2 + L_A\langle N_A(t)\rangle - J_A = 0, \tag{3.1}$$

reads

$$\begin{aligned} t &= \frac{1}{\alpha}\ln\left(c\left|\frac{\frac{\alpha+L_A}{4K_{AA}} + \langle N_A(t)\rangle}{\frac{\alpha-L_A}{4K_{AA}} - \langle N_A(t)\rangle}\right|\right), \\ \alpha &:= \sqrt{8K_{AA}J_A + L_A^2}, \end{aligned} \tag{3.2}$$

with c being a positive integration constant. When investigating the behaviour of the denominator of the argument of the natural logarithm one finds that a vanishing

denominator leads to the steady state solution

$$\langle N_A \rangle^{ss} = \frac{\alpha - L_A}{4K_{AA}}, \tag{3.3}$$

that is, the solution to the stationary equation

$$2K_{AA} \left(\langle N_A \rangle^{ss} \right)^2 + L_A \langle N_A \rangle^{ss} - J_A = 0. \tag{3.4}$$

If one wants to restrict the results to solutions in the real plane one has to expect a division of the space of solutions to the evolution equation (3.1) into two regimes —see equation (3.2):

$$\begin{aligned} &\text{case I:} \quad \langle N_A(t) \rangle < \langle N_A \rangle^{ss}, \\ &\text{case II:} \quad \langle N_A(t) \rangle > \langle N_A \rangle^{ss}. \end{aligned} \tag{3.5}$$

For initial data satisfying $\langle N_A(0) \rangle < \langle N_A \rangle^{ss}$ one stays in the regime corresponding to case I, for initial data satisfying $\langle N_A(0) \rangle > \langle N_A \rangle^{ss}$ one has case II. In the case when the initial data takes exactly the steady state value one obtains the constant solution (3.3). The dynamical mean-field solution to case I gives

$$\begin{aligned} \langle N_A(t) \rangle_I &= \frac{-L_A + \alpha \, \tanh(\frac{\alpha}{2}(t + \beta_I))}{4K_{AA}}, \\ \beta_I &:= 2/\alpha \, \operatorname{arctanh}\big((4K_{AA}\langle N_A(0) \rangle_I + L_A)/\alpha\big), \end{aligned} \tag{3.6}$$

which is the correct real solution for an initial value that is less than the steady state value. For case II one obtains the solution

$$\begin{aligned} \langle N_A(t) \rangle_{II} &= \frac{-L_A + \alpha \, \coth(\frac{\alpha}{2}(t + \beta_{II}))}{4K_{AA}}, \\ \beta_{II} &:= 2/\alpha \, \operatorname{arccoth}\big((4K_{AA}\langle N_A(0) \rangle_{II} + L_A)/\alpha\big), \end{aligned} \tag{3.7}$$

which is the correct real solution for an initial value that is greater than the steady state value. At a later point we will pay special attention to situations where the incoming flux of molecules J_A is small compared to the other rate coefficients. In this case, the class I solution to the mean-field evolution equation (3.6) becomes complex which is a consequence of the nature of the function of the inverse hyperbolic tangent that is incorporated in that solution whereas for large values of the source rate compared to the other rate coefficients, the class II solution to the mean-field evolution equation becomes complex for a similar reason. Consequently, for fixed initial data one expects

class I solutions to give the mean particle population of the A molecules for a large source rate compared to the other rate coefficients and the class II solutions to represent the average particle population of the reactants for a small source rate compared to the other rate coefficients.
Analysing solutions (3.6) and (3.7) one can verify that in the mean-field model the asymptotic values of the solutions to the evolution equation (3.1) with respect to time give the steady state solution (3.3) to the stationary equation (3.4) since for $t \in \mathbb{R}$

$$\begin{aligned} \tanh(t) &\longrightarrow 1 \quad \text{as} \quad t \to \infty, \\ \coth(t) &\longrightarrow 1 \quad \text{as} \quad t \to \infty. \end{aligned} \tag{3.8}$$

Note that the late time behaviour of the dynamic mean-field evolution equations

$$\lim_{t\to\infty} \langle N_A(t) \rangle = \frac{\alpha - L_A}{4K_{AA}}. \tag{3.9}$$

is independent of the initial data.
The solution to the mean-field evolution equation for the reaction products of chemical species type C

$$\frac{\mathrm{d}}{\mathrm{d}t}\langle N_C(t)\rangle - K_{AA}\langle N_A(t)\rangle^2 + L_C\langle N_C(t)\rangle - J_C = 0, \tag{3.10}$$

in zero space dimensions is

$$\langle N_C(t)\rangle = e^{-L_C t}\left(\int_0^t e^{L_C s}\left(J_C + K_{AA}\langle N_A(s)\rangle^2\right)\mathrm{d}s + \langle N_C(0)\rangle\right). \tag{3.11}$$

The steady state solution $\langle N_C\rangle^{ss}$ reads

$$\langle N_C\rangle^{ss} = \frac{K_{AA}\left(\langle N_A\rangle^{ss}\right)^2 + J_C}{L_C}, \tag{3.12}$$

with $\langle N_A\rangle^{ss}$ the steady state solution for the chemical species A (3.3). The form of equation (3.10) implies that none of the chemical reaction products C are immediately released into the gas phase upon formation and all molecules of type C are left on the surface of the grain particle. In order to account for the possibility of spontaneous desorption of C molecules into the gas phase one has to rewrite equation (3.10) in the following way:

$$\frac{\mathrm{d}}{\mathrm{d}t}\langle N_C(t)\rangle - \mu K_{AA}\langle N_A(t)\rangle^2 + L_C\langle N_C(t)\rangle - J_C = 0, \tag{3.13}$$

where the parameter μ accounts for the fraction of reaction products remaining on the surface of the grain particle upon formation. Accordingly, the term $(1-\mu)\langle N_C(t)\rangle$ represents the fraction of C molecules that is spontaneously desorbed into the gas phase due to the excess energy released during the chemical recombination. As stated in [4] the parameter μ takes the following experimentally obtained values: $\mu(olivine) = 0.33$ and $\mu(carbon) = 0.413$ in the hydrogen-hydrogen recombination. The inclusion of the process of release into the gas phase is sensible because it is not possible to observe the number of molecules on the surface of seed particles in interstellar clouds. Instead, one has to resort to observations of the molecules in the gas phase. We will, however, continue to analyse equation (3.10) since the determination of the values of the parameter μ is relatively crude and there are hardly any data available other than for the above given cases.

In general, the values of the rate coefficients are temperature dependent. More precisely, the coefficients K_{AA} and L_A increase as the temperature increases —see [7, 57]. Therefore, the lower the temperature the smaller the value of the source rate at which one switches from case I solutions to case II solutions as can be seen from equation (3.12). In the numerical calculations it is observed that the transient time, that is, the time span until the average particle population reaches an equilibrium value is increasing for decreasing value of the source rate as we will see in sections 3.4.1 and 3.4.2.

Now, we want to list a few special cases that will be relevant later on when comparing the mean-field solutions to the stochastic solutions.

3.1.1 Special Case: Vanishing Reaction Rate

For vanishing reaction rate, $K_{AA} \equiv 0$, the solution to the mean-field rate equation for the chemical species A reduces to

$$\langle N_A(t)\rangle = \frac{J_A}{L_A}(1-e^{-L_A t}) + \langle N_A(0)\rangle e^{-L_A t}, \tag{3.14}$$

which approaches the following late time value:

$$\lim_{t\to\infty}\langle N_A(t)\rangle = \frac{J_A}{L_A}. \tag{3.15}$$

3.1.2 Special Case: Vanishing Source Rate

In the special case of a vanishing source rate, $J_A \equiv 0$, the solution to the mean-field evolution equation for the reaction partners reads

$$\langle N_A(t)\rangle = \frac{\langle N_A(0)\rangle L_A}{2K_{AA}\langle N_A(0)\rangle(e^{L_A t}-1)+L_A e^{L_A t}}, \tag{3.16}$$

which exhibits the following late time behaviour:

$$\lim_{t\to\infty}\langle N_A(t)\rangle = 0. \tag{3.17}$$

3.1.3 Special Case: Vanishing Evaporation Rate

The solution to the equation for vanishing evaporation rate, $L_A \equiv 0$, is a special solution to the full mean-field solution where the evaporation rate is taken to be zero in (3.6) and (3.7) respectively. The late time limit of the solutions is, accordingly:

$$\lim_{t\to\infty}\langle N_A(t)\rangle = \sqrt{\frac{J_A}{2K_{AA}}}. \tag{3.18}$$

3.2 Stochastic Steady State Solution

Explicit steady state solutions for the stationary master equation have been calculated in [27, 40, 5]. As a *steady state solution* we understand the solution to equation (2.1) where the right hand side of the master equation is set to zero, that is

$$\frac{\mathrm{d}P(\{N_A\},\{N_C\};t)}{\mathrm{d}t} \equiv 0. \tag{3.19}$$

The authors of [27, 40] employed methods of *generating functions* to derive an exact solution to the stationary master equation whereas the authors of [5] resorted to linear operations of the stationary master equation and the *continued fraction expansion* of Bessel functions. We will discuss in detail the approach of [27, 40] and will comment on [5] later on.

The stationary master equation (3.19) implies the following equation:

$$K_{AA}(z+1)\frac{\mathrm{d}^2F(z)}{\mathrm{d}z^2} + L_A\frac{\mathrm{d}F(z)}{\mathrm{d}z} - J_A F(z) = 0, \tag{3.20}$$

where $F(z)$ is the generating function defined as a *MacClaurin series*[1]

$$F(z) := \sum_{N_A=0}^{\infty} z^{N_A} P(N_A). \tag{3.22}$$

According to [27, 40], the solution of the stationary master equation (3.20) in terms of the above generating function is given by

$$F(z) = \left(\frac{1+z}{2}\right)^{\frac{1}{2}\left(1-\frac{L_A}{K_{AA}}\right)} \frac{I_{\frac{L_A}{K_{AA}}-1}\left(\sqrt{\frac{J_A(z+1)}{K_{AA}}}\right)}{I_{\frac{L_A}{K_{AA}}-1}\left(\sqrt{\frac{8J_A}{K_{AA}}}\right)}, \tag{3.23}$$

where the function $I_\nu(\xi)$ denotes a *modified Bessel function of the first kind*, where, in general, $\nu \in \mathbb{C}$ and $\xi \in \mathbb{C}$. The average number of reactants in the steady state model $\langle \mathcal{N}_A \rangle_{lit}^{ss}$ as presented in the literature [27, 40, 5] can be obtained via the following relation:

$$\langle \mathcal{N}_A \rangle_{lit}^{ss} \equiv \left.\frac{\mathrm{d}F(z)}{\mathrm{d}z}\right|_{z=1} = \sum_{N_A=0}^{\infty} N_A P(N_A), \tag{3.24}$$

which leads to the expression

$$\langle \mathcal{N}_A \rangle_{lit}^{ss} = \sqrt{\frac{J_A}{2K_{AA}}} \frac{I_{\frac{L_A}{K_{AA}}}\left(\sqrt{\frac{8J_A}{K_{AA}}}\right)}{I_{\frac{L_A}{K_{AA}}-1}\left(\sqrt{\frac{8J_A}{K_{AA}}}\right)}, \tag{3.25}$$

and which satisfies the normalisation condition

$$F(1) = \sum_{N_A=0}^{\infty} P(N_A) \equiv 1. \tag{3.26}$$

The class of solution (3.25) can be obtained by either of the following two conditions:

[1] A MacClaurin series is a *Taylor series expansion* of a function $f(z)$

$$f(z) = \sum_{i=0}^{\infty} \frac{f^{(i)}(z_0)}{i!}(z-z_0)^i, \tag{3.21}$$

about $z_0 = 0$.

Condition 1.

$$\left.\frac{dF(z)}{dz}\right|_{z=-1} = \sum_{N_A=0}^{\infty} (-1)^{N_A-1} N_A P(N_A) \leq \sum_{N_A=0}^{\infty} N_A P(N_A) = \left.\frac{dF(z)}{dz}\right|_{z=1},$$
$$\left.\frac{dF(z)}{dz}\right|_{z=-1} = \sum_{N_A=0}^{\infty} (-1)^{N_A-1} N_A P(N_A) \geq -\sum_{N_A=0}^{\infty} N_A P(N_A) = -\left.\frac{dF(z)}{dz}\right|_{z=1}. \tag{3.27}$$

The above condition for the generating function was introduced in [40].

Condition 2.

$$F(z) \text{ smooth for all } z \in \mathbb{R}. \tag{3.28}$$

The above condition for the generating function was employed in [27].

Since the generating function has no physical meaning *per se* we regard the latter condition as overly restrictive and not physically justified. However, differentiability at certain values of the argument is a necessary condition if the function and derivatives thereof have a physical interpretation at this specific point. The first line of argument will be considered at a later point.
The above result (3.25) has to be reviewed and reinterpreted. Let us start considering various special cases that should still be correctly embedded in the mathematical framework. To the best of my knowledge, until now there has not been any thorough discussion on the convergence of the MacClaurin series of the solutions to equation (3.20) and derivatives thereof. This is essential in order to be able to identify the MacClaurin series of the solution which, in the sequel, we will call *generating function candidate* —$G(z)$— with the series defining the generating function —$F(z)$— via equation (3.22).

In the rest of the section we will refer to the following list of formulae for Bessel functions as taken from [66]:

Compendium 1. *Summary of formulae for the Bessel functions*

- *Symmetry Relation of Bessel functions with respect to the indices:*

$$I_n(\xi) \equiv I_{-n}(\xi) \quad \forall n \in \mathbb{N}. \tag{3.29}$$

- *Relation between the first derivative of Bessel functions and Bessel functions:*

$$\frac{dI_\nu(\xi)}{d\xi} = \frac{\nu}{\xi} I_\nu(\xi) + I_{\nu+1}(\xi). \tag{3.30}$$

- *Recurrence relation for Bessel functions:*

$$I_{\nu-1}(\xi) - I_{\nu+1}(\xi) = \frac{2\nu}{\xi} I_\nu(\xi). \tag{3.31}$$

- *Series expansion of a modified Bessel function of the first kind:*

$$I_\nu(\xi) = \left(\frac{\xi}{2}\right)^\nu \Omega_\nu(\xi), \tag{3.32}$$

for $\nu \neq -1, -2, -3, ...$ and complex ξ and with

$$\Omega_\nu(\xi) := \sum_{k=0}^{\infty} \frac{1}{\Gamma(k+1+\nu)k!} \left(\frac{\xi}{2}\right)^{2k}, \tag{3.33}$$

where Γ is the Gamma function which can be defined as a definite integral

$$\Gamma(z) = \int_0^\infty t^{z-1} e^{-t} dt \quad for \;\; \Re(z) > 0. \tag{3.34}$$

The Gamma function satisfies

$$\Gamma(z+1) = z\Gamma(z). \tag{3.35}$$

The above relation (3.32) *implies*

$$I_\nu(\xi) = \frac{1}{\Gamma(\nu+1)} \left(\frac{\xi}{2}\right)^\nu (1 + \mathcal{O}(z^2)). \tag{3.36}$$

This leads to

$$\frac{I_{\nu_1}(\xi)}{I_{\nu_2}} = \frac{\Gamma(\nu_2+1)}{\Gamma(\nu_1+1)} \left(\frac{\xi}{2}\right)^{\nu_1-\nu_2} (1 + \mathcal{O}(\xi^2)). \tag{3.37}$$

- *Expansion of Bessel functions for small perturbations of the index:*

$$I_{\nu+\epsilon}(\xi) = I_\nu(\xi) + \Theta(\nu, \xi)\epsilon + \mathcal{O}(\epsilon^2), \tag{3.38}$$

with

$$\Theta(\nu, \xi) := I_\nu(\xi) \ln\left(\frac{\xi}{2}\right) - \sum_{k=0}^{\infty} \frac{F(k+\nu+1)}{k!\Gamma(k+\nu+1)} \left(\frac{\xi}{2}\right)^{2k+\nu}, \tag{3.39}$$

where $\digamma(m)$ is the Digamma function.

3.2.1 Special Case: Vanishing Reaction Rate

Since the special case of a vanishing reaction rate reduces the master equation to an ordinary differential equation of first order

$$L_A \frac{\mathrm{d}F(z)}{\mathrm{d}z} - J_A F(z) = 0 \quad L_A \neq 0 \text{ and } J_A \neq 0, \tag{3.40}$$

we only have to determine one integration constant A for the generating function candidate

$$G(z) = A e^{\frac{J_A z}{L_A}}, \tag{3.41}$$

which can be determined from the condition

$$G(1) \stackrel{!}{=} 1, \tag{3.42}$$

and leads to the solution

$$G(z) = e^{\frac{J_A}{L_A}(z-1)}. \tag{3.43}$$

The MacClaurin series of the above generating function candidate $G(z)$ converges for all values of z, therefore we have

$$\frac{\mathrm{d}^m F(z)}{\mathrm{d}z^m} \equiv \frac{\mathrm{d}^m G(z)}{\mathrm{d}z^m} \quad m \in [0, \infty]. \tag{3.44}$$

Since the source for potential stochastic effects, namely the chemical reaction itself, has been neglected the stochastic steady state solution, $\langle \mathcal{N}_A \rangle^{ss}$, has to coincide with the mean-field solution. This is indeed the case —cfr. with the late-time limit of the dynamical mean-field solution (3.15):

$$\langle \mathcal{N}_A \rangle^{ss} := \left. \frac{\mathrm{d}F(z)}{\mathrm{d}z} \right|_{z=1} = \frac{J_A}{L_A} = \langle N_A(t_\infty) \rangle, \tag{3.45}$$

where t_∞ is the time that is needed to reach equilibrium.

3.2.2 Special Case: Vanishing Source Rate

For vanishing source rate coefficient, the master equation can be represented by

$$K_{AA}(z+1) \frac{\mathrm{d}^2 F(z)}{\mathrm{d}z^2} + L_A \frac{\mathrm{d}F(z)}{\mathrm{d}z} = 0 \quad L_A \neq 0, \text{ and } K_{AA} \neq 0. \tag{3.46}$$

One possible solution of the above ordinary differential equation is $F(z) = constant$ for all z which has as a consequence that the average number of reactants is zero. On the other hand, equation (3.46) is potentially solved by the following generating function candidate:

$$G(z) = A + B(1+z)^{1-\frac{L_A}{K_{AA}}}. \tag{3.47}$$

From the condition

$$G(z)|_{z=1} \stackrel{!}{=} 1, \tag{3.48}$$

one integration constant can be eliminated, for example,

$$A = 1 - B2^{1-\frac{L_A}{K_{AA}}}. \tag{3.49}$$

In order to be able to use the normalisation condition (3.48) one has to verify that

$$F(z)|_{z=1} \equiv G(z)|_{z=1}. \tag{3.50}$$

For this, we define

$$\begin{aligned} F(z) &:= \sum_{N_A=0}^{\infty} z^{N_A} P(N_A), \\ G(z) &:= A + B(1+z)^{1-\frac{L_A}{K_{AA}}}. \end{aligned} \tag{3.51}$$

Under which circumstances

$$F(z) \equiv G(z), \tag{3.52}$$

or, in other words, under which circumstances converges $F(z)$ towards $G(z)$? One can write $G(z)$ as a MacClaurin series

$$G(z) = \sum_{N=0}^{\infty} C(N) z^N = C_0 + C_1 \sum_{s=0}^{\infty} \binom{1-\frac{L_A}{K_{AA}}}{s} z^s. \tag{3.53}$$

The convergence of the MacClaurin series is based on the convergence of the binomial series

$$(1+x)^{\alpha} = \sum_{k=0}^{\infty} \binom{\alpha}{k} x^k \quad \alpha \in \mathbb{C}. \tag{3.54}$$

The exact conditions —which we will give without proof— under which this series converges are taken from [11]:

Theorem 1. *"If the index α is an integer and $\alpha \geq 0$, the series terminates and is therefore valid for all values of x (becoming the ordinary binomial theorem). For all*

other values of α the series is absolutely convergent for $|\alpha| < 1$ and divergent for $|\alpha| > 1$. For $x = +1$ the series converges absolutely if $\alpha > 0$, converges conditionally[2] *if $-1 < \alpha < 0$ and diverges if $\alpha \leq -1$. Finally, at $x = -1$ the series is absolutely convergent if $\alpha > 0$, divergent if $\alpha < 0$."*

This leaves us with the following observation:
The series (3.53) is absolutely convergent for $0 < L_A K_{AA}^{-1} < 1$. For $x = +1$ the series converges absolutely if $L_A K_{AA}^{-1} < 1$, converges conditionally if $2 > L_A K_{AA}^{-1} > 1$ and diverges if $2 \leq L_A K_{AA}^{-1}$. Finally, at $x = -1$ the series is absolutely convergent if $L_A K_{AA}^{-1} < 1$, divergent if $L_A K_{AA}^{-1} > 1$. The condition $L_A K_{AA}^{-1} < 1$ is relevant especially for situations where one expects to find stochastic behaviour since a fast reaction rate compared to the other rate coefficients will lead away from the deterministic regime towards the stochastic regime.
According to the above criteria, one can divide the analysis into two cases:

- $L_A K_{AA}^{-1} < 2$: $G(z) = A + B(1+z)^{1-\frac{L_A}{K_{AA}}}$,
- $L_A K_{AA}^{-1} \geq 2$: $G(z) = A$, since the series expansion of $(1+z)^{1-\frac{L_A}{K_{AA}}}$ diverges if $L_A K_{AA}^{-1} \geq 2$.

Furthermore, if one assumes that $L_A K_{AA}^{-1} < 1$, from the uniqueness of MacClaurin series it follows that,

$$P(N_A) \equiv C(N), \tag{3.55}$$

which can be confronted with the common expression

$$P(N_A) = \frac{1}{N_A!} \frac{\mathrm{d}^{N_A} F(z)}{\mathrm{d}z^{N_A}}\bigg|_{z=0}. \tag{3.56}$$

In order to reexamine the regularity conditions (3.27) and (3.28) one has to consider the first derivative of the generating function candidate with respect to its argument

$$\frac{\mathrm{d}G(z)}{\mathrm{d}z} = B\left(1 - \frac{L_A}{K_{AA}}\right)(1+z)^{-\frac{L_A}{K_{AA}}}. \tag{3.57}$$

The above expression is regular in $z = 1$ but singular in $z = -1$ as $L_A > 0$ and $K_{AA} > 0$. This, according to the argumentative line of [27] —cfr. Condition (3.28)—, is the reason why one class of solutions can be discarded, namely $B = 0$, which leaves us with

$$G(z) = 1 \Longrightarrow \frac{\mathrm{d}G(z)}{\mathrm{d}z} = 0 \quad \forall z, \tag{3.58}$$

[2] A series is said to converge conditionally if the limit of the corresponding sequence exists and is a finite number but the series of the modulus of the coeffients is not finite.

in particular,

$$\langle \mathcal{N}_A \rangle^{ss} := \left. \frac{\mathrm{d}G(z)}{\mathrm{d}z} \right|_{z=1} = 0, \tag{3.59}$$

for any value of L_A, K_{AA}. However, the evaluation of the first derivative of the generating function candidate at the point $z = -1$ is not of physical interest and regularity at this point is not a necessary condition for the derivation of the average particle number $\langle \mathcal{N}_A \rangle^{ss}$.

In the following we want to reexamine the regularity conditions (3.27) —see [40]— in the light of convergence criteria. The mathematical manipulations leading to condition (3.27) require that the series expansion of the first derivative of the generating function is convergent at the points $z = 1$ and $z = -1$. Therefore, one has to verify whether the generating function candidate fulfills this requirement. The convergence criteria —cfr. Theorem 1— indicate that for the first derivative of the generating function candidate (3.57) we have the following:

- at the point $z = 1$, the series expansion of the generating function candidate converges absolutely if and only if $L_A K_{AA}^{-1} < 1$ and the MacClaurin series of the first derivative of the generating function candidate in $z = 1$ converges conditionally if and only if $L_A K_{AA}^{-1} < 1$.

- at the point $z = -1$, the series expansion of the generating function candidate converges absolutely if and only if $L_A K_{AA}^{-1} < 1$. However, at $z = -1$, the MacClaurin series of the first derivative of the generating function candidate diverges for all $L_A > 0$ and $K_{AA} > 0$.

This leads to the conclusion that if $B = 0$, the conditions 3.27 are fulfilled. However, since the convergence criteria at point $z = -1$ are not fulfilled, from

$$\left. \frac{\mathrm{d}F(z)}{\mathrm{d}z} \right|_{z=-1} \leq \left| \left. \frac{\mathrm{d}F(z)}{\mathrm{d}z} \right|_{z=1} \right| \quad \not\Leftrightarrow \quad \left. \frac{\mathrm{d}G(z)}{\mathrm{d}z} \right|_{z=-1} \leq \left| \left. \frac{\mathrm{d}G(z)}{\mathrm{d}z} \right|_{z=1} \right|, \tag{3.60}$$

it does not follow that one necessarily needs $B = 0$. In [40], absolute convergence of the first derivative of the generating function candidate at $z = -1$ was assumed and Condition 3.27 was used to disregard one part of the solution that did not fulfill Condition 3.27. Yet, in fact, one is left with the following:

- if $L_A K_{AA}^{-1} < 1$:

$$\langle \mathcal{N}_A \rangle^{ss} \equiv \langle \mathcal{N}_A \rangle^{ss}_{L_A K_{AA}^{-1} < 1} = B 2^{-\frac{L_A}{K_{AA}}} \left(1 - \frac{L_A}{K_{AA}} \right), \tag{3.61}$$

  where we will determine the second integration constant B at a later point;

- if $L_A K_{AA}^{-1} \geq 1$:

$$\langle \mathcal{N}_A \rangle^{ss} \equiv \langle \mathcal{N}_A \rangle^{ss}_{L_A K_{AA}^{-1} \geq 1} = 0. \tag{3.62}$$

  Note that in the literature the expression for the average number of reactants $\langle \mathcal{N}_A \rangle^{ss}_{lit}$ was given by

$$\langle \mathcal{N}_A \rangle^{ss}_{lit} = \langle \mathcal{N}_A \rangle^{ss}_{L_A K_{AA}^{-1} \geq 1}, \tag{3.63}$$

  for any values of L_A and K_{AA} and it was not realised that this expression is only true if $L_A K_{AA}^{-1} \geq 1$.

In a first step, for $L_A K_{AA}^{-1} < 1$, we want to find bounds for the value of the average reactant partner population by means of the probability for an even number of particles P_{even} and the probability for an odd number of particles P_{odd}. It is true that

$$P_{even} + P_{odd} = 1, \tag{3.64}$$

where

$$\begin{aligned} P_{even} &:= \sum_{N_A=0}^{\infty} P(2N_A), \\ P_{odd} &:= \sum_{N_A=0}^{\infty} P(2N_A + 1). \end{aligned} \tag{3.65}$$

It follows from the definition of the generating function $F(z)$ in (3.51) that

$$\begin{aligned} F(1) &= \sum_{N_A=0}^{\infty} P(N_A), \\ F(-1) &= \sum_{N_A=0}^{\infty} (-1)^{N_A} P(N_A). \end{aligned} \tag{3.66}$$

Adding the above two expressions together we derive the following:

$$\begin{aligned} F(1) + F(-1) &= P(0) + P(1) + P(2) + P(3) + ... \\ &\quad P(0) - P(1) + P(2) - P(3) + ... \\ &= 2 \sum_{N_A=0}^{\infty} P(2N_A) = 2P_{even}. \end{aligned} \tag{3.67}$$

Furthermore, we have that

$$F(1) \equiv 1. \tag{3.68}$$

Therefore, one derives

$$P_{even} = \frac{1}{2}\big(1 + F(-1)\big),$$
$$P_{odd} = \frac{1}{2}\big(1 - F(-1)\big). \tag{3.69}$$

Let us now consider the two extreme cases, namely,

$$\text{(i) } P_{even} = 1 \rightarrow P_{odd} = 0,$$
$$\text{(ii) } P_{even} = 0 \rightarrow P_{odd} = 1. \tag{3.70}$$

This has the following implication:

$$\text{(i) } F(-1) = 1,$$
$$\text{(ii) } F(-1) = -1. \tag{3.71}$$

Since the MacClaurin series of the generating function candidate $G(z)$ is absolutely convergent at $|z| = 1$, for $L_A K_{AA}^{-1} < 1$ we have that

$$G(z)\big|_{|z|=1} \equiv F(z)\big|_{|z|=1} \quad \text{for } \frac{L_A}{K_{AA}} < 1. \tag{3.72}$$

Consequently, we can use the following identities to determine the integration constants, namely,

$$G(z)|_{z=1} \stackrel{!}{=} 1,$$
$$G(z)|_{z=-1} \stackrel{!}{=} \pm 1. \tag{3.73}$$

In the particular case of a vanishing source rate this means that in case (i) we have

$$A = 1, \quad \text{and}, \quad B = 0,$$
$$\text{so that: } \langle \mathcal{N}_A \rangle^{ss} = 0, \tag{3.74}$$

and in case (ii),

$$A = -1, \quad \text{and}, \quad B = 2^{\frac{L_A}{K_{AA}}},$$
$$\text{so that: } \langle \mathcal{N}_A \rangle^{ss} = 1 - \frac{L_A}{K_{AA}}, \tag{3.75}$$

which gives a lower and an upper limit for the possible value of the average population

of A molecules,

$$\langle \mathcal{N}_A \rangle^{ss} \in \left[0, 1 - \frac{L_A}{K_{AA}} \right]. \tag{3.76}$$

3.2.3 Special Case: Vanishing Evaporation Rate

The special case of a negligible evaporation process is of specific interest for the chemical recombination of oxygen and nitrogen atoms, respectively, since the thermal evaporation rate is of the order of 10^{-23} s^{-1}. The generating function candidate that might solve

$$K_{AA}(z+1)\frac{\mathrm{d}^2 F(z)}{\mathrm{d}z^2} - J_A F(z) = 0 \quad K_{AA} \neq 0, \text{ and } J_A \neq 0, \tag{3.77}$$

reads

$$G(z) = A(1+z)^{\frac{1}{2}} I_{-1}\left(2\sqrt{\frac{J_A}{K_{AA}}}(1+z)^{\frac{1}{2}} \right) + B(1+z)^{\frac{1}{2}} I_1\left(2\sqrt{\frac{J_A}{K_{AA}}}(1+z)^{\frac{1}{2}} \right).$$

According to the symmetry relation of Bessel functions with respect to the indices (3.29), the above generating function candidate is equivalent to

$$G(z) = C(1+z)^{\frac{1}{2}} I_1\left(2\sqrt{\frac{J_A}{K_{AA}}}(1+z)^{\frac{1}{2}} \right).$$

From the condition

$$G(z)|_{z=1} \stackrel{!}{=} 1, \tag{3.78}$$

it follows that

$$C \equiv \frac{1}{\sqrt{2} I_1\left(\sqrt{\frac{8J_A}{K_{AA}}} \right)}. \tag{3.79}$$

In order to investigate the convergence behaviour of the MacClaurin series of the generating function candidate we rewrite (3.78) in the following way

$$G(z) = C\sqrt{\frac{J_A}{K_{AA}}}(1+z)\Omega_1(z), \tag{3.80}$$

with $\Omega_1(z)$ as given by (3.33). According to the criteria for the convergence of the binomial series, the expansion of $1+z$ converges absolutely for $|z| = 1$ and the series Ω_1 has infinite convergence radius. Therefore, the convergence radius of the generating function candidate $G(z)$ is the minimum of the two separately determined convergence radii, that is, the generating function candidate $G(z)$ converges absolutely for $|z| = 1$ and the above derivation for the normalisation constant is justified.

In order to compute the derivatives of the generating function candidate $G(z)$ it is useful to employ the relation between the derivative of a modified Bessel function of the first kind and modified Bessel functions and the recurrence relation of Bessel functions —see (3.30) and (3.31). The first and second derivatives of the generating function candidate are found to be

$$\begin{aligned}\frac{\mathrm{d}G(z)}{\mathrm{d}z} &= \frac{1}{\sqrt{2}I_1\left(\sqrt{\frac{8J_A}{K_{AA}}}\right)}\left((1+z)^{-\frac{1}{2}}I_1\left(2\sqrt{\frac{J_A}{K_{AA}}}(1+z)^{\frac{1}{2}}\right)+\right.\\ &\qquad\left.\sqrt{\frac{J_A}{K_{AA}}}I_2\left(2\sqrt{\frac{J_A}{K_{AA}}}(1+z)^{\frac{1}{2}}\right)\right),\\ \frac{\mathrm{d}^2G(z)}{\mathrm{d}z^2} &= \frac{1}{\sqrt{2}I_1\left(\sqrt{\frac{8J_A}{K_{AA}}}\right)}\left(2\sqrt{\frac{J_A}{K_{AA}}}(1+z)^{-1}I_2\left(2\sqrt{\frac{J_A}{K_{AA}}}(1+z)^{\frac{1}{2}}\right)+\right.\\ &\qquad\left.\frac{J_A}{K_{AA}}(1+z)^{-\frac{1}{2}}I_3\left(2\sqrt{\frac{J_A}{K_{AA}}}(1+z)^{\frac{1}{2}}\right)\right).\end{aligned} \tag{3.81}$$

The average particle number of the chemical reactants of species A can be obtained by evaluating the first derivative of the generating function candidate with respect to z at $z=1$

$$\langle\mathcal{N}_A\rangle^{ss} := \left.\frac{\mathrm{d}G(z)}{\mathrm{d}z}\right|_{z=1} = \frac{1}{2}+\sqrt{\frac{J_A}{2K_{AA}}}\frac{I_2\left(\sqrt{\frac{8J_A}{K_{AA}}}\right)}{I_1\left(\sqrt{\frac{8J_A}{K_{AA}}}\right)}. \tag{3.82}$$

Concerning the convergence of the series of the first derivative of the generating function candidate at $z=1$ we write

$$\frac{\mathrm{d}G(z)}{\mathrm{d}z} = C\sqrt{\frac{J_A}{K_{AA}}}\left(\Omega_1(z)+\frac{J_A}{K_{AA}}(1+z)\Omega_2(z)\right), \tag{3.83}$$

and in accordance with the arguments for the convergence of the series of the generating function candidate $G(z)$ the above series converges absolutely for $|z|=1$. To the best of my knowledge this is the first time the explicit result (3.82) has been obtained in this way.

Let us now compare the findings concerning the solution to the stationary steady state equation for vanishing evaporation rate with the results for vanishing source rate. In order to do so, we have to expand the expression for the mean population of chemical reaction partners (3.82) for small source rate according to (3.32). The average number

of molecules of type A for small $J_A K_{AA}^{-1}$ is given by

$$\langle \mathcal{N}_A(L_A \equiv 0)\rangle^{ss} = \frac{1}{2} + \frac{J_A}{2K_{AA}}\left(1 + \mathcal{O}\left(\frac{J_A}{K_{AA}}\right)\right). \tag{3.84}$$

Accordingly, the limit of (3.84) for a source rate approaching zero and for fixed reaction rate reads

$$\lim_{J_A \to 0} \langle \mathcal{N}_A(L_A \equiv 0)\rangle^{ss} = \frac{1}{2}. \tag{3.85}$$

This can be confronted with the result from earlier calculations where we found that the value of the average number of A molecules for vanishing source rate has to lie in the interval

$$\langle \mathcal{N}_A(J_A \equiv 0)\rangle^{ss} \in \left[0, 1 - \frac{L_A}{K_{AA}}\right] \quad \text{for } \frac{L_A}{K_{AA}} < 1. \tag{3.86}$$

For the additional condition of an evporation rate approaching zero with fixed reaction rate this leads to

$$\lim_{L_A \to 0} \langle \mathcal{N}_A(J_A \equiv 0)\rangle^{ss} \in [0, 1] \quad \text{for } \frac{L_A}{K_{AA}} < 1, \tag{3.87}$$

which is consistent with (3.85). Recall that the expression for the average particle number in the literature is given by

$$\langle \mathcal{N}_A(J_A \equiv 0)\rangle_{lit}^{ss} = 0. \tag{3.88}$$

Note that it is not possible to reach the above value from (3.84) since from (3.84) one has that

$$\langle \mathcal{N}_A(L_A \equiv 0)\rangle^{ss} \geq \frac{1}{2} \quad \text{for all } J_A \geq 0, \text{ and } K_{AA} > 0. \tag{3.89}$$

In view of the preceeding result I continue with a reexamination of the general solution to the equation (3.20).

3.2.4 Reexamination of the Stochastic Steady State Solution to the Full Master Equation

The way to obtain a solution to the full differential equation

$$K_{AA}(z+1)\frac{\mathrm{d}^2 F(z)}{\mathrm{d}z^2} + L_A \frac{\mathrm{d}F(z)}{\mathrm{d}z} - J_A F(z) = 0, \tag{3.90}$$

with $J_A > 0,\ L_A > 0,\ K_{AA} > 0$ results from the following Ansatz for the generating function candidate:

$$G(z) = G_0(1+z)^{-\frac{\nu}{2}}\phi(\xi), \tag{3.91}$$

which solves the equation

$$\xi^2\frac{\mathrm{d}^2\phi(\xi)}{\mathrm{d}\xi^2} + \xi\frac{\mathrm{d}\phi(\xi)}{\mathrm{d}\xi} - (\xi^2+\nu^2)\phi(\xi) = 0, \tag{3.92}$$

where

$$\begin{aligned}\nu &:= \frac{L_A}{K_{AA}} - 1 \quad \nu \in [-1,\infty),\\ \xi = \xi(z) &:= 2\sqrt{\frac{J_A}{K_{AA}}(1+z)}.\end{aligned} \tag{3.93}$$

This renders a solution which is a linear combination of the following form

$$\begin{aligned}G(z) &= G_+(z) + G_-(z),\\ G_+(z) &:= A(1+z)^{-\frac{\nu}{2}}I_\nu[\xi(z)],\\ G_-(z) &:= B(1+z)^{-\frac{\nu}{2}}I_{-\nu}[\xi(z)],\end{aligned} \tag{3.94}$$

with A and B the normalisation constants. In order to acknowledge the full potential of this solution it is advantageous to resubstitute for the original constants J_A, L_A, K_{AA}:

$$\begin{aligned}G(z) = A(1+z)^{-\frac{1}{2}\left(\frac{L_A}{K_{AA}}-1\right)}I_{\frac{L_A}{K_{AA}}-1}\left(2\sqrt{\frac{J_A}{K_{AA}}}(1+z)^{\frac{1}{2}}\right) +\\ B(1+z)^{-\frac{1}{2}\left(\frac{L_A}{K_{AA}}-1\right)}I_{1-\frac{L_A}{K_{AA}}}\left(2\sqrt{\frac{J_A}{K_{AA}}}(1+z)^{\frac{1}{2}}\right).\end{aligned} \tag{3.95}$$

In the following, we will also use the first and second derivatives of the above generating function candidate with respect to its argument z:

$$\begin{aligned}\frac{\mathrm{d}G(z)}{\mathrm{d}z} = A\sqrt{\frac{J_A}{K_{AA}}}(1+z)^{-\frac{L_A}{2K_{AA}}}I_{\frac{L_A}{K_{AA}}}\left(2\sqrt{\frac{J_A}{K_{AA}}}(1+z)^{\frac{1}{2}}\right) +\\ B(1-\frac{L_A}{K_{AA}})(1+z)^{-\frac{1}{2}\left(\frac{L_A}{K_{AA}}+1\right)}I_{1-\frac{L_A}{K_{AA}}}\left(2\sqrt{\frac{J_A}{K_{AA}}}(1+z)^{\frac{1}{2}}\right) +\\ B\sqrt{\frac{J_A}{K_{AA}}}(1+z)^{-\frac{L_A}{2K_{AA}}}I_{2-\frac{L_A}{K_{AA}}}\left(2\sqrt{\frac{J_A}{K_{AA}}}(1+z)^{\frac{1}{2}}\right),\end{aligned} \tag{3.96}$$

and

$$\frac{\mathrm{d}^2G(z)}{\mathrm{d}z^2} = A\frac{J_A}{K_{AA}}(1+z)^{-\frac{1}{2}\left(\frac{L_A}{K_{AA}}+1\right)} I_{\frac{L_A}{K_{AA}}+1}\left(2\sqrt{\frac{J_A}{K_{AA}}}(1+z)^{\frac{1}{2}}\right) - B\left(1-\frac{L_A}{K_{AA}}\right)\frac{L_A}{K_{AA}}(1+z)^{-\frac{1}{2}\left(\frac{L_A}{K_{AA}}+3\right)} I_{1-\frac{L_A}{K_{AA}}}\left(2\sqrt{\frac{J_A}{K_{AA}}}(1+z)^{\frac{1}{2}}\right) + 2B\left(1-\frac{L_A}{K_{AA}}\right)\sqrt{\frac{J_A}{K_{AA}}}(1+z)^{-\frac{1}{2}\left(\frac{L_A}{K_{AA}}+2\right)} I_{2-\frac{L_A}{K_{AA}}}\left(2\sqrt{\frac{J_A}{K_{AA}}}(1+z)^{\frac{1}{2}}\right) + B\frac{J_A}{K_{AA}}(1+z)^{-\frac{1}{2}\left(\frac{L_A}{K_{AA}}+1\right)} I_{3-\frac{L_A}{K_{AA}}}\left(2\sqrt{\frac{J_A}{K_{AA}}}(1+z)^{\frac{1}{2}}\right). \tag{3.97}$$

The average number of molecules of species A can be calculated from

$$\langle \mathcal{N}_A\rangle^{ss} := \left.\frac{\mathrm{d}G(z)}{\mathrm{d}z}\right|_{z=1} = A\sqrt{\frac{J_A}{K_{AA}}}2^{-\frac{L_A}{2K_{AA}}} I_{\frac{L_A}{K_{AA}}}\left(\sqrt{\frac{8J_A}{K_{AA}}}\right) + B\left(1-\frac{L_A}{K_{AA}}\right)2^{-\frac{1}{2}\left(\frac{L_A}{K_{AA}}+1\right)} I_{1-\frac{L_A}{K_{AA}}}\left(\sqrt{\frac{8J_A}{K_{AA}}}\right) + B\sqrt{\frac{J_A}{K_{AA}}}2^{-\frac{L_A}{2K_{AA}}} I_{2-\frac{L_A}{K_{AA}}}\left(\sqrt{\frac{8J_A}{K_{AA}}}\right). \tag{3.98}$$

Let us now ignore the regularity conditions (3.27) and (3.28) as presented in [27, 40] and proceed to analyse the behaviour of the two special solutions $B = 0$ and $A = 0$ respectively. The first case corresponds to the results obtained by [27, 40].

Special Case: $A \neq 0$ **and** $B \equiv 0$

In the case that $A \neq 0$ and $B = 0$ the generating function candidate reduces to

$$G(z) = G_+(z), \tag{3.99}$$

and the only remaining integration constant A can be determined from the condition

$$G_+(z)|_{z=1} \stackrel{!}{=} 1, \tag{3.100}$$

which gives us

$$A = \frac{2^{\frac{1}{2}\left(\frac{L_A}{K_{AA}}-1\right)}}{I_{\frac{L_A}{K_{AA}}-1}\left(\sqrt{\frac{8J_A}{K_{AA}}}\right)}. \tag{3.101}$$

For the above normalisation condition we have to check the convergence behaviour in the point $z = 1$ of the series expansion

$$G_+(z) = A \left(\frac{J_A}{K_{AA}} \right)^{\frac{1}{2}\left(\frac{L_A}{K_{AA}} - 1\right)} \Omega_{\frac{L_A}{K_{AA}} - 1}(z), \tag{3.102}$$

where the series $\Omega_{\frac{L_A}{K_{AA}} - 1}(z)$ —see (3.33)— has infinite radius of convergence. Consequently, the series expansion of the generating function candidate converges for all values of z.

We derive the following expression for the average chemical reactant population —cfr. with (3.25)—

$$\langle \mathcal{N}_A \rangle_+^{ss} := \left. \frac{\mathrm{d}G(z)}{\mathrm{d}z} \right|_{z=1} \equiv \left. \frac{\mathrm{d}G_+(z)}{\mathrm{d}z} \right|_{z=1} = \sqrt{\frac{J_A}{2K_{AA}}} \frac{I_{\frac{L_A}{K_{AA}}} \left(\sqrt{\frac{8J_A}{K_{AA}}} \right)}{I_{\frac{L_A}{K_{AA}} - 1} \left(\sqrt{\frac{8J_A}{K_{AA}}} \right)}. \tag{3.103}$$

The series expansion for the first derivative of the generating function candidate converges everywhere since

$$\frac{\mathrm{d}G_+(z)}{\mathrm{d}z} = A \left(\frac{J_A}{K_{AA}} \right)^{\frac{1}{2}\left(1 + \frac{L_A}{K_{AA}}\right)} \Omega_{\frac{L_A}{K_{AA}}}(z), \tag{3.104}$$

with $\Omega_{\frac{L_A}{K_{AA}}}(z)$ as given by (3.33), converges everywhere.

We are interested in the limit $L_A \to 0$. If the fraction $L_A K_{AA}^{-1}$ is small we have that (3.103) can be expanded according to (3.38) and (3.39)

$$\langle \mathcal{N}_A \rangle_+^{ss} = \sqrt{\frac{J_A}{2K_{AA}}} \left(\frac{I_0 \left(\sqrt{\frac{8J_A}{K_{AA}}} \right)}{I_1 \left(\sqrt{\frac{8J_A}{K_{AA}}} \right)} - \frac{L_A}{K_{AA}} \left(\frac{I_0 \left(\sqrt{\frac{8J_A}{K_{AA}}} \right) \left(\Theta \left(1, \sqrt{\frac{8J_A}{K_{AA}}} \right) + \sqrt{\frac{K_{AA}}{2J_A}} I_0 \left(\sqrt{\frac{8J_A}{K_{AA}}} \right) \right)}{I_1^2 \left(\sqrt{\frac{8J_A}{K_{AA}}} \right)} - \right. \right.$$
$$\left. \left. \frac{\Theta \left(0, \sqrt{\frac{8J_A}{K_{AA}}} \right)}{I_1 \left(\sqrt{\frac{8J_A}{K_{AA}}} \right)} \right) + \mathcal{O}\left(\left(\frac{L_A}{K_{AA}} \right)^2 \right) \right), \tag{3.10}$$

where we have used that for small enough x

$$\frac{1}{1+x} = 1 - x + \mathcal{O}(x^2). \tag{3.106}$$

For fixed reaction rate coefficient K_{AA}, in the limit of the evaporation rate coefficient L_A approaching zero we obtain

$$\lim_{L_A \to 0} \langle \mathcal{N}_A \rangle_+^{ss} = \frac{1}{2} + \frac{J_A}{2K_{AA}} \frac{I_2\left(\sqrt{\frac{8J_A}{K_{AA}}}\right)}{I_1\left(\sqrt{\frac{8J_A}{K_{AA}}}\right)}, \tag{3.107}$$

taking (3.30) into account. This result coincides with the exact solution to the master equation for vanishing evaporation rate (3.82).
In addition, we are interested in the regime where the source rate J_A is small. For small $J_A K_{AA}^{-1}$ we have, according to (3.37):

$$\langle \mathcal{N}_A \rangle_+^{ss} = \frac{J_A}{L_A} \left(1 + \mathcal{O}\left(\frac{J_A}{K_{AA}}\right)\right), \tag{3.108}$$

so that in the limit of the source rate coefficient approaching zero and for fixed reaction rate coefficient we have

$$\lim_{J_A \to 0} \langle \mathcal{N}_A \rangle_+^{ss} = 0, \tag{3.109}$$

for fixed non-zero and finite evaporation rate which corresponds to the exact solution to the master equation with zero source rate (3.46) for $B = 0$. Note that

$$\langle \mathcal{N}_A \rangle_{lit}^{ss} \equiv \langle \mathcal{N}_A \rangle_+^{ss}. \tag{3.110}$$

For the same reasons as mentioned in subsection 3.2.3, limit (3.107) and limit (3.109) are not consistent. Expression (3.107) has one half as a lower bound as the term containing the Bessel functions is always non-negative for all $J_A \geq 0$ and $K_{AA} > 0$ which contradicts expression (3.109). This issue has not been realised in the literature.

Special Case: $A \equiv 0$ **and** $B \neq 0$

Let us now consider the special case where $A = 0$ and $B \neq 0$ in (3.95), that is,

$$G(z) = G_-(z). \tag{3.111}$$

The only remaining integration constant B can, again, be determined from the condition

$$G(z)|_{z=1} \stackrel{!}{=} 1, \tag{3.112}$$

which gives us

$$B = \frac{2^{\frac{1}{2}\left(\frac{L_A}{K_{AA}}-1\right)}}{I_{1-\frac{L_A}{K_{AA}}}\left(\sqrt{\frac{8J_A}{K_{AA}}}\right)}. \tag{3.113}$$

Using (3.32) we can write

$$G_-(z) = B(1+z)^{1-\frac{L_A}{K_{AA}}}\left(\frac{J_A}{K_{AA}}\right)^{\frac{1}{2}\left(1-\frac{L_A}{K_{AA}}\right)}\Omega_{1-\frac{L_A}{K_{AA}}}(z). \tag{3.114}$$

The series expansion $\Omega_{1-\frac{L_A}{K_{AA}}}(z)$ —cfr. (3.33)— converges for all values of z, whereas the MacClaurin series of $(1+z)^{1-\frac{L_A}{K_{AA}}}$ converges absolutely for $|z|=1$ if and only if $L_A K_{AA}^{-1} < 1$. Therefore, we have that the MacClaurin expansion of $G_-(z)$ converges absolutely for $|z|=1$ if and only if $L_A K_{AA}^{-1} < 1$.
In this special case, the average population of the chemical reactants[3] is given by

$$\langle \mathcal{N}_A \rangle_-^{ss} := \left.\frac{\mathrm{d}G(z)}{\mathrm{d}z}\right|_{z=1} \equiv \left.\frac{\mathrm{d}G_-(z)}{\mathrm{d}z}\right|_{z=1} = \frac{1}{2}\left(1-\frac{L_A}{K_{AA}}\right) + \sqrt{\frac{J_A}{2K_{AA}}}\frac{I_{2-\frac{L_A}{K_{AA}}}\left(\sqrt{\frac{8J_A}{K_{AA}}}\right)}{I_{1-\frac{L_A}{K_{AA}}}\left(\sqrt{\frac{8J_A}{K_{AA}}}\right)}. \tag{3.115}$$

The MacClaurin series of the first derivative of the generating function candidate converges conditionally, since

$$\begin{aligned}\frac{\mathrm{d}G_-(z)}{\mathrm{d}z} = {} & B\left(1-\frac{L_A}{K_{AA}}\right)\left(\frac{J_A}{K_{AA}}\right)^{\frac{1}{2}\left(1-\frac{L_A}{K_{AA}}\right)}(1+z)^{-\frac{L_A}{K_{AA}}}\Omega_{1-\frac{L_A}{K_{AA}}}(z) + \\ & B\left(\frac{J_A}{K_{AA}}\right)^{\frac{1}{2}\left(3-\frac{L_A}{K_{AA}}\right)}(1+z)^{1-\frac{L_A}{K_{AA}}}\Omega_{2-\frac{L_A}{K_{AA}}}(z),\end{aligned} \tag{3.116}$$

with the series $\Omega_{1-\frac{L_A}{K_{AA}}}(z)$ and $\Omega_{2-\frac{L_A}{K_{AA}}}(z)$ as defined in (3.33). The latter series converge everywhere, whereas the convergence radii of the expansions of $(1+z)^{-\frac{L_A}{K_{AA}}}$ and $(1+z)^{1-\frac{L_A}{K_{AA}}}$ have to be determined from Theorem 1; the series expansion converges conditionally for $z=1$ if $L_A K_{AA}^{-1} < 1$. As a consequence, the MacClaurin series of the

[3]This last expression should be understood in a statistical sense. More precisely, the rate coefficients describe statistical properties of the processes of adsorption, evaporation and chemical reaction of molecules, and as such they are not well-defined for a single given molecule. In this sense, these constants are analogous to the mean life of radioactive materials: one cannot say that a single radioactive atom has a 50 % probability of decaying during a mean life period. Similarly, although L_A expresses the probability of evaporation, one cannot speak of the probability of a single particular molecule to evaporate during the time span of observation. Instead one refers to the decay of any molecule in an ensemble of molecules. The same line of argument is true for the reaction rate. Therefore, it is reasonable to have a non-zero late-time value for the average particle population of the chemical reactants even if the source rate is zero.

first derivative of the generating function candidate converges conditionally for $z = 1$ if $L_A K_{AA}^{-1} < 1$ which is the value of physical interest.
In the case of small $L_A K_{AA}^{-1}$ we employ (3.38) which gives us

$$\langle \mathcal{N}_A \rangle_-^{ss} = \frac{1}{2} + \frac{I_2\left(\sqrt{\frac{8J_A}{K_{AA}}}\right)}{I_1\left(\sqrt{\frac{8J_A}{K_{AA}}}\right)} - \frac{L_A}{K_{AA}}\left(\frac{1}{2} + \frac{I_2\left(\sqrt{\frac{8J_A}{K_{AA}}}\right)\Theta\left(1, \sqrt{\frac{8J_A}{K_{AA}}}\right)}{I_1^2\left(\sqrt{\frac{8J_A}{K_{AA}}}\right)} + \frac{\Theta\left(2, \sqrt{\frac{8J_A}{K_{AA}}}\right)}{I_1\left(\sqrt{\frac{8J_A}{K_{AA}}}\right)}\right) + \mathcal{O}\left(\left(\frac{L_A}{K_{AA}}\right)^2\right), \quad (3.117)$$

which for fixed K_{AA} in the limit of vanishing evaporation rate L_A leads to

$$\lim_{L_A \to 0} \langle \mathcal{N}_A \rangle_-^{ss} = \frac{1}{2} + \frac{J_A}{2K_{AA}} \frac{I_2\left(\sqrt{\frac{8J_A}{K_{AA}}}\right)}{I_1\left(\sqrt{\frac{8J_A}{K_{AA}}}\right)}, \quad (3.118)$$

which is the same result as obtained before —(3.107).
In the series expansion for small $J_A K_{AA}^{-1}$ we derive the following expression for the average chemical reactant population[4]

$$\langle \mathcal{N}_A \rangle_-^{ss} = \frac{1}{2}\left(1 - \frac{L_A}{K_{AA}}\right) + \frac{J_A}{K_{AA}\left(2 - \frac{L_A}{K_{AA}}\right)}\left(1 + \mathcal{O}\left(\frac{J_A}{K_{AA}}\right)\right). \quad (3.119)$$

This means that in the limit of the source rate approaching zero and for fixed reaction rate we have

$$\lim_{J_A \to 0} \langle \mathcal{N}_A \rangle_-^{ss} = \frac{1}{2}\left(1 - \frac{L_A}{K_{AA}}\right), \quad (3.120)$$

which gives the same expression as the exact solution to the master equation with zero source rate (3.46) for $A = 0$. This result differs greatly from the computation of the limit in the special case where $A \neq 0$ and $B \equiv 0$ —cfr. equation (3.109). In contrast to (3.109) where the equivalent limit value is zero, the above limit is consistent with the limit (3.84).

[4]As we will see later on, the lower bound of the late-time limit of the modulus of a solution to the first stochastic constraint equation (3.177) corresponds to the leading order term in the above expansion.

General Case: $A \neq 0$ **and** $B \neq 0$

First, let us consider the normalisation condition

$$G(z)|_{z=1} = G_+(z)|_{z=1} + G_-(z)|_{z=1}. \tag{3.121}$$

The radius of convergence of the MacClaurin expansion of the full solution

$$G(z) = A\left(\frac{J_A}{K_{AA}}\right)^{\frac{1}{2}\left(\frac{L_A}{K_{AA}}-1\right)} \Omega_{\frac{L_A}{K_{AA}}-1}(z) + B(1+z)^{1-\frac{L_A}{K_{AA}}}\left(\frac{J_A}{K_{AA}}\right)^{\frac{1}{2}\left(1-\frac{L_A}{K_{AA}}\right)} \Omega_{1-\frac{L_A}{K_{AA}}}(z), \tag{3.122}$$

with the series $\Omega_{\frac{L_A}{K_{AA}}-1}(z)$ and $\Omega_{1-\frac{L_A}{K_{AA}}}(z)$ as given by (3.33), follows from the radii of convergence of the MacClaurin expansion of the special solutions $G_+(z)$ and $G_-(z)$ and one has the following:
(i) if $L_A K_{AA}^{-1} < 1$:

$$G(z) \equiv G_{L_A K_{AA}^{-1}<1}(z) = G_+(z) + G_-(z), \tag{3.123}$$

(ii) if $L_A K_{AA}^{-1} \geq 1$:

$$G(z) \equiv G_{L_A K_{AA}^{-1}\geq 1}(z) = G_+(z), \tag{3.124}$$

since the MacClaurin series of $(1+z)^{1-\frac{L_A}{K_{AA}}}$ does not converge absolutely in $z=1$ and, therefore, we have that $B=0$ if $L_A K_{AA}^{-1} \geq 1$. In that case, the analysis undertaken for the special case: $A \neq 0$ and $B = 0$ gives the average number of reactants

$$\langle \mathcal{N}_A \rangle^{ss} \equiv \langle \mathcal{N}_A \rangle^{ss}_{L_A K_{AA}^{-1}\geq 1} = \langle \mathcal{N}_A \rangle^{ss}_{+}, \tag{3.125}$$

if and only if $L_A K_{AA}^{-1} \geq 1$. In the literature this expression was assumed to hold for any value of $L_A > 0$ and $K_{AA} > 0$.
Let us now consider the case $L_A K_{AA}^{-1} < 1$. We assign the values $p \in [0,1]$ to the probabilities for even and odd populations in the following way

$$P_{even} = p, \quad \longrightarrow \quad P_{odd} = 1 - p, \tag{3.126}$$

which —see (3.69)— is equivalent to

$$G_{L_A K_{AA}^{-1}<1}(z)|_{z=-1} = 2p - 1, \tag{3.127}$$

if convergence of the expansion is given in $z = -1$. The above condition will be used to fix one of the two integration constants $A \neq 0$ and $B \neq 0$ in the expression (3.123). For this, we expand the generating function candidate (3.123) for $(1+z) \approx 0$ according

to (3.36). We derive

$$G_{L_A K_{AA}^{-1}<1}(z) = \frac{A\left(\frac{J_A}{K_{AA}}\right)^{\frac{1}{2}\left(\frac{L_A}{K_{AA}}-1\right)}}{\Gamma\left(\frac{L_A}{K_{AA}}\right)}\left(1+\mathcal{O}\left(1+z\right)\right) + \frac{B\left(\frac{J_A}{K_{AA}}\right)^{\frac{1}{2}\left(1-\frac{L_A}{K_{AA}}\right)}\left(1+z\right)^{1-\frac{L_A}{K_{AA}}}}{\Gamma\left(2-\frac{L_A}{K_{AA}}\right)}\left(1+\mathcal{O}\left(1+z\right)\right), \tag{3.128}$$

so that for $L_A K_{AA}^{-1} < 1$ we have the following:

$$G_{L_A K_{AA}^{-1}<1}(z)\big|_{z=-1} = \frac{A\left(\frac{J_A}{K_{AA}}\right)^{\frac{1}{2}\left(\frac{L_A}{K_{AA}}-1\right)}}{\Gamma\left(\frac{L_A}{K_{AA}}\right)}. \tag{3.129}$$

Together with the condition

$$G_{L_A K_{AA}^{-1}<1}(z)|_{z=1} \stackrel{!}{=} 1, \tag{3.130}$$

one can determine the second integration constant, so that

$$\begin{aligned} A &= (2p-1)\Gamma\left(\frac{L_A}{K_{AA}}\right)\left(\frac{J_A}{K_{AA}}\right)^{\frac{1}{2}\left(1-\frac{L_A}{K_{AA}}\right)}, \\ B &= \frac{2^{\frac{1}{2}\left(\frac{L_A}{K_{AA}}-1\right)}}{I_{1-\frac{L_A}{K_{AA}}}\left(\sqrt{\frac{8J_A}{K_{AA}}}\right)} - (2p-1)\frac{\Gamma\left(\frac{L_A}{K_{AA}}\right)\left(\frac{J_A}{K_{AA}}\right)^{\frac{1}{2}\left(1-\frac{L_A}{K_{AA}}\right)} I_{\frac{L_A}{K_{AA}}-1}\left(\sqrt{\frac{8J_A}{K_{AA}}}\right)}{I_{1-\frac{L_A}{K_{AA}}}\left(\sqrt{\frac{8J_A}{K_{AA}}}\right)}, \end{aligned} \tag{3.131}$$

where it is assumed that $L_A K_{AA}^{-1} < 1$. Inserting the latter expressions in (3.98) we get

$$\begin{aligned}\langle \mathcal{N}_A \rangle^{ss}_{L_A K_{AA}^{-1}<1} = \frac{1}{2}\left(1-\frac{L_A}{K_{AA}}\right) + \sqrt{\frac{J_A}{2K_{AA}}}\frac{I_{2-\frac{L_A}{K_{AA}}}\left(\sqrt{\frac{8J_A}{K_{AA}}}\right)}{I_{1-\frac{L_A}{K_{AA}}}\left(\sqrt{\frac{8J_A}{K_{AA}}}\right)} - \\ (2p-1)\left(1-\frac{L_A}{K_{AA}}\right)\Gamma\left(\frac{L_A}{K_{AA}}\right)\left(\frac{J_A}{K_{AA}}\right)^{\frac{1}{2}\left(1-\frac{L_A}{K_{AA}}\right)} 2^{-\frac{1}{2}\left(\frac{L_A}{K_{AA}}+1\right)} I_{\frac{L_A}{K_{AA}}-1}\left(\sqrt{\frac{8J_A}{K_{AA}}}\right) + \\ (2p-1)\Gamma\left(\frac{L_A}{K_{AA}}\right)\left(\frac{J_A}{K_{AA}}\right)^{1-\frac{L_A}{2K_{AA}}} 2^{-\frac{L_A}{2K_{AA}}} I_{\frac{L_A}{K_{AA}}}\left(\sqrt{\frac{8J_A}{K_{AA}}}\right) - \\ (2p-1)\Gamma\left(\frac{L_A}{K_{AA}}\right)\left(\frac{J_A}{K_{AA}}\right)^{1-\frac{L_A}{2K_{AA}}} 2^{-\frac{L_A}{2K_{AA}}} \frac{I_{2-\frac{L_A}{K_{AA}}}\left(\sqrt{\frac{8J_A}{K_{AA}}}\right) I_{\frac{L_A}{K_{AA}}-1}\left(\sqrt{\frac{8J_A}{K_{AA}}}\right)}{I_{1-\frac{L_A}{K_{AA}}}\left(\sqrt{\frac{8J_A}{K_{AA}}}\right)}.\end{aligned} \tag{3.132}$$

Next, let us rewrite expression (3.132) in the following way

$$\begin{aligned}\langle \mathcal{N}_A \rangle^{ss}_{L_A K_{AA}^{-1}<1} = \frac{1}{2}\left(1-\frac{L_A}{K_{AA}}\right) + \sqrt{\frac{J_A}{2K_{AA}}}\frac{I_{2-\frac{L_A}{K_{AA}}}\left(\sqrt{\frac{8J_A}{K_{AA}}}\right)}{I_{1-\frac{L_A}{K_{AA}}}\left(\sqrt{\frac{8J_A}{K_{AA}}}\right)} + \\ (2p-1)\Gamma\left(\frac{L_A}{K_{AA}}\right)\left(\mathcal{A} I_{\frac{L_A}{K_{AA}}}\left(\sqrt{\frac{8J_A}{K_{AA}}}\right) - \right. \\ \mathcal{A} I_{2-\frac{L_A}{K_{AA}}}\left(\sqrt{\frac{8J_A}{K_{AA}}}\right)\frac{I_{1+\frac{L_A}{K_{AA}}}\left(\sqrt{\frac{8J_A}{K_{AA}}}\right) + \mathcal{C} I_{\frac{L_A}{K_{AA}}}\left(\sqrt{\frac{8J_A}{K_{AA}}}\right)}{I_{1-\frac{L_A}{K_{AA}}}\left(\sqrt{\frac{8J_A}{K_{AA}}}\right)} - \\ \left.\mathcal{B}\left(I_{1+\frac{L_A}{K_{AA}}}\left(\sqrt{\frac{8J_A}{K_{AA}}}\right) + \mathcal{C} I_{\frac{L_A}{K_{AA}}}\left(\sqrt{\frac{8J_A}{K_{AA}}}\right)\right)\right),\end{aligned} \tag{3.133}$$

with

$$\begin{aligned}\mathcal{A} &:= \left(\frac{J_A}{K_{AA}}\right)^{1-\frac{L_A}{2K_{AA}}} 2^{-\frac{L_A}{2K_{AA}}}, \\ \mathcal{B} &:= \left(1-\frac{L_A}{K_{AA}}\right)\left(\frac{J_A}{K_{AA}}\right)^{\frac{1}{2}\left(1-\frac{L_A}{K_{AA}}\right)} 2^{-\frac{1}{2}\left(\frac{L_A}{K_{AA}}+1\right)}, \\ \mathcal{C} &:= \frac{L_A}{\sqrt{2J_A K_{AA}}},\end{aligned} \tag{3.134}$$

where we used the recurrence relation for Bessel functions (3.31). We will compare the above general expression for the mean molecule population with the particular cases

discussed previously. The above expression (3.132) for small $J_A K_{AA}^{-1}$ can be written as

$$\langle \mathcal{N}_A \rangle^{ss}_{L_A K_{AA}^{-1}<1} = \frac{1}{2}\left(1 - \frac{L_A}{K_{AA}}\right) + \left(\frac{J_A}{2K_{AA} - L_A} + (2p-1)\left(\frac{J_A}{L_A} - \frac{J_A}{2K_{AA} - L_A} - \frac{1}{2}\left(1 - \frac{L_A}{K_{AA}}\right)\right)\right)\left(1 + \mathcal{O}\left(\frac{J_A}{K_{AA}}\right)\right), \tag{3.135}$$

so that the limit of $\langle \mathcal{N}_A \rangle^{ss}_{L_A K_{AA}^{-1}<1}$ for the source rate approaching zero and for fixed K_{AA} is given by

$$\lim_{J_A \to 0} \langle \mathcal{N}_A \rangle^{ss}_{L_A K_{AA}^{-1}<1} = \frac{1}{2}\left(1 - \frac{L_A}{K_{AA}}\right) - (2p-1)\frac{1}{2}\left(1 - \frac{L_A}{K_{AA}}\right). \tag{3.136}$$

Consequently, the range for the value of the average population of reaction partners of chemical species type A, which is determined by taking the minimum and maximum value of p, namely $p = 0$ and $p = 1$, is

$$\lim_{J_A \to 0} \langle \mathcal{N}_A \rangle^{ss}_{L_A K_{AA}^{-1}<1} \in \left[0, 1 - \frac{L_A}{K_{AA}}\right], \tag{3.137}$$

which coincides with the result found in the section concerned with the solution to the stationary stochastic equation for vanishing source rate coefficient —cfr. with (3.76).

In addition, we want to evaluate the above mean particle population $\langle \mathcal{N}_A \rangle^{ss}_{L_A K_{AA}^{-1}<1}$ for the limit of the evaporation constant L_A approaching zero in order to compare the full steady state solution to the exact solution for vanishing evaporation constant (3.82). Therefore, we consider expansions of Bessel functions for small perturbations of the index (3.38). Using the approximation for sufficiently small values of $L_A K_{AA}^{-1}$, we have

$$\frac{1}{I_{1-\frac{L_A}{K_{AA}}}\left(\sqrt{\frac{8J_A}{K_{AA}}}\right)} = \frac{1}{I_1\left(\sqrt{\frac{8J_A}{K_{AA}}}\right)}\left(1 + \frac{\frac{L_A}{K_{AA}}\Theta\left(1, \sqrt{\frac{8J_A}{K_{AA}}}\right) + \mathcal{O}\left(\left(\frac{L_A}{K_{AA}}\right)^2\right)}{I_1\left(\sqrt{\frac{8J_A}{K_{AA}}}\right)}\right). \tag{3.138}$$

Taking the above approximation into account we conclude that

$$\langle \mathcal{N}_A \rangle^{ss}_{L_A K_{AA}^{-1}<1} = \frac{1}{2}\left(1-\frac{L_A}{K_{AA}}\right)+$$
$$\sqrt{\frac{J_A}{2K_{AA}}}\left(\frac{I_2\left(\sqrt{\frac{8J_A}{K_{AA}}}\right)}{I_1\left(\sqrt{\frac{8J_A}{K_{AA}}}\right)}-\frac{L_A}{K_{AA}}\left(\frac{\Theta\left(2,\sqrt{\frac{8J_A}{K_{AA}}}\right)}{I_1\left(\sqrt{\frac{8J_A}{K_{AA}}}\right)}-\frac{\Theta\left(1,\sqrt{\frac{8J_A}{K_{AA}}}\right)I_2\left(\sqrt{\frac{8J_A}{K_{AA}}}\right)}{I_1^2\left(\sqrt{\frac{8J_A}{K_{AA}}}\right)}\right)+\right.$$
$$\left.\mathcal{O}\left(\left(\frac{L_A}{K_{AA}}\right)^2\right)\right)+$$
$$(2p-1)\Gamma\left(\frac{L_A}{K_{AA}}\right)\left[\mathcal{A}\left(I_0\left(\sqrt{\frac{8J_A}{K_{AA}}}\right)+\Theta\left(0,\sqrt{\frac{8J_A}{K_{AA}}}\right)\frac{L_A}{K_{AA}}-I_2\left(\sqrt{\frac{8J_A}{K_{AA}}}\right)-\right.\right.$$
$$2I_2\left(\sqrt{\frac{8J_A}{K_{AA}}}\right)\frac{\Theta\left(1,\sqrt{\frac{8J_A}{K_{AA}}}\right)\frac{L_A}{K_{AA}}}{I_1\left(\sqrt{\frac{8J_A}{K_{AA}}}\right)}+\Theta\left(2,\sqrt{\frac{8J_A}{K_{AA}}}\right)\frac{L_A}{K_{AA}}+\mathcal{O}\left(\left(\frac{L_A}{K_{AA}}\right)^2\right)-$$
$$\mathcal{C}\left(\frac{I_0\left(\sqrt{\frac{8J_A}{K_{AA}}}\right)I_2\left(\sqrt{\frac{8J_A}{K_{AA}}}\right)}{I_1\left(\sqrt{\frac{8J_A}{K_{AA}}}\right)}+\frac{I_0\left(\sqrt{\frac{8J_A}{K_{AA}}}\right)I_2\left(\sqrt{\frac{8J_A}{K_{AA}}}\right)\Theta\left(1,\sqrt{\frac{8J_A}{K_{AA}}}\right)\frac{L_A}{K_{AA}}}{I_1^2\left(\sqrt{\frac{8J_A}{K_{AA}}}\right)}-\right.$$
$$\frac{I_0\left(\sqrt{\frac{8J_A}{K_{AA}}}\right)\Theta\left(2,\sqrt{\frac{8J_A}{K_{AA}}}\right)\frac{L_A}{K_{AA}}}{I_1\left(\sqrt{\frac{8J_A}{K_{AA}}}\right)}+\frac{I_2\left(\sqrt{\frac{8J_A}{K_{AA}}}\right)\Theta\left(0,\sqrt{\frac{8J_A}{K_{AA}}}\right)\frac{L_A}{K_{AA}}}{I_1\left(\sqrt{\frac{8J_A}{K_{AA}}}\right)}+$$
$$\left.\left.\mathcal{O}\left(\left(\frac{L_A}{K_{AA}}\right)^2\right)\right)\right)-$$
$$\mathcal{B}\left(I_1\left(\sqrt{\frac{8J_A}{K_{AA}}}\right)+\Theta\left(1,\sqrt{\frac{8J_A}{K_{AA}}}\right)\frac{L_A}{K_{AA}}+\mathcal{O}\left(\left(\frac{L_A}{K_{AA}}\right)^2\right)+\right.$$
$$\left.\left.\mathcal{C}\left(I_0\left(\sqrt{\frac{8J_A}{K_{AA}}}\right)+\Theta\left(0,\sqrt{\frac{8J_A}{K_{AA}}}\right)\frac{L_A}{K_{AA}}+\mathcal{O}\left(\left(\frac{L_A}{K_{AA}}\right)^2\right)\right)\right)\right]. \qquad (3.139)$$

The terms of zeroth order in $L_A K_{AA}^{-1}$ arising from the modified Bessel functions in the terms multiplying $(2p-1)\Gamma\left(\frac{L_A}{K_{AA}}\right)$ cancel each other, so that the leading order terms

are of first order in $L_A K_{AA}^{-1}$, so that

$$\begin{aligned}\langle \mathcal{N}_A \rangle^{ss}_{L_A K_{AA}^{-1}<1} &= \left(\frac{1}{2} + \sqrt{\frac{J_A}{2K_{AA}}} \frac{I_2\left(\sqrt{\frac{8J_A}{K_{AA}}}\right)}{I_1\left(\sqrt{\frac{8J_A}{K_{AA}}}\right)} \right) \left(1 + \mathcal{O}\left(\frac{L_A}{K_{AA}} \right) \right) + \\ (2p-1) &\left(\left(\frac{L_A}{K_{AA}} \right)^{-1} + \mathcal{O}(1) \right) \left(f(J_A, K_{AA}) \left(\frac{L_A}{K_{AA}} \right) + \mathcal{O}\left(\left(\frac{L_A}{K_{AA}} \right)^{1+\epsilon} \right) \right) \\ &= \left(\frac{1}{2} + \sqrt{\frac{J_A}{2K_{AA}}} \frac{I_2\left(\sqrt{\frac{8J_A}{K_{AA}}}\right)}{I_1\left(\sqrt{\frac{8J_A}{K_{AA}}}\right)} \right) \left(1 + \mathcal{O}\left(\frac{L_A}{K_{AA}} \right) \right) + \\ &\quad (2p-1) \left(f(J_A, K_{AA}) + \mathcal{O}\left(\left(\frac{L_A}{K_{AA}} \right)^{\epsilon} \right) \right), \end{aligned} \tag{3.140}$$

where $\epsilon > 0$ and $f(J_A, K_{AA}) \neq 0$ and where we have used the form of the Laurent expansion of the Gamma function at the point $z = 0$. We know that the average number of chemical reaction partners for vanishing evaporation rate reads

$$\langle \mathcal{N}_A(L_A \equiv 0) \rangle^{ss} = \frac{1}{2} + \sqrt{\frac{J_A}{2K_{AA}}} \frac{I_2\left(\sqrt{\frac{8J_A}{K_{AA}}}\right)}{I_1\left(\sqrt{\frac{8J_A}{K_{AA}}}\right)}, \tag{3.141}$$

so that we have to set

$$p \equiv \frac{1}{2}, \tag{3.142}$$

in order for the limit of (3.140) for $L_A \to 0$ and fixed $K_{AA} \neq 0$ to reproduce this exact result. From (3.142) it follows that, in general,

$$G(z)_{z=-1} \equiv 0, \tag{3.143}$$

for $L_A K_{AA}^{-1} < 1$ which is equivalent to

$$A \equiv 0. \tag{3.144}$$

The full expression for the average particle number of chemical reactants A for $L_A K_{AA}^{-1} < 1$ reduces to

$$\langle \mathcal{N}_A \rangle^{ss}_{L_A K_{AA}^{-1}<1} \equiv \left. \frac{\mathrm{d}G_-(z)}{\mathrm{d}z} \right|_{z=1}. \tag{3.145}$$

We argue that the expression for the average population of molecules of chemical species type A (3.103) presented in the literature has to be replaced by the following:

$$\boxed{\langle \mathcal{N}_A \rangle^{ss} = \begin{cases} \frac{1}{2}\left(1 - \frac{L_A}{K_{AA}}\right) + \sqrt{\frac{J_A}{2K_{AA}}} \frac{I_{2-\frac{L_A}{K_{AA}}}\left(\sqrt{\frac{8J_A}{K_{AA}}}\right)}{I_{1-\frac{L_A}{K_{AA}}}\left(\sqrt{\frac{8J_A}{K_{AA}}}\right)} & : \quad L_A K_{AA}^{-1} < 1 \\ \sqrt{\frac{J_A}{2K_{AA}}} \frac{I_{\frac{L_A}{K_{AA}}}\left(\sqrt{\frac{8J_A}{K_{AA}}}\right)}{I_{\frac{L_A}{K_{AA}}-1}\left(\sqrt{\frac{8J_A}{K_{AA}}}\right)} & : \quad L_A K_{AA}^{-1} \geq 1 \end{cases}.} \tag{3.146}$$

Let us stress that the case $L_A K_{AA}^{-1} < 1$ is of great physical relevance when employing the M1 data which we will discuss in detail in the next section.

Production Rate

The stochastic *production rate* for the average number of molecules of chemical species type C is defined as

$$\mathcal{P}_C := K_{AA} \frac{\mathrm{d}^2 F(z)}{\mathrm{d}z^2}\bigg|_{z=1} = K_{AA} \sum_{N_A=0}^{\infty} N_A(N_A - 1) P(N_A), \tag{3.147}$$

which can be compared to the production rate for the average number of molecules of chemical species type C in the mean-field framework

$$P_C := K_{AA} \left(\langle N_A \rangle^{ss}\right)^2 = \frac{J_A - L_A \langle N_A \rangle^{ss}}{2}. \tag{3.148}$$

In the special case of a vanishing reaction rate the generating function candidate reads

$$G(z) = e^{\frac{J_A}{L_A}(z-1)}. \tag{3.149}$$

The MacClaurin series of the generating function candidate and its first and second derivatives converge absolutely for $z = 1$. However, the production rate of the chemical species C is zero for vanishing reaction rate coefficient —see equation (3.147).

The second derivative of the generating function candidate derived for the spe-

cial case that the evaporation rate is zero reads

$$\frac{\mathrm{d}^2G(z)}{\mathrm{d}z^2} = \frac{1}{\sqrt{2}I_1\left(\sqrt{\frac{8J_A}{K_{AA}}}\right)}\left(2\sqrt{\frac{J_A}{K_{AA}}}(1+z)^{-1}I_2\left(2\sqrt{\frac{J_A}{K_{AA}}}(1+z)^{\frac{1}{2}}\right) + \frac{J_A}{K_{AA}}(1+z)^{-\frac{1}{2}}I_3\left(2\sqrt{\frac{J_A}{K_{AA}}}(1+z)^{\frac{1}{2}}\right)\right). \quad (3.150)$$

Using (3.32) one can rewrite the above expression for the second derivative of the generating function candidate in the following way

$$\frac{\mathrm{d}^2G(z)}{\mathrm{d}z^2} = \frac{1}{\sqrt{2}I_1\left(\sqrt{\frac{8J_A}{K_{AA}}}\right)}\left(2\left(\frac{J_A}{K_{AA}}\right)^{\frac{3}{2}}\Omega_2(z) + (1+z)\left(\frac{J_A}{K_{AA}}\right)^{\frac{5}{2}}\Omega_3(z)\right), \quad (3.151)$$

where the two series $\Omega_2(z)$ and $\Omega_3(z)$ according to (3.33) converge absolutely everywhere. The MacClaurin series of $(1+z)$ converges absolutely for $z=1$ since its power is strictly positive —see Theorem 1. Hence, the MacClaurin series of the second derivative of the generating function candidate for zero evaporation rate converges absolutely for $z=1$. Therefore, the production rate of chemical reaction products of species C for vanishing evporation rate reads

$$\mathcal{P}_C = \frac{K_{AA}}{I_1\left(\sqrt{\frac{8J_A}{K_{AA}}}\right)}\left(\sqrt{\frac{J_A}{2K_{AA}}}I_2\left(\sqrt{\frac{8J_A}{K_{AA}}}\right) + \frac{J_A}{2K_{AA}}I_3\left(\sqrt{\frac{8J_A}{K_{AA}}}\right)\right) \equiv \frac{J_A}{2}, \quad (3.152)$$

which corresponds to the production rate in the mean-field framework.

In the special case of zero source rate coefficient, the following generating function candidate was obtained

$$G(z) = A + B(1+z)^{1-\frac{L_A}{K_{AA}}}. \quad (3.153)$$

For $L_AK_{AA}^{-1} < 1$, the second derivative of the above generating function candidate reads

$$\frac{\mathrm{d}^2G(z)}{\mathrm{d}z^2} = -B\frac{L_A}{K_{AA}}\left(1-\frac{L_A}{K_{AA}}\right)(1+z)^{-1-\frac{L_A}{K_{AA}}}, \quad (3.154)$$

which does not converge for $z=1$ since the real part of the power $-L_AK_{AA}^{-1}-1$ is not strictly greater than -1 even if $L_AK_{AA}^{-1}=0$. This has as a consequence that one can not make use of the methods of generating functions to derive an expression for the

production rate as given in (3.147) in the case that $L_A K_{AA}^{-1} < 1$. For $L_A K_{AA}^{-1} \geq 1$, the production rate is zero since the second derivative of the generating function candidate is zero for all values of z.

In general, that is for the full master equation (3.20), the second derivative of the generating function candidate reads

$$\begin{aligned}\frac{\mathrm{d}^2 G(z)}{\mathrm{d}z^2} = & A\frac{J_A}{K_{AA}}(1+z)^{-\frac{1}{2}\left(\frac{L_A}{K_{AA}}+1\right)} I_{\frac{L_A}{K_{AA}}+1}\left(2\sqrt{\frac{J_A}{K_{AA}}}(1+z)^{\frac{1}{2}}\right) - \\ & B\left(1-\frac{L_A}{K_{AA}}\right)\frac{L_A}{K_{AA}}(1+z)^{-\frac{1}{2}\left(\frac{L_A}{K_{AA}}+3\right)} I_{1-\frac{L_A}{K_{AA}}}\left(2\sqrt{\frac{J_A}{K_{AA}}}(1+z)^{\frac{1}{2}}\right) + \\ & 2B\left(1-\frac{L_A}{K_{AA}}\right)\sqrt{\frac{J_A}{K_{AA}}}(1+z)^{-\frac{1}{2}\left(\frac{L_A}{K_{AA}}+2\right)} I_{2-\frac{L_A}{K_{AA}}}\left(2\sqrt{\frac{J_A}{K_{AA}}}(1+z)^{\frac{1}{2}}\right) + \\ & B\frac{J_A}{K_{AA}}(1+z)^{-\frac{1}{2}\left(\frac{L_A}{K_{AA}}+1\right)} I_{3-\frac{L_A}{K_{AA}}}\left(2\sqrt{\frac{J_A}{K_{AA}}}(1+z)^{\frac{1}{2}}\right). \end{aligned} \tag{3.155}$$

Assuming that $L_A K_{AA}^{-1} \geq 1$, the production rate $\mathcal{P}_{C_+}$ is given by

$$\mathcal{P}_{C_+} = \frac{J_A}{2}\frac{I_{\frac{L_A}{K_{AA}}+1}\left(\sqrt{\frac{8J_A}{K_{AA}}}\right)}{I_{\frac{L_A}{K_{AA}}-1}\left(\sqrt{\frac{8J_A}{K_{AA}}}\right)}. \tag{3.156}$$

Using (3.103) one can show that

$$\mathcal{P}_{C_+} \equiv \frac{J_A - L_A\langle \mathcal{N}_A\rangle_+^{ss}}{2}. \tag{3.157}$$

The convergence criteria are satisfied for every value of z since

$$\frac{\mathrm{d}^2 G_+(z)}{\mathrm{d}z^2} = A\left(\frac{J_A}{K_{AA}}\right)^{\frac{1}{2}\left(\frac{L_A}{K_{AA}}+3\right)} \Omega_{\frac{L_A}{K_{AA}}+1}. \tag{3.158}$$

On the other hand, if $L_A K_{AA}^{-1} < 1$, we have the following production rate, namely,

$$\mathcal{P}_{C_-} = K_{AA}\left(\frac{L_A}{4K_{AA}}\left(\frac{L_A}{K_{AA}}-1\right)+\sqrt{\frac{J_A}{2K_{AA}}}\left(1-\frac{L_A}{K_{AA}}\right)\frac{I_{2-\frac{L_A}{K_{AA}}}\left(\sqrt{\frac{8J_A}{K_{AA}}}\right)}{I_{1-\frac{L_A}{K_{AA}}}\left(\sqrt{\frac{8J_A}{K_{AA}}}\right)}+\right.$$
$$\left.\frac{J}{2K_{AA}}\frac{I_{3-\frac{L_A}{K_{AA}}}\left(\sqrt{\frac{8J_A}{K_{AA}}}\right)}{I_{2-\frac{L_A}{K_{AA}}}\left(\sqrt{\frac{8J_A}{K_{AA}}}\right)}\right). \tag{3.159}$$

Again, using (3.115) one can write

$$\mathcal{P}_{C_-} \equiv \frac{J_A - L_A\langle\mathcal{N}_A\rangle_-^{ss}}{2}. \tag{3.160}$$

However, absolute convergence has to be investigated before the above expression for the production rate can be taken seriously. The above expression for the second derivative of the generating function candidate can be rewritten using (3.32):

$$\frac{\mathrm{d}^2G_-(z)}{\mathrm{d}z^2} = B\left(2\left(\frac{J_A}{K_{AA}}\right)^{\frac{1}{2}\left(3-\frac{L_A}{K_{AA}}\right)}(1+z)^{-\frac{L_A}{K_{AA}}}\Omega_{2-\frac{L_A}{K_{AA}}}(z)+\right.$$
$$\left(\frac{J_A}{K_{AA}}\right)^{\frac{1}{2}\left(5-\frac{L_A}{K_{AA}}\right)}(1+z)^{1-\frac{L_A}{K_{AA}}}\Omega_{3-\frac{L_A}{K_{AA}}}(z)-$$
$$\left.\left(1-\frac{L_A}{K_{AA}}\right)\frac{L_A}{K_{AA}}\left(\frac{J_A}{K_{AA}}\right)^{\frac{1}{2}\left(1-\frac{L_A}{K_{AA}}\right)}(1+z)^{-1-\frac{L_A}{K_{AA}}}\Omega_{1-\frac{L_A}{K_{AA}}}(z)\right), \tag{3.161}$$

where the three series $\Omega_{2-\frac{L_A}{K_{AA}}}(z)$, $\Omega_{3-\frac{L_A}{K_{AA}}}(z)$ and $\Omega_{1-\frac{L_A}{K_{AA}}}(z)$ which are defined by (3.33) converge absolutely everywhere. Furthermore, we assume —as in preceding calculations— that $L_A K_{AA}^{-1} < 1$. The MacClaurin series of $(1+z)^{1-\frac{L_A}{K_{AA}}}$ converges absolutely for $z = 1$ since its power is strictly greater than -1 as required, and the MacClaurin series of $(1+z)^{-\frac{L_A}{K_{AA}}}$ only converges for $z = 1$ if $L_A K_{AA}^{-1} < 1$. However, the MacClaurin series of $(1+z)^{-1-\frac{L_A}{K_{AA}}}$ does not converge for $z = 1$ since the power $-1-\frac{L_A}{K_{AA}}$ is never strictly greater than -1 since $L_A \geq 0$ and $K_{AA} \geq 0$. Hence, the MacClaurin series of the second derivative of the generating function candidate does not converge for $z = 1$. Again, the methods of generating functions can not be used to calculate the production rate. Finding an alternative procedure to calculate the production rate of the chemical reaction product is beyond the scope of this thesis.

Comment on the Alternative Approach

Let us recall the alternative approach to derive an exact solution to the stationary master equation as presented in [5]. At this point we do not want to go into details about regularity conditions in the mentioned publication. However, we would like to point out that the reduced form of the non-vanishing off-diagonal elements of the matrix $\mathbf{M}''$ which fulfills the stationary master equation

$$\mathbf{M}''\mathbf{p} = 0, \tag{3.162}$$

with $\mathbf{p}$ the probability vector

$$\mathbf{p} := (P(\{N_A\} = 0), P(\{N_A\} = 1), P(\{N_A\} = 2), ...), \tag{3.163}$$

can not only be expressed as continued fractions of the ratio of Bessel functions as stated by the authors, namely,

$$\frac{I_{\frac{L_A}{K_{AA}}+N-1}\left(2\sqrt{\frac{J_A}{K_{AA}}}\right)}{I_{\frac{L_A}{K_{AA}}+N}\left(2\sqrt{\frac{J_A}{K_{AA}}}\right)}, \tag{3.164}$$

but also as continued fractions of the ratio of Bessel functions[5]

$$\frac{I_{1-\frac{L_A}{K_{AA}}-N}\left(2\sqrt{\frac{J_A}{K_{AA}}}\right)}{I_{-\frac{L_A}{K_{AA}}-N}\left(2\sqrt{\frac{J_A}{K_{AA}}}\right)}. \tag{3.165}$$

Consequently, from the latter observation one has to conclude that the alternative approach by [5] also leads to a second exact solution of the stationary master equation, in fact to a superposition of two solutions, that was not mentioned in the publication. This result is consistent with the results presented in this thesis.

3.3 Stochastic Dynamical Solutions

This section is concerned with exact and numerical solutions to the stochastic constraint equations arising in the Doi-Peliti formalism in order to determine the average particle population of chemical reactants and reaction products in a single spatial site model for a heterogeneous chemical reaction of type $A + A \to C$.

[5] A detailed calculation can be found in Appendix B.

3.3.1 Special Case: Vanishing Source Rate

Exact Solutions

The mean-field rate equation for the evolution of the average particle population of chemical reactants of species A in the single spatial site model for vanishing source rate reads[6]

$$\frac{\mathrm{d}}{\mathrm{d}t}\langle N_A(t)\rangle + 2K_{AA}\langle N_A(t)\rangle^2 + L_A\langle N_A(t)\rangle = 0, \tag{3.166}$$

where $\langle N_A(t)\rangle$ denotes the mean particle population of the A molecules in the mean-field approximation. The mean-field evolution equation (3.166) is solved by

$$\langle N_A(t)\rangle = \frac{L_A}{2K_{AA}}\frac{1}{e^{L_A t}\big(1+\frac{L_A}{2K_{AA}}\langle N_A(0)\rangle^{-1}\big)-1}, \tag{3.167}$$

for $\langle N_A(0)\rangle \neq 0$. The stochastic constraint equation (2.61) for the complex fluctuating field $\bar{\Phi}_A(t)$ in zero spatial dimensions with vanishing source rate takes the form

$$\frac{\mathrm{d}}{\mathrm{d}t}\bar{\Phi}_A(t) + 2K_{AA}\bar{\Phi}_A^2(t) + L_A\bar{\Phi}_A(t) - \mathrm{i}\sqrt{2K_{AA}}\bar{\Phi}_A(t)\eta(t) = 0. \tag{3.168}$$

The mean-field equation for the average particle population of the A molecules (3.166) and the stochastic constraint equation associated with the A molecules (3.168) seem to resemble each other. But, as mentioned before, a solution of the stochastic differential equation (3.168) is a complex, fluctuating field that can only be interpreted as an average particle population after it has been averaged in the sense of equation (2.64). For vanishing source rate it is possible to find an analytic solution of equation (3.168). The stochastic constraint equation (3.168) has to be understood[7] in terms of a stochastic integral equation [22]

$$\bar{\Phi}_A(t) - \bar{\Phi}_A(0) = \int_0^t \mathrm{d}s\; a[\bar{\Phi}_A(s), s] + \int_0^t \mathrm{d}s\; b[\bar{\Phi}_A(s), s]\eta(s), \tag{3.169}$$

[6]Note that the Langmuir-Hinshelwood rejection mechanism has been neglected which means that the Langmuir-Hinshelwood rejection terms $-J_A\langle N_A\rangle$ and $-J_A\langle N_C\rangle$ in equation (3.166) have been omitted. In the Langmuir-Hinshelwood rejection mechanism atoms of chemical species A that are deposited on top of A or C molecules already present on the grain surface are rejected. This assumption is a good approximation as long as the coverage of A and C atoms is low which is the case for interstellar conditions. However, at very low temperatures A atoms are immobile and may pile up on the surface leading to a high coverage. In order to include the Langmuir-Hinshelwood rejection mechanism in the stochastic model one would have to include that via the joint probability distribution in the master equation. In the sequel, we ignore this particular mechanism which enables us to compare our results more readily to the computations by other groups, for example, [4].

[7]This is due to the continuous but not smooth nature of a stochastic process. The first integral is the standard Riemann-Lebesgue integral and the second integral an Itô integral.

with

$$a[\bar{\Phi}_A(t),t] = -L_A\bar{\Phi}_A(t) - 2K_{AA}\bar{\Phi}_A^2(t): \ \textit{drift coefficient},$$
$$b[\bar{\Phi}_A(t),t] = \mathrm{i}\sqrt{2K_{AA}}\bar{\Phi}_A(t): \ \textit{diffusion coefficient}. \tag{3.170}$$

The stochastic noise $\eta(t)$ is rewritten in terms of the *Wiener process*[8] $W(t)$

$$\eta(t)\mathrm{d}t = \mathrm{d}W(t), \tag{3.171}$$

and, accordingly, equation (3.168) reads

$$\mathrm{d}\bar{\Phi}_A(t) = \big[-2K_{AA}\bar{\Phi}_A^2(t) - L_A\bar{\Phi}_A(t)\big]\mathrm{d}t + \mathrm{i}\sqrt{2K_{AA}}\bar{\Phi}_A(t)\mathrm{d}W(t). \tag{3.172}$$

The above equation is interpreted as a nonlinear reducible stochastic differential equation with polynomial drift of degree two in the Itô picture[9]. In contrast to a *Stratonovich stochastic differential equation*, an *Itô stochastic differential equation* can not be solved directly by methods of classical calculus[10]. In order to obtain an analytical solution of an Itô stochastic differential equation one has to use a modified version of the drift coefficient

$$a[\bar{\Phi}_A(t),t] \longrightarrow a[\bar{\Phi}_A(t),t] - \frac{1}{2}b[\bar{\Phi}_A(t),t]\frac{\delta}{\delta\bar{\Phi}_A(t)}b[\bar{\Phi}_A(t),t], \tag{3.173}$$

where the derivative in the last term is a functional derivative[11]. Equation (3.172) is a stochastic version of a Verhulst-like equation[12] —see [37]. It can be reduced to a linear stochastic differential equation with multiplicative noise. We obtain the solution to the

[8] See Appendix A.

[9] A stochastic differential equation is ambiguous in the sense that the noise term can be interpreted in various ways. The two standard interpretations are the Itô picture and the Stratonovich picture. If one intuitively views the stochastic noise as a random sequence of delta distributions, which cause jumps in the unknown function, the value of the function at the time the delta distribution arrives is undetermined. In the Itô picture the diffusion term is evaluated before the jump whereas in the Stratonovich picture the mean of the value before and after the jump is assumed. For a more detailed discussion see, for example, [62]. According to [37] *"...the Stratonovich interpretation of a stochastic differential equation is the appropriate one when the white noise is used as an idealization of a smooth real noise process."*. However, if the underlying physical process is a discrete Markov process —see Appendix A— *"...diffusion processes satisfying Itô stochastic differential equations are a convenient and mathematically tractable approximation of the actual process."* —see [37]

[10] Sample paths of a Wiener process are —with reasonable certainty— neither differentiable nor of bounded variation. As a consequence one is left with different interpretations of stochastic equations, namely the Itô and the Stratonovich interpretation. For a further reading we refer to [37].

[11] A functional derivative is a generalisation of the directional derivative. It differentiates in the direction of a function.

[12] See Appendix A.

first stochastic constraint equation in zero spatial dimensions for vanishing source rate —equation (3.172)—, namely,

$$\bar{\Phi}_A(t) = \frac{\bar{\Phi}_A(0) e^{(K_{AA}-L_A)t+\mathrm{i}\sqrt{2K_{AA}}W(t)}}{1+2K_{AA}\bar{\Phi}_A(0)\int_0^t e^{(K_{AA}-L_A)s+\mathrm{i}\sqrt{2K_{AA}}W(s)}\mathrm{d}s}. \tag{3.174}$$

Inserting the above solution into the path integral average (2.64) one obtains the average particle population for the A molecules in the stochastic framework[13]. If the initial conditions are taken to be $\bar{\Phi}_A(0) = 0$ one obtains the trivial solution[14] which is also a solution derived from the corresponding stationary master equation. In order to compare the behaviour of the explicit solution to numerical findings as well as to the stochastic steady state solution, we consider the following estimate for the modulus of the above solution (3.174),

$$\begin{aligned}
\left|\bar{\Phi}_A(t)\right| &= \left|\bar{\Phi}_A(0)\frac{e^{(K_{AA}-L_A)t}e^{\mathrm{i}\sqrt{2K_{AA}}W(t)}}{1+2K_{AA}\bar{\Phi}_A(0)\int_0^t e^{(K_{AA}-L_A)s}e^{\mathrm{i}\sqrt{2K_{AA}}W(s)}\mathrm{d}s}\right| \\
&= \left|\bar{\Phi}_A(0)\frac{e^{(K_{AA}-L_A)t}}{1+2K_{AA}\bar{\Phi}_A(0)\int_0^t e^{(K_{AA}-L_A)s}e^{\mathrm{i}\sqrt{2K_{AA}}W(s)}\mathrm{d}s}\right| \\
&\geq \left|\bar{\Phi}_A(0)\right| \frac{e^{(K_{AA}-L_A)t}}{1+\frac{2K_{AA}\left|\bar{\Phi}_A(0)\right|\left(e^{(K_{AA}-L_A)t}-1\right)}{K_{AA}-L_A}},
\end{aligned} \tag{3.175}$$

where we used the fact that $\left|e^{\mathrm{i}\sqrt{2K_{AA}}W(s)}\right| \equiv 1$ and

$$\begin{aligned}
&\left|1+2K_{AA}\bar{\Phi}_A(0)\int_0^t e^{(K_{AA}-L_A)s}e^{\mathrm{i}\sqrt{2K_{AA}}W(s)}\mathrm{d}s\right| \\
&\qquad \leq 1+2K_{AA}\left|\bar{\Phi}_A(0)\int_0^t e^{(K_{AA}-L_A)s}e^{\mathrm{i}\sqrt{2K_{AA}}W(s)}\mathrm{d}s\right|.
\end{aligned} \tag{3.176}$$

We are interested in the late-time behaviour of the solution to the constraint equations. Therefore, we take the limit $t \to \infty$ in inequality (3.175). According to the rule of L'Hôspital we obtain

$$\lim_{t\to\infty}\left|\bar{\Phi}_A(t)\right| \geq \frac{1}{2}\left(1-\frac{L_A}{K_{AA}}\right) =: \mathcal{L}. \tag{3.177}$$

[13] In Appendix D we also present the exact solution to the constraint equation that is associated with the reaction partners for the recombination of type $A + A \to A$.

[14] This feature is verified also by the numerical evaluation of the constraint equations and the insertion of their solutions into the path integral average.

The modulus of the exact solution to the constraint equation for the chemical reactants in the late-time limit is bounded from below. The lower bound depends on the evaporation rate coefficient and the reaction rate coefficient. This finding differs from the late-time behaviour of the explicit solution to the corresponding mean-field equation, (3.167), for which

$$\lim_{t\to\infty} |\langle N_A(t)\rangle| = 0, \tag{3.178}$$

for $L_A \neq 0$. Furthermore, we know from the previous subsection that

$$\lim_{J_A\to 0} \langle \mathcal{N}_A\rangle^{ss} = \mathcal{L}. \tag{3.179}$$

Let us note that, in general, the averaged modulus of a solution to the stochastic constraint does not coincide with the modulus of the averaged solution to the stochastic constraint. One has that

$$\begin{aligned}
&\langle \left|\bar{\Phi}_A(t)\right|\rangle := \langle \sqrt{\Re\big(\bar{\Phi}_A(t)\big)^2 + \Im\big(\bar{\Phi}_A(t)\big)^2}\rangle, \\
&\left|\langle\bar{\Phi}_A(t)\rangle\right| := \left|\sqrt{\Re\big(\langle\bar{\Phi}_A(t)\rangle\big)^2 + \Im\big(\langle\bar{\Phi}_A(t)\rangle\big)^2}\right|, \\
&\Longrightarrow \langle \left|\bar{\Phi}_A(t)\right|\rangle \geq \left|\langle\bar{\Phi}_A(t)\rangle\right|.
\end{aligned} \tag{3.180}$$

The stochastic constraint equation that is related to the reaction product, the C particles,—equation (2.60)— in zero dimensions and for non-vanishing source rate J_C

$$\frac{\mathrm{d}}{\mathrm{d}t}\bar{\Phi}_C(t) + L_C\bar{\Phi}_C(t) - K_{AA}\bar{\Phi}_A^2(t) - J_C = 0, \tag{3.181}$$

looks formally identical to the mean-field evolution equation for the average population of C particles, $\langle N_C(t)\rangle$:

$$\frac{\mathrm{d}}{\mathrm{d}t}\langle N_C(t)\rangle + L_C\langle N_C(t)\rangle - K_{AA}\langle N_A(t)\rangle^2 - J_C = 0. \tag{3.182}$$

However, since $\bar{\Phi}_A(t)$ is a complex fluctuating field, $\bar{\Phi}_C(t)$, is as well. Again, solutions to the second constraint equation (3.181) need to be averaged in the sense of (2.64). In the single spatial site model, a solution of the full second constraint equation (3.181), that is for non-vanishing source rate, is given by

$$\bar{\Phi}_C(t) = \bigg(\int_0^t e^{L_C s}\big(K_{AA}\bar{\Phi}_A^2(s) + J_C\big)\mathrm{d}s + \bar{\Phi}_C(0)\bigg)e^{-L_C t}. \tag{3.183}$$

The stochasticity of the above solution is hidden in the first term containing the fluctuating solution $\bar{\Phi}_A(t)$ of the first constraint equation (3.174).

Once solutions to the stochastic constraint equations (3.174) and (3.183) are known, one has to insert the respective solutions into the path integral average (2.64) and compute the path integral by means of a *Monte Carlo calculation* in order to obtain the average particle population for the A or C molecules, respectively. Random samples are generated according to the Gaussian probability distribution (2.55); that is, we generate Wiener processes. We estimate the path integral (2.64) by summing a large number of solutions of the constraint equations associated with the set of random samples generated in the above sense and divide the sum by the number of random samples. The Monte Carlo method displays a convergence of $1/\sqrt{N}$ where N is the number of random samples —see [49]. The numerical results presented in the whole of this section are obtained by our own code written in the `GNU C` language.

Instead of using the expressions of the explicit solutions —equation (3.174) and equation (3.183)— to generate solutions to the stochastic constraint equations one can alternatively compute the paths directly from the stochastic differential equations (3.172) and (3.181). The latter method turns out to be less time consuming. The numerical implementation of the numerical schemes is in agreement with the exact solution (3.174). This will be discussed further in the following paragraphs.

Numerical Implementation

The stochastic differential equation (3.172) can be converted into

$$X_{A,n+1} = X_{A,n} + (-L_A X_{A,n} - 2K_{AA} X_{A,n}^2)\triangle_n + \mathrm{i}\sqrt{2K_{AA}} X_{A,n} \triangle W_n, \qquad (3.184)$$

where $X_{A,n} := \Phi_A(t_n)$ are the unknown variables in discretised time t_n for $n = 0, .., N$. The symbols $\triangle_n := t_{n+1} - t_n$ give the time increments and $\triangle W_n := W_{t_{n+1}} - W_{t_n}$ are the Wiener increments. The increments $\triangle W_n$ are generated by two uniformly distributed independent random variables via the *Box-Müller transformation* —see, for example, [37]. According to the Box-Müller method two independent standard Gaussian random variables G_1 and G_2 are given by

$$\begin{aligned} G_1 &= \sqrt{-2\ln(U_1)}\cos(2\pi U_2), \\ G_2 &= \sqrt{-2\ln(U_1)}\sin(2\pi U_2), \end{aligned} \qquad (3.185)$$

where U_1 and U_2 are two independent uniformly distributed random variables. These variables are obtained by means of the standard pseudo-random number generator

included in the `math.h` library of the `GNU C` language. Alternatively, one can use the pseudo random number generator described in [49]. These generators provide pseudo-random numbers which are uniformly distributed. The numerical scheme (3.184) is called the *Euler scheme* and is the most straightforward approach to undertake some numerical investigations. Accordingly, the second constraint equation in the single spatial site model for vanishing source rate —equation (3.181)— takes the following form

$$X_{C,n+1} = X_{C,n} + (-L_C X_{C,n} + K_{AA} X_{A,n}^2)\triangle_n. \tag{3.186}$$

As stochastic differential equations are extremely sensitive to numerical instabilities one has to convince oneself that the code is stable and converging. Numerical schemes that we have employed in order to check whether they might be more accurate or stable than the Euler method are the Milstein scheme, the simplified order 2.0 weak Taylor scheme, the implicit order 1.0 strong Runge-Kutta scheme, the predictor-corrector method of order 1.0 with modified trapezoidal method of weak order 1.0. The numerical schemes were taken from [37] and are presented in Appendix C. We observe that all of the before mentioned numerical schemes are stable and there is only very little difference noticable in the accuracy of the numerical results. If not otherwise stated we implement the Milstein scheme which is an order 1.0 strong Taylor obtained from the Itô-Taylor expansion. The stochastic constraint equation associated with the reaction partners A expressed in the Milstein scheme reads

$$\begin{aligned} X_{A,n+1} = X_{A,n} + \big(- L_A X_{A,n} - 2K_{AA} X_{A,n}^2 \big)\triangle_n + \\ \mathrm{i}\sqrt{2K_{AA}} X_{A,n} \triangle W_n - K_{AA} X_{A,n} \big((\triangle W_n)^2 - \triangle_n \big). \end{aligned}$$

More accurate strong Taylor schemes can be obtained by including further multiple stochastic integrals from the stochastic Taylor expansion in the scheme. In the case of an elapse of a long time until equilibrium is reached we saved only a multiple of the time step to be evaluated in order to avoid computational complications.

For the numerical evaluation of the dynamical stochastic differential equations we employ values for the rate coefficients that can be found in realistic physical set-ups. Before we go into any further details about the physical background let us refer to [30]: *"If we consider the totality of surface experiments done to date, we can generalize that laboratory work is at the stage where it has confirmed the view of astrochemists as to what types of diffusive thermal processes can occur on low temperature surfaces, but is only approaching the stage where it can give us unambigous parameters to be used to determine actual rates under interstellar conditions."* Ex-

periments designed to measure the reaction rate most often involve the techniques of temperature programmed desorption where atoms are deposited with tiny deposition rates on very cold surfaces. Diffusive reaction and desorption start to occur when the temperature is raised slowly. In addition to thermal reactive processes, there is also the possibility that energetic particles can drive a photochemistry. However, the laboratory experiments that have been undertaken up until today were performed at fluxes that are too great to be relevant for the interstellar scenario.

On the Choice of the Rate Coefficients

Throughout the rest of the thesis we will present our calculations based on two different types of data. One set of rate coefficients is taken from the work of [29] and [53] that employ lower estimates for the energy barriers than, for example, [4]. The first set of parameteres are referred to as the *M1 model parameters* of [53], the second set of parameters are the *M2 model parameters* of [53]. In the M1 model a radius of a spherically symmetric grain particle $R = 10^{-7}$m is assumed.
The following derivation for the rate coefficients and their specific values for hydrogen recombination is based on [4] and on the experimental results and their analysis by [35, 47, 46, 48]. In general, the actual values of the rate coefficients are temperature dependent. Although we are concentrating on the single spatial site model, some of the following Ansätze are subliminally based on the assumption that the geometry of the grains is of spherically symmetry so that the number of lattice sites N_S is given by

$$N_S = 4\pi R^2 s \quad \text{[per monolayer]}, \tag{3.187}$$

with R [m] is the seed radius[15], and s [$\mathrm{m}^{-2}\mathrm{monolayer}^{-1}$] the surface density of lattice sites which can be determined experimentally for the various materials under consideration. In diffusive clouds, it is assumed that grain particles have a diameter of $2R \in [1 \times 10^{-8}\mathrm{m},\ 5 \times 10^{-7}\mathrm{m}]$. For grains consisting of amorphous carbon the surface density of lattice sites takes the value $s(carbon) = 5.07 \times 10^{17}\mathrm{m}^{-2}\mathrm{monolayer}^{-1}$ and for olivine $s(olivine) = 1.85 \times 10^{18}\mathrm{m}^{-2}\mathrm{monolayer}^{-1}$ as presented in [4]. In what follows we restrict our analysis to a single monolayer.

The reaction rate coefficient K_{AA} [s^{-1}] is determined by the sum of inverse diffusion times $\left(t_S^{-1}\right)\big|_A$ for each atom A sweeping over the entire surface of the grain via

[15]This quantity —among others— has to be understood not as the radius of a particular particle but as the radii of an ensemble of grain particles of the exact same size.

thermal hopping or tunnelling —see [57]—,

$$K_{AA} = \frac{\left(t_S^{-1}\right)\big|_A + \left(t_S^{-1}\right)\big|_A}{2} \quad [\mathrm{s}^{-1}]. \tag{3.188}$$

The factor of one half arises since the reactants are of the same type and not distinguishable. The inverse diffusion times for the various considered processes are determined via an *Arrhenius-like Ansatz*[16]

$$\begin{aligned} t_S^{-1} &= N_S^{-1}\nu_v \exp\left(\frac{-E_d}{kT}\right) \quad \text{thermal hopping,} \\ t_S^{-1} &= N_S^{-1}\nu_v \exp\left(\frac{-\sqrt{8\mathfrak{l}^2 m E_d}}{h}\right) \quad \text{tunnelling,} \end{aligned} \tag{3.189}$$

where ν_v [s^{-1}] is the frequency of vibration of the adsorbed species, E_d [J] is the energy barrier against diffusion from one lattice site to another, $\mathfrak{l}$ [m] is the tunnelling length, m [kg] the mass of the adsorbate, T [K] the temperature of the grain surface, k [JK^{-1}] the Boltzmann constant, and h [Js^{-1}] the Planck constant. The size of the grain is related to the size of the lattice by means of the site density of the particular adsorbate-substrate system [58] —see (3.187). If the material of the grain particle is known, the reaction rate coefficient is a function of the temperature and the size of the grain, that is, in the case of thermal hopping,

$$K_{AA}(R,T) = \frac{\nu_v}{4\pi R^2 s} \exp\left(\frac{-E_d}{kT}\right) \quad [\mathrm{s}^{-1}]. \tag{3.190}$$

A vibration frequency that is typical for physiorption problems would be $\nu_v = 10^{12}\ \mathrm{s}^{-1}$. The temperature frame that is usually considered in diffusive clouds is $T \in [15\mathrm{K}, 20\mathrm{K}]$. The exponents E_d/k for atomic hydrogen as determined in laboratory experiments are 287K for an olivine surface and 511K for amorphous carbon. The mass of hydrogen atoms is given by $m = 1.67 \times 10^{-27}\mathrm{kg}$. The particular form of the above expression of the reaction rate coefficient is true as long as the assumption of instantaneous reaction on occupation of the same lattice site is justified.

The evaporation rate coefficient L_A [s^{-1}] is equal to the inverse evaporation time t_E^{-1} for the A particles. We assume that the form of the desorption rate is given by the simplified *Polanyi-Wigner relation*:

$$t_E^{-1} = \nu_v \exp\left(\frac{-E_e}{kT}\right) \quad [\mathrm{s}^{-1}] \tag{3.191}$$

[16] See Appendix A.

with E_e [J] the energy needed for evaporation. Note that the evaporation rate coefficient is a function only of the temperature of the grain surface for a given type of material of the grain. The evaporation energy term E_e/k for atomic hydrogen is 373K for olivine grain surfaces and 658K for surfaces made of amorphous carbon. In general, it is true that

$$E_d \gg E_e. \tag{3.192}$$

As stated in [30], most species that are heavier than hydrogen exhibit desorption energies that are too large for evaporation to occur in cold clouds. This special case will be of interest later on.

The source rate coefficient is defined as

$$J_A = \mathcal{S} v_A \sigma n(A) \quad [\mathrm{s}^{-1}], \tag{3.193}$$

where v_A [ms^{-1}] is the speed of the gas-phase species, σ [m^2] is the cross section of the seed particle, $n(A)$ [m^{-3}] gives the gas phase concentration of the chemical species A and $\mathcal{S}$ is the sticking coefficient. For low temperature adsorption, the sticking coefficient can be assumed to be unity. We assume that the grain is spherical which leads to an expression for the cross section

$$\sigma = \pi R^2 \quad [\mathrm{m}^2]. \tag{3.194}$$

The speed in the gas phase is given by

$$v_A = \sqrt{\frac{8kT_{gas}}{\pi m}} \quad [\mathrm{ms}^{-1}], \tag{3.195}$$

with T_{gas} [K] the temperature of the gas phase. In diffusive clouds this temperature is estimated to be $T_{gas} = 100$K which leads to a value of $v_H = 1.451 \times 10^3 \mathrm{ms}^{-1}$ for hydrogen atoms. The gas phase concentration for hydrogen atoms in diffusive clouds is taken to be $n(H) = 1 \times 10^7 [\mathrm{m}^{-3}]$ so that the source rate coefficient for hydrogen atoms is the following function of the radius of the seed particle

$$J_H(R) = v_H n(H) \sigma(R) = 4.56 \times 10^{10} \ R^2 \quad [\mathrm{s}^{-1}]. \tag{3.196}$$

Note that the source rate coefficient only depends on the geometry of the seed but not on the material the grain particle is made of.

Discussion of the Numerical Results

The following plots were generated for the situation where two hydrogen atoms react on the surface of an interstellar dust particle at a temperature $T = 10\text{K}$. According to [7], the gas phase concentration of atomic hydrogen in interstellar clouds is $n_H \in [10^{-1}\text{cm}^{-3}, 10^{4}\text{cm}^{-3}]$. In [7] the rate coefficients at a temperature of $T = 10\text{K}$ are derived under the assumption that the number of binding sites on the grain is about $N_S = 10^6$ per monolayer. The reaction rate for the hydrogen atoms takes the value of $K_{HH} = 5.1 \times 10^{4}\text{s}^{-1}$, the evaporation rate $L_H = 1.9 \times 10^{-3}\text{s}^{-1}$ and the evaporation rate for the reaction product, diatomic hydrogen, $L_{H_2} = 6.9 \times 10^{-8}\text{s}^{-1}$. As initial values in our calculations we used $\bar{\Phi}_H(0) = \bar{\Phi}_{H_2}(0) = 6$. In Figure 3.1 we generate the real part of one solution to the stochastic constraint equation (3.172) for the hydrogen atoms under the above conditions. Figure 3.2 shows the imaginary part of the same solution of the stochastic constraint equation for the reaction partners. In the following figures, Figure 3.3 and Figure 3.4, Figure 3.5 and Figure 3.6, and Figure 3.7 and Figure 3.8, the respective real and imaginary parts of the path integral average —equation (2.64)— over 10, 100 and 1000 realisations of the white Gaussian noise for the H atoms are shown, respectively. One observes that the real part of the path integral average smoothes out and the fluctuations in the imaginary part decrease in intensity the more realisations of the noise are employed in the path integral average. In particular, the imaginary part of the PIA tends to zero for an increasing number of paths. Therefore, it is safe to interpret the real part of the path integral average as the average particle population.

Occasionally, the numerical evaluation of the stochastic differential equations exhibits extreme spikes. This seems to be an unavoidable feature of this approach. Therefore, it is crucial to compare simple cases with explicit analytical solutions if available and to finetune the numerical schemes.

Figures 3.9 and 3.10 show the real and imaginary part of the solution to the second stochastic equation in zero spatial dimensions for vanishing source rate —equation (3.181)— associated with the reaction products H_2. The same realisation of the stochastic noise have been used to generate Figures 3.9 and 3.10 as in Figure 3.1 and Figure 3.2. Again, the fluctuations are smoothed out in Figure 3.11 and Figure 3.12 when the path integral average (2.64) for the diatomic hydrogen is taken over 1000 realisations of the stochastic noise.

From Figure 3.7 it is clear that the mean number of hydrogen atoms approaches asymptotically the value $\langle \bar{\Phi}_H(t_\infty) \rangle_{1000} \approx 0.5$, where t_∞ denotes the time after the transient processes when a constant late-time limit is reached. This is consistent with the estimate of the late-time behaviour of the modulus of the explicit solution to the constraint

equation —see (3.177)— and with the stochastic steady state solution —see (3.120). From the numerial calculations we find that the late-time limit for the average of the modulus of solutions to the first stochastic constraint (3.177) is not sharp, that is,

$$\lim_{t\to\infty}\langle\left|\bar{\Phi}_A(t)\right|\rangle \geq \frac{1}{2}\big(1-\frac{L_A}{K_{AA}}\big)+\epsilon \quad \epsilon>0, \tag{3.197}$$

for small ϵ. Furthermore, we find that

$$\lim_{t\to\infty}\langle\left|\bar{\Phi}_A(t)\right|\rangle = \lim_{t\to\infty}\left|\langle\bar{\Phi}_A(t)\rangle\right|+\tilde{\epsilon} \quad \tilde{\epsilon}>0, \tag{3.198}$$

for small $\tilde{\epsilon}$. The overall behaviour of $\langle\left|\bar{\Phi}_A(t)\right|\rangle$ is smoother than the one of $\left|\langle\bar{\Phi}_A(t)\rangle\right|$. In addition, we checked that $\langle\left|\bar{\Phi}_A(t)\right|\rangle_1 = \left|\langle\bar{\Phi}_A(t)\rangle_1\right|$ where the average is taken over only one path. The ratio between the averaged modulus of the solutions and the modulus of the averaged solution does not change if the average is taken over ten or one thousand paths. For completeness, Figure 3.13 shows the modulus of the same solution to the first stochastic constraint, as plotted in Figure 3.1 and Figure 3.2, and Figure 3.14 gives the average of the modulus of the same solutions averaged over 1000 paths as plotted in Figure 3.7 and 3.8. The above discussion can be compared with the results obtained from the solution to the mean-field evolution equation (3.166) which predicts an asymptotic value $\langle N_A(t)\rangle \longrightarrow 0$ as $t\longrightarrow\infty$ for $L_A\neq 0$.

The errors in our calculations of the path integral average are mostly due to the errors occurring from the Monte Carlo estimation of the PIA. The order of the error due to the summing of paths according to (2.64) is proportional to the inverse of the square-root of the number of paths employed in the summation. We choose the proportionality constant to be equal to one which is a rather conservative estimation. As can be seen from calculations presented later on, the errors in the stochastic results are in fact much smaller than our worst-case scenario would predict.

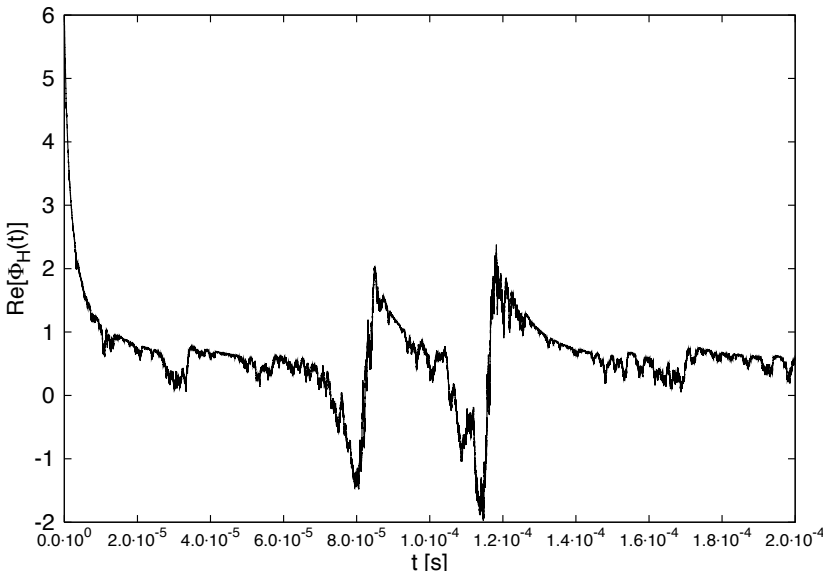

Figure 3.1: Real part of one possible solution to the first constraint equation (3.172) for hydrogen atoms under interstellar space conditions ($K_{HH} = 5.1 \times 10^4 \mathrm{s}^{-1}$, $L_H = 1.9 \times 10^{-3} \mathrm{s}^{-1}$) with vanishing source rate ($J_H = 0 \mathrm{s}^{-1}$) and for the initial condition $\bar{\Phi}_H(0) = 6$.

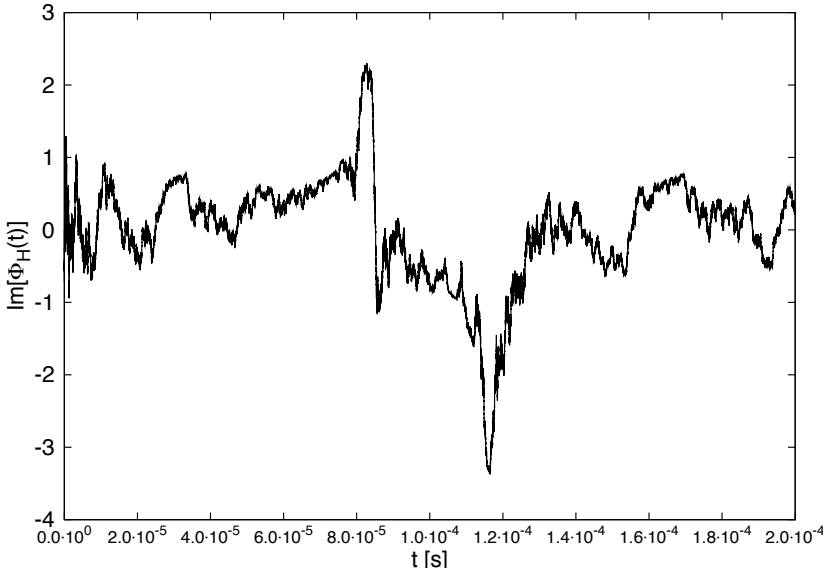

Figure 3.2: Imaginary part of the solution to the first constraint equation (3.172) for the same stochastic noise as in Figure 3.1 for the reaction partners H under interstellar space conditions ($K_{HH} = 5.1 \times 10^4 \mathrm{s}^{-1}$, $L_H = 1.9 \times 10^{-3} \mathrm{s}^{-1}$), for zero source rate ($J_H = 0 \mathrm{s}^{-1}$) and for the initial condition $\bar{\Phi}_H(0) = 6$.

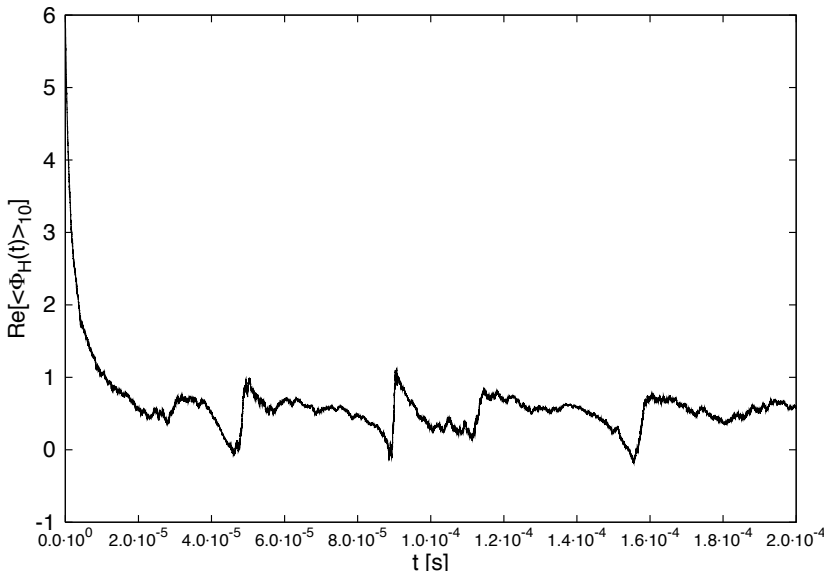

Figure 3.3: Real part of the path integral average (PIA) of solutions to the first constraint equation (3.172) with vanishing source rate ($J_H = 0\mathrm{s}^{-1}$) for hydrogen atoms under interstellar conditions ($K_{HH} = 5.1 \times 10^4\mathrm{s}^{-1}$, $L_H = 1.9 \times 10^{-3}\mathrm{s}^{-1}$) over 10 possible paths and for the initial condition $\bar{\Phi}_H(0) = 6$.

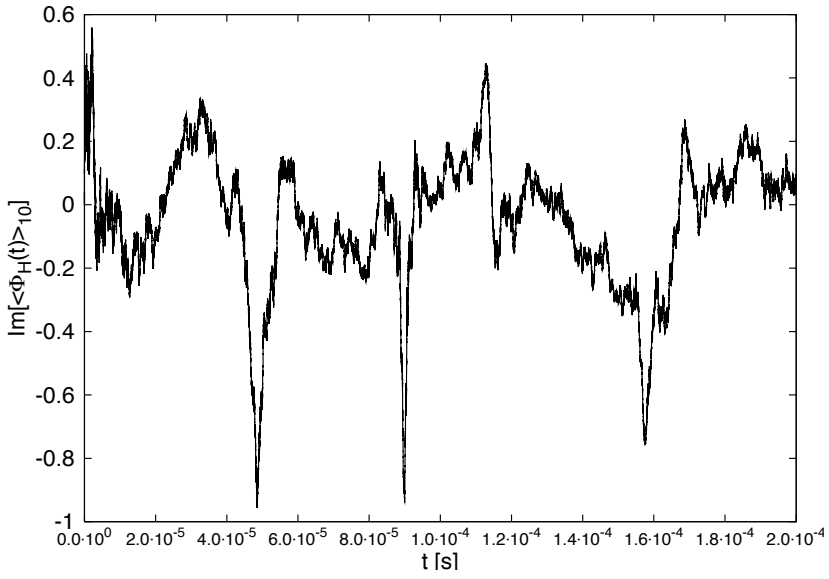

Figure 3.4: Respective imaginary part of the path integral average (PIA) of solutions to the first constraint equation (3.172) with zero source rate ($J_H = 0\mathrm{s}^{-1}$) for hydrogen atoms under interstellar conditions ($K_{HH} = 5.1 \times 10^4\mathrm{s}^{-1}$, $L_H = 1.9 \times 10^{-3}\mathrm{s}^{-1}$) over 10 paths and for the initial condition $\bar{\Phi}_H(0) = 6$.

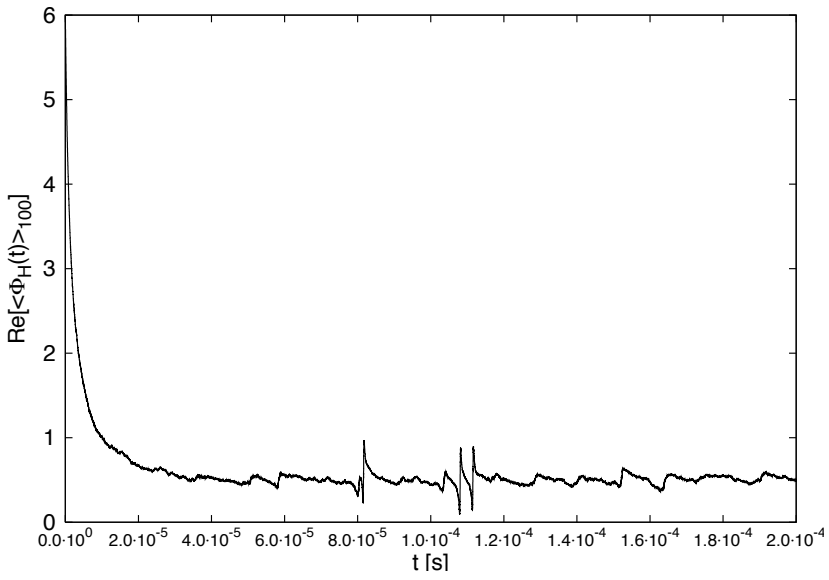

Figure 3.5: Real part of the path integral average (PIA) of solutions to the first constraint equation (3.172) with vanishing source rate ($J_H = 0\mathrm{s}^{-1}$) for hydrogen atoms under interstellar conditions ($K_{HH} = 5.1 \times 10^4\mathrm{s}^{-1}$, $L_H = 1.9 \times 10^{-3}\mathrm{s}^{-1}$) over 100 possible paths and for the initial condition $\bar{\Phi}_H(0) = 6$.

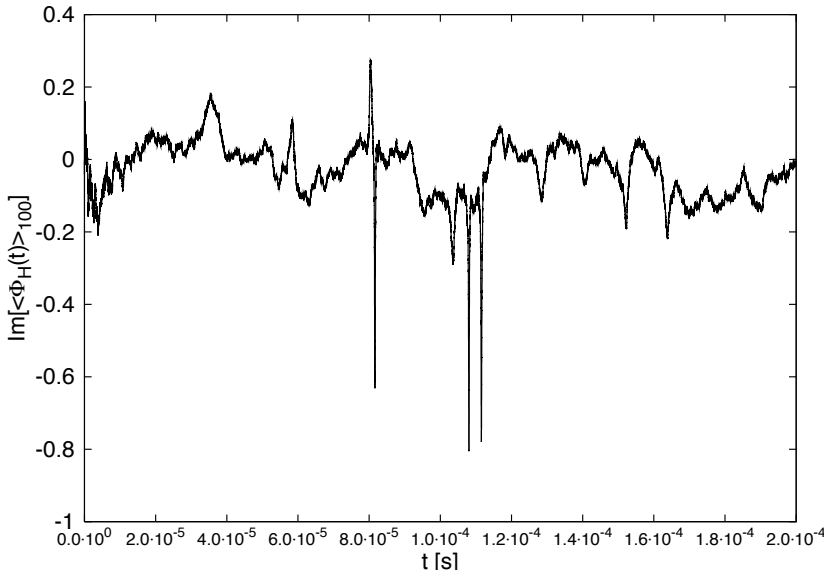

Figure 3.6: Respective imaginary part of the path integral average (PIA) of solutions to the first constraint equation (3.172) with zero source rate ($J_H = 0\mathrm{s}^{-1}$) for hydrogen atoms under interstellar conditions ($K_{HH} = 5.1 \times 10^4\mathrm{s}^{-1}$, $L_H = 1.9 \times 10^{-3}\mathrm{s}^{-1}$) over 100 paths and for the initial condition $\bar{\Phi}_H(0) = 6$.

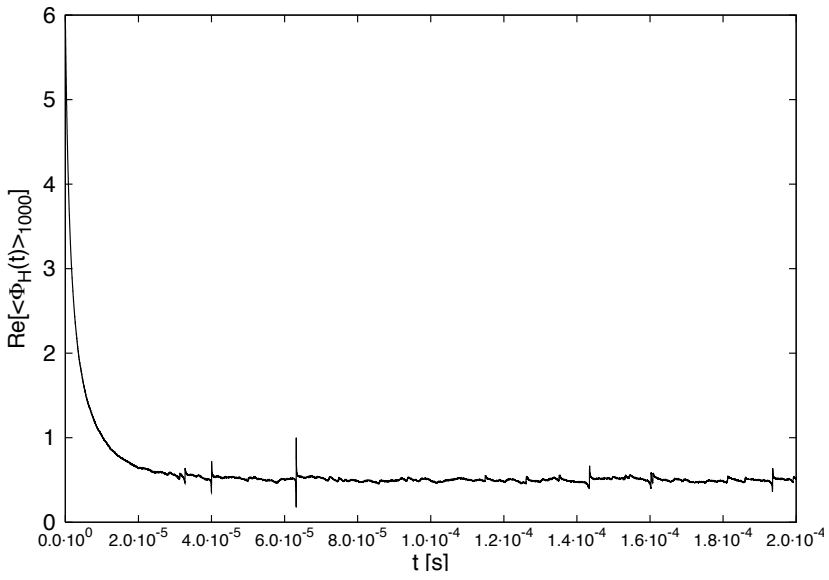

Figure 3.7: Real part of the path integral average (PIA) of solutions to the first constraint equation (3.172) with vanishing source rate ($J_H = 0\mathrm{s}^{-1}$) for hydrogen atoms under interstellar conditions ($K_{HH} = 5.1 \times 10^4\mathrm{s}^{-1}$, $L_H = 1.9 \times 10^{-3}\mathrm{s}^{-1}$) over 1000 possible paths and for the initial condition $\bar{\Phi}_H(0) = 6$.

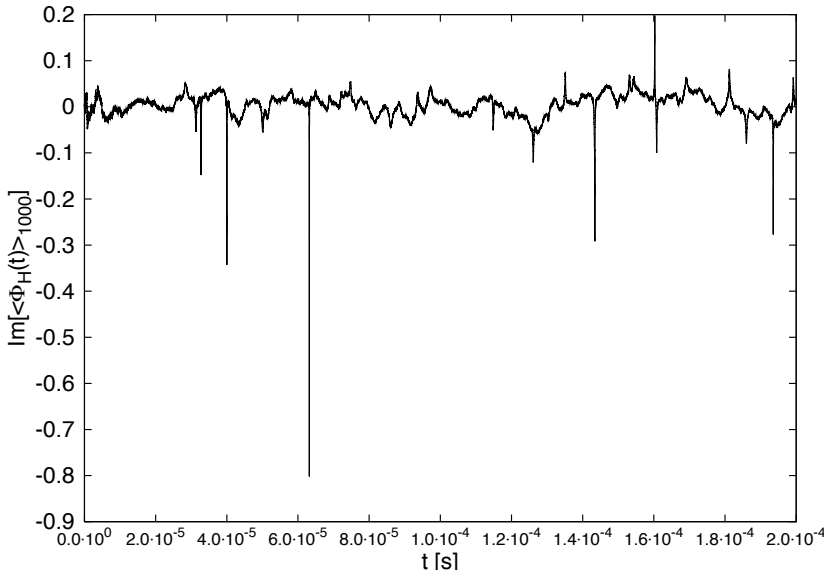

Figure 3.8: Respective imaginary part of the path integral average (PIA) of solutions to the first constraint equation (3.172) with zero source rate ($J_H = 0\mathrm{s}^{-1}$) for hydrogen atoms under interstellar conditions ($K_{HH} = 5.1 \times 10^4\mathrm{s}^{-1}$, $L_H = 1.9 \times 10^{-3}\mathrm{s}^{-1}$) over 1000 paths and for the initial condition $\bar{\Phi}_H(0) = 6$.

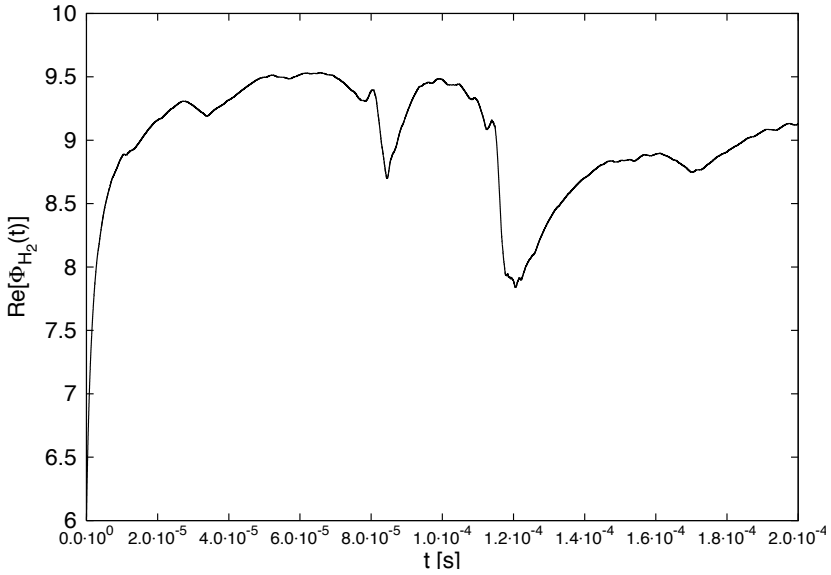

Figure 3.9: Real part of a possible solution of the second constraint equation (3.181) for the same specific realisation of the stochastic noise as in Figure 3.1 for vanishing source rates ($J_H = J_{H_2} = 0\mathrm{s}^{-1}$), the constraint equation for diatomic hydrogen under interstellar conditions ($K_{HH} = 5.1 \times 10^4\mathrm{s}^{-1}$, $L_{H_2} = 6.9 \times 10^{-8}\mathrm{s}^{-1}$) and for the initial conditions $\bar{\Phi}_H(0) = \bar{\Phi}_{H_2}(0) = 6$.

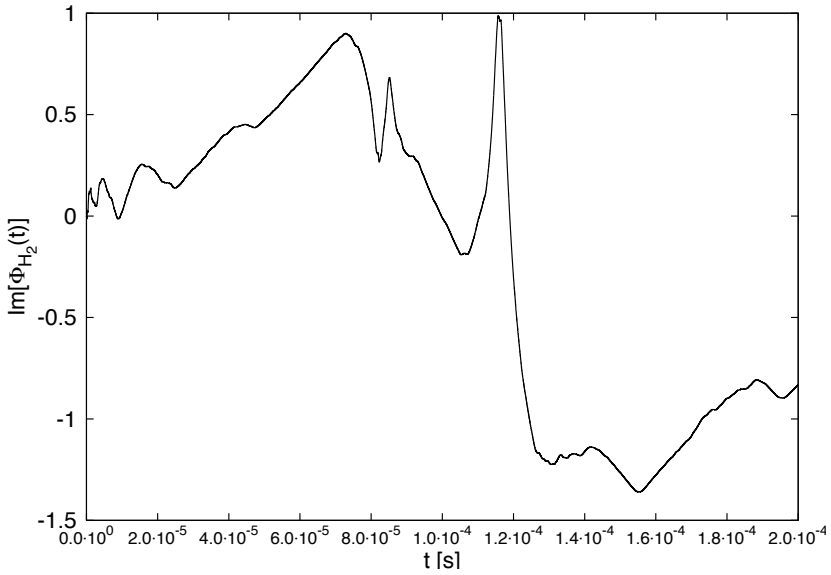

Figure 3.10: Imaginary part of a possible solution to the second constraint equation (3.181) for the same specific realisation of the stochastic noise as in Figure 3.2 with zero source rates ($J_H = J_{H_2} = 0\mathrm{s}^{-1}$) under interstellar conditions ($K_{HH} = 5.1 \times 10^4\mathrm{s}^{-1}$, $L_{H_2} = 6.9 \times 10^{-8}\mathrm{s}^{-1}$) and for the initial conditions $\bar{\Phi}_H(0) = \bar{\Phi}_{H_2}(0) = 6$.

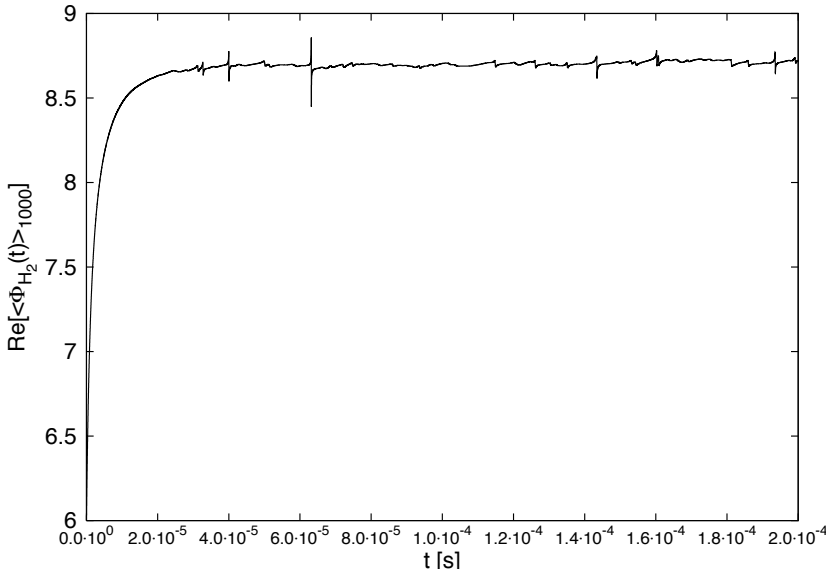

Figure 3.11: Real part of the path integral average (PIA) of solutions to the second constraint equation (3.181) for the reaction product H_2 under interstellar conditions ($K_{HH} = 5.1 \times 10^4 \mathrm{s}^{-1}$, $L_{H_2} = 6.9 \times 10^{-8} \mathrm{s}^{-1}$) over 1000 paths with vanishing source rates ($J_H = J_{H_2} = 0 \mathrm{s}^{-1}$) and for the initial conditions $\bar{\Phi}_H(0) = \bar{\Phi}_{H_2}(0) = 6$.

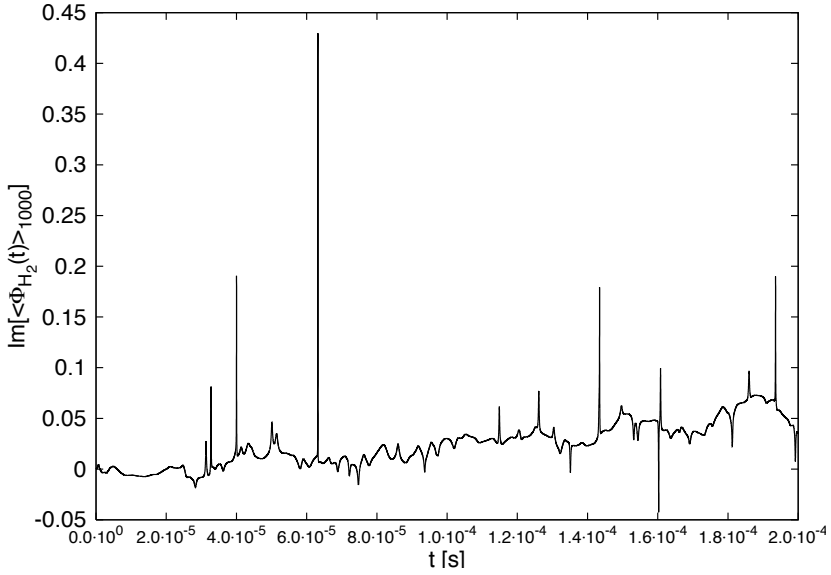

Figure 3.12: Respective imaginary part of the path integral average (PIA) of solutions to the second constraint equation (3.181) for diatomic hydrogen under interstellar conditions ($K_{HH} = 5.1 \times 10^5 \mathrm{s}^{-1}$, $L_{H_2} = 6.9 \times 10^{-8} \mathrm{s}^{-1}$) over 1000 realisations of the stochastic noise for zero source rates ($J_H = J_{H_2} = 0 \mathrm{s}^{-1}$) and for the initial conditions $\bar{\Phi}_H(0) = \bar{\Phi}_{H_2}(0) = 6$.

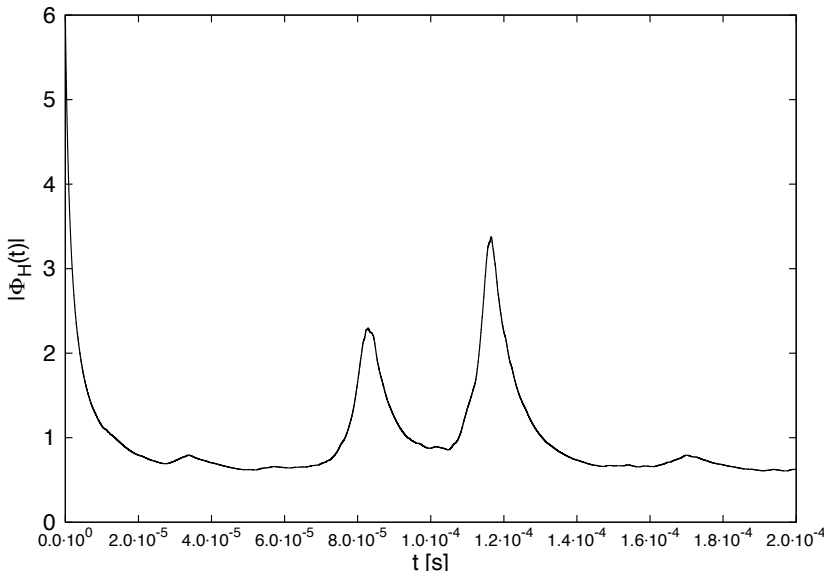

Figure 3.13: Modulus of one solution to the first stochastic constraint equation for vanishing source rate for hydrogen recombination under interstellar conditions with $J_H = 0\mathrm{s}^{-1}$, $K_{HH} = 5.1 \times 10^4\mathrm{s}^{-1}$, $L_H = 1.9 \times 10^{-3}\mathrm{s}^{-1}$ and for the initial condition $\bar{\Phi}_H(0) = 6$.

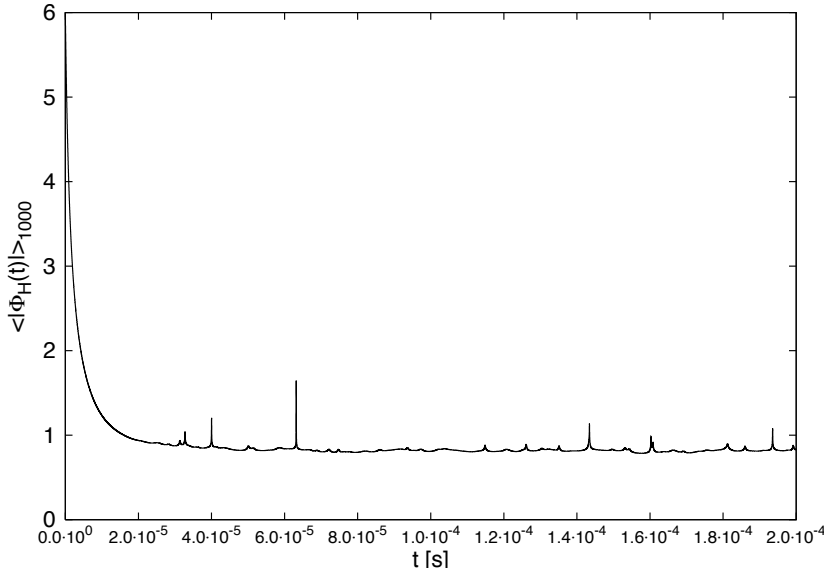

Figure 3.14: Modulus of solutions to the first stochastic constraint equation for vanishing source rate for hydrogen recombination under interstellar conditions with $J_H = 0\mathrm{s}^{-1}$, $K_{HH} = 5.1 \times 10^4\mathrm{s}^{-1}$, $L_H = 1.9 \times 10^{-3}\mathrm{s}^{-1}$ and for the initial condition $\bar{\Phi}_H(0) = 6$ averaged over 1000 paths.

3.3.2 Full Stochastic Dynamical Solution

As in the previous section, we generate solutions to the constraint equations (2.61) and (2.60) in zero spatial dimensions yet with a positive source rate and compare the qualitative form of the solutions to the mean-field evolution equations.

For a positive source rate, the stochastic constraint equations (2.61) and (2.60) in the single spatial site model

$$-\frac{\mathrm{d}\bar{\Phi}_A(t)}{\mathrm{d}t} - 2K_{AA}\bar{\Phi}_A^2(t) - L_A\bar{\Phi}_A(t) + J_A + \mathrm{i}\sqrt{2K_{AA}}\bar{\Phi}_A(t)\eta(t) = 0, \tag{3.199}$$

$$-\frac{\mathrm{d}\bar{\Phi}_C(t)}{\mathrm{d}t} + K_{AA}\bar{\Phi}_A^2(t) - L_C\bar{\Phi}_C(t) + J_C = 0. \tag{3.200}$$

can not be solved analytically. Therefore, one is left with numerical investigations undertaken as described in the previous subsection.

Discussion of the Numerical Results

The plots in Figures 3.15 —giving the real part of a possible solution to the constraint equation associated with the reactant hydrogen population— and 3.17 —representing the real part of the path integral average of the hydrogen atoms population averaged over 1000 realisations of the noise— are obtained for a source rate, $J_H = 10^8\mathrm{s}^{-1}$, that is large in comparison to the other rate coefficients, $K_{HH} = 5.1 \times 10^4\mathrm{s}^{-1}$, $L_H = 1.9 \times 10^{-3}\mathrm{s}^{-1}$. The initial conditions were chosen to be $\bar{\Phi}_H(0) = 0$. In Figure 3.16 —plot of the real part of a possible solution to the first constraint— and Figure 3.18 —plot of the real part of the corresponding path integral average over 1000 realisations of the noise— the source rate was chosen to be small, $J_H = 10^{-8}\mathrm{s}^{-1}$ whereas all other parameters were the same as for Figures 3.15 and 3.17. It can be readily seen that the fluctuations in Figures 3.15 and 3.17 are much larger than in Figures 3.16 and 3.18. In particular, the real part of the path integral average in Figure 3.17 is very smooth. If one compares the above mentioned figures to Figure 3.19 —representing the average hydrogen population in the mean-field framework for $J_H = 10^8\mathrm{s}^{-1}$, $K_{HH} = 5.1 \times 10^4\mathrm{s}^{-1}$, $L_H = 1.9 \times 10^{-3}\mathrm{s}^{-1}$ and $\langle N_H(0)\rangle = 0$— and Figure 3.20 —giving the average hydrogen population in the mean-field model with the same parameters as employed for the production of Figure 3.19 yet for small source rate $J_H = 10^{-8}\mathrm{s}^{-1}$, one observes that the result obtained from the stochastic formalism —Figure 3.17— corresponds to the mean-field result —Figure 3.19. This is not the case when confronting Figure 3.18 —the stochastic mean hydrogen population— with Figure 3.20 —the corresponding average number of hydrogen atoms in the mean-field

model. The dependence of the threshold between the deterministic and the stochastic regime will be explored further in the following section.

For the present discussion we shall assume the values of parameters corresponding to the conditions occuring in interstellar clouds. Therefore, we numerically compare the late-time stochastic average particle population, $\langle \Phi_X(t_\infty) \rangle$, to the late-time average particle population in the mean-field framework, $\langle N_X(t_\infty) \rangle$, of two chemical reactants X under interstellar conditions, namely hydrogen and oxygen. Hydrogen and oxygen recombination are important chemical reactions, for example, in the hydrogen-oxygen reaction network —see Chapter 5. The estimates for the corresponding rate coefficients are available in [58]. Quantum Tunnelling effects have been taken into account in the derivation for the rate coefficients concerning the hydrogen-hydrogen reaction. Quantum Tunnelling becomes more important for decreasing mass of the chemical reactants and/or decreasing temperature. The value for the evaporation rate coefficient of the reactants has to be understood as a lower limit whereas the evaporation rate coefficient of the reaction products is better defined. The results of our calculations are summarised in Table 3.1 for a temperature of $T = 10\text{K}$, in Table 3.2 for a temperature of $T = 15\text{K}$ and in Table 3.3 for a temperature of $T = 20\text{K}$. Note that $J_X = \mathfrak{J}_X n(X)$ with, for example, $n(H) \in [10^5\text{m}^{-3}, 10^{10}\text{m}^{-3}]$ and $n(O) = 10^6\text{m}^{-3}$ the gas phase densities. In the numerical computations we choose $n(H) = 10^6\text{m}^{-3}$ and take the initial conditions to be equal to zero for all chemical species. One observes that in all cases except for the hydrogen reaction at a temperature of $T = 20\text{K}$ the stochastic average population of the chemical reactants approximates 0.5 whereas the values of the average population of the chemical reactants in the mean-field framework are much lower. This behaviour is consistent with the observations in the latter section where the stochastic limit of the average reactant population for vanishing source rate is one half for the particular choice of rate coefficients. In the exceptional case of the hydrogen reaction at the highest temperature under consideration, the stochastic and the mean-field average hydrogen population coincide since the evaporation rate coefficient dominates over the reaction rate coefficient. Due to the lack of data we are not able to give a quantitative description of the behaviour of the reaction products although it is very important to investigate the qualitative behaviour of the dimolecular species in order to make sure that the numerical results are stable. In general,

$$\langle \bar{\Phi}_C(t_\infty) \rangle \lesssim \bar{\Phi}_C(0) + \frac{\langle \bar{\Phi}_A(t_\infty) \rangle}{2}, \tag{3.201}$$

for $J_C = 0\text{s}^{-1}$.

Furthermore, we make the following observation: the transient time, that is, the time

span until the average particle population reaches a constant late-time limit, differs between the various chemical reactions. In the calculations presented in Tables 3.1, 3.2 and 3.3 one notes that the higher the temperature the less time needed to reach equilibrium. We will explore this aspect in detail later on.

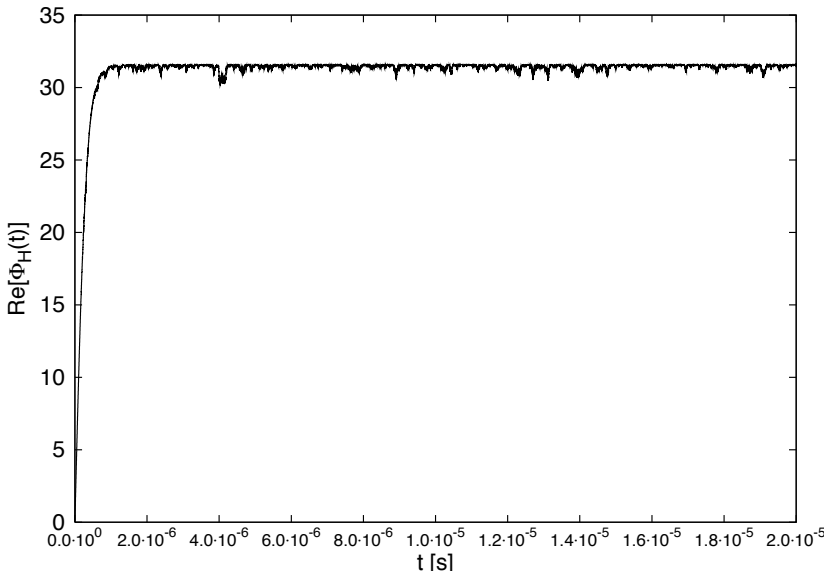

Figure 3.15: Real part of one possible solution to the first constraint equation (2.61) in the single spatial site model for a value of the source rate of $J_H = 10^8 \mathrm{s}^{-1}$ for the hydrogen reactants as well as for $K_{HH} = 5.1 \times 10^4 \mathrm{s}^{-1}$, $L_H = 1.9 \times 10^{-3} \mathrm{s}^{-1}$ and for the initial condition $\bar{\Phi}_H(0) = 0$.

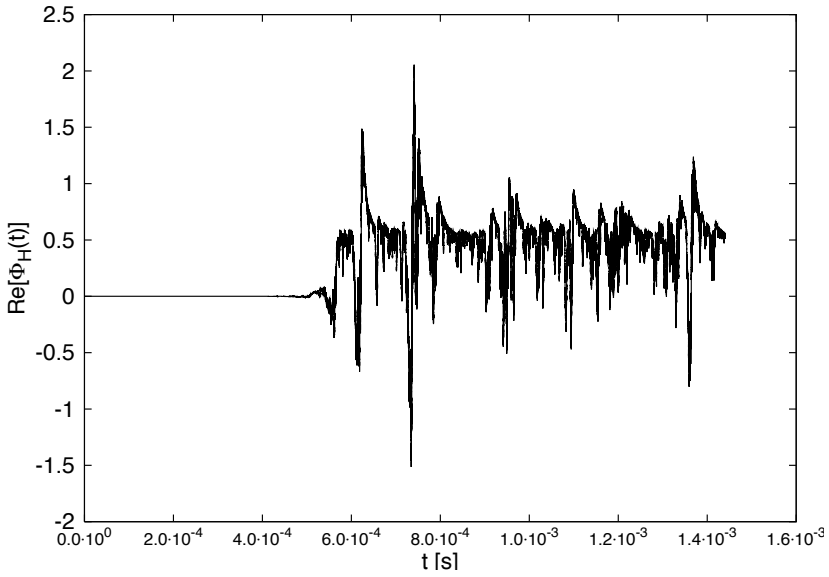

Figure 3.16: Real part of a solution to the stochastic equation (2.61) in zero space dimensions constraining the hydrogen reaction partners ($K_{HH} = 5.1 \times 10^4 \mathrm{s}^{-1}$, $L_H = 1.9 \times 10^{-3} \mathrm{s}^{-1}$) with a source rate for the hydrogen atoms of value $J_H = 10^{-8} \mathrm{s}^{-1}$ and for the initial condition $\bar{\Phi}_H(0) = 0$.

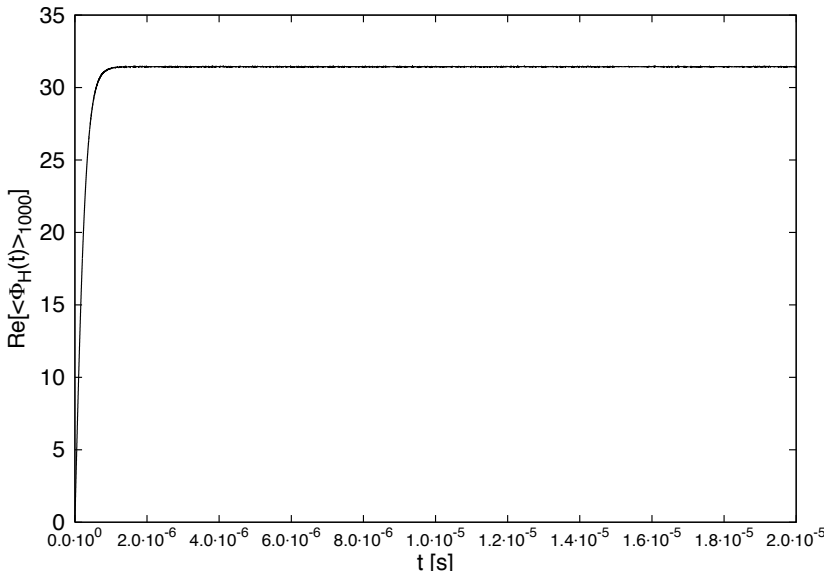

Figure 3.17: Real part of the path integral average of 1000 possible solutions to the first constraint equation (2.61) in the single spatial site model for a value of the source rate of $J_H = 10^8 \mathrm{s}^{-1}$ for the hydrogen reactants as well as for $K_{HH} = 5.1 \times 10^4 \mathrm{s}^{-1}$, $L_H = 1.9 \times 10^{-3} \mathrm{s}^{-1}$ and for the initial condition $\bar{\Phi}_H(0) = 0$.

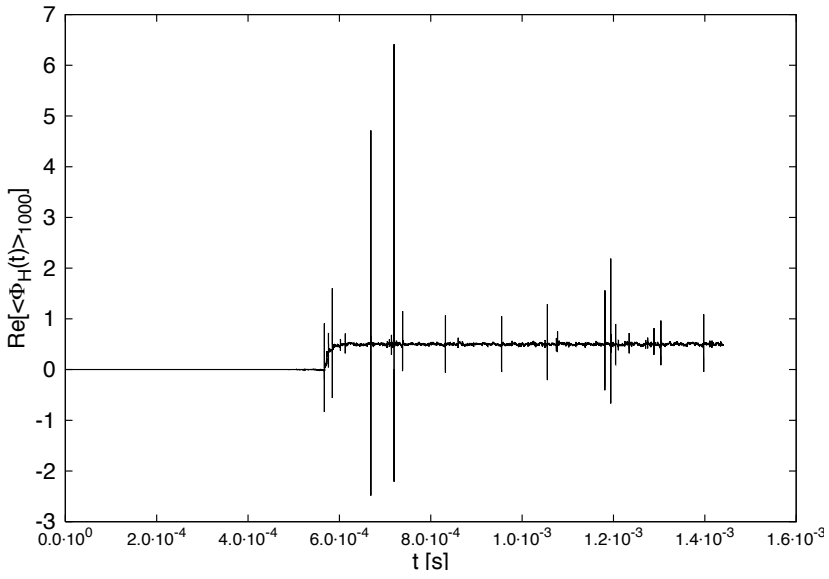

Figure 3.18: Real part of the path integral average of 1000 possible solution to the stochastic equation (2.61) in zero space dimensions constraining the hydrogen reaction partners ($K_{HH} = 5.1 \times 10^4 \mathrm{s}^{-1}$, $L_H = 1.9 \times 10^{-3} \mathrm{s}^{-1}$) with a source rate for the hydrogen atoms of value $J_H = 10^{-8} \mathrm{s}^{-1}$ and for the initial condition $\bar{\Phi}_H(0) = 0$.

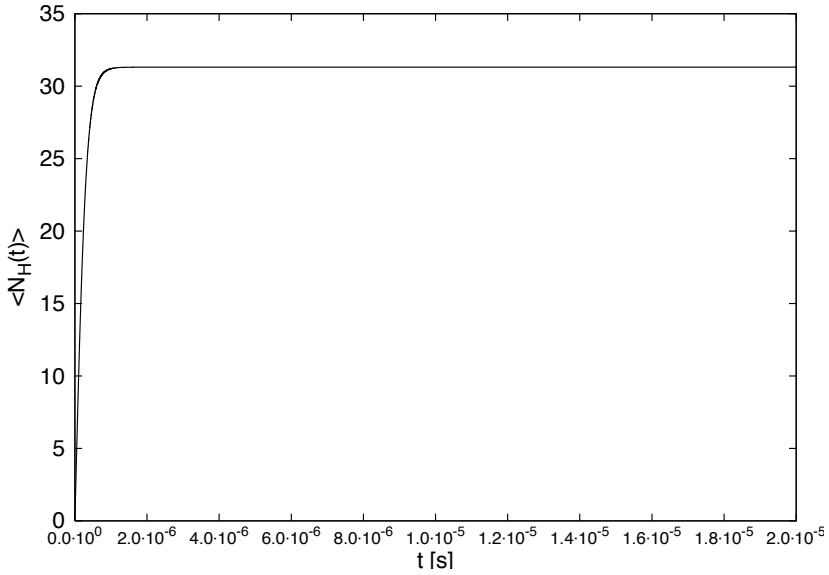

Figure 3.19: Solution to the mean-field rate equation in the single spatial site model for a value of the source rate of $J_H = 10^8 \mathrm{s}^{-1}$ for the hydrogen reactants for $K_{HH} = 5.1 \times 10^4 \mathrm{s}^{-1}$, $L_H = 1.9 \times 10^{-3} \mathrm{s}^{-1}$ and for the initial condition $\langle N_H(0) \rangle = 0$.

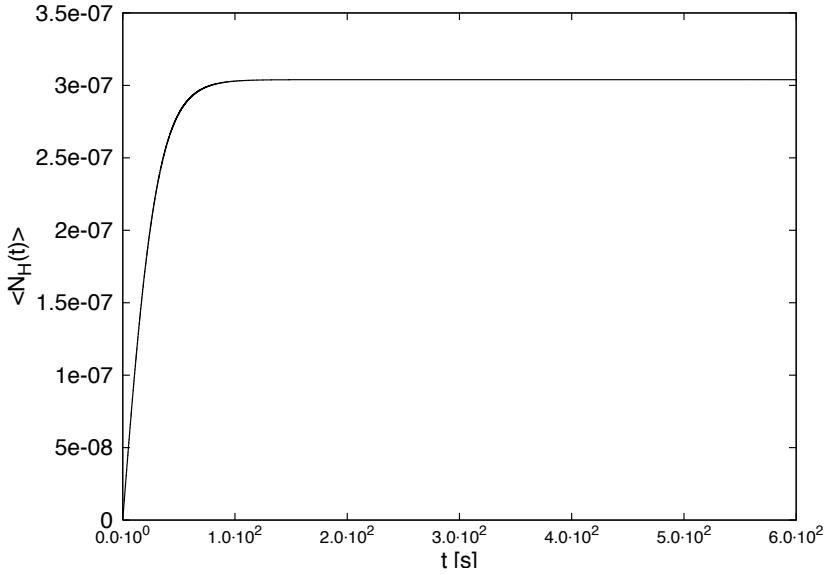

Figure 3.20: Solution to the mean-field rate equation in zero space dimensions for the hydrogen reaction partners ($K_{HH} = 5.1 \times 10^4 \mathrm{s}^{-1}$, $L_H = 1.9 \times 10^{-3} \mathrm{s}^{-1}$) with a source rate for the hydrogen atoms of value $J_H = 10^{-8} \mathrm{s}^{-1}$ and for the initial condition $\langle N_H(0) \rangle = 0$.

	$K[\mathrm{s}^{-1}]$	$L[\mathrm{s}^{-1}]$	$\mathfrak{J}[\mathrm{s}^{-1}\mathrm{cm}^{-3}]$	$\langle N(t_\infty)\rangle$	$\langle\Phi(t_\infty)\rangle_{1000}$
H	5.1×10^{4}	1.9×10^{-3}	1.5×10^{-5}	1.2×10^{-5}	5×10^{-1}
O	4.2×10^{-5}	3.7×10^{-12}	3.6×10^{-6}	2.1×10^{-1}	5×10^{-1}

Table 3.1: Late-time average particle population of hydrogen atoms and oxygen atoms under interstellar conditions at $T = 10\mathrm{K}$ with zero initial conditions according to the mean-field theory, $\langle N(t_\infty)\rangle$, and according to the stochastic framework, $\langle\Phi(t_\infty)\rangle_{1000}$. The evaporation for hydrogen was dominated by thermodynamic evaporation and the evaporation for oxygen was dominated by cosmic ray desorption. The values of the rate coefficients —K reaction rate, L evaporation rate, and $\mathfrak{J} := Jn^{-1}$ where J is the source rate and n the gas phase density— are taken from [58].

	$K[\mathrm{s}^{-1}]$	$L[\mathrm{s}^{-1}]$	$\mathfrak{J}[\mathrm{s}^{-1}\mathrm{cm}^{-3}]$	$\langle N(t_\infty)\rangle$	$\langle\Phi(t_\infty)\rangle_{1000}$
H	5.5×10^{4}	2.2×10^{2}	1.8×10^{-5}	8.2×10^{-8}	5×10^{-1}
O	1.3×10^{-1}	1.14×10^{-11}	4.4×10^{-6}	4.1×10^{-3}	5×10^{-1}

Table 3.2: Late-time average particle population of hydrogen atoms and oxygen atoms under interstellar conditions at $T = 15\mathrm{K}$ with zero initial conditions according to the mean-field theory, $\langle N(t_\infty)\rangle$, and according to the stochastic framework, $\langle\Phi(t_\infty)\rangle_{1000}$. The evaporation for hydrogen was dominated by thermodynamic evaporation and the evaporation for oxygen was due to cosmic ray desorption as well as due to the thermodynamics. The values of the rate coefficients —K reaction rate, L evaporation rate, and $\mathfrak{J} := Jn^{-1}$ where J is the source rate and n the gas phase density— are taken from [58].

	$K[\mathrm{s}^{-1}]$	$L[\mathrm{s}^{-1}]$	$\mathfrak{J}[\mathrm{s}^{-1}\mathrm{cm}^{-3}]$	$\langle N(t_\infty)\rangle$	$\langle \Phi(t_\infty)\rangle_{1000}$
H	7.1×10^{4}	7.5×10^{4}	2.0×10^{-5}	2.7×10^{-10}	2.67×10^{-10}
O	7.1×10^{0}	4.8×10^{-6}	5.1×10^{-6}	6.0×10^{-4}	5×10^{-1}

Table 3.3: Late-time average particle population of hydrogen atoms and oxygen atoms under interstellar conditions at $T = 20\mathrm{K}$ with zero initial conditions according to the mean-field theory, $\langle N(t_\infty)\rangle$, and according to the stochastic framework, $\langle \Phi(t_\infty)\rangle_{1000}$. The evaporation for all chemical species was due to thermodynamic desorption. The values of the rate coefficients —K reaction rate, L evaporation rate, and $\mathfrak{J} := Jn^{-1}$ where J is the source rate and n the gas phase density— are taken from [58].

3.4 Comparison between the Solutions

In the following, we want to investigate the similarities and discrepancies between the stochastic and the deterministic regime depending on the source rate coefficient and on the temperature of the grain surface, respectively.

3.4.1 Comparison between the Mean-Field Steady State Solution and the Stochastic Steady State Solution

In this part of the thesis, we compare the average population of chemical reactants of type A as computed from the stationary mean-field equation

$$\langle N_A \rangle^{ss} = \frac{\sqrt{8K_{AA}J_A + L_A^2} - L_A}{4K_{AA}}, \tag{3.202}$$

to the average number of reactants as given by the stochastic steady state solution to the stationary master equation

$$\langle \mathcal{N}_A \rangle^{ss} = \begin{cases} \frac{1}{2}\left(1 - \frac{L_A}{K_{AA}}\right) + \sqrt{\frac{J_A}{2K_{AA}}} \frac{I_{2-\frac{L_A}{K_{AA}}}\left(\sqrt{\frac{8J_A}{K_{AA}}}\right)}{I_{1-\frac{L_A}{K_{AA}}}\left(\sqrt{\frac{8J_A}{K_{AA}}}\right)} =: \langle \mathcal{N}_A \rangle^{ss}_{L_A K_{AA}^{-1}<1} & : \quad L_A K_{AA}^{-1} < 1 \\ \sqrt{\frac{J_A}{2K_{AA}}} \frac{I_{\frac{L_A}{K_{AA}}}\left(\sqrt{\frac{8J_A}{K_{AA}}}\right)}{I_{\frac{L_A}{K_{AA}}-1}\left(\sqrt{\frac{8J_A}{K_{AA}}}\right)} =: \langle \mathcal{N}_A \rangle^{ss}_{L_A K_{AA}^{-1}\geq 1} & : \quad L_A K_{AA}^{-1} \geq 1 \end{cases}. \tag{3.203}$$

For reference, we also give the stochastic steady state solution as presented in the literature

$$\langle \mathcal{N}_A \rangle^{ss}_{lit} \equiv \langle \mathcal{N}_A \rangle^{ss}_{L_A K_{AA}^{-1}\geq 1}. \tag{3.204}$$

In Table 3.4 we present the available data taken from [58] for the oxygen rate coefficients at different temperatures of the grain surface. These parameters correspond to the so-called M1 model and represent low estimates for silicate surfaces or surfaces that are partially icy. For any of the temperatures under consideration, namely, $T = 10\text{K}$, $T = 15\text{K}$ and $T = 20\text{K}$, the condition $L_O/K_{OO} < 1$ is satisfied. In Table 3.5, we give the average number of oxygen atoms on the surface of a grain particle which has a surface temperature of $T = 10\text{K}$ according to the mean-field theory, $\langle N_O \rangle^{ss}$, and according to the stochastic framework, $\langle \mathcal{N}_O \rangle^{ss}_{lit}$ and $\langle \mathcal{N}_O \rangle^{ss}_{L_O/K_{OO}<1}$ depending on the value of the source rate coefficient J_O. Table 3.6 lists the same quantities for a grain surface temperature of $T = 15\text{K}$ and Table 3.7 for $T = 20\text{K}$. For a grain surface temperature of $T = 10\text{K}$, the mean-field results and the stochastic results coincide

down to a source rate coefficient of $J_O = 1 \times 10^{-3}\text{s}^{-1}$. The mean-field steady state solution approaches zero for decreasing value of the source rate whereas the stochastic steady state solution reaches a value of 0.5 regardless of the choice of the source rate if J_O is small enough. Both of the stochastic steady state values coincide for all values of the source rate coefficient. For a grain surface temperature of $T = 15\text{K}$ the threshold between the deterministic regime and the stochastic regime is at a source rate of $J_O = 1 \times 10^{1}\text{s}^{-1}$. One observes small deviations between the two stochastic steady state solutions at very small values of the source rate. At a grain surface temperature of $T = 20\text{K}$ the mean-field framework seems to fail for values of the source rate coefficient that are less than $J_O = 1 \times 10^{3}\text{s}^{-1}$. In addition, the stochastic steady state solution $\langle \mathcal{N}_O \rangle^{ss}_{lit}$ decreases for decreasing source rate whereas the stochastic steady state solution $\langle \mathcal{N}_O \rangle^{ss}_{L_O/K_{OO}<1}$ stays —after a critical value of the source rate is reached— at the value of one half even if the source rate decreases further.

The above statements can be visualised in Figure 3.21 —for $T = 10\text{K}$—, in Figure 3.22 —for $T = 15\text{K}$— and in Figure 3.23 —for $T = 20\text{K}$—, where we have plotted the mean-field steady state solution, $\langle N_O \rangle^{ss}$, and the two stochastic steady state solutions, $\langle \mathcal{N}_O \rangle^{ss}_{L_O/K_{OO}<1}$ and $\langle \mathcal{N}_O \rangle^{ss}_{lit}$.

In addition, the stochastic steady state values for small source rate coefficient can be compared to the leading order terms of the expansion of the exact solutions for small $J_A K_{AA}^{-1}$, namely $J_A L_A^{-1}$ for the expansion of the stochastic steady state solution $\langle \mathcal{N}_A \rangle^{ss}_{L_A K_{AA}^{-1} \geq 1}$ and $0.5(1 - L_A K_{AA}^{-1})$ for the stochastic steady state solution $\langle \mathcal{N}_A \rangle^{ss}_{L_A K_{AA}^{-1}<1}$. For a temperature of $T = 10\text{K}$, the leading order in the expansion $\langle \mathcal{N}_O \rangle^{ss}_{L_O K_{OO}^{-1} \geq 1}(J_O K_{OO}^{-1}$ small) reads $J_O \times 2.7027 \times 10^{11}$ and the leading order term in the expansion $\langle \mathcal{N}_O \rangle^{ss}_{L_O K_{OO}^{-1}<1}(J_O K_{OO}^{-1}$ small) is given by 5×10^{-1}. If the temperature of the grain surface is $T = 15\text{K}$, the leading order term in the expansion $\langle \mathcal{N}_O \rangle^{ss}_{L_O K_{OO}^{-1} \geq 1}(J_O K_{OO}^{-1}$ small) reads $J_O \times 8.7719 \times 10^{10}$ and the leading order term in the expansion $\langle \mathcal{N}_O \rangle^{ss}_{L_O K_{OO}^{-1}<1}(J_O K_{OO}^{-1}$ small) is given by 5×10^{-1}. For a temperature of $T = 20\text{K}$, the leading order in the expansion $\langle \mathcal{N}_O \rangle^{ss}_{L_O K_{OO}^{-1} \geq 1}(J_O K_{OO}^{-1}$ small) reads $J_O \times 2.0833 \times 10^{5}$ and the leading order term in the expansion $\langle \mathcal{N}_O \rangle^{ss}_{L_O K_{OO}^{-1}<1}(J_O K_{OO}^{-1}$ small) is given by 5×10^{-1}. From the comparison between the above values with the mean oxygen population —see Table 3.5, Table 3.6 and Table 3.7— one can conclude that the higher the temperature the greater the value of the source rate at which the leading order term is a good approximation for the full stochastic steady state solution. This is even more the case when considering the hydrogen-hydrogen recombination at the same temperatures of the surface of the grain particle.

In Table 3.8 we list the M1 model data according to [58] for the heterogeneous chemical reaction between two hydrogen atoms producing diatomic hydrogen at the grain surface temperatures $T = 10\text{K}$, where $L_H K_{HH}^{-1} < 1$, $T = 15\text{K}$, where $L_H K_{HH}^{-1} < 1$, and $T = 20\text{K}$, where $L_H K_{HH}^{-1} \geq 1$. The latter implies that for $T = 20\text{K}$, the stochastic steady state solution as presented in the standard literature $\langle \mathcal{N}_H \rangle_{lit}^{ss} \equiv \langle \mathcal{N}_H \rangle_{L_H K_{HH}^{-1} \geq 1}^{ss}$ will give the correct stochastic result whereas for $T = 10\text{K}$ and $T = 15\text{K}$, the stochastic steady state solution $\langle \mathcal{N}_H \rangle_{L_H K_{HH}^{-1} < 1}^{ss}$ has to be employed. In Table 3.9 we give the average hydrogen population according to the stationary mean-field rate equations $\langle N_H \rangle^{ss}$ depending on the value of the source rate coefficient $J_H \in [10^8 \text{s}^{-1}, 10^{-8} \text{s}^{-1}]$ and compare the mean-field results with the corresponding stochastic steady state solutions in the case where the surface of the grain particle has a temperature of $T = 10\text{K}$. For values of the source rate of less than $J_H = 10^4 \text{s}^{-1}$ the mean-field steady state solution does not reproduce the value of the stochastic steady state solution. Furthermore, the stochastic steady state solution according to the literature does not coincide with the stochastic steady state solution presented in this thesis for values of the source rate which are less than $J_H = 10^{-2} \text{s}^{-1}$. In Table 3.10 the same quantities are listed for a grain surface temperature of $T = 15\text{K}$. The threshold between deterministic and stochastic regime occurs for slightly greater value of the source rate, namely $J_H = 10^5 \text{s}^{-1}$, as before, where the discrepancies between the two stochastic steady state solutions are found for much greater value of the source rate —$J_H = 10^3 \text{s}^{-1}$— as for a colder grain. In the case where the temperature of the grain surface is $T = 20\text{K}$, the mean-field steady state solution and the stochastic solution give the same result for any value of the source rate.

The numerical findings are depicted in Figure 3.24 for a temperature of $T = 10\text{K}$, in Figure 3.25 for a temperature of $T = 15\text{K}$, and in Figure 3.26 for a temperature of $T = 20\text{K}$.

As we have done for the oxygen-oxygen recombination, one can compare the stochastic steady state values for small source rate coefficient to the leading order terms of the expansion of the exact solutions for small $J_A K_{AA}^{-1}$, namely $J_A L_A^{-1}$ for the expansion of the stochastic steady state solution $\langle \mathcal{N}_A \rangle_{L_A K_{AA}^{-1} \geq 1}^{ss}$ and $0.5(1 - L_A K_{AA}^{-1})$ for the stochastic steady state solution $\langle \mathcal{N}_A \rangle_{L_A K_{AA}^{-1} < 1}^{ss}$. For a hydrogen recombination taking place on the surface of a grain with a temperature of $T = 10\text{K}$ the leading order in the expansion $\langle \mathcal{N}_H \rangle_{L_H K_{HH}^{-1} \geq 1}^{ss} (J_H K_{HH}^{-1}$ small) reads $J_H \times 5.26316 \times 10^2$ and the leading order term in the expansion $\langle \mathcal{N}_H \rangle_{L_H K_{HH}^{-1} < 1}^{ss} (J_H K_{HH}^{-1}$ small) is given by 5×10^{-1}. In case the temperature of the grain surface takes the value $T = 15\text{K}$ the leading order term in the expansion $\langle \mathcal{N}_H \rangle_{L_H K_{HH}^{-1} \geq 1}^{ss} (J_H K_{HH}^{-1}$ small) reads $J_H \times 4.54545 \times 10^{-3}$ and the leading order term in the expansion $\langle \mathcal{N}_H \rangle_{L_H K_{HH}^{-1} < 1}^{ss} (J_H K_{HH}^{-1}$ small) is given by

4.98×10^{-1}. For a grain surface temperature of $T = 20$K one has that the leading order term of $\langle \mathcal{N}_H \rangle^{ss}_{L_H K_{HH}^{-1} \geq 1} (J_H K_{HH}^{-1}$ small) is $J_H \times 1.33333 \times 10^{-3}$. As can be seen from Table 3.9, Table 3.10 and Table 3.11, there is only a small difference between the values of the source rate at different grain surface temperatures for which the leading order of the expansion of the stochastic steady state solution corresponds to the full stochastic steady state solution.
In general, the average reactant population as predicted by the mean-field framework approaches zero for decreasing value of the source rate which is not necessarily true for the average reactant population as obtained from the stochastic steady state solution.

Next, we want to examine the dependence of the average hydrogen population on the grain surface temperature. In Table 3.12 we reproduce the values of the thermal evaporation rate coefficient according to [4] —M2 parameters— for a grain particle made of either olivine or amorphous carbon in a temperature range of $T \in [5\text{K}, 30\text{K}]$. In Table 3.13 we list the reaction rate coefficients depending on the grain surface temperature which are computed as described in the section on the numerical implementation of the Doi-Peliti formalism for a grain diameter of $d_1 := 10^{-8}$m and $d_2 := 5 \times 10^{-7}$m, assuming that the grain is made of either olivine or amorphous carbon. The hydrogen source rate for a grain diameter of $d_1 := 10^{-8}$m is given by $J_H = 1.14 \times 10^{-6}\text{s}^{-1}$, and for a grain diameter of $d_2 := 5 \times 10^{-7}$m it reads $J_H = 2.85 \times 10^{-3}\text{s}^{-1}$.
For a seed surface made of amorphous carbon we compare the dependence of the average hydrogen population in the stationary mean-field model, $\langle N_H \rangle^{ss}$, in the stationary stochastic model , $\langle \mathcal{N}_H \rangle^{ss}_{L_H/K_{HH} \geq 1}$ and $\langle \mathcal{N}_H \rangle^{ss}_{L_H/K_{HH} < 1}$ in Table 3.14 and Figure 3.27 for a grain diameter of $d_1 := 10^{-8}$m and in Table 3.15 and Figure 3.28 for a grain diameter of $d_2 := 5 \times 10^{-7}$m. For a seed surface made of olivine the dependence of the average hydrogen population in the stationary mean-field model, $\langle N_H \rangle^{ss}$, in the stationary stochastic model , $\langle \mathcal{N}_H \rangle^{ss}_{L_H/K_{HH} \geq 1}$ and $\langle \mathcal{N}_H \rangle^{ss}_{L_H/K_{HH} < 1}$ are summarised in Table 3.16 and plotted in Figure 3.29 for a grain diameter of $d_1 := 10^{-8}$m and in Table 3.17 and Figure 3.30 for a grain diameter of $d_2 := 5 \times 10^{-7}$m. In general, the average hydrogen population on the smaller grains is less than the average hydrogen population on the bigger grain particles. For both the specific materials forming the grain particle and for the particular range of temperature, one observes that for the larger grain size $d_2 := 5 \times 10^{-7}$m all the results lie in the deterministic regime. For the smaller seed size, $d_1 := 10^{-8}$m, and on cold grains, the average hydrogen population according to the mean-field framework corresponds to the average hydrogen population as predicted by the stochastic framework, in the case of olivine for $T = 5$K, and in

the case of amorphous carbon for $T = 10\text{K}$. However, increasing the grain surface temperature the stochastic regime is entered, that is for $T = 10\text{K}$ the mean-field steady state solution and the stochastic steady state solution for a grain particle made of olivine differ as do the mean-field steady state solution and the stochastic steady state solution for a grain particle made of amorphous carbon in the temperature range of $T \in [15\text{K}, 25\text{K}]$. For any of the two materials under consideration and for higher temperatures one observes that the average hydrogen population obtained from the stationary mean-field rate equations and the average hydrogen population derived from the stochastic steady state solution have the same values.

$T = 10\text{K}$	$K_{OO} = 4.2 \times 10^{-5}\text{s}^{-1}$	$L_O^{thd} = 2.0 \times 10^{-23}\text{s}^{-1}$	$L_O^{crd} = 3.7 \times 10^{-12}\text{s}^{-1}$
$T = 15\text{K}$	$K_{OO} = 1.3 \times 10^{-1}\text{s}^{-1}$	$L_O^{thd} = 7.7 \times 10^{-12}\text{s}^{-1}$	$L_O^{crd} = 3.7 \times 10^{-12}\text{s}^{-1}$
$T = 20\text{K}$	$K_{OO} = 7.1 \times 10^{0}\text{s}^{-1}$	$L_O^{thd} = 4.8 \times 10^{-6}\text{s}^{-1}$	$L_O^{crd} = 3.7 \times 10^{-12}\text{s}^{-1}$

Table 3.4: Dependence of oxygen rate coefficients, namely the reaction rate coefficient K_{OO}, the thermal desorption rate L_O^{thd} and the cosmic ray desorption rate L_O^{crd}, on the temperature of the grain surface according to [58].

J_O [s^{-1}]	$\langle N_O \rangle^{ss}$	$\langle \mathcal{N}_O \rangle_{lit}^{ss}$	$\langle \mathcal{N}_O \rangle_{L_O/K_{OO}<1}^{ss}$
10^{8}	$1.091089451 \times 10^{6}$	$1.091089576 \times 10^{6}$	$1.091089576 \times 10^{6}$
10^{7}	$3.450327798 \times 10^{5}$	$3.450329046 \times 10^{5}$	$3.450329045 \times 10^{5}$
10^{6}	$1.091089451 \times 10^{5}$	$1.091090701 \times 10^{5}$	$1.091090701 \times 10^{5}$
10^{5}	$3.450327798 \times 10^{4}$	$3.450340296 \times 10^{4}$	$3.450340296 \times 10^{4}$
10^{4}	$1.091089451 \times 10^{4}$	$1.091101951 \times 10^{4}$	$1.091101951 \times 10^{4}$
10^{3}	$3.450327798 \times 10^{3}$	$3.450452802 \times 10^{3}$	$3.450452802 \times 10^{3}$
10^{2}	$1.091089451 \times 10^{3}$	$1.091214472 \times 10^{3}$	$1.091214473 \times 10^{3}$
10^{1}	$3.450327798 \times 10^{2}$	$3.451578476 \times 10^{2}$	$3.451578476 \times 10^{2}$
10^{0}	$1.091089451 \times 10^{2}$	$1.092341604 \times 10^{2}$	$1.092341604 \times 10^{2}$
10^{-1}	$3.450327795 \times 10^{1}$	$3.462896218 \times 10^{1}$	$3.462896222 \times 10^{1}$
10^{-2}	$1.091089449 \times 10^{1}$	$1.103809333 \times 10^{1}$	$1.103809334 \times 10^{1}$
10^{-3}	$3.450327775 \times 10^{0}$	$3.582666587 \times 10^{0}$	$3.582666585 \times 10^{0}$
10^{-4}	$1.091089429 \times 10^{0}$	$1.245245686 \times 10^{0}$	$1.245245687 \times 10^{0}$
10^{-5}	$3.450327575 \times 10^{-1}$	$6.105975638 \times 10^{-1}$	$6.105976225 \times 10^{-1}$
10^{-6}	$1.091089231 \times 10^{-1}$	$5.118104648 \times 10^{-1}$	$5.118113469 \times 10^{-1}$
10^{-7}	$3.450325595 \times 10^{-2}$	$5.011802821 \times 10^{-1}$	$5.011894885 \times 10^{-1}$
10^{-8}	$1.091087249 \times 10^{-2}$	$5.000265503 \times 10^{-1}$	$5.001189942 \times 10^{-1}$
10^{-9}	$3.450305772 \times 10^{-3}$	$4.990885627 \times 10^{-1}$	$5.000118607 \times 10^{-1}$

Table 3.5: Dependence of the mean-field steady state values $\langle N_O \rangle^{ss}$, the stochastic steady state values as given in the literature $\langle \mathcal{N}_O \rangle_{lit}^{ss}$, and the stochastic steady state values $\langle \mathcal{N}_O \rangle_{L_O/K_{OO}<1}^{ss}$ of the average oxygen population on the source rate J_O at $T = 10\text{K}$ for an evaporation coefficient $L_O = 3.7 \times 10^{-12}\text{s}^{-1}$ and $K_{OO} = 4.2 \times 10^{-5}\text{s}^{-1}$.

J_O [s^{-1}]	$\langle N_O \rangle^{ss}$	$\langle \mathcal{N}_O \rangle^{ss}_{lit}$	$\langle \mathcal{N}_O \rangle^{ss}_{L_O/K_{OO}<1}$
10^{8}	$1.961161352 \times 10^{4}$	$1.961173851 \times 10^{4}$	$1.961173852 \times 10^{4}$
10^{7}	$6.201736730 \times 10^{3}$	$6.201861733 \times 10^{3}$	$6.201861733 \times 10^{3}$
10^{6}	$1.961161352 \times 10^{3}$	$1.961286363 \times 10^{3}$	$1.961286363 \times 10^{3}$
10^{5}	$6.201736730 \times 10^{2}$	$6.202987107 \times 10^{2}$	$6.202987110 \times 10^{2}$
10^{4}	$1.961161352 \times 10^{2}$	$1.962412548 \times 10^{2}$	$1.962412548 \times 10^{2}$
10^{3}	$6.201736730 \times 10^{1}$	$6.214274671 \times 10^{1}$	$6.214274674 \times 10^{1}$
10^{2}	$1.961161352 \times 10^{1}$	$1.973782408 \times 10^{1}$	$1.973782409 \times 10^{1}$
10^{1}	$6.201736730 \times 10^{0}$	$6.330676928 \times 10^{0}$	$6.330676929 \times 10^{0}$
10^{0}	$1.961161352 \times 10^{0}$	$2.099972434 \times 10^{0}$	$2.099972434 \times 10^{0}$
10^{-1}	$6.201736730 \times 10^{-1}$	$8.129370893 \times 10^{-1}$	$8.129370895 \times 10^{-1}$
10^{-2}	$1.961161352 \times 10^{-1}$	$5.375117811 \times 10^{-1}$	$5.375117818 \times 10^{-1}$
10^{-3}	$6.201736728 \times 10^{-2}$	$5.038363263 \times 10^{-1}$	$5.038363297 \times 10^{-1}$
10^{-4}	$1.961161350 \times 10^{-2}$	$5.003844841 \times 10^{-1}$	$5.003845168 \times 10^{-1}$
10^{-5}	$6.201736708 \times 10^{-3}$	$5.000381355 \times 10^{-1}$	$5.000384606 \times 10^{-1}$
10^{-6}	$1.961161331 \times 10^{-3}$	$5.000005961 \times 10^{-1}$	$5.000038461 \times 10^{-1}$
10^{-7}	$6.201736510 \times 10^{-4}$	$4.999678867 \times 10^{-1}$	$5.000003846 \times 10^{-1}$
10^{-8}	$1.961161133 \times 10^{-4}$	$4.996752493 \times 10^{-1}$	$5.000000385 \times 10^{-1}$
10^{-9}	$6.201734538 \times 10^{-5}$	$4.967709927 \times 10^{-1}$	$5.000000038 \times 10^{-1}$

Table 3.6: Dependence of the mean-field steady state values $\langle N_O \rangle^{ss}$, the stochastic steady state values according to the literature $\langle \mathcal{N}_O \rangle^{ss}_{lit}$, and the stochastic steady state values $\langle \mathcal{N}_O \rangle^{ss}_{L_O/K_{OO}<1}$ of the average oxygen population on the source rate J_O at $T =$ 15K for an evaporation coefficient $L_O = 1.14 \times 10^{-11}\text{s}^{-1}$ and $K_{OO} = 1.3 \times 10^{-1}\text{s}^{-1}$.

J_O [s^{-1}]	$\langle N_O \rangle^{ss}$	$\langle \mathcal{N}_O \rangle^{ss}_{lit}$	$\langle \mathcal{N}_O \rangle^{ss}_{L_O/K_{OO}<1}$
10^{8}	$2.653724462 \times 10^{3}$	$2.653849471 \times 10^{3}$	$2.653849472 \times 10^{3}$
10^{7}	$8.391813585 \times 10^{2}$	$8.393063858 \times 10^{2}$	$8.393063861 \times 10^{2}$
10^{6}	2.65372446×10^{2}	$2.654975344 \times 10^{2}$	$2.654975345 \times 10^{2}$
10^{5}	$8.391813568 \times 10^{1}$	$8.404341580 \times 10^{1}$	$8.404341574 \times 10^{1}$
10^{4}	$2.653724445 \times 10^{1}$	$2.666313606 \times 10^{1}$	$2.666313607 \times 10^{1}$
10^{3}	$8.391813415 \times 10^{0}$	$8.519692942 \times 10^{0}$	$8.519692944 \times 10^{0}$
10^{2}	$2.653724292 \times 10^{0}$	$2.788512506 \times 10^{0}$	$2.788512506 \times 10^{0}$
10^{1}	$8.391811895 \times 10^{-1}$	$1.007112387 \times 10^{0}$	$1.007112398 \times 10^{0}$
10^{0}	$2.653722772 \times 10^{-1}$	$5.673316669 \times 10^{-1}$	$5.673325782 \times 10^{-1}$
10^{-1}	$8.391796682 \times 10^{-2}$	$5.069974190 \times 10^{-1}$	$5.070090867 \times 10^{-1}$
10^{-2}	$2.653707560 \times 10^{-2}$	$5.005839158 \times 10^{-1}$	$5.007035572 \times 10^{-1}$
10^{-3}	$8.391644570 \times 10^{-3}$	$4.988732148 \times 10^{-1}$	$5.000700813 \times 10^{-1}$
10^{-4}	$2.653555452 \times 10^{-3}$	$4.882875494 \times 10^{-1}$	$5.000067042 \times 10^{-1}$
10^{-5}	$8.390123612 \times 10^{-4}$	$4.032214441 \times 10^{-1}$	$5.000003662 \times 10^{-1}$
10^{-6}	$2.652034860 \times 10^{-4}$	$1.470521550 \times 10^{-1}$	$4.999997324 \times 10^{-1}$
10^{-7}	$8.374929192 \times 10^{-5}$	$1.999876063 \times 10^{-2}$	$4.999996690 \times 10^{-1}$
10^{-8}	$2.636876875 \times 10^{-5}$	$2.074555378 \times 10^{-3}$	$4.999996627 \times 10^{-1}$
10^{-9}	$8.224501328 \times 10^{-6}$	$2.082331212 \times 10^{-4}$	$4.999996621 \times 10^{-1}$

Table 3.7: Dependence of the mean-field steady state values $\langle N_O \rangle^{ss}$, the stochastic steady state values as derived in the literature $\langle \mathcal{N}_O \rangle^{ss}_{lit}$, and the stochastic steady state values $\langle \mathcal{N}_O \rangle^{ss}_{L_O/K_{OO}<1}$ of the average oxygen population on the source rate J_O at $T =$ 20K for an evaporation coefficient $L_O = 4.8 \times 10^{-6}\text{s}^{-1}$ and $K_{OO} = 7.1 \times 10^{0}\text{s}^{-1}$.

$T = 10\text{K}$	$K_{HH} = 5.1 \times 10^4 \text{s}^{-1}$	$L_H^{thd} = 1.9 \times 10^{-3} \text{s}^{-1}$	$L_H^{crd} = 6.0 \times 10^{-9} \text{s}^{-1}$
$T = 15\text{K}$	$K_{HH} = 5.5 \times 10^4 \text{s}^{-1}$	$L_H^{thd} = 2.2 \times 10^2 \text{s}^{-1}$	$L_H^{crd} = 6.0 \times 10^{-9} \text{s}^{-1}$
$T = 20\text{K}$	$K_{HH} = 7.1 \times 10^4 \text{s}^{-1}$	$L_H^{thd} = 7.5 \times 10^4 \text{s}^{-1}$	$L_H^{crd} = 6.0 \times 10^{-9} \text{s}^{-1}$

Table 3.8: Dependence of hydrogen rate coefficients, namely the reaction rate coefficient K_{HH}, the thermal desorption rate L_H^{thd} and the cosmic ray desorption rate L_H^{crd}, on the grain surface temperature T according to [58].

J_H [s^{-1}]	$\langle N_H \rangle^{ss}$	$\langle \mathcal{N}_H \rangle_{lit}^{ss}$	$\langle \mathcal{N}_H \rangle_{L_H/K_{HH}<1}^{ss}$
10^8	3.131121×10^1	3.14470×10^1	3.14470×10^1
10^7	9.901475×10^0	1.003890×10^1	1.003890×10^1
10^6	3.131121×10^0	3.264278×10^0	3.264278×10^0
10^5	9.901475×10^{-1}	1.149676×10^0	1.149676×10^0
10^4	3.131121×10^{-1}	5.922002×10^{-1}	5.922002×10^{-1}
10^3	9.901474×10^{-2}	5.097340×10^{-1}	5.097404×10^{-1}
10^2	3.131121×10^{-2}	5.009750×10^{-1}	5.009797×10^{-1}
10^1	9.901466×10^{-3}	5.000505×10^{-1}	5.000980×10^{-1}
10^0	3.131112×10^{-3}	4.995352×10^{-1}	5.000098×10^{-1}
10^{-1}	9.901382×10^{-4}	4.952957×10^{-1}	5.000010×10^{-1}
10^{-2}	3.131028×10^{-4}	4.566211×10^{-1}	5.000001×10^{-1}
10^{-3}	9.901544×10^{-5}	2.563103×10^{-1}	5.0×10^{-1}
10^{-4}	3.130190×10^{-5}	4.761905×10^{-2}	5.0×10^{-1}
10^{-5}	9.892166×10^{-6}	5.202333×10^{-3}	5.0×10^{-1}
10^{-6}	3.121821×10^{-6}	5.257624×10^{-4}	5.0×10^{-1}
10^{-7}	9.808776×10^{-7}	5.262604×10^{-5}	5.0×10^{-1}
10^{-8}	3.039369×10^{-7}	5.257102×10^{-6}	5.0×10^{-1}

Table 3.9: Dependence of the mean-field steady state values, $\langle N_H \rangle^{ss}$, the stochastic steady state values according to the literature $\langle \mathcal{N}_H \rangle_{lit}^{ss}$, and the stochastic steady state values $\langle \mathcal{N}_H \rangle_{L_H/K_{HH}<1}^{ss}$ of the average hydrogen population on the source rate J_H at $T = 10\text{K}$ for the evaporation coefficient $L_H = 1.9 \times 10^{-3} \text{s}^{-1}$ and $K_{HH} = 5.1 \times 10^4 \text{s}^{-1}$.

J_H [s^{-1}]	$\langle N_H \rangle^{ss}$	$\langle \mathcal{N}_H \rangle^{ss}_{lit}$	$\langle \mathcal{N}_H \rangle^{ss}_{L_H/K_{HH}<1}$
10^8	3.015013×10^1	3.027591×10^1	3.027591×10^1
10^7	9.533626×10^0	9.661124×10^0	9.661124×10^0
10^6	3.014114×10^0	3.147523×10^0	3.147523×10^0
10^5	9.524631×10^{-1}	1.112528×10^0	1.112557×10^0
10^4	3.005130×10^{-1}	5.801986×10^{-1}	5.840125×10^{-1}
10^3	9.435150×10^{-2}	4.593738×10^{-1}	5.070542×10^{-1}
10^2	2.916771×10^{-2}	2.387524×10^{-1}	4.989104×10^{-1}
10^1	8.586923×10^{-3}	4.168113×10^{-2}	4.980911×10^{-1}
10^0	2.176619×10^{-3}	4.504667×10^{-3}	4.980091×10^{-1}
10^{-1}	3.816986×10^{-4}	4.541343×10^{-4}	4.980009×10^{-1}
10^{-2}	4.446594×10^{-5}	4.5450430×10^{-5}	4.98×10^{-1}
10^{-3}	4.535171×10^{-6}	4.545413×10^{-6}	4.98×10^{-1}
10^{-4}	4.544422×10^{-7}	4.545450×10^{-7}	4.98×10^{-1}
10^{-5}	4.545351×10^{-8}	4.545351×10^{-8}	4.98×10^{-1}
10^{-6}	4.545444×10^{-9}	4.545455×10^{-9}	4.98×10^{-1}
10^{-7}	4.545453×10^{-10}	4.545455×10^{-10}	4.98×10^{-1}
10^{-8}	4.545454×10^{-11}	4.545455×10^{-11}	4.98×10^{-1}

Table 3.10: Dependence of the mean-field steady state values, $\langle N_H \rangle^{ss}$, the stochastic steady state values according to the literature $\langle \mathcal{N}_H \rangle^{ss}_{lit}$, and the stochastic steady state values $\langle \mathcal{N}_H \rangle^{ss}_{L_H/K_{HH}<1}$ of the average hydrogen population on the source rate J_H at $T = 15$K for the evaporation coefficient $L_H = 2.2 \times 10^2 \text{s}^{-1}$ and $K_{HH} = 5.5 \times 10^4 \text{s}^{-1}$.

J_H [s^{-1}]	$\langle N_H \rangle^{ss}$	$\langle \mathcal{N}_H \rangle^{ss}_{lit} \equiv \langle \mathcal{N}_H \rangle^{ss}_{L_H/K_{HH} \geq 1}$
10^8	2.627447×10^1	2.639787×10^1
10^7	8.131883×10^0	8.251781×10^0
10^6	2.402748×10^0	2.511409×10^0
10^5	6.156689×10^{-1}	6.856860×10^{-1}
10^4	1.102992×10^{-1}	1.185992×10^{-1}
10^3	1.301273×10^{-2}	1.316339×10^{-2}
10^2	1.329984×10^{-3}	1.331607×10^{-3}
10^1	1.332997×10^{-4}	1.333160×10^{-4}
10^0	1.33330×10^{-5}	1.333316×10^{-5}
10^{-1}	1.333330×10^{-6}	1.333332×10^{-6}
10^{-2}	1.333330×10^{-7}	1.333333×10^{-7}
10^{-3}	1.333333×10^{-8}	1.333333×10^{-8}
10^{-4}	1.333333×10^{-9}	1.333333×10^{-9}
10^{-5}	1.333333×10^{-10}	1.333333×10^{-10}
10^{-6}	1.333333×10^{-11}	1.333333×10^{-11}
10^{-7}	1.333333×10^{-12}	1.333333×10^{-12}
10^{-8}	1.333333×10^{-13}	1.333333×10^{-13}

Table 3.11: Dependence of the mean-field steady state values, $\langle N_H \rangle^{ss}$, the stochastic steady state values according to the literature $\langle \mathcal{N}_H \rangle^{ss}_{lit}$ which in this case coincides with the stochastic steady state values $\langle \mathcal{N}_H \rangle^{ss}_{L_H/K_{HH} \geq 1}$ of the average hydrogen population on the source rate J_H at $T = 20$K for the evaporation coefficient $L_H = 7.5 \times 10^4 \text{s}^{-1}$ and $K_{HH} = 7.1 \times 10^4 \text{s}^{-1}$.

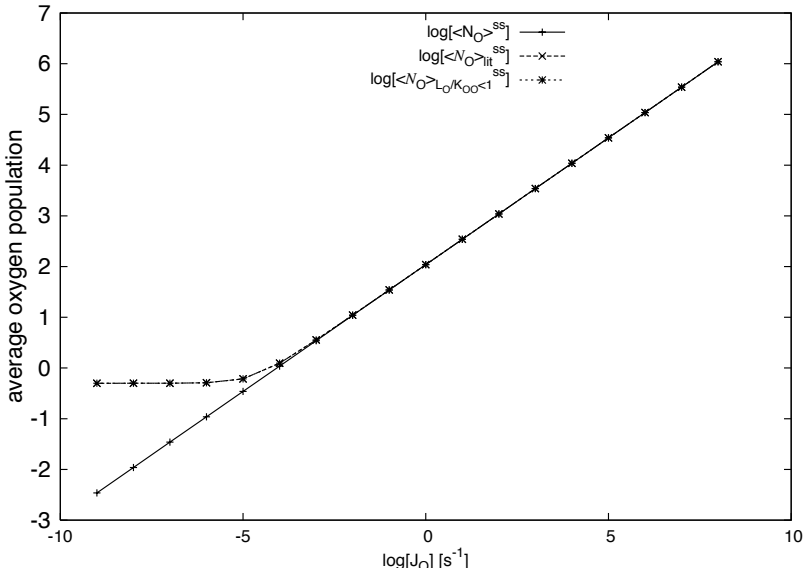

Figure 3.21: Dependence of the average oxygen population on the source rate J_O according to the mean-field framework, $\langle N_O \rangle^{ss}$, and the stochastic framework, $\langle \mathcal{N}_O \rangle^{ss}_{lit}$ and $\langle \mathcal{N}_O \rangle^{ss}_{L_O/K_{OO}<1}$, generated from the M1 data ($K_{OO} = 4.2 \times 10^{-5}\text{s}^{-1}$, $L_O = 3.7 \times 10^{-12}\text{s}^{-1}$) for a grain surface temperature of $T = 10$K. The lines are a guide to the eye.

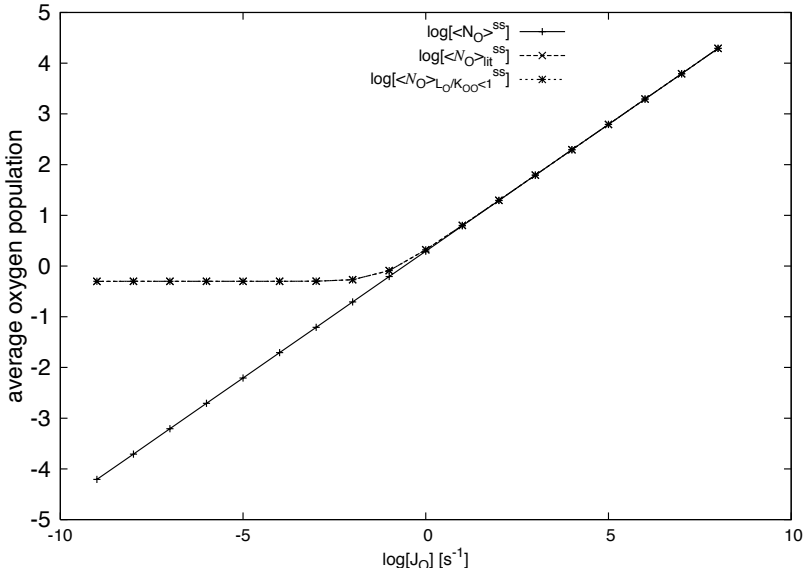

Figure 3.22: Dependence of the average oxygen population on the source rate J_O according to the mean-field framework, $\langle N_O \rangle^{ss}$, and the stochastic framework, $\langle \mathcal{N}_O \rangle^{ss}_{lit}$ and $\langle \mathcal{N}_O \rangle^{ss}_{L_O/K_{OO}<1}$, generated from the M1 data ($K_{OO} = 1.3 \times 10^{-1}\text{s}^{-1}$, $L_O = 1.14 \times 10^{-11}\text{s}^{-1}$) for a grain surface temperature of $T = 15$K. The lines are a guide to the eye.

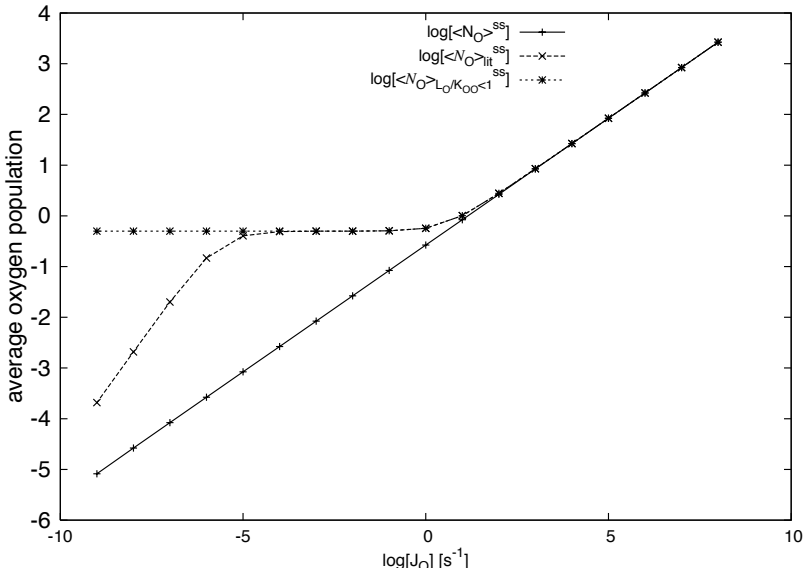

Figure 3.23: Dependence of the average oxygen population on the source rate J_O according to the mean-field framework, $\langle N_O \rangle^{ss}$, and the stochastic framework, $\langle \mathcal{N}_O \rangle^{ss}_{lit}$ and $\langle \mathcal{N}_O \rangle^{ss}_{L_O/K_{OO}<1}$, generated from the M1 data ($K_{OO} = 7.1 \times 10^0 \mathrm{s}^{-1}$, $L_O = 4.8 \times 10^{-6} \mathrm{s}^{-1}$) for a grain surface temperature of $T = 20$K. The lines are a guide to the eye.

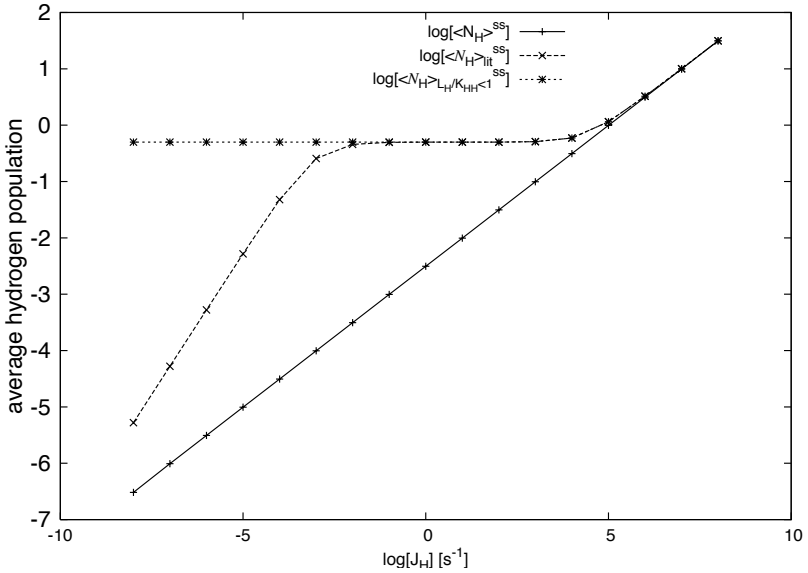

Figure 3.24: Dependence of the average hydrogen population on the source rate J_H according to the mean-field framework, $\langle N_H \rangle^{ss}$, and the stochastic framework, $\langle \mathcal{N}_H \rangle^{ss}_{lit}$ and $\langle \mathcal{N}_H \rangle^{ss}_{L_H/K_{HH}<1}$, generated from the M1 data ($K_{HH} = 5.1 \times 10^4 \mathrm{s}^{-1}$, $L_H = 1.9 \times 10^{-3} \mathrm{s}^{-1}$) for a grain surface temperature of $T = 10$K. The lines are a guide to the eye.

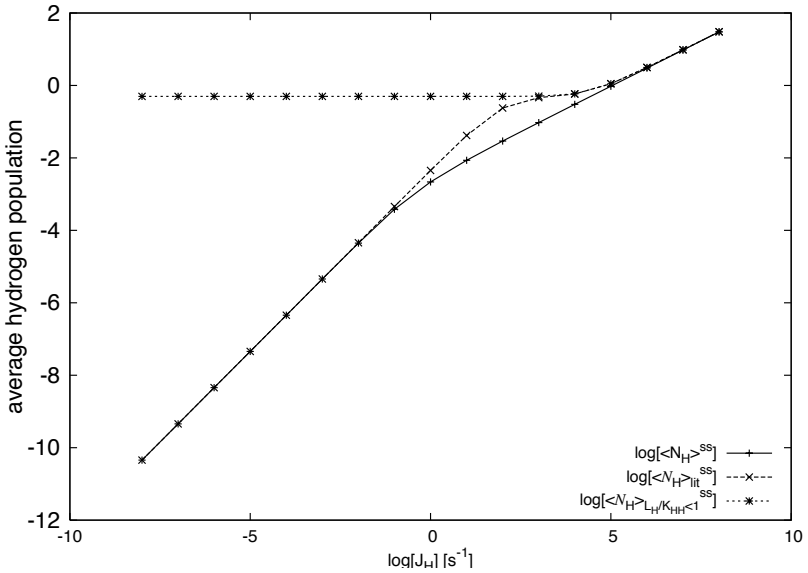

Figure 3.25: Dependence of the average hydrogen population on the source rate J_H according to the mean-field framework, $\langle N_H \rangle^{ss}$, and the stochastic framework, $\langle \mathcal{N}_H \rangle^{ss}_{lit}$ and $\langle \mathcal{N}_H \rangle^{ss}_{L_H/K_{HH}<1}$, generated from the M1 data ($K_{HH} = 5.5 \times 10^4 \mathrm{s}^{-1}$, $L_H = 2.2 \times 10^2 \mathrm{s}^{-1}$) for a grain surface temperature of $T = 15\mathrm{K}$. The lines are a guide to the eye.

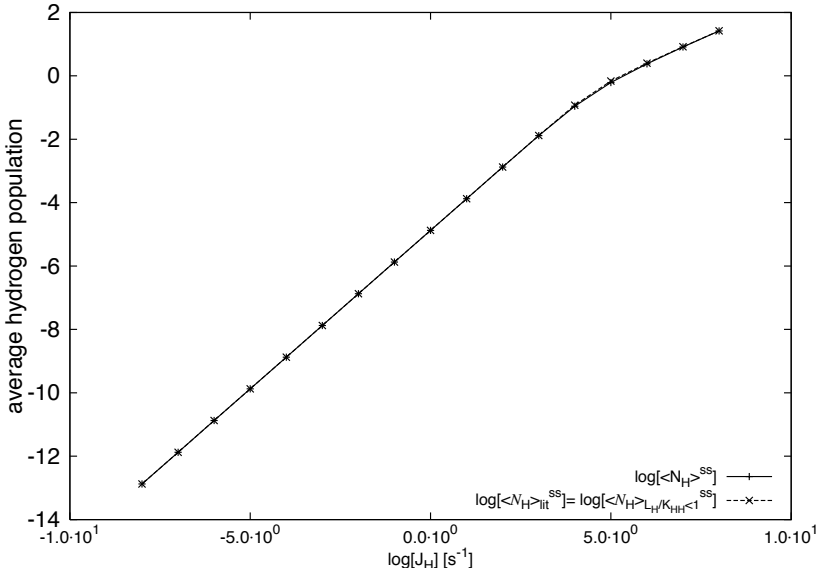

Figure 3.26: Dependence of the average hydrogen population on the source rate J_H according to the mean-field framework, $\langle N_H \rangle^{ss}$, and the stochastic framework, $\langle \mathcal{N}_H \rangle^{ss}_{lit}$ and $\langle \mathcal{N}_H \rangle^{ss}_{L_H/K_{HH}<1}$, generated from the M1 data ($K_{HH} = 7.1 \times 10^4 \mathrm{s}^{-1}$, $L_H = 7.5 \times 10^4 \mathrm{s}^{-1}$) for a grain surface temperature of $T = 20\mathrm{K}$. The lines are a guide to the eye.

T [K]	$L_H^{olivine}$ [s^{-1}]	L_H^{carbon} [s^{-1}]
5	3.9961×10^{-21}	7.0282×10^{-46}
10	6.321×10^{-5}	2.6511×10^{-17}
15	1.5869×10^{1}	8.891×10^{-8}
20	7.951×10^{3}	5.149×10^{-3}
25	3.314×10^{5}	3.71×10^{0}
30	3.984×10^{6}	2.982×10^{2}

Table 3.12: Dependence of thermal evaporation rate L_H on the grain surface temperature T for an olivine grain surface and a seed surface consisting of amorphous carbon in a hydrogen recombination process.

T [K]	$K_{HH}^{olivine}(d_1)$ [s^{-1}]	$K_{HH}^{carbon}(d_1)$ [s^{-1}]	$K_{HH}^{olivine}(d_2)$ [s^{-1}]	$K_{HH}^{carbon}(d_2)$ [s^{-1}]
5	2.0285×10^{-16}	2.5879×10^{-35}	8.114×10^{-20}	1.0352×10^{-38}
10	5.908×10^{-4}	4.0308×10^{-13}	2.363×10^{-7}	1.612×10^{-16}
15	8.4368×10^{0}	1.007×10^{-5}	3.3747×10^{-3}	4.0266×10^{-9}
20	1.0082×10^{3}	5.031×10^{-2}	4.033×10^{-1}	2.012×10^{-5}
25	1.778×10^{4}	8.334×10^{0}	7.113×10^{0}	3.334×10^{-3}
30	1.205×10^{5}	2.514×10^{2}	4.819×10^{1}	1.006×10^{-1}

Table 3.13: Dependence of the reaction rate coefficient K_{HH} on the grain surface temperature for a grain diameter of $d_1 := 10^{-8}$m and $d_2 := 5 \times 10^{-7}$m, and for a grain made of olivine or amorphous carbon in a hydrogen recombination process.

T [K]	$\langle N_H \rangle^{ss}$	$\langle \mathcal{N}_H \rangle^{ss}_{L_H/K_{HH} \geq 1}$	$\langle \mathcal{N}_H \rangle^{ss}_{L_H/K_{HH} < 1}$
5	1.484102×10^{14}	—	undefined
10	1.189164×10^{3}	—	1.189289×10^{3}
15	2.357184×10^{-1}	—	5.503949×10^{-1}
20	2.204525×10^{-4}	—	4.488392×10^{-1}
25	3.072772×10^{-7}	—	2.774179×10^{-1}
30	3.822938×10^{-9}	3.822938×10^{-9}	—

Table 3.14: Dependence of the average hydrogen population according to the steady state mean-field expression $\langle N_H \rangle^{ss}$, compared to the average hydrogen population according to the stochastic steady state values $\langle \mathcal{N}_H \rangle^{ss}_{L_H/K_{HH} \geq 1}$ and $\langle \mathcal{N}_H \rangle^{ss}_{L_H/K_{HH} < 1}$ for a grain diameter of $d_1 := 10^{-8}$m and a seed surface made of amorphous carbon.

T [K]	$\langle N_H \rangle^{ss}$	$\langle \mathcal{N}_H \rangle^{ss}_{L_H/K_{HH} \geq 1}$	$\langle \mathcal{N}_H \rangle^{ss}_{L_H/K_{HH} < 1}$
5	3.710183×10^{17}	—	undefined
10	2.973205×10^{6}	—	2.973205×10^{6}
15	5.893975×10^{2}	5.895203×10^{2}	—
20	5.511317×10^{-1}	5.511408×10^{-1}	—
25	7.681930×10^{-4}	7.68193×10^{-4}	—
30	9.557344×10^{-6}	9.557344×10^{-6}	—

Table 3.15: Dependence of the average hydrogen population according to the steady state mean-field expression $\langle N_H \rangle^{ss}$, compared to the average hydrogen population according to the stochastic steady state values $\langle \mathcal{N}_H \rangle^{ss}_{L_H/K_{HH} \geq 1}$ and $\langle \mathcal{N}_H \rangle^{ss}_{L_H/K_{HH} < 1}$ for a grain diameter of $d_2 := 5 \times 10^{-7}$m and a seed surface made of amorphous carbon.

T [K]	$\langle N_H \rangle^{ss}$	$\langle \mathcal{N}_H \rangle^{ss}_{L_H/K_{HH} \geq 1}$	$\langle \mathcal{N}_H \rangle^{ss}_{L_H/K_{HH} < 1}$
5	5.300904×10^{4}	—	5.300916×10^{4}
10	1.424297×10^{-2}	—	4.475233×10^{-1}
15	7.183817×10^{-8}	7.183817×10^{-8}	—
20	1.433793×10^{-10}	1.433782×10^{-10}	—
25	3.439952×10^{-12}	3.439952×10^{-12}	—
30	2.861446×10^{-13}	2.861446×10^{-13}	—

Table 3.16: Dependence of the average hydrogen population according to the steady state mean-field expression $\langle N_H \rangle^{ss}$, compared to the average hydrogen population according to the stochastic steady state values $\langle \mathcal{N}_H \rangle^{ss}_{L_H/K_{HH} \geq 1}$ and $\langle \mathcal{N}_H \rangle^{ss}_{L_H/K_{HH} < 1}$ for a grain diameter of $d_1 := 10^{-8}$m and a seed surface made of olivine.

T [K]	$\langle N_H \rangle^{ss}$	$\langle \mathcal{N}_H \rangle^{ss}_{L_H/K_{HH} \geq 1}$	$\langle \mathcal{N}_H \rangle^{ss}_{L_H/K_{HH} < 1}$
5	1.325226×10^{8}	—	1.325226×10^{8}
10	3.560795×10^{1}	3.562303×10^{1}	—
15	1.792752×10^{-4}	1.795954×10^{-4}	—
20	3.584428×10^{-7}	3.584455×10^{-7}	—
25	8.599879×10^{-9}	8.599879×10^{-9}	—
30	7.153614×10^{-10}	7.153614×10^{-10}	—

Table 3.17: Dependence of the average hydrogen population according to the steady state mean-field expression n_H^{ss}, compared to the average hydrogen population according to the stochastic steady state values $\langle N_H \rangle^{ss}_{L_H/K_{HH} \geq 1}$ and $\langle N_H \rangle^{ss}_{L_H/K_{HH} < 1}$ for a grain diameter of $d_2 := 5 \times 10^{-7}$m and a seed surface made of olivine.

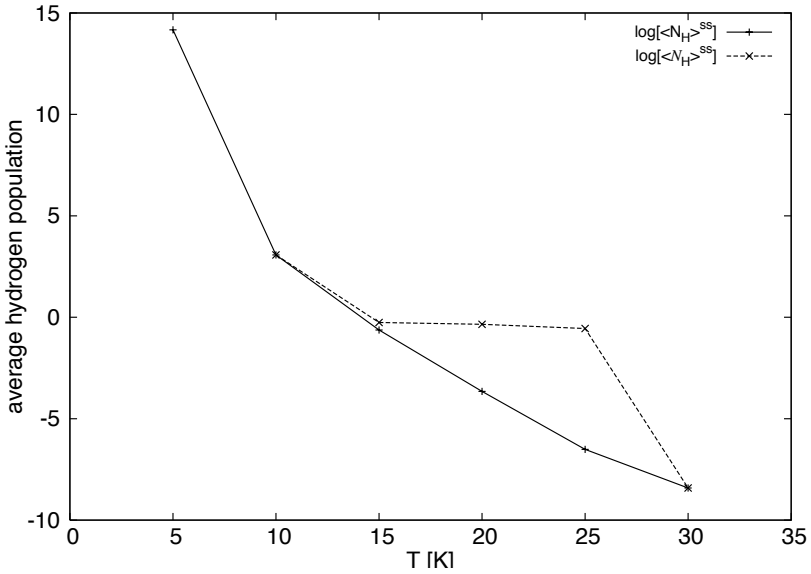

Figure 3.27: Dependence of the average hydrogen population on the grain surface temperature T according to the mean-field framework, $\langle N_H \rangle^{ss}$, and the stochastic framework, $\langle \mathcal{N}_H \rangle^{ss}$, generated from the M2 data for a grain made of amorphous carbon and a grain diameter of $d_1 := 1 \times 10^{-8}$m. The lines are a guide to the eye.

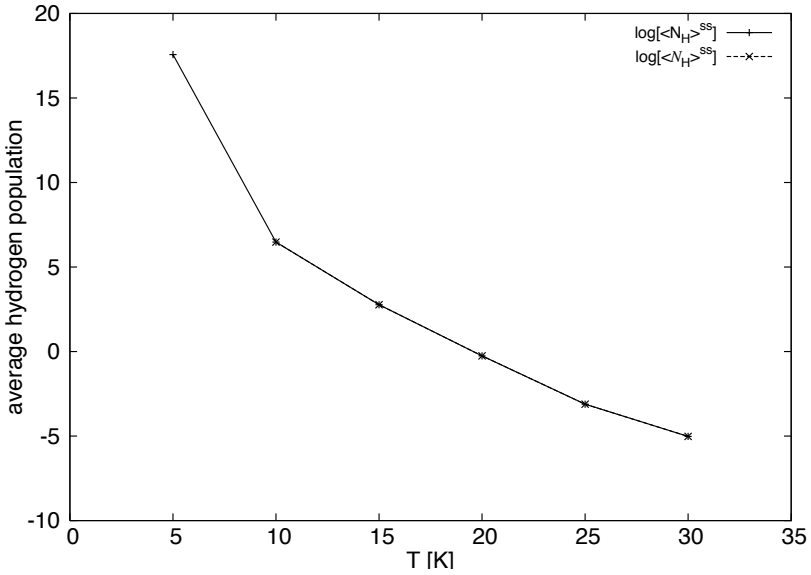

Figure 3.28: Dependence of the average hydrogen population on the grain surface temperature T according to the mean-field framework, $\langle N_H \rangle^{ss}$, and the stochastic framework, $\langle \mathcal{N}_H \rangle^{ss}$, generated from the M2 data for a grain made of amorphous carbon and a grain diameter of $d_2 := 5 \times 10^{-7}$m. The lines are a guide to the eye.

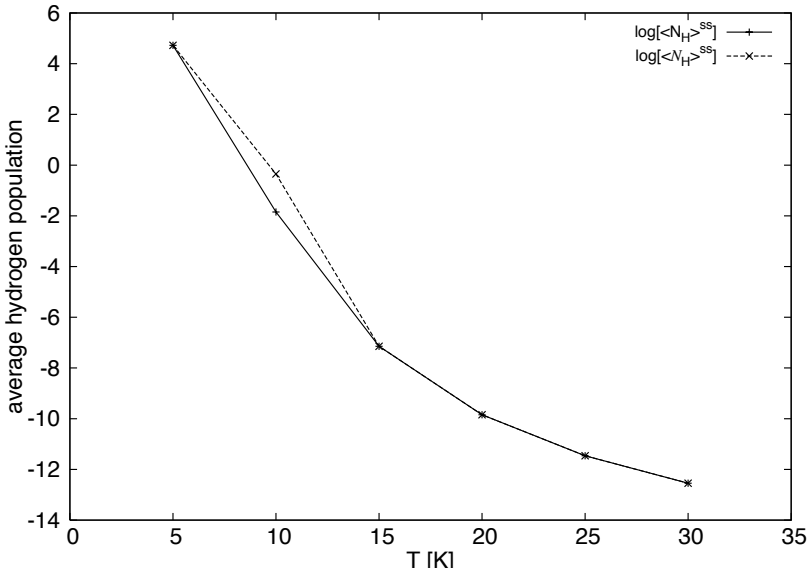

Figure 3.29: Dependence of the average hydrogen population on the grain surface temperature T according to the mean-field framework, $\langle N_H \rangle^{ss}$, and the stochastic framework, $\langle \mathcal{N}_H \rangle^{ss}$, generated from the M2 data for a grain made of olivine and a grain diameter of $d_1 := 1 \times 10^{-8}$m. The lines are a guide to the eye.

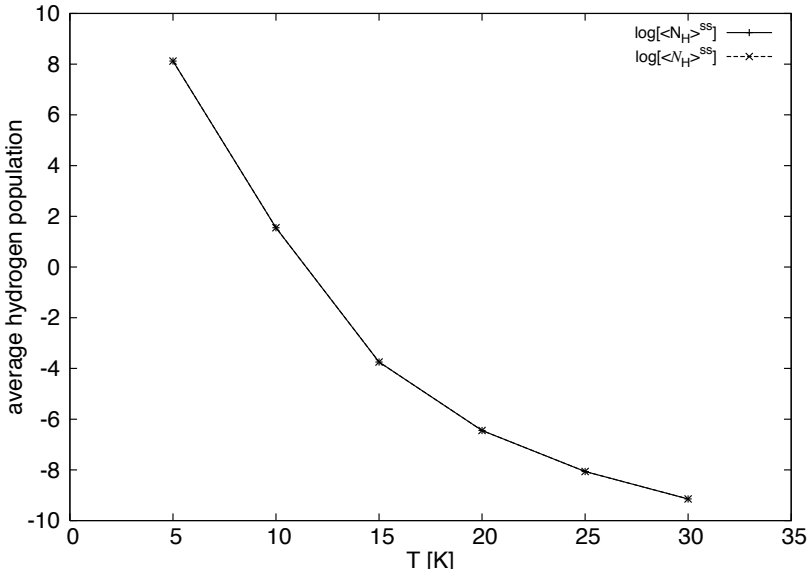

Figure 3.30: Dependence of the average hydrogen population on the grain surface temperature T according to the mean-field framework, $\langle N_H \rangle^{ss}$, and the stochastic framework, $\langle \mathcal{N}_H \rangle^{ss}$, generated from the M2 data for a grain made of olivine and a grain diameter of $d_2 := 5 \times 10^{-7}$m. The lines are a guide to the eye.

3.4.2 Comparison between Mean-Field Dynamical And Stochastic Dynamical Solutions

In this part of the thesis, we compare solutions to the full evolution equations in the mean-field framework

$$\frac{\mathrm{d}}{\mathrm{d}t}\langle N_A(t)\rangle + 2K_{AA}\langle N_A(t)\rangle^2 + L_A\langle N_A(t)\rangle - J_A = 0, \tag{3.205}$$

to the results of the stochastic dynamical formalism

$$\langle\bar{\Phi}_A(t)\rangle = \frac{\int \mathrm{D}\eta\bar{\Phi}_A(t)P[\eta(t)]}{\int \mathrm{D}\eta P[\eta(t)]}, \tag{3.206}$$

with the stochastic constraint equation

$$\frac{\mathrm{d}}{\mathrm{d}t}\bar{\Phi}_A(t) + 2K_{AA}\bar{\Phi}_A^2(t) + L_A\bar{\Phi}_A(t) - J_A - \mathrm{i}\sqrt{2K_{AA}}\bar{\Phi}_A(t)\eta(t) = 0. \tag{3.207}$$

Furthermore, we confront the stochastic steady state solutions

$$\langle\mathcal{N}_A\rangle^{ss} = \begin{cases} \frac{1}{2}\left(1-\frac{L_A}{K_{AA}}\right) + \sqrt{\frac{J_A}{2K_{AA}}}\frac{I_{2-\frac{L_A}{K_{AA}}}\left(\sqrt{\frac{8J_A}{K_{AA}}}\right)}{I_{1-\frac{L_A}{K_{AA}}}\left(\sqrt{\frac{8J_A}{K_{AA}}}\right)} =: \langle\mathcal{N}_A\rangle^{ss}_{L_AK_{AA}^{-1}<1} & : \quad L_AK_{AA}^{-1} < 1 \\ \sqrt{\frac{J_A}{2K_{AA}}}\frac{I_{\frac{L_A}{K_{AA}}}\left(\sqrt{\frac{8J_A}{K_{AA}}}\right)}{I_{\frac{L_A}{K_{AA}}-1}\left(\sqrt{\frac{8J_A}{K_{AA}}}\right)} =: \langle\mathcal{N}_A\rangle^{ss}_{L_AK_{AA}^{-1}\geq 1} & : \quad L_AK_{AA}^{-1} \geq 1 \end{cases}. \tag{3.208}$$

with the late-time values of the stochastic dynamical solutions, $\langle\bar{\Phi}_A(t_\infty)\rangle_{1000}$.

We proceed by employing the values for the rate coefficients as given by the M1 model data for the heterogeneous chemical reaction of two hydrogen atoms —see Table 3.8. For the initial value $\bar{\Phi}_H(0) = 0$ we generate solutions to the first constraint equation for the hydrogen reaction partners in zero space dimensions for different values of the source rate J_H in the range of $[10^8\mathrm{s}^{-1}, 10^{-8}\mathrm{s}^{-1}]$ and compute the path integral average $\langle\bar{\Phi}_H(t)\rangle_{1000}$ according to (2.64). We compare the late-time results to the solutions of the mean-field dynamical equations $\langle N_H(t_\infty)\rangle$ at late times t_∞ for the initial conditions $\langle N_H(0)\rangle = 0$ and the stochastic steady state value for the average hydrogen population $\langle\mathcal{N}_A\rangle^{ss}$ —see Table 3.18 for a grain surface temperature of $T = 10$K, Table 3.19 for a grain surface temperature of $T = 15$K and Table 3.20 for a grain surface temperature of $T = 20$K. We find that the late-time average number of hydrogen atoms, $\langle N_H(t_\infty)\rangle$, corresponds —within numerical errors— to the average

number of hydrogen atoms as obtained from the stationary mean-field equations, $\langle N_H \rangle^{ss}$. The results of the latter section are reproduced, that is, the numerical exploitation of the Doi-Peliti formalism delivers the same value for the mean hydrogen population as the exact stochastic steady state solution. Therefore, all conclusions from the latter section apply.

The M2 model data —see Tables — are used to compare the late-time average hydrogen population according to the dynamical mean-field expression $\langle N_H(t_\infty) \rangle$, the late-time average hydrogen population according to the stochastic dynamical expression $\langle \bar{\Phi}_A(t_\infty) \rangle_{1000}$ and the stochastic steady state value $\langle \mathcal{N}_A \rangle^{ss}$. In Table 3.21 we consider grain particles made of amorphous carbon with a diameter of $d_1 = 10^{-8}$m in a temperature range of $T \in [5\text{K}, 30\text{K}]$, and in Table 3.22 we analyse the average hydrogen population on a grain under the same conditions yet for a smaller size of the seed, namely, $d_2 = 5 \times 10^{-7}$m. We summarise the outcome of our numerical investigations for the average hydrogen population in Table 3.23 for olivine seeds of size $d_1 = 10^{-8}$m in a temperature range of $T \in [5\text{K}, 30\text{K}]$ and in Table 3.24 for the smaller size of $d_2 = 5 \times 10^{-7}$m. Again, the results obtained from the Doi-Peliti formalism coincide with the results that stem from the stochastic steady state calculations. In addition, we have listed the values of the transient time. One observes in both, the mean-field and the Doi-Peliti framework, that the transient time decreases for increasing temperature and that they are of the same order of magnitude in both dynamical models. The transient time does not seem to be affected by the size of the seed. However, it takes longer for the average hydrogen population on a grain made of amorphous carbon to reach equilibrium than on an olivine seed.

J_H [s^{-1}]	$\langle N_H \rangle^{ss} = \langle N_H(t_\infty) \rangle$	$\langle \mathcal{N}_H \rangle^{ss}_{L_H/K_{HH}<1}$	$\langle \bar{\Phi}_H(t_\infty) \rangle_{1000}$
10^8	3.131121×10^1	3.14470×10^1	3.143×10^1
10^7	9.901475×10^0	1.003890×10^1	1.003×10^1
10^6	3.131121×10^0	3.264278×10^0	3.26×10^0
10^5	9.901475×10^{-1}	1.149676×10^0	1.15×10^0
10^4	3.131121×10^{-1}	5.922002×10^{-1}	5.9×10^{-1}
10^3	9.901474×10^{-2}	5.097404×10^{-1}	5.0×10^{-1}
10^2	3.131121×10^{-2}	5.009797×10^{-1}	5.0×10^{-1}
10^1	9.901466×10^{-3}	5.000980×10^{-1}	5.0×10^{-1}
10^0	3.131112×10^{-3}	5.000098×10^{-1}	5.0×10^{-1}
10^{-1}	9.901382×10^{-4}	5.000010×10^{-1}	5.0×10^{-1}
10^{-2}	3.131028×10^{-4}	5.000001×10^{-1}	5.0×10^{-1}
10^{-3}	9.901544×10^{-5}	5.0×10^{-1}	5.0×10^{-1}
10^{-4}	3.130190×10^{-5}	5.0×10^{-1}	5.0×10^{-1}
10^{-5}	9.892166×10^{-6}	5.0×10^{-1}	5.0×10^{-1}
10^{-6}	3.121821×10^{-6}	5.0×10^{-1}	5.0×10^{-1}
10^{-7}	9.808776×10^{-7}	5.0×10^{-1}	5.0×10^{-1}
10^{-8}	3.039369×10^{-7}	5.0×10^{-1}	5.0×10^{-1}

Table 3.18: Dependence of the mean-field steady state values $\langle N_H \rangle^{ss}$ and the late-time mean-field values $\langle N_H(t_\infty) \rangle$, the stochastic steady state values $\langle \mathcal{N}_H \rangle^{ss}_{L_H/K_{HH}<1}$, and the stochastic late-time values $\langle \bar{\Phi}_H(t_\infty) \rangle_{1000}$ averaged over 1000 paths of the average hydrogen population on the source rate J_H at a grain surface temperature of $T = 10$K for the evaporation coefficient $L_H = 1.9 \times 10^{-3}\text{s}^{-1}$ and $K_{HH} = 5.1 \times 10^4\text{s}^{-1}$, and for the initial condition $\bar{\Phi}_H(0) = 0$.

J_H [s^{-1}]	$\langle N_H \rangle^{ss} = \langle N_H(t_\infty) \rangle$	$\langle \mathcal{N}_H \rangle^{ss}_{L_H/K_{HH}<1}$	$\langle \bar{\Phi}_H(t_\infty) \rangle_{1000}$
10^8	3.015013×10^1	3.027591×10^1	3.028×10^1
10^7	9.533626×10^0	9.661124×10^0	9.66×10^0
10^6	3.014114×10^0	3.147523×10^0	3.15×10^0
10^5	9.524631×10^{-1}	1.112557×10^0	1.11×10^0
10^4	3.005130×10^{-1}	5.840125×10^{-1}	5.8×10^{-1}
10^3	9.435150×10^{-2}	5.070542×10^{-1}	5.1×10^{-1}
10^2	2.916771×10^{-2}	4.989104×10^{-1}	5.0×10^{-1}
10^1	8.586923×10^{-3}	4.980911×10^{-1}	5.0×10^{-1}
10^0	2.176619×10^{-3}	4.980091×10^{-1}	5.0×10^{-1}
10^{-1}	3.816986×10^{-4}	4.980009×10^{-1}	5.0×10^{-1}
10^{-2}	4.446594×10^{-5}	4.98×10^{-1}	5.0×10^{-1}
10^{-3}	4.535171×10^{-6}	4.98×10^{-1}	5.0×10^{-1}
10^{-4}	4.544422×10^{-7}	4.98×10^{-1}	5.0×10^{-1}
10^{-5}	4.545351×10^{-8}	4.98×10^{-1}	5.0×10^{-1}
10^{-6}	4.545444×10^{-9}	4.98×10^{-1}	5.0×10^{-1}
10^{-7}	4.545453×10^{-10}	4.98×10^{-1}	5.0×10^{-1}
10^{-8}	4.545454×10^{-11}	4.98×10^{-1}	5.0×10^{-1}

Table 3.19: Dependence of the mean-field steady state values $\langle N_H \rangle^{ss}$ and the late-time mean-field values $\langle N_H(t_\infty) \rangle$, the stochastic steady state values $\langle \mathcal{N}_H \rangle^{ss}_{L_H/K_{HH}<1}$, and the stochastic late-time values $\langle \bar{\Phi}_H(t_\infty) \rangle_{1000}$ averaged over 1000 paths of the average hydrogen population on the source rate J_H at a grain surface temperature of $T = 15$K for the evaporation coefficient $L_H = 2.2 \times 10^2 \text{s}^{-1}$ and $K_{HH} = 5.5 \times 10^4 \text{s}^{-1}$, and for the initial condition $\bar{\Phi}_H(0) = 0$.

J_H [s^{-1}]	$\langle N_H \rangle^{ss} = \langle N_H(t_\infty) \rangle$	$\langle \mathcal{N}_H \rangle^{ss}_{lit} \equiv \langle \mathcal{N}_H \rangle^{ss}_{L_H/K_{HH} \geq 1}$	$\langle \bar{\Phi}_H(t_\infty) \rangle_{stochastic}$
10^8	2.627447×10^1	2.639787×10^1	2.640×10^1
10^7	8.131883×10^0	8.251781×10^1	8.25×10^1
10^6	2.402748×10^0	2.511409×10^0	2.51×10^0
10^5	6.156689×10^{-1}	6.856860×10^{-1}	6.9×10^{-1}
10^4	1.102992×10^{-1}	1.185992×10^{-1}	1.2×10^{-1}
10^3	1.301273×10^{-2}	1.316339×10^{-2}	1.32×10^{-2}
10^2	1.329984×10^{-3}	1.331607×10^{-3}	1.33×10^{-3}
10^1	1.332997×10^{-4}	1.333160×10^{-4}	1.33×10^{-4}
10^0	1.33330×10^{-5}	1.333316×10^{-5}	1.33×10^{-5}
10^{-1}	1.333330×10^{-6}	1.333332×10^{-6}	1.33×10^{-6}
10^{-2}	1.333330×10^{-7}	1.333333×10^{-7}	1.33×10^{-7}
10^{-3}	1.333333×10^{-8}	1.333333×10^{-8}	1.33×10^{-8}
10^{-4}	1.333333×10^{-9}	1.333333×10^{-9}	1.33×10^{-9}
10^{-5}	1.333333×10^{-10}	1.333333×10^{-10}	1.33×10^{-10}
10^{-6}	1.333333×10^{-11}	1.333333×10^{-11}	1.33×10^{-11}
10^{-7}	1.333333×10^{-12}	1.333333×10^{-12}	1.33×10^{-12}
10^{-8}	1.333333×10^{-13}	1.333333×10^{-13}	1.33×10^{-13}

Table 3.20: Dependence of the mean-field steady state values $\langle N_H \rangle^{ss}$ and the late-time mean-field values $\langle N_H(t_\infty) \rangle$, the stochastic steady state values $\langle \mathcal{N}_H \rangle^{ss}_{L_H/K_{HH} \geq 1}$, and the stochastic late-time values $\langle \bar{\Phi}_H(t_\infty) \rangle_{1000}$ averaged over 1000 paths of the average hydrogen population on the source rate J_H at a grain surface temperature of $T = 20$K for the evaporation coefficient $L_H = 7.5 \times 10^4 \text{s}^{-1}$ and $K_{HH} = 7.1 \times 10^4 \text{s}^{-1}$, and for the initial condition $\bar{\Phi}_H(0) = 0$.

T [K]	$\langle N_H(t_\infty)\rangle$	$\langle \mathcal{N}_H(t_\infty)\rangle$	$\langle \mathcal{N}_H\rangle^{ss}$	$t_{transient}$ [s]
5	1.484102×10^{14}	1.4841×10^{14}		10^{20}
10	1.189164×10^{3}	1.1891×10^{3}	1.189289×10^{3}	10^{9}
15	2.357184×10^{-1}	5.5×10^{-1}	5.503949×10^{-1}	10^{6}
20	2.204525×10^{-4}	4.5×10^{-1}	4.488392×10^{-1}	10^{3}
25	3.072772×10^{-7}	2.7×10^{-1}	2.774179×10^{-1}	10^{0}
30	3.822938×10^{-9}	3.8×10^{-9}	3.822938×10^{-9}	10^{-2}

Table 3.21: Dependence of the late-time average hydrogen population on the grain surface temperature T according to the dynamical mean-field expression $\langle N_H(t_\infty)\rangle$, compared to the late-time average hydrogen population according to the stochastic dynamical values $\langle \mathcal{N}_H(t_\infty)\rangle$ and the stochastic steady state solution $\langle \mathcal{N}_H\rangle^{ss}$ for a grain diameter of $d_1 := 10^{-8}$m and a seed surface made of amorphous carbon and the transient time $t_{transient}$.

T [K]	$\langle N_H(t_\infty)\rangle$	$\langle \mathcal{N}_H(t_\infty)\rangle$	$\langle \mathcal{N}_H\rangle^{ss}$	$t_{transient}$ [s]
5	3.710183×10^{17}	3.71018×10^{17}		10^{20}
10	2.973205×10^{6}	2.97321×10^{6}	2.973205×10^{6}	10^{9}
15	5.893975×10^{2}	5.893×10^{2}	5.895203×10^{2}	10^{6}
20	5.511317×10^{-1}	5.5106×10^{-1}	5.511408×10^{-1}	10^{3}
25	7.681930×10^{-4}	7.682×10^{-4}	7.68193×10^{-4}	10^{0}
30	9.557344×10^{-6}	9.56×10^{-6}	9.557344×10^{-6}	10^{-2}

Table 3.22: Dependence of the late-time average hydrogen population on the grain surface temperature T according to the dynamical mean-field expression $n_H(t_\infty)$, compared to the late-time average hydrogen population according to the stochastic dynamical values $\langle N_H(t_\infty)\rangle$ and the stochastic steady state solution $\langle N_H\rangle^{ss}$ for a grain diameter of $d_2 := 5 \times 10^{-7}$m and a seed surface made of amorphous carbon and the transient time $t_{transient}$.

T [K]	$\langle N_H(t_\infty)\rangle$	$\langle \mathcal{N}_H(t_\infty)\rangle$	$\langle \mathcal{N}_H\rangle^{ss}$	$t_{transient}$ [s]
5	5.300904×10^{4}	5.30091×10^{4}	5.300916×10^{4}	10^{11}
10	1.424297×10^{-2}	4.5×10^{3}	4.475233×10^{-1}	10^{5}
15	7.183817×10^{-8}	7.2×10^{-8}	7.183817×10^{-8}	10^{-1}
20	1.433782×10^{-10}	1.4×10^{-10}	1.433782×10^{-10}	10^{-3}
25	3.439952×10^{-12}	3.4×10^{-12}	3.439952×10^{-12}	10^{-5}
30	2.861446×10^{-13}	2.85×10^{-13}	2.861446×10^{-13}	10^{-6}

Table 3.23: Dependence of the late-time average hydrogen population on the grain surface temperature T according to the dynamical mean-field expression $\langle N_H(t_\infty)\rangle$, compared to the late-time average hydrogen population according to stochastic dynamical values $\langle \mathcal{N}_H(t_\infty)\rangle$ and the stochastic steady state solution $\langle \mathcal{N}_H\rangle^{ss}$ for a grain diameter of $d_1 := 10^{-8}$m and a seed surface made of olivine and the transient time $t_{transient}$.

T [K]	$\langle N_H(t_\infty)\rangle$	$\langle \mathcal{N}_H(t_\infty)\rangle$	$\langle \mathcal{N}_H\rangle^{ss}$	$t_{transient}$ [s]
5	1.325226×10^{8}	1.32523×10^{8}	1.325226×10^{8}	10^{11}
10	3.560795×10^{1}	3.5632×10^{1}	3.562303×10^{1}	10^{5}
15	1.795954×10^{-4}	1.796×10^{-4}	1.795954×10^{-4}	10^{0}
20	3.584455×10^{-7}	3.584×10^{-7}	3.584455×10^{-7}	10^{-3}
25	8.599879×10^{-9}	8.6×10^{-9}	8.599879×10^{-9}	10^{-4}
30	7.153614×10^{-10}	7.154×10^{-10}	7.153614×10^{-10}	10^{-6}

Table 3.24: Dependence of the late-time average hydrogen population on the grain surface temperature T according to the dynamical mean-field expression $\langle N_H(t_\infty)\rangle$, compared to the late-time average hydrogen population according to the stochastic dynamical values $\langle \mathcal{N}_H(t_\infty)\rangle$ and the stochastic steady state solution $\langle \mathcal{N}_H\rangle^{ss}$ for a grain diameter of $d_2 := 5 \times 10^{-7}$m and a seed surface made of olivine compared to the stochastic steady state solution $\langle N_H^{ss}\rangle$ and the transient time $t_{transient}$.

3.4.3 Stochastic Gauge Representation

According to [25] and [17], in the numerical evaluation of the constraint equations possible systematic errors may occur. In the language of the Positive P representation —see the end of the latter chapter— these problems arise due to the presence of boundary term errors that occur in the derivation of the stochastic constraint equations from the Positive P representation based on the same master equation as employed in the Doi-Peliti formalism. Unfortunately, there are no rigorous results on these instabilities. The author of [14] defines four classes of indications for boundary term errors: Moving Singularities, Noise Divergences, Discontinuous Drift, and Broadness of Initial Distribution. In the sequel, we will concentrate on the first two. In deterministic equations, moving singularities are detected when solutions diverge in a finite time. When moving singularities are present in the drift term of the stochastic differential equation, boundary term errors seem to occur [17, 25]. Noise divergences are instabilities in the diffusion term and systematic errors result by an analogous mechanism as for instabilities of the drift terms. Moving singularities or noise divergences do not occur provided that the limits

$$\begin{aligned} &\lim_{|\Phi_A|\to\infty} \frac{a[\Phi_A]}{|\Phi_A|}, \\ &\lim_{|\Phi_A|\to\infty} \frac{b[\Phi_A]}{|\Phi_A|}, \end{aligned} \tag{3.209}$$

converge for $\Phi_A \in \mathbb{C}$. The functional a is the drift coefficient and the functional b the diffusion coefficient as given in (3.170). The first constraint equation (3.168) for the path integral average in the Doi-Peliti formalism does not fulfill the conditions for the absence of moving singularities or noise divergences as defined in [14]. According to [17] accumulating errors could occur due to occasional excursions of single trajectories into the negative half-space. After having made a large loop to large negative values of the real part of a solution to the stochastic differential equation, the trajectories return almost immediately to large positive values of the real part of a solution. These loops are predicted to distort the averages and to cause a systematic error that sometimes is non-negligible.

In [17], a way of minimising these accumulating errors is presented, namely Stochastic Gauge methods. The introduction of an extra variable is used to stabilise the stochastic differential equations accepting the draw-back of introducing an additional stochastic differential equation in the new variable. Sampling errors are estimated and controlled by the choice of gauge and by increasing the number of realisations of the noise over

which the average is taken. In general, they have

$$\begin{aligned}
&\frac{\mathrm{d}\Upsilon}{\mathrm{d}t} = \Upsilon g_i[\hat{\Phi}_k(t)]\eta_i(t), \\
&\frac{\mathrm{d}\hat{\Phi}_j(t)}{\mathrm{d}t} = a_j[\hat{\Phi}_k(t)] + b_{ji}[\hat{\Phi}_k(t)]\Big(\eta_i(t) - g_i[\hat{\Phi}_k(t)]\Big),
\end{aligned} \tag{3.210}$$

where Υ is the new complex Gauge variable, g_k are the components of the complex Gauge functional, a_k the components of the drift coefficient vector, b_{kl} the components of the diffusion coefficient matrix and η_k are white, Gaussian noises satisfying

$$\begin{aligned}
&\langle \eta_k(t) \rangle_{\mathcal{P}[\eta]} = 0, \\
&\langle \eta_i(t)\eta_j(t') \rangle_{\mathcal{P}[\eta]} = \delta_{ij}\delta(t - t').
\end{aligned} \tag{3.211}$$

The Gauge variable Υ has to satisfy the following conditions:

$$\begin{aligned}
&\Upsilon(0) = 1, \\
&\langle \Upsilon(t) \rangle_{\mathcal{P}[\eta]} = 1, \\
&\langle \mathrm{d}\Upsilon(t) \rangle_{\mathcal{P}[\eta]} = 0.
\end{aligned} \tag{3.212}$$

The average population of the chemical reactants in the Stochastic Gauge Theory, $\langle . \rangle_{SG}$, is then calculated via

$$\langle \hat{\Phi}_A(t) \rangle_{SG} := \langle \Upsilon(t)\hat{\Phi}_A(t) \rangle \equiv \langle \bar{\Phi}_A(t) \rangle, \tag{3.213}$$

where the latter average is the standard path integral average, (3.206), with solutions to the constraint equations (3.207). In [17], three possible choices for the Gauge functional are presented: namely, the Amplitude Gauge:

$$g_A := \mathrm{i}\sqrt{2K_{AA}}\Big(\hat{\Phi}_A(t) - |\hat{\Phi}_A(t)|\Big); \tag{3.214}$$

the Phase Gauge:

$$g_P := \mathrm{i}\sqrt{2K_{AA}}\Big(\Re\big(\hat{\Phi}_A(t)\big) - |\hat{\Phi}_A(t)|\Big); \tag{3.215}$$

and the Step Gauge:

$$g_S := \mathrm{i}\sqrt{8K_{AA}}\Re\big(\hat{\Phi}_A(t)\big)\Theta(-\Re\big(\hat{\Phi}_A(t)\big)), \tag{3.216}$$

where Θ is the *Heaviside step function*[17]. This leads to the modified versions of the first constraint equation (3.168) for vanishing source rate in the Amplitude Gauge:

$$\frac{\mathrm{d}}{\mathrm{d}t}\hat{\Phi}_A(t) + 2K_{AA}\hat{\Phi}_A(t)|\hat{\Phi}_A(t)| + L_A\hat{\Phi}_A(t) - J_A - \mathrm{i}\sqrt{2K_{AA}}\hat{\Phi}_A(t)\eta(t) = 0; \tag{3.218}$$

in the Phase Gauge:

$$\frac{\mathrm{d}}{\mathrm{d}t}\hat{\Phi}_A(t) + 2K_{AA}\hat{\Phi}_A(t)|\hat{\Phi}_A(t)| + 2\mathrm{i}K_{AA}\hat{\Phi}_A(t)\Im\big(\hat{\Phi}_A(t)\big) + L_A\hat{\Phi}_A(t) - J_A - \mathrm{i}\sqrt{2K_{AA}}\hat{\Phi}_A(t)\eta(t) = 0; \tag{3.219}$$

and in the Step Gauge:

$$\frac{\mathrm{d}}{\mathrm{d}t}\hat{\Phi}_A(t) + 2K_{AA}\hat{\Phi}_A(t)|\Re\big(\hat{\Phi}_A(t)\big)| + 2\mathrm{i}K_{AA}\hat{\Phi}_A(t)\Im\big(\hat{\Phi}_A(t)\big) + L_A\hat{\Phi}_A(t) - J_A - \mathrm{i}\sqrt{2K_{AA}}\hat{\Phi}_A(t)\eta(t) = 0. \tag{3.220}$$

The authors of [12] argue that —for their particular choice of parameters— the specific value of one half for the averaged stochastic solution in the late-time limit arises from the fact that the master equation leaves the subspaces of even $\{N_A\}$ and odd $\{N_A\}$ invariant. Their claim is that the excursion of a trajectory to large real values of a solution to the stochastic constraint equations is close to an even or odd number of chemical reactants with the same probability. The total probability is redistributed equally over both invariant subspaces. The latter argument is a valid one since, indeed, —as we have seen in the subsection concerned with the derivation of the stochastic steady state solutions to the full master equation,

$$P_{even} = P_{odd} \equiv \frac{1}{2}. \tag{3.221}$$

In this regard, the result for the stochastic steady state solution as presented in this thesis is consistent with the observation made in the numerical calculations in both the Doi-Peliti formalism as well as in the Positive P representation. The above line of argument, however, is not the correct explanation why the average number of A molecules takes exactly the value of one half. In fact, the value of one half is only the result for a specific set of parameters as can be seen from Table 3.25. The values

[17]The Heaviside step function in its generalised form is defined via

$$\int \Theta(z)\frac{\mathrm{d}h(z)}{\mathrm{d}z}\mathrm{d}z = -h(0), \tag{3.217}$$

for a sufficiently smooth function $h(z)$ with sufficiently quick decay.

J [s^{-1}]	$\langle \mathcal{N}_A \rangle^{ss}_{L_A/K_{AA} \geq 1}$	$\langle \mathcal{N}_A \rangle^{ss}_{L_A/K_{AA} < 1}$	$\langle \bar{\Phi}_A \rangle_{1000}(t_\infty)$
10^2	1.00763×10^1	1.00763×10^1	1.007×10^1
10^1	3.24148	3.24148	3.24
10^0	1.09201	1.09289	1.09
10^{-1}	4.06934×10^{-1}	5.03211×10^{-1}	5.0×10^{-1}
10^{-2}	8.58964×10^{-2}	4.11024×10^{-1}	4.1×10^{-1}
10^{-3}	9.83631×10^{-3}	4.01110×10^{-1}	4.0×10^{-1}
10^{-4}	9.98336×10^{-4}	4.00111×10^{-1}	4.0×10^{-1}

Table 3.25: Comparison between the stochastic steady state solution $\langle \mathcal{N}_A \rangle^{ss}_{L_A/K_{AA} \geq 1}$ according to (3.103), the stochastic steady state solution $\langle \mathcal{N}_A \rangle^{ss}_{L_A/K_{AA} < 1}$ according to (3.115) and the late-time value of the mean stochastic dynamical solution averaged over 1000 realisations of the path $\langle \bar{\Phi}_A \rangle_{1000}(t_\infty)$ according to (2.64) for $L_A = 0.1\text{s}^{-1}$ and $K_{AA} = 0.5\text{s}^{-1}$ and varying source rate J_A.

$J_A = 0.1\text{s}^{-1}$, $L_A = 0.1\text{s}^{-1}$ and $K_{AA} = 0.5\text{s}^{-1}$ were employed in article [17]. The limit for fixed reaction rate coefficient and a source rate coefficient approaching zero of the stochastic steady state solution presented in this thesis is given by

$$\lim_{J_A \to 0} \langle N_A^{ss} \rangle_{L_A K_{AA}^{-1} < 1} = \frac{1}{2} \left(1 - \frac{L_A}{K_{AA}} \right) = 0.4. \tag{3.222}$$

We do not claim stability for the stochastic constraint equations under all circumstances. In our calculations, we have observed the excursion of particular paths with very high spikes that caused an explosion of the path in finite time. These paths, however, could be identified by inspection and were excluded from the rest of the calculations. We still would like to point out that the argument that the numerical evaluation of the stochastic constraint equations had to be altered by means of stochastic gauge methods in order to obtain results consistent with the stochastic steady state solution is not valid. The numerical results that stem from the unaltered stochastic constraint equations do not coincide with the evaluation of the stochastic steady state solution as presented in the standard literature yet they coincide with the evaluation of the stochastic steady state solution as presented in this thesis. Since $L_A K_{AA}^{-1} = 0.2 < 1$, solution $\langle \mathcal{N}_A \rangle^{ss}_{L_A/K_{AA} < 1}$ is the correct stochastic steady state solution to compare the stochastic late-time value of the dynamical calculations with. Furthermore, the leading order term in the expansion of the stochastic steady state solution for small $J_A K_{AA}^{-1}$ is indeed $0.5(1 - L_A K_{AA}^{-1}) = 0.4$ which corresponds to the results presented in Table 3.25.

3.5 Conclusions and Outlook

In this chapter we analysed the late-time behaviour of solutions to the mean-field rate equations describing the evolution of the mean number of reactants and reactions products involved in a heterogeneous chemical reaction of type $A + A \rightarrow C$. We revised the steady state solution to a stationary master equation that replaces the set of mean-field evolution equations in order to take statistical fluctuations into account. We found that the exact solution as presented in the standard literature was of limited validity and an exact solution to the stationary master equation was derived for the subspace of the parameter space where the commonly used steady state solution does not apply. In our numerical calculations we concentrated on chemical reactions taking place on the surface of interstellar dust particles. We compared the mean-field steady state solution, the solution to the mean-field evolution equations, and the stochastic steady state solution for two sets of model data and investigated the dependence of the mean reactant population on the adsorption rate as well as on the surface grain temperature. Furthermore, we confronted the predictions for the mean number of reactants present on the surface of the seed as given by the Doi-Peliti formalism, which is a stochastic framework for the dynamics of certain populations, with the results obtained in the mean-field framework. We explored the parameter space, that is, the space for the adsorption rate coefficient, desorption rate coefficient and reaction rate coefficient, in order to identify the threshold between the deterministic regime and the stochastic regime. In addition, we found in our numerical simulations that the consistency between the corrected stochastic steady state solution and the late-time value of the stochastic dynamical solution is remarkable.

However, an alternative derivation for the production rate of the chemical species C for a specific subspace of the parameter space is still outstanding since the commonly used way of calculating the production rate is not consistent under certain circumstances. Since it is nearly impossible to make any statement on the population of chemical reactants or chemical reaction products remaining on the surface of the grain from an observational point of view, the Astrophysics community is especially interested in the recombination rate and the recombination efficiency.

From the numerical calculations it is also clear that the conclusion as to where the threshold between the deterministic regime and the stochastic regime lies in the parameter space is very sensitive to the choice of model data. In order to make a well founded statement it would, therefore, be highly desirable to have more experimental data at hand as well as to develop a more detailed model for the rate coefficients.

In the following chapter, we will extend our previous analysis from considerations of

only a single lattice site to a one-dimensional problem.

Chapter 4

Chemical Surface Reactions of Type $A + A \longrightarrow C$ in One Space Dimension

In this chapter, we expand the calculations based on the Doi-Peliti formalism from a model on a single spatial lattice site to a model in one space dimension for which we have to adapt the rate coefficients available in the literature and to develop further the numerical code. We impose simple boundary conditions on the grain particle which are, nevertheless, a good approximation for a realistic interstellar dust particle. In the same fashion as in the previous chapter we undertake numerical investigations by comparing the predictions that stem from mean-field theory to the results arising from the stochastic framework. We explore the parameter space and investigate the behaviour of the late-time value of the average reactant density on the surface of the grain in dependence of the size of the seed and in dependence of the diffusion rate coefficient.

4.1 Constraint Equations in One Space Dimension

We start our investigations by comparing the stochastic ordinary differential equations that appear as constraint equations in the Doi-Peliti formalism in zero space dimensions to the equivalent stochastic partial differential equations in one space dimension. The rate coefficients are adapted with respect to the particular choice of geometry of the grain particle.

Quantity	SI units
eigenvalue function of coherent state: $\bar{\Phi}_A(t)$	1
reaction rate coefficient: K_{AA}	s^{-1}
evaporation rate coefficient: L_A	s^{-1}
source rate coefficient: J_A	s^{-1}
stochastic noise: $\eta(t)$	$\mathrm{s}^{-\frac{1}{2}}$
Wiener process: $W(t)$	$\mathrm{s}^{\frac{1}{2}}$

Table 4.1: Dimensionality of the quantities employed in the stochastic constraint equation in zero space dimensions (4.1).

4.1.1 Comparison between Stochastic Constraints in Zero and One Space Dimensions

First, let us recall the form of the stochastic constraint equations in zero space dimensions. The stochastic ordinary differential equation that constrains the complex fluctuating field $\Phi_A(t)$ associated with the reaction partners A at a single lattice point reads

$$\frac{\mathrm{d}}{\mathrm{d}t}\bar{\Phi}_A(t) + 2K_{AA}\bar{\Phi}_A^2(t) + L_A\bar{\Phi}_A(t) - J_A + \mathtt{i}\sqrt{2K_{AA}}\bar{\Phi}_A(t)\eta(t) = 0, \tag{4.1}$$

where the stochastic noise is determined by the following statistical properties:

$$\langle\eta(t)\rangle_{\mathcal{P}[\eta]} = 0, \quad \langle\eta(t)\eta(t')\rangle_{\mathcal{P}[\eta]} = \delta(t-t'), \tag{4.2}$$

where

$$\mathcal{P}[\eta] = e^{-\frac{1}{2}\int \eta^2(t)\mathrm{d}t}. \tag{4.3}$$

For the numerical evaluation it is reasonable to approximate the stochastic noise $\eta(t)$ by the well-defined Wiener process $W(t)$

$$\eta(t) = \frac{\mathrm{d}}{\mathrm{d}t}W(t). \tag{4.4}$$

The SI units of the quantities employed in the stochastic constraint equation (4.1) are listed in Table 4.1. The one-dimensional first stochastic constraint equation is a

Quantity	SI units
eigenvalue function of coherent state: $\bar{\phi}_A(x,t)$	m^{-1}
diffusion rate coefficient: d_A	$\mathrm{m}^2\mathrm{s}^{-1}$
reaction rate coefficient: k_{AA}	ms^{-1}
evaporation rate coefficient: l_A	s^{-1}
source rate coefficient: j_A	$\mathrm{s}^{-1}\mathrm{m}^{-1}$
stochastic noise: $\eta(x,t)$	$\mathrm{s}^{-\frac{1}{2}}\mathrm{m}^{-\frac{1}{2}}$
Wiener process: $w(x,t)$	$\mathrm{m}^{\frac{1}{2}}\mathrm{s}^{\frac{1}{2}}$

Table 4.2: Dimensionality of the quantities employed in the stochastic constraint equation in one space dimensions (4.5).

stochastic partial differential equation, namely,

$$\frac{\partial}{\partial t}\bar{\phi}_A(x,t) - d_A\frac{\partial^2}{\partial x^2}\bar{\phi}_A(x,t) + 2k_{AA}\bar{\phi}_A^2(x,t) + l_A\bar{\phi}_A(x,t) - j_A + \mathtt{i}\sqrt{2k_{AA}}\bar{\phi}_A(x,t)\eta(x,t) = 0, \tag{4.5}$$

where the stochastic noise $\eta(x,t)$ satisfies the following correlations:

$$\langle\eta(x,t)\rangle_{\mathcal{P}[\eta]} = 0, \quad \langle\eta(x,t)\eta(x',t')\rangle_{\mathcal{P}[\eta]} = \delta(x-x')\delta(t-t'), \tag{4.6}$$

with $\mathcal{P}[\eta]$ the Gaussian probability distribution

$$\mathcal{P}[\eta] = e^{-\frac{1}{2}\int\int\eta^2(x,t)\mathrm{d}t\mathrm{d}x}. \tag{4.7}$$

The stochastic noise $\eta(x,t)$ is understood as a derivative of a Wiener process $w(x,t)$ in the following way

$$\eta(x,t) = \frac{\partial^2}{\partial x\partial t}w(x,t). \tag{4.8}$$

Solutions to the stochastic constraint equations (4.5) can be employed to compute the path integral average

$$\langle\phi_A(x,t)\rangle = \frac{\int \mathrm{D}\eta\ \bar{\phi}_A(x,t)\mathcal{P}[\eta]}{\int \mathrm{D}\eta\mathcal{P}[\eta]}. \tag{4.9}$$

The SI units of the quantities in the stochastic constraint equation for one space dimension (4.5) are given in Table 4.2. The Wiener noise $w(x,t)$ corresponds to a Brownian sheet —see Figure 4.1. For completeness, we give the evolution equation for the average

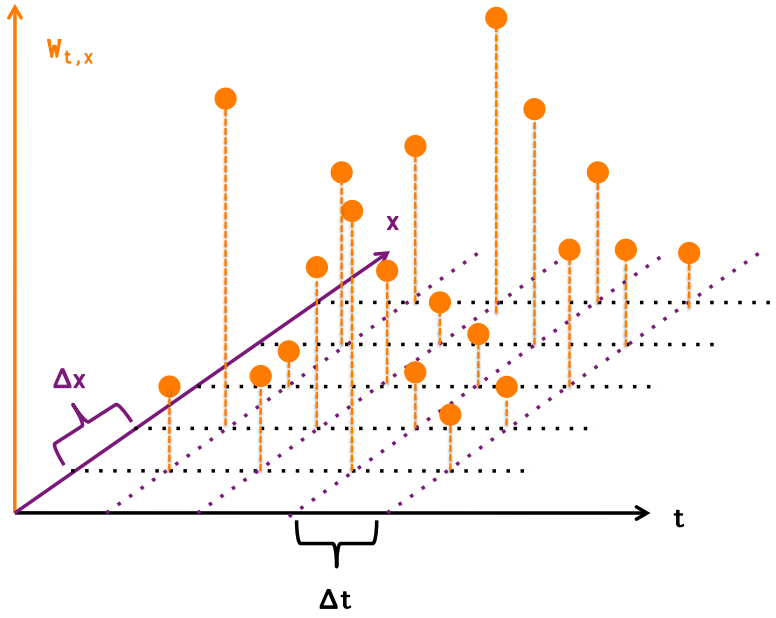

Figure 4.1: Schematic of a Brownian sheet in one space dimension with $\triangle t$ the time increment, $\triangle x$ the space increment and $W_{t,x}$ the Wiener noise.

particle density $\langle n_A(x,t)\rangle$ in the mean-field framework in one space dimension

$$\frac{\partial}{\partial t}\langle n_A(x,t)\rangle - d_A\frac{\partial^2}{\partial x^2}\langle n_A(x,t)\rangle + 2k_{AA}\langle n_A(x,t)\rangle^2 + l_A\langle n_A(x,t)\rangle - j_A = 0. \tag{4.10}$$

4.1.2 Choice of Geometry of the Grain Particle

In the sequel, we neglect the fact that the chemical species have a finite volume and we assume that the atoms or molecules adsorbed onto the grain surface are point particles. Furthermore, we assume that the grain particle is cold, that is $T \in [5\text{K}, 30\text{K}]$. In addition, we impose the condition that all binding sites are equidistant and equivalent which means we allocate the same rate coefficients to all binding sites. The boundary conditions are chosen to be periodic which, in one space dimension, give a ring as the grain particle as illustrated in Figure 4.2. According to the established view[1] on the form of grain particles within the astrochemistry community, the choice of periodic boundary conditions is well justified. Since we make the Ansatz of a smooth surface it follows that the circumference is, indeed, $\mathcal{C} = 2\pi R$ where R is the radius of the

[1]Dr Herma Cuppen: private communication

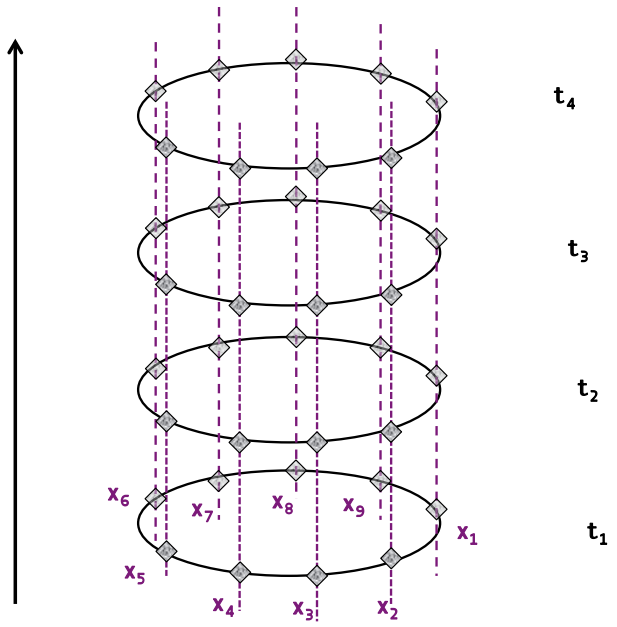

Figure 4.2: Schematic of the discretised grain particle in one space dimension with periodic boundary conditions where the symbols x denote numerical grid points and t the time slices.

ring. Note that even if some of the rate coefficients are in fact microscopic parameters we have to rewrite the expressions for the rate coefficients in terms of macroscopic quantities —including geometrical quantities— in order to be able to assign a specific value to the rate coefficients. The diffusion constant d_A is obtained from rather crude statistical considerations and is defined as the product of the mean velocity of the molecules times the mean free pathway and —for higher space dimensions— has to be divided by the dimension [19]. Accordingly, in one space dimension the diffusion rate coefficient d_A takes the following form:

$$d_A = \frac{(\triangle l)^2}{\triangle t} = \frac{\nu_v \exp\left(-\frac{E_d}{kT}\right)}{4R^2 s^2} \quad [\mathrm{m^2 s^{-1}}], \tag{4.11}$$

where we have used the following properties

$$\begin{aligned}
\triangle l &= \frac{\mathcal{C}}{N_S} \quad [\mathrm{m}], \\
\triangle t &= \frac{t_S}{N_S} \quad [\mathrm{s}], \\
t_S^{-1} &= N_S^{-1} \nu_v \exp\left(-\frac{E_d}{kT}\right) \quad [\mathrm{s}^{-1}], \\
N_S &= 4\pi R^2 s \quad [1].
\end{aligned} \tag{4.12}$$

with $\triangle l$ denoting the lattice constant, N_S the number of binding sites, $\triangle t$ the time increment, t_S the sweeping time with respect to the entire surface, ν_v the vibration frequency, E_d the diffusion barrier, T the temperature of the grain surface and k the Boltzmann constant. In this model, the form of the diffusion rate coefficient does not change for higher space dimensions except for the multiplying factor. The reaction rate coefficient k_{AA} in one space dimension[2] reads

$$k_{AA} = \frac{\triangle l}{\triangle t} \quad [\mathrm{ms}^{-1}], \tag{4.15}$$

or, given in the macroscopic parameters,

$$k_{AA} = \frac{\mathcal{C}}{2}\left(t_S^{-1} + t_S^{-1}\right) = \mathcal{C} K_{AA} \quad [\mathrm{ms}^{-1}]. \tag{4.16}$$

The evaporation rate coefficient l_A in one space dimension does not differ from the evaporation rate coefficient L_A in zero space dimensions

$$l_A = t_E^{-1} \equiv L_A \quad [\mathrm{s}^{-1}], \tag{4.17}$$

whereas the source rate coefficient j_A in one space dimension becomes

$$j_A = \frac{J_A}{\mathcal{C}} \quad [\mathrm{m}^{-1}\mathrm{s}^{-1}], \tag{4.18}$$

[2]The corresponding reaction rate coefficient in two space dimensions is defined via

$$k_{AA}^{(2)} = \frac{(\triangle l)^2}{\triangle t}. \tag{4.13}$$

If, for example, one has a square of lattice points with each side of equal length a and imposing periodic boundary conditions one has that

$$k_{AA}^{(2)} = \frac{a^2 \nu_v \exp\left(-\frac{E_d}{kT}\right)}{4\pi R^2 s}. \tag{4.14}$$

where J_A is the source rate coefficient in zero space dimensions.

In Table 4.3 we recapitulate the values of the evaporation rate coefficients of hydrogen reactants with respect to grain particles made of either olivine or amorphous carbon depending on the value of the temperature T of the surface of the seed. Table 4.4 gives the dependence of the adsorption rate j_H on the grain surface radius R in a hydrogen recombination process. Tables 4.5, 4.6, 4.7, and 4.8 list the reaction rate coefficients and the diffusion rate coefficients in a hydrogen recombination process for specific surface temperatures and for a grain radius of $R = 10^{-9}$m, $R = 10^{-8}$m, $R = 10^{-7}$m, and $R = 10^{-6}$m with regard to an olivine grain surface and a seed surface consisting of amorphous carbon, respectively.

T [K]	$l_H^{olivine}$ [s^{-1}]	l_H^{carbon} [s^{-1}]
5	3.9961×10^{-21}	7.0282×10^{-46}
10	6.321×10^{-5}	2.6511×10^{-17}
15	1.5869×10^{1}	8.891×10^{-8}
20	7.951×10^{3}	5.149×10^{-3}
25	3.314×10^{5}	3.71×10^{0}
30	3.984×10^{6}	2.982×10^{2}

Table 4.3: Dependence of the thermal evaporation rate coefficient l_H on the grain surface temperature T for an olivine grain surface and a seed surface consisting of amorphous carbon in a hydrogen recombination process.

R [m]	j_H [$s^{-1}m^{-1}$]
10^{-9}	7.257×10^{0}
10^{-8}	7.257×10^{1}
10^{-7}	7.257×10^{2}
10^{-6}	7.257×10^{3}

Table 4.4: Dependence of the adsorption rate coefficient j_H on the grain surface radius R in a hydrogen recombination process.

T [K]	$k_{HH}^{olivine}$ [ms^{-1}]	k_{HH}^{carbon} [ms^{-1}]	$d_H^{olivine}$ [m^2s^{-1}]	d_H^{carbon} [m^2s^{-1}]
5	3.186×10^{-23}	4.065×10^{-42}	8.612×10^{-33}	4.009×10^{-51}
10	9.280×10^{-11}	6.332×10^{-20}	2.508×10^{-20}	6.244×10^{-29}
15	1.325×10^{-6}	1.581×10^{-12}	3.582×10^{-16}	1.559×10^{-21}
20	1.584×10^{-4}	7.902×10^{-9}	4.280×10^{-14}	7.793×10^{-18}
25	2.793×10^{-3}	1.309×10^{-6}	7.549×10^{-13}	1.291×10^{-15}
30	1.893×10^{-2}	3.949×10^{-5}	5.115×10^{-12}	3.894×10^{-14}

Table 4.5: Dependence of the reaction rate coefficient k_{HH} and the diffusion rate coefficient d_H on the grain surface temperature T for an olivine grain surface and a seed surface consisting of amorphous carbon in a hydrogen recombination process for a grain particle radius of $R = 10^{-9}$m.

T [K]	$k_{HH}^{olivine}$ [ms^{-1}]	k_{HH}^{carbon} [ms^{-1}]	$d_H^{olivine}$ [m^{2}s^{-1}]	d_H^{carbon} [m^{2}s^{-1}]
5	3.186×10^{-24}	4.065×10^{-43}	8.612×10^{-35}	4.009×10^{-53}
10	9.280×10^{-12}	6.332×10^{-21}	2.508×10^{-22}	6.244×10^{-31}
15	1.325×10^{-7}	1.581×10^{-13}	3.582×10^{-18}	1.559×10^{-23}
20	1.584×10^{-5}	7.902×10^{-10}	4.280×10^{-16}	7.793×10^{-20}
25	2.793×10^{-4}	1.309×10^{-7}	7.549×10^{-15}	1.291×10^{-17}
30	1.893×10^{-3}	3.949×10^{-6}	5.115×10^{-14}	3.894×10^{-16}

Table 4.6: Dependence of the reaction rate coefficient k_{HH} and the diffusion rate coefficient d_H on the grain surface temperature T for an olivine grain surface and a seed surface consisting of amorphous carbon in a hydrogen recombination process for a grain particle radius of $R = 10^{-8}$m.

T [K]	$k_{HH}^{olivine}$ [ms^{-1}]	k_{HH}^{carbon} [ms^{-1}]	$d_H^{olivine}$ [m^{2}s^{-1}]	d_H^{carbon} [m^{2}s^{-1}]
5	3.186×10^{-25}	4.065×10^{-44}	8.612×10^{-37}	4.009×10^{-55}
10	9.280×10^{-13}	6.332×10^{-22}	2.508×10^{-24}	6.244×10^{-33}
15	1.325×10^{-8}	1.581×10^{-14}	3.582×10^{-20}	1.559×10^{-25}
20	1.584×10^{-6}	7.902×10^{-11}	4.280×10^{-18}	$7.79291747 \times 10^{-22}$
25	2.793×10^{-5}	1.309×10^{-8}	7.549×10^{-17}	1.291×10^{-19}
30	1.893×10^{-4}	3.949×10^{-7}	5.115×10^{-16}	3.894×10^{-18}

Table 4.7: Dependence of the reaction rate coefficient k_{HH} and the diffusion rate coefficient d_H on the grain surface temperature T for an olivine grain surface and a seed surface consisting of amorphous carbon in a hydrogen recombination process for a grain particle radius of $R = 10^{-7}$m.

T [K]	$k_{HH}^{olivine}$ [ms^{-1}]	k_{HH}^{carbon} [ms^{-1}]	$d_H^{olivine}$ [m^{2}s^{-1}]	d_H^{carbon} [m^{2}s^{-1}]
5	3.186×10^{-26}	4.065×10^{-45}	8.612×10^{-39}	4.009×10^{-57}
10	9.280×10^{-14}	6.332×10^{-23}	2.508×10^{-26}	6.244×10^{-35}
15	1.325×10^{-9}	1.581×10^{-15}	3.582×10^{-22}	1.559×10^{-27}
20	1.584×10^{-7}	7.902×10^{-12}	4.280×10^{-20}	7.793×10^{-24}
25	2.793×10^{-6}	1.309×10^{-9}	7.549×10^{-19}	1.291×10^{-21}
30	1.892×10^{-5}	3.949×10^{-8}	5.115×10^{-18}	3.894×10^{-20}

Table 4.8: Dependence of the reaction rate coefficient k_{HH} and the diffusion rate coefficient d_H on the grain surface temperature T for an olivine grain surface and a seed surface consisting of amorphous carbon in a hydrogen recombination process for a grain particle radius of $R = 10^{-6}$m.

4.2 Numerical Evaluation

In this section, we present the numerical results obtained from the evaluation of the mean-field evolution equations (4.10) in one space dimension with periodic boundary conditions as well as the corresponding dynamical values derived from the numerical exploitation of the Doi-Peliti formalism —see equation (4.21)— under the same phyiscal assumptions. Necessarily, we have to modify the numerical code according to the discretised constraints in one space dimension. If not otherwise stated the initial conditions were chosen to be zero.

4.2.1 Discretisation of Stochastic Constraint Equations

In order to generate solutions to the constraint equation (4.5) we have to appropriately discretise this stochastic partial differential equation. Therefore, we integrate equation (4.5) and get

$$\begin{aligned}
&\int\int \frac{\partial}{\partial t}\bar{\phi}_A(x,t)\mathrm{d}x\mathrm{d}t - d_A\int\int \frac{\partial^2}{\partial x^2}\bar{\phi}_A(x,t)\mathrm{d}x\mathrm{d}t + \\
&2k_{AA}\int\int \bar{\phi}_A^2(x,t)\mathrm{d}x\mathrm{d}t + l_A\int\int \bar{\phi}_A(x,t)\mathrm{d}x\mathrm{d}t - j_A\int\int \mathrm{d}x\mathrm{d}t + \\
&\mathrm{i}\sqrt{2k_{AA}}\int\int \bar{\phi}_A(x,t)\eta(x,t)\mathrm{d}x\mathrm{d}t = 0.
\end{aligned} \tag{4.19}$$

The discretisation of the Laplace term is obtained via the Forward Time Centred Space Discretisation (FTCS) method —see [49]. Hence, the discretised version of equation (4.19) is given by

$$\begin{aligned}
&\frac{\bar{\phi}_{A;(t+1,x)} - \bar{\phi}_{A;(t,x)}}{\triangle t}\triangle x\triangle t - d_A\frac{\bar{\phi}_{A;(t,x+1)} - 2\bar{\phi}_{A;(t,x)} + \bar{\phi}_{A;(t,x-1)}}{(\triangle x)^2}\triangle x\triangle t + \\
&2k_{AA}\bar{\phi}^2_{A;(t,x)}\triangle x\triangle t + l_A\bar{\phi}_{A;(t,x)}\triangle x\triangle t - j_A\triangle x\triangle t + \\
&\mathrm{i}\sqrt{2k_{AA}}\bar{\phi}_{A;(t,x)}\frac{\triangle w_{t,x}}{\triangle x\triangle t}\triangle x\triangle t = 0,
\end{aligned} \tag{4.20}$$

which leads to

$$\begin{aligned}
&\bar{\phi}_{A;(t+1,x)} = \bar{\phi}_{A;(t,x)} + d_A\frac{\bar{\phi}_{A;(t,x+1)} - 2\bar{\phi}_{A;(t,x)} + \bar{\phi}_{A;(t,x-1)}}{(\triangle x)^2}\triangle t - \\
&2k_{AA}\bar{\phi}^2_{A;(t,x)}\triangle t - l_A\bar{\phi}_{A;(t,x)}\triangle t + j_A\triangle t - \\
&\mathtt{i}\sqrt{2k_{AA}}\bar{\phi}_{A;(t,x)}\frac{\triangle w_{t,x}}{\triangle x},
\end{aligned} \tag{4.21}$$

with $\triangle w_{t,x} := g\sqrt{\triangle t}\sqrt{\triangle x}$, where g is a stochastic variable with Gaussian distribution, namely $\langle g\rangle = 0$ and $\langle g^2\rangle = 1$. The variable g is generated via a Box-Müller transformation —see Section 3.3. The stability criterion arising from the FTCS for deterministic differential equations is

$$\frac{2d_A\triangle t}{(\triangle x)^2} < 1. \tag{4.22}$$

It can be verified in our numerical calculations that for increasing value of the diffusion rate d_A one has to decrease the value of the chosen time increment $\triangle t$ in order to ensure stability. In the following numerical computations we find that, in general, the value of the stability parameter for the corresponding stochastic differential equation is in fact less than the stability parameter for deterministic differential equations. We choose a certain number N of numerical grid points X that guarantees a satisfying convergence. Accordingly, we have $N\triangle x = \mathcal{C}$ where $\triangle x$ denotes the separation between the numerical grid points. With decreasing $\triangle x$, the time increment $\triangle t$ has to be decreased to ensure stability. This means that for decreasing $\triangle x$ the numerical calculations will be more time consuming since for fixed circumference $\mathcal{C}$ and decreasing increment $\triangle x$ the number of numerical grid points N has to be increased and the time steps $\triangle t$ have to be decreased.

4.2.2 Numerical Results

The late-time value of the average reactant density $\langle n_A(X, t_\infty)\rangle$ on a homogeneous grain particle in one space dimension and with periodic boundary conditions that stems from the mean-field equations (4.10) is independent of the diffusion constant for each numerical grid point X. In particular, for Figure 4.3 the rate coefficients were chosen to be $k_{AA} = 0.5\ \mathrm{ms}^{-1}$, $l_A = 0.1\mathrm{s}^{-1}$, $j_A = 10^1\mathrm{s}^{-1}\mathrm{m}^{-1}$ and $d_A = 10^{-1}\mathrm{ms}^{-1}$ and the radius of the grain was taken to be $R = 10^{-3}\mathrm{m}$. In addition, the late-time value of the average reactant density is independent of the number of numerical grid points which, in that particular example, was equal to ten. The independence on the diffusion rate coefficient is due to the fact that in the particular chosen set-up and for homogeneous inital data there is no gradient in the spatial dimension. This is different for the stochastic partial differential equations since there is a different noise for each spatial point hence there is a gradient in the spatial dimension for a particular solution.

In Figures 4.4 and 4.5 we plot the real and imaginary part of one possible set of solutions to the discretised version of the first constraint equation (4.21) on a ring of radius $R = 10^3\mathrm{m}$ with the same rate coefficients as employed for the generation of Figure 4.3. We observe that the overall behaviour of each individual evolution is

similar to the ones at other numerical grid points which underpins the infinite speed of propagation of perturbations in diffusive systems as in the one presented here. We choose the number of numerical grid points to be ten since the numerical error that arises due to a smaller number of numerical grid points is less significant than the numerical error that is due to a smaller number of paths employed in the path integral average. A generation of only 100 paths to be employed in a path integral for ten numerical grid points is equivalent to the generation of 1000 paths employed in the path integral in the single lattice site model yet it can be even more time consuming which stems from the fact that in order to ensure stability one usually has smaller time increments and, therefore, longer running times in the one-dimensional model. Figures 4.6 and 4.7 where we present the real and imaginary part of a path integral average of solutions to the discretised version of the first constraint equation (4.21) on a ring of radius $R = 10^3$m with the same rate coefficients as above averaged over only 10 realisations of the noise illustrate the occasional occurence of larger spikes that might give rise to computational issues.

In Figure 4.8 we investigate the dependence of the late-time value of the average reactant density on a ring with radius $R = 10^{-3}$m (with ten numerical grid points) on the value of the diffusion rate d_A in the mean-field framework and in the stochastic framework. The remaining rate coefficients were chosen to be $k_{AA} = 0.5$ ms^{-1}, $l_A = 0.1$ s^{-1}, $j_A = 10^1$s^{-1}m^{-1}. The same comparison is made in Figure 4.9 with a source rate coefficient of $j_A = 10^9$s^{-1}m^{-1}. For the smaller source rate coefficient one observes a greater late-time value of the average reactant density derived from the stochastic framework than the one obtained from mean-field theory. The latter is constant for all values of the diffusion rate coefficient. Furthermore, the diffusion constant tends to homogenise the fluctuations of the stochastic field to a certain extent: for increasing value of the diffusion rate coefficient the average reactant density decreases until it levels out beyond a certain value of the diffusion rate. In the case of the larger source rate coefficient the stochastic theory and the mean-field theory predict the same late-time value of the average reactant density. The same overall behaviour can be seen from Figures 4.10 and 4.11 where the same rate coefficients were used to give the average reactant density on a ring with radius $R = 10^{-1}$m. In general, it is true that for fixed values of the rate coeffiecients the late-time value of the average reactant density according to the Doi-Peliti formalism gets closer to the late-time value of the average molecule density on the grain according to the mean-field theory for larger sizes of the grain —cfr. Figures 4.8, 4.9, 4.10 and 4.11.

We proceed by employing values for the rate coefficients as given in Tables 4.3,

4.4, 4.5, 4.6, 4.7 and 4.8, which correspond to the heterogeneous hydrogen-hydrogen reaction taking place on olivine grains of different sizes and at different temperatures. We observe that the late-time value of the average density of hydrogen atoms on the ring according to the mean-field evolution equation, $\langle n_H(x, t_\infty)\rangle$, and the late-time value of the average density of hydrogen atoms on the ring according to the path integral average in the stochastic framework, $\langle \phi_H(x, t_\infty)\rangle$, coincide at each lattice site for the specific choices of parameters. This result is somewhat to be expected from the observations in zero space dimensions —cfr. Figure 3.29 and Figure 3.30— where deterministic behaviour of the average hydrogen population was found. From Figure 4.12 it is clear that the cooler the surface of the grain the higher the density of hydrogen atoms on the ring. For a fixed temperature the hydrogen density decreases with decreasing size of the grain. This generic behaviour can also be observed when considering the heterogeneous hydrogen-hydrogen reaction taking place on the surface of a grain particle made of amorphous carbon for the rate coefficients as given in Tables 4.3, 4.4, 4.5, 4.6, 4.7 and 4.8. The transient time is much greater for grain particles consisting of amorphous carbon than for olivine seeds so that, at present, a thorough discussion of the evolution of the average hydrogen density on an amorphous carbon grain is not viable since the numerical computation is too time consuming with regard to the evaluation of the path integral average. However, the present results indicate that for almost all situations under consideration the value of the average hydrogen density lies in the deterministic regime except for a grain size of $R = 10^{-9}$m and at a temperature of $T = 20$K.

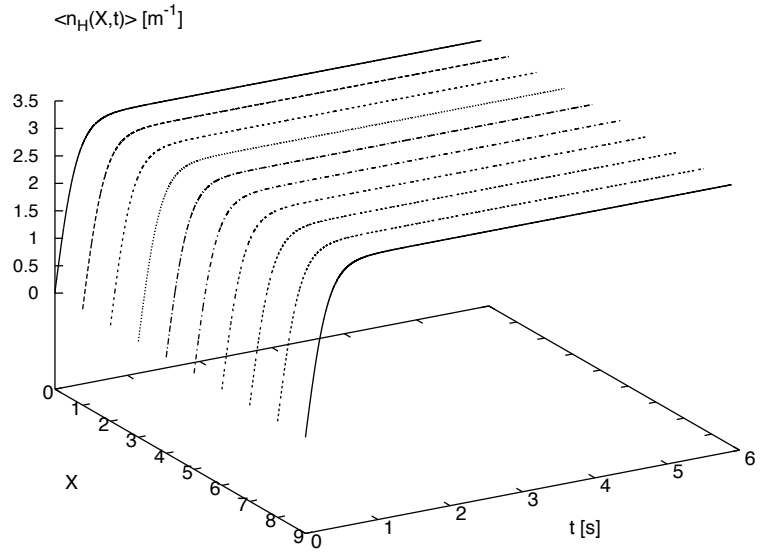

Figure 4.3: Evolution of average reactant density in time t on a ring with radius $R = 10^{-3}$m according to the mean-field equations and ten numerical grid points X. The rate coefficients were chosen in the following way: $k_{AA} = 0.5$ ms^{-1}, $l_A = 0.1$s^{-1}, $j_A = 10^1$s^{-1}m^{-1} and $d_A = 10^{-1}$m^{2}s^{-1}.

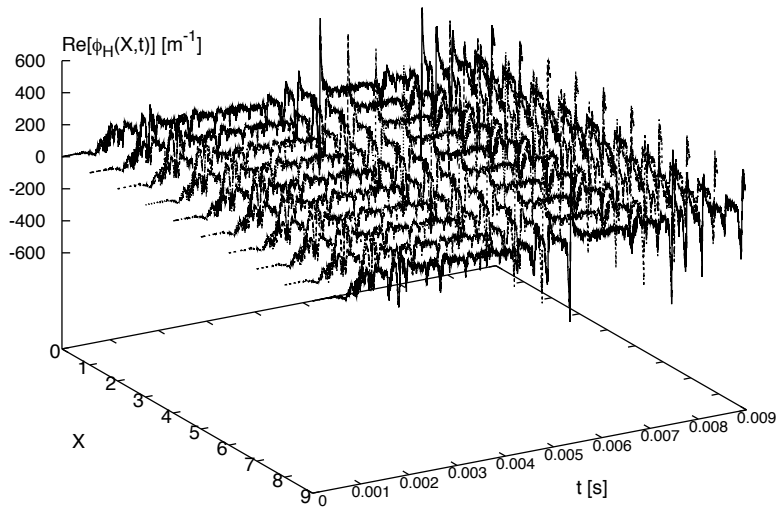

Figure 4.4: Evolution of the real part of one possible solution to the first stochastic constraint equation in one space dimension with periodic boundary conditions, that is, a ring with radius $R = 10^{-3}$m, in time t and ten numerical grid points X. The rate coefficients were chosen in the following way: $k_{AA} = 0.5$ ms^{-1}, $l_A = 0.1$s^{-1}, $j_A = 10^1$s^{-1}m^{-1} and $d_A = 10^{-1}$m^{2}s^{-1}.

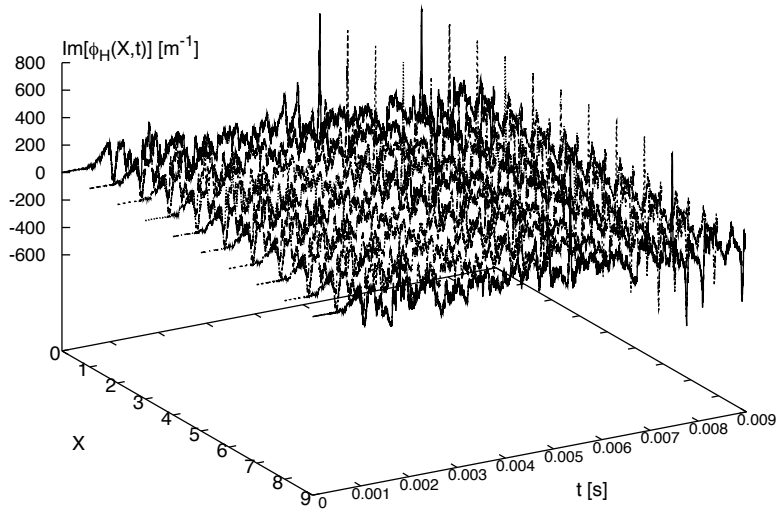

Figure 4.5: Evolution in time t of the corresponding imaginary part of the same solution to the first stochastic constraint equation in one space dimension with periodic boundary conditions as presented in Figure 4.4 for a radius $R = 10^{-3}$m, and ten numerical grid points X. The rate coefficients were chosen in the following way: $k_{AA} = 0.5$ ms^{-1}, $l_A = 0.1$s^{-1}, $j_A = 10^1$s^{-1}m^{-1} and $d_A = 10^{-1}$m^{2}s^{-1}.

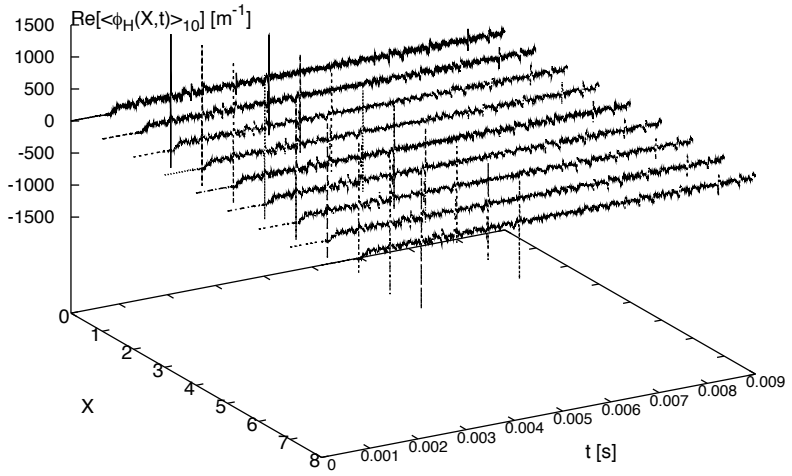

Figure 4.6: Evolution of the average reactant density in time t on a ring with radius $R = 10^{-3}$m according to the Doi-Peliti framework and ten numerical grid points X. The path integral average was taken over 10 realisations of the noise. The rate coefficients were chosen in the following way: $k_{AA} = 0.5$ ms^{-1}, $l_A = 0.1$s^{-1}, $j_A = 10^1$s^{-1}m^{-1} and $d_A = 10^{-1}$m^{2}s^{-1}.

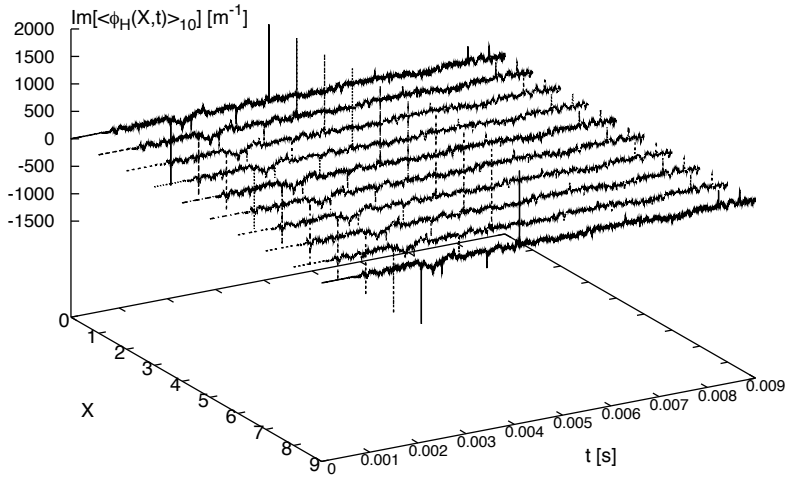

Figure 4.7: Evolution of the imaginary part of the solutions presented in Figure 4.6 in time t on a ring with radius $R = 10^{-3}$m according to the Doi-Peliti formalism and ten numerical grid points X. The rate coefficients were chosen in the following way: $k_{AA} = 0.5$ ms^{-1}, $l_A = 0.1$ s^{-1}, $j_A = 10^1$s^{-1}m^{-1} and $d_A = 10^{-1}$m^{2}s^{-1}.

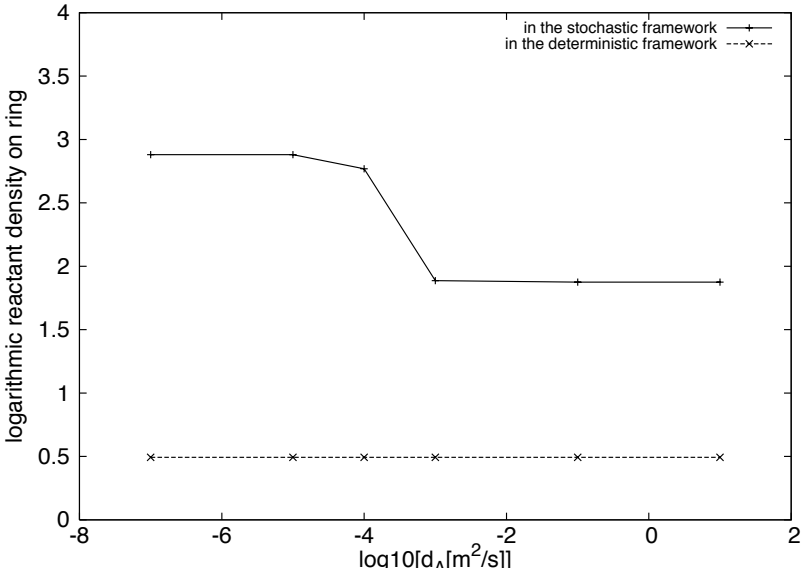

Figure 4.8: Dependence of the late-time value of the average reactant density on a ring with radius $R = 10^{-3}$m (with ten numerical grid points) on the value of the diffusion rate d_A in the mean-field framework and in the stochastic framework. The remaining rate coefficients were chosen to be $k_{AA} = 0.5$ ms^{-1}, $l_A = 0.1$ s^{-1}, $j_A = 10^1$s^{-1}m^{-1}. The lines are a guide to the eye.

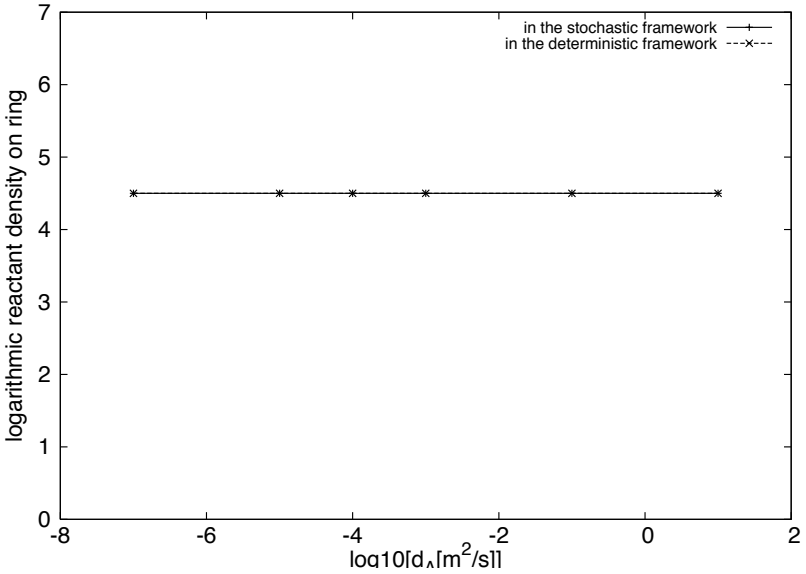

Figure 4.9: Dependence of the late-time value of the average reactant density on a ring with radius $R = 10^{-3}$m (with ten numerical grid points) on the value of the diffusion rate d_A in the mean-field framework and in the stochastic framework. The remaining rate coefficients were chosen to be $k_{AA} = 0.5$ ms^{-1}, $l_A = 0.1$ s^{-1}, $j_A = 10^9$s^{-1}m^{-1}. The lines are a guide to the eye.

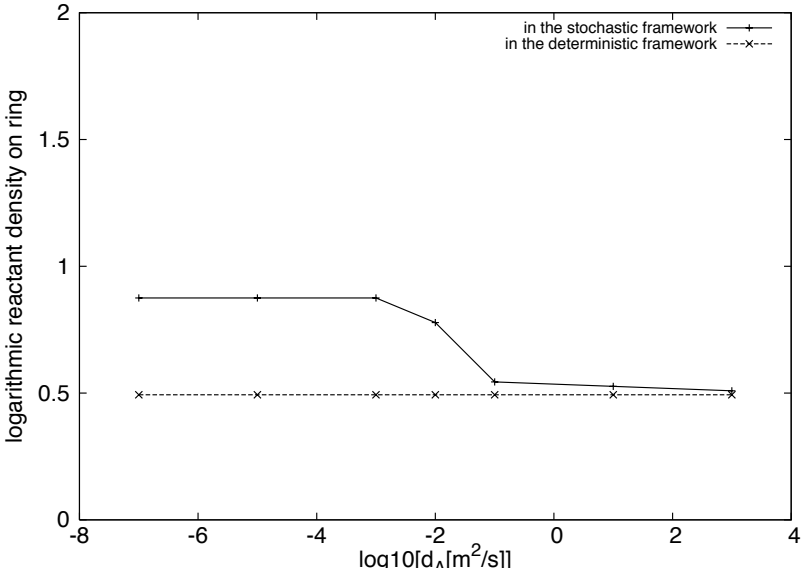

Figure 4.10: Dependence of the late-time value of the average reactant density on a ring with radius $R = 10^{-1}$m (with ten numerical grid points) on the value of the diffusion rate d_A in the mean-field framework and in the stochastic framework. The remaining rate coefficients were chosen to be $k_{AA} = 0.5$ ms^{-1}, $l_A = 0.1$ s^{-1}, $j_A = 10^1$s^{-1}m^{-1}. The lines are a guide to the eye.

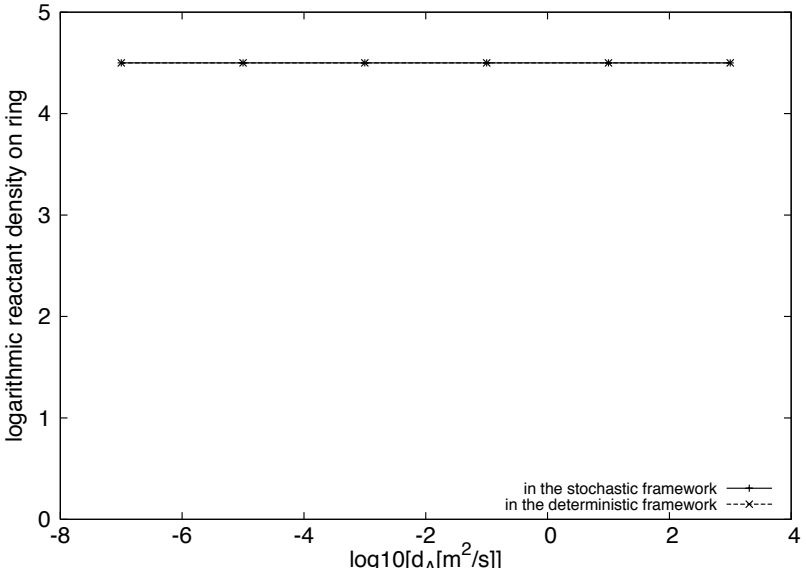

Figure 4.11: Dependence of the late-time value of the average reactant density on a ring with radius $R = 10^{-1}$m (with ten numerical grid points) on the value of the diffusion rate d_A in the mean-field framework and in the stochastic framework. The remaining rate coefficients were chosen to be $k_{AA} = 0.5$ ms^{-1}, $l_A = 0.1$ s^{-1}, $j_A = 10^9$s^{-1}m^{-1}. The lines are a guide to the eye.

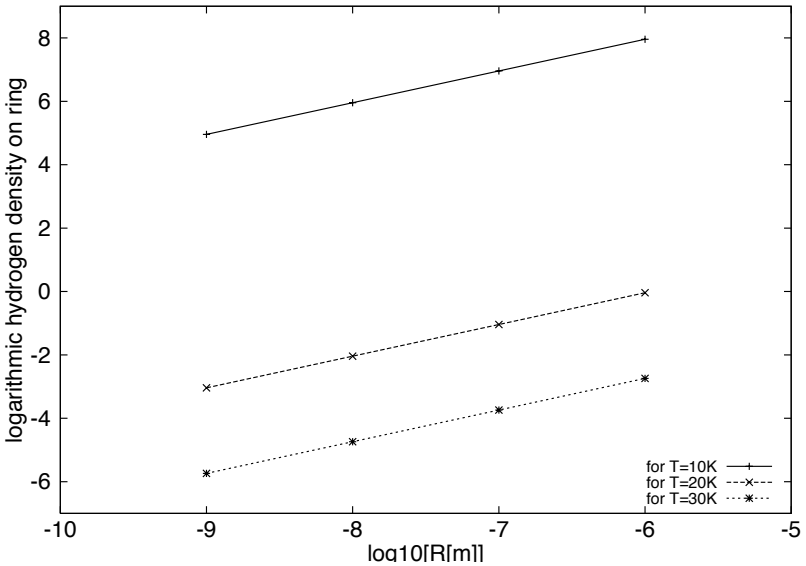

Figure 4.12: Dependence of the late-time value of the hydrogen density on olivine rings of various sizes and surface temperatures. The lines are a guide to the eye.

4.3 Conclusions and Outlook

For the M2 model data, the particular choice of the geometrical form of a grain particle in one space dimension and the assumption of homogeneity of the seed do not seem to lead to results that differ greatly from the observations in the single spatial site model. We conclude that, for general rate coefficients that are independent of the size of the seed, stochastic effects for larger grains are less important than for smaller seed particles. A rapid diffusion can enhance this feature.

Although so far, the astrochemical community has been satisfied with the restriction to periodic boundary conditions it would be desirable to impose non-periodic boundary conditions and consider a finite string instead of a ring —see Figure 4.13— where interesting behaviour at the edges is to be expected. A natural next step in our investigations which is illustrated in Figure 4.14 is to move from one to two space dimensions where, again, one can choose periodic boundary conditions —corresponding to a torus— or non-periodic boundary conditions, that is, a finite plane. A further improvement of our calculations lies in the possibility to consider inhomogeneous grain surfaces. Such configurations can be readily achieved by assigning different values to a specific rate coefficient, for example, the diffusion rate or the reaction rate, at different binding sites as visualised in Figure 4.15. Hence, we are able to model grain particles that consist of patches of different materials. Another challenge concerns finding an alternative form of the rate coefficients. Already in zero space dimensions assumptions on the geometry in two space dimensions are made to derive tractable expressions for the model parameters. This issue remains in the calculations in one space dimension. Especially if one is interested in imposing non-periodic boundary conditions the non-spherical geometry contradicts the common assumptions introduced in the previous chapter and one has

$$N_S \neq 4\pi R^2 s, \tag{4.23}$$

$$J_A \neq n(A) v_A \sigma(R). \tag{4.24}$$

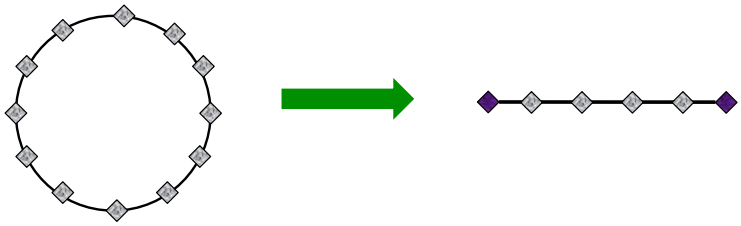

Figure 4.13: Schematic of possible geometrical choices for the grain particle in one space dimension.

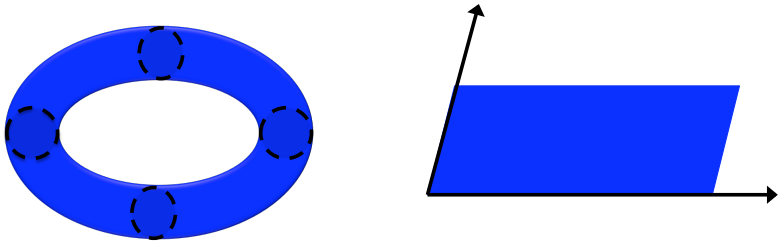

Figure 4.14: Schematic of possible geometrical choices for the grain particle in two space dimensions.

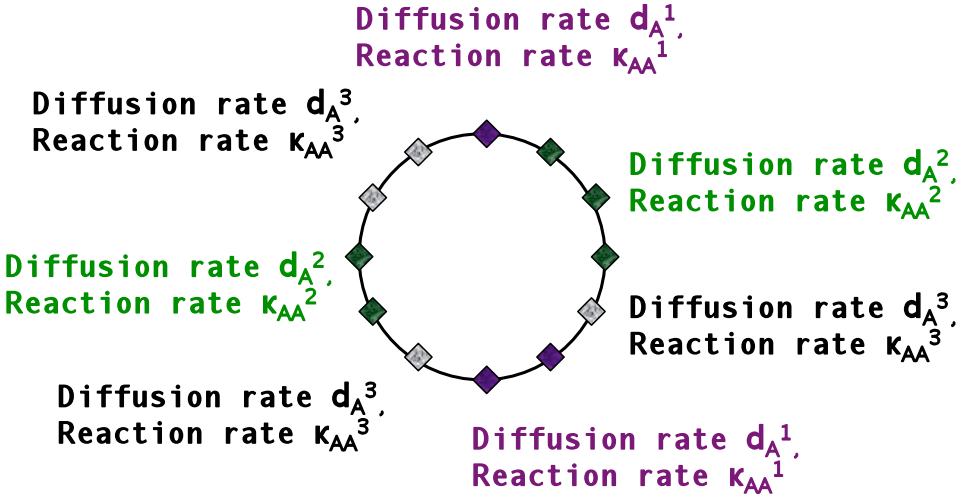

Figure 4.15: Schematic of an inhomogeneous ($d_A^1 \neq d_A^2 \neq d_A^3$, $k_{AA}^1 \neq k_{AA}^2 \neq k_{AA}^3$) one-dimensional grain particle with periodic boundary conditions.

Chapter 5

Chemical Reaction Networks

In this chapter, we present a stochastic alternative to the mean-field rate equations describing the evolution of several distinct chemical species involved in a chemical reaction network based on the Doi-Peliti formalism. We start with the inspection of a single chemical reaction of type $A + B \to C$ taking place on a grain particle, and combine the results of Chapter 2 with the outcome of the computations for the heterogeneous chemical reaction of type $A + B \to C$ to study the stochastic framework by means of the hydrogen-oxygen reaction network.

5.1 Heterogeneous Chemical Reaction of Type $A + B \longrightarrow C$

The process in which molecules of a chemical species A and of another distinct species B deposit onto the surface of a solid or liquid particle and eventually form a third type of chemical species C as a reaction product can be treated in the same fashion as described in Chapter 2. In the sequel, we exclude the scenario where both A and B species can react with themselves, otherwise additional terms would have to be added to the evolution equations.

5.1.1 Stability Analysis Of The Dynamical Mean-Field Equations

The evolution equations for the average molecule densities $\langle \mathrm{n}(\mathbf{x},t)\rangle$ in the mean-field model

$$\begin{aligned}
&-\frac{\partial\langle \mathrm{n}_A(\mathbf{x},t)\rangle}{\partial t} + \zeta_A\Delta\langle \mathrm{n}_A(\mathbf{x},t)\rangle - \kappa_{AB}\langle \mathrm{n}_A(\mathbf{x},t)\rangle\langle \mathrm{n}_B(\mathbf{x},t)\rangle - \lambda_A\langle \mathrm{n}_A(\mathbf{x},t)\rangle + \iota_A = 0,\\
&-\frac{\partial\langle \mathrm{n}_B(\mathbf{x},t)\rangle}{\partial t} + \zeta_B\Delta\langle \mathrm{n}_B(\mathbf{x},t)\rangle - \kappa_{AB}\langle \mathrm{n}_A(\mathbf{x},t)\rangle\langle \mathrm{n}_B(\mathbf{x},t)\rangle - \lambda_B\langle \mathrm{n}_B(\mathbf{x},t)\rangle + \iota_B = 0,\\
&-\frac{\partial\langle \mathrm{n}_C(\mathbf{x},t)\rangle}{\partial t} + \zeta_C\Delta\langle \mathrm{n}_C(\mathbf{x},t)\rangle + \kappa_{AB}\langle \mathrm{n}_A(\mathbf{x},t)\rangle\langle \mathrm{n}_B(\mathbf{x},t)\rangle - \lambda_C\langle \mathrm{n}_C(\mathbf{x},t)\rangle + \iota_C = 0,
\end{aligned} \tag{5.1}$$

reduce in zero space dimensions to

$$-\frac{\mathrm{d}\langle N_A(t)\rangle}{\mathrm{d}t} - K_{AB}\langle N_A(t)\rangle\langle N_B(t)\rangle - L_A\langle N_A(t)\rangle + J_A = 0, \tag{5.2}$$

$$-\frac{\mathrm{d}\langle N_B(t)\rangle}{\mathrm{d}t} - K_{AB}\langle N_A(t)\rangle\langle N_B(t)\rangle - L_B\langle N_B(t)\rangle + J_B = 0, \tag{5.3}$$

$$-\frac{\mathrm{d}\langle N_C(t)\rangle}{\mathrm{d}t} + K_{AB}\langle N_A(t)\rangle\langle N_B(t)\rangle - L_C\langle N_C(t)\rangle + J_C = 0. \tag{5.4}$$

In general, it is not possible to give an exact solution to this system of non-linear first order equations.

When an n-dimensional system of non-linear first order equations

$$\frac{\mathrm{d}}{\mathrm{d}t}\mathbf{n}(t) = \mathbf{a}[\mathbf{n}(t)], \tag{5.5}$$

where $\mathbf{a}[\mathbf{n}(t)]$ is a vector depending on the unknown functions $\mathbf{n}(t) := (n_1(t), n_2(t), n_3(t), ...)^T$, has no exact solution it is important to study the behaviour of the solutions to the equations in a qualitative way. In what follows we make use of the general ideas of Chapter IX in [28]. The steady state solution is defined as the solution $\mathring{\mathbf{n}}$ for which

$$\mathbf{a}(\mathring{\mathbf{n}}) \equiv 0. \tag{5.6}$$

The Taylor expansion of equation (5.5) around the steady state solution $\mathring{\mathbf{n}}$ reads

$$\frac{\mathrm{d}}{\mathrm{d}t}\mathbf{n}(t) = \mathbf{a}(\mathring{\mathbf{n}}) + \mathbf{J}|_{\mathring{\mathbf{n}}}\left(\mathbf{n}(t) - \mathring{\mathbf{n}}\right) + \mathcal{O}\left(\left(\mathbf{n}(t) - \mathring{\mathbf{n}}\right)^2\right), \tag{5.7}$$

with $\mathbf{J}$ the Jacobian matrix

$$\mathbf{J}|_{\mathring{\mathbf{n}}} := \begin{pmatrix} \frac{\delta a_1}{\delta n_1} & \frac{\delta a_1}{\delta n_2} & \cdots \\ \frac{\delta a_2}{\delta n_1} & \frac{\delta a_2}{\delta n_2} & \cdots \\ \vdots & \vdots & \ddots \end{pmatrix} \Bigg|_{\mathring{\mathbf{n}}}. \tag{5.8}$$

The first term of the Taylor expansion vanishes by definition. By means of the function $\mathbf{v}(t) := \mathbf{n}(t) - \mathring{\mathbf{n}}$, equation (5.7) can be rewritten as

$$\frac{\mathrm{d}}{\mathrm{d}t}\mathbf{v}(t) = \mathbf{J}|_{\mathring{\mathbf{n}}}\mathbf{v}(t) + \mathcal{O}(\mathbf{v}^2(t)). \tag{5.9}$$

This set of equations is now an n-dimensional system of linear first order ordinary differential equations. We proceed by solving the eigenequation

$$\mathbf{J}|_{\mathring{\mathbf{n}}}\mathbf{e}_i = l_i\mathbf{e}_i, \tag{5.10}$$

for the eigenvalues l_i and the eigenvectors $\mathbf{e}_i$. Ignoring all higher orders $\mathcal{O}\left((\mathbf{n}(t) - \mathring{\mathbf{n}})^2\right)$ the general solution to equation (5.7) yields

$$\mathbf{n}(t) = \sum_i c_i\mathbf{e}_i \exp(l_i t), \tag{5.11}$$

where

$$\sum_i c_i\mathbf{e}_i \equiv \mathbf{n}(0). \tag{5.12}$$

This solution satisfies the initial conditions. From the uniqueness of the Taylor expansion this is the only solution. In order to analyse the flows of the trajectories in the vicinity of the steady state solution we consider the eigenvalues of the Jacobian matrix. The form and signs of the eigenvalues will prove the steady state solution to be stable or unstable.

General Case: $L_A > 0,\ L_B > 0,\ J_A > 0,\ J_B > 0,\ K_{AB} > 0$

In order to perform a stability analysis of the solutions to equations (5.2), (5.3) and (5.4) we linearise the set of evolution equations in a neighbourhood of the steady state solution. First, we have to compute the steady state solutions $\mathring{N}_A$, $\mathring{N}_B$ and $\mathring{N}_C$ to the above system of equations, that is solutions to the mean-field equations with

$$\frac{\mathrm{d}\langle N_i(t)\rangle}{\mathrm{d}t} \equiv 0 \quad \text{for} \quad i \in \{A, B, C\}. \tag{5.13}$$

The steady state solutions as obtained by `MAPLE 11` read

$$\mathring{N}_A = \frac{-L_B\mathring{N}_B + J_B}{K_{AB}\mathring{N}_B}, \tag{5.14}$$

$$\mathring{N}_B = \frac{(J_B - J_A)K_{AB} - L_AL_B \pm \sqrt{K_{AB}^2(J_B - J_A)^2 + L_AL_B\big(2K_{AB}(J_A + J_B) + L_AL_B\big)}}{2L_BK_{AB}}, \tag{5.15}$$

$$\mathring{N}_C = \frac{J_C + K_{AB}\mathring{N}_A\mathring{N}_B}{L_C}. \tag{5.16}$$

The first two evolution equations (5.2) and (5.3) are independent from the third evolution equation (5.4) and therefore we concentrate on the equations governing the reaction partners, molecules of species A and B, in the sequel. The linearised equations in the sense of equation (5.9) take the form

$$\frac{\mathrm{d}}{\mathrm{d}t}\begin{pmatrix} v_A(t) \\ v_B(t) \end{pmatrix} + \begin{pmatrix} J_{11} & J_{12} \\ J_{21} & J_{22} \end{pmatrix}\begin{pmatrix} v_A(t) \\ v_B(t) \end{pmatrix} + \begin{pmatrix} w_A \\ w_B \end{pmatrix} = 0, \tag{5.17}$$

with

$$\begin{aligned} J_{11} &= L_A + K_{AB}\mathring{N}_B, \\ J_{12} &= K_{AB}\mathring{N}_A, \\ J_{21} &= K_{AB}\mathring{N}_B, \\ J_{22} &= L_B + K_{AB}\mathring{N}_A, \\ w_A &= L_A\mathring{N}_A + K_{AB}\mathring{N}_A\mathring{N}_B - J_A, \\ w_B &= L_B\mathring{N}_B + K_{AB}\mathring{N}_A\mathring{N}_B - J_B. \end{aligned} \tag{5.18}$$

This system is not homogeneous so we perform a shift of the constant vector $\mathbf{w}$ by introducing $\tilde{\mathbf{v}}(t) := \mathbf{v}(t) - \mathbf{u}$, where

$$\begin{aligned} u_A &= \frac{J_{12}w_B - J_{22}w_A}{J_{11}J_{22} - J_{12}J_{21}}, \\ u_B &= \frac{J_{21}w_A - J_{11}w_B}{J_{11}J_{22} - J_{12}J_{21}}. \end{aligned} \tag{5.19}$$

and obtain a homogeneous set of equations

$$\frac{\mathrm{d}}{\mathrm{d}t}\begin{pmatrix} \tilde{v}_A(t) \\ \tilde{v}_B(t) \end{pmatrix} + \begin{pmatrix} J_{11} & J_{12} \\ J_{21} & J_{22} \end{pmatrix}\begin{pmatrix} \tilde{v}_A(t) \\ \tilde{v}_B(t) \end{pmatrix} = 0, \tag{5.20}$$

The eigenvalues of the above system according to (5.10) are

$$\begin{aligned} l_{1,2} &= \frac{J_{11}+J_{22} \pm \sqrt{(J_{11}-J_{22})^2+4J_{12}J_{21}}}{2} \\ &= \frac{L_A+L_B+K_{AB}(\mathring{N}_A+\mathring{N}_B) \pm \sqrt{(L_A-L_B+K_{AB}(\mathring{N}_B-\mathring{N}_A))^2+4K_{AB}^2\mathring{N}_A\mathring{N}_B}}{2}, \end{aligned} \tag{5.21}$$

and have multiplicity one. In the sequel we denote the eigenvalue l_1 as the eigenvalue with positive square root and the eigenvalue l_2 as the eigenvalue with negative square root. The corresponding eigenvectors to the eigenvalues (5.21) read

$$\begin{aligned} \mathbf{e}_{1,2} &= \begin{pmatrix} \frac{J_{11}-J_{22} \pm \sqrt{(J_{11}-J_{22})^2+4J_{12}J_{21}}}{2J_{21}} \\ 1 \end{pmatrix} \\ &= \begin{pmatrix} \frac{L_A-L_B+K_{AB}(\mathring{N}_B-\mathring{N}_A) \pm \sqrt{(L_A-L_B+K_{AB}(\mathring{N}_B-\mathring{N}_A))^2+4K_{AB}^2\mathring{N}_A\mathring{N}_B)}}{2K_{AB}\mathring{N}_B} \\ 1 \end{pmatrix}. \end{aligned} \tag{5.22}$$

Hence, the general solution to equation (5.7) is given by

$$\mathbf{n}(t) = c_+\mathbf{e}_1 \exp(l_1 t) + c_-\mathbf{e}_2 \exp(l_2 t), \tag{5.23}$$

with eigenvalues (5.21) and eigenvectors (5.22) as calculated above and with the integration constants

$$\begin{aligned} c_+ &= \frac{\langle N_B(0)\rangle}{2} + \frac{\langle N_A(0)\rangle J_{21}}{\sqrt{(J_{11}-J_{22})^2+4J_{12}J_{21}}} - \frac{(J_{11}-J_{22})\langle N_B(0)\rangle}{2\sqrt{(J_{11}-J_{22})^2+4J_{12}J_{21}}}, \\ c_- &= \langle N_B(0)\rangle - c_+. \end{aligned} \tag{5.24}$$

In terms of the rate coefficients the integration constants take the following form

$$
\begin{aligned}
c_+ = \frac{\langle N_B(0)\rangle}{2} + \frac{\langle N_A(0)\rangle K_{AB}\mathring{N}_B}{\sqrt{(L_A - L_B + K_{AB}(\mathring{N}_B - \mathring{N}_A))^2 + 4K_{AB}^2\mathring{N}_A\mathring{N}_B}} - \\
\frac{(L_A - L_B + K_{AB}(\mathring{N}_B - \mathring{N}_A))\langle N_B(0)\rangle}{2\sqrt{(L_A - L_B + K_{AB}(\mathring{N}_B - \mathring{N}_A))^2 + 4K_{AB}^2\mathring{N}_A\mathring{N}_B}}, \\
c_- = \frac{\langle N_B(0)\rangle}{2} - \frac{\langle N_A(0)\rangle K_{AB}\mathring{N}_B}{\sqrt{(L_A - L_B + K_{AB}(\mathring{N}_B - \mathring{N}_A))^2 + 4K_{AB}^2\mathring{N}_A\mathring{N}_B}} + \\
\frac{(L_A - L_B + K_{AB}(\mathring{N}_B - \mathring{N}_A))\langle N_B(0)\rangle}{2\sqrt{(L_A - L_B + K_{AB}(\mathring{N}_B - \mathring{N}_A))^2 + 4K_{AB}^2\mathring{N}_A\mathring{N}_B}}.
\end{aligned}
\tag{5.25}
$$

In a next step we analyse the phase space portraits for specific forms of the rate coefficients that are of special physical interest.

Special Case I: $L_A = L_B > 0$**,** $J_A > 0$, $J_B > 0$**,** $K_{AB} > 0$

For the chemical reaction where the evaporation rates of the reaction partners are equal

$$
L_A = L_B \equiv L. \tag{5.26}
$$

In this case the steady state solutions $\mathring{N}_A$, $\mathring{N}_B$ and $\mathring{N}_C$ read

$$
\begin{aligned}
\mathring{N}_A &= \frac{-L\mathring{N}_B + J_B}{K_{AB}\mathring{N}_B}, \\
\mathring{N}_B &= \frac{(J_B - J_A)K_{AB} - L^2 \pm \sqrt{K_{AB}^2(J_B - J_A)^2 + L^2\big(2K_{AB}(J_A + J_B) + L^2\big)}}{2LK_{AB}}, \\
\mathring{N}_C &= \frac{J_{AB} + K_{AB}\mathring{N}_A\mathring{N}_B}{L_{AB}}.
\end{aligned}
\tag{5.27}
$$

The eigenvalues with multiplicity one according to equation (5.21) reduce to

$$
\begin{aligned}
l_1 &= L + K_{AB}(\mathring{N}_A + \mathring{N}_B), \\
l_2 &= L.
\end{aligned}
\tag{5.28}
$$

The corresponding eigenvectors take the form

$$\mathbf{e}_1 = \begin{pmatrix} -\frac{\mathring{N}_A}{\mathring{N}_B} \\ 1 \end{pmatrix},$$
$$\mathbf{e}_2 = \begin{pmatrix} 1 \\ 1 \end{pmatrix}. \tag{5.29}$$

The constants c_+ and c_- in the general solution

$$\mathbf{n}(t) = c_+ \mathbf{e}_1 \exp(l_1 t) + c_- \mathbf{e}_2 \exp(l_2 t), \tag{5.30}$$

are given by

$$c_+ = \frac{\langle N_B(0)\rangle - \langle N_A(0)\rangle}{1 + \frac{\mathring{N}_A}{\mathring{N}_B}},$$
$$c_- = \langle N_B(0)\rangle - c_+. \tag{5.31}$$

Both eigenvalues l_1 and l_2 are strictly positive for $L, K_{AB}, \mathring{N}_A, \mathring{N}_B$ strictly positive and we are faced with an unstable node. The flow away from the fixed point will —for large t— be dominated by the larger eigenvalue l_1. For a particular chemical reaction with $L \lll 1$, the phase space portrait almost corresponds to the one created by a non-simple fixed point where one observes a flow in only one direction and the fixed point turns into a fixed line. We conclude that it is not possible for the late-time dynamical solution to reach the fixed point.

Special Case II: $L_A > 0$**,** $L_B = 0$**,** $J_A > 0$**,** $J_B > 0$**,** $K_{AB} > 0$

For certain chemical reactions — for example, for the reaction $H + O \longrightarrow HO$ — the evaporation rates for one of the reaction partners, namely the oxygen molecules, and the evaporation rate for the reaction product are very small. In fact, in the numerical computations they can be set to zero for practical purposes. Therefore we will assume $L_B = L_C = 0$ in the sequel. In this special case the steady state values for the reaction partners (5.14) and (5.16) are obtained when considering equations (5.2) and (5.3) with $L_B = 0$

$$\mathring{N}_A = \frac{J_A - J_B}{L_A},$$
$$\mathring{N}_B = \frac{J_B L_A}{K_{AB}(J_A - J_B)}. \tag{5.32}$$

Inserting the above steady state solutions into the evolution equation for the reaction product (5.4) yet with $L_C = 0$ one finds that

$$\frac{\mathrm{d}\langle N_C(t)\rangle}{\mathrm{d}t} = J_B + J_C, \tag{5.33}$$

so that $\langle N_C(t)\rangle \longrightarrow \infty$ for $t \longrightarrow \infty$ since the adsorption rate J_C is always positive and the adsorption rate J_B is taken to be strictly positive.
It is important to note that the possibility $J_A = J_B$ is not allowed —see equations (5.2) and (5.3). The eigenvalues (multiplicity one)

$$l_{1,2} = \frac{L_A + K_{AB}(\mathring{N}_A + \mathring{N}_B) \pm \sqrt{(L_A + K_{AB}(\mathring{N}_B - \mathring{N}_A))^2 + 4K_{AB}^2 \mathring{N}_A \mathring{N}_B}}{2}, \tag{5.34}$$

are determined by the eigenequation (5.10). The corresponding eigenvectors read

$$\mathbf{e}_{1,2} = \begin{pmatrix} \frac{L_A + K_{AB}(\mathring{N}_B - \mathring{N}_A) \pm \sqrt{(L_A + K_{AB}(\mathring{N}_B - \mathring{N}_A))^2 + 4K_{AB}^2 \mathring{N}_A \mathring{N}_B}}{2K_{AB}\mathring{N}_B} \\ 1 \end{pmatrix}, \tag{5.35}$$

and the constants c_+ and c_- in the general solution

$$\mathbf{n}(t) = c_+ \mathbf{e}_1 \exp(l_1 t) + c_- \mathbf{e}_2 \exp(l_2 t), \tag{5.36}$$

are given by

$$\begin{aligned} c_+ = {} & \frac{\langle N_B(0)\rangle}{2} + \frac{\langle N_A(0)\rangle K_{AB}\mathring{N}_B}{\sqrt{(L_A + K_{AB}(\mathring{N}_B - \mathring{N}_A))^2 + 4K_{AB}^2 \mathring{N}_A \mathring{N}_B}} - \\ & \frac{(L_A + K_{AB}(\mathring{N}_B - \mathring{N}_A))\langle N_B(0)\rangle}{2\sqrt{(L_A + K_{AB}(\mathring{N}_B - \mathring{N}_A))^2 + 4K_{AB}^2 \mathring{N}_A \mathring{N}_B}}, \\ c_- = {} & \langle N_B(0)\rangle - c_+. \end{aligned} \tag{5.37}$$

It is clear that $l_1 > 0$ for all feasible values of the constants. To analyse the sign of eigenvalue l_2 —that is, the eigenvalue with negative square root— let us first assume that

$$0 \leq \frac{L_A + K_{AB}(\mathring{N}_A + \mathring{N}_B) - \sqrt{(L_A + K_{AB}(\mathring{N}_B - \mathring{N}_A))^2 + 4K_{AB}^2 \mathring{N}_A \mathring{N}_B}}{2}. \tag{5.38}$$

This inequality is equivalent to

$$-2L_A K_{AB} \mathring{N}_A \leq 2L_A K_{AB} \mathring{N}_A. \tag{5.39}$$

On the other hand, the assumption

$$0 \geq \frac{L_A + K_{AB}(\mathring{N}_A + \mathring{N}_B) - \sqrt{(L_A + K_{AB}(\mathring{N}_B - \mathring{N}_A))^2 + 4K_{AB}^2 \mathring{N}_A \mathring{N}_B}}{2}, \tag{5.40}$$

leads to the inequality

$$-2L_A K_{AB} \mathring{N}_A \geq 2L_A K_{AB} \mathring{N}_A. \tag{5.41}$$

This leaves us with two possibilites: if either of the constants L_A, K_{AB}, $\mathring{N}_A$ equals zero the second eigenvalue takes the form $l_2 = 0$. In this case the steady state solution is a degenerated fixed point and there is only flow in one direction away from the fixed point. If all of the constants L_A, K_{AB}, $\mathring{N}_A$ are strictly positive it follows that the second eigenvalue l_2 is strictly positive for all choices of constants and the phase space portrait delivers an unstable node.

The potential occurrence of instabilities in the mean-field dynamical model indicates that one should take extra care in the numerical exploitation of the stochastic dynamical model where a similar analysis as undertaken in the latter paragraphs is not possible.

5.1.2 The Stochastic Dynamical Model

In analogy to the previous chapters we replace the mean-field rate equations with a master equation incorporating stochastic fluctuations. For heterogeneous chemical reactions where two atoms or molecules from different chemical species A and B react

and form molecules of the chemical species type C the master equation takes the form

$$\frac{\mathrm{d}P(\{N_A\},\{N_B\},\{N_C\};t)}{\mathrm{d}t} =$$
$$\bar{\iota}_A \sum_i \big(P(...,N_{A_i}-1,...,\{N_B\},\{N_C\};t) - P(\{N_A\},\{N_B\},\{N_C\};t)\big) +$$
$$\bar{\iota}_B \sum_i \big(P(\{N_A\}...,N_{B_i}-1,...,\{N_C\};t) - P(\{N_A\},\{N_B\},\{N_C\};t)\big) +$$
$$\bar{\iota}_C \sum_i \big(P(\{N_A\},\{N_B\},...,N_{C_i}-1,...;t) - P(\{N_A\},\{N_B\},\{N_C\};t)\big) +$$
$$\frac{\bar{\kappa}_{AB}}{V} \sum_i \big((N_{A_i}+1)(N_{B_i}+1)P(...,N_{A_i}+1,...,N_{B_i}+1,...,N_{C_i}-1,...;t) -$$
$$N_{A_i}N_{B_i}P(\{N_A\},\{N_B\},\{N_C\};t)\big) +$$
$$\bar{\lambda}_A \sum_i \big((N_{A_i}+1)P(...,N_{A_i}+1,...,\{N_B\},\{N_C\};t) -$$
$$N_{A_i}P(\{N_A\},\{N_B\},\{N_C\};t)\big) +$$
$$\bar{\lambda}_B \sum_i \big((N_{B_i}+1)P(\{N_A\},...,N_{B_i}+1,...,\{N_C\};t) -$$
$$N_{B_i}P(\{N_A\},\{N_B\},\{N_C\};t)\big) +$$
$$\bar{\lambda}_C \sum_i \big((N_{C_i}+1)P(\{N_A\},\{N_B\},...,N_{C_i}+1,...;t) -$$
$$N_{C_i}P(\{N_A\},\{N_B\},\{N_C\};t)\big) +$$
$$\bar{\zeta}_A \sum_{\langle ij\rangle} \big((N_{A_i}+1)P(...,N_{A_i}+1,N_{A_j}-1,...,\{N_B\},\{N_C\};t) -$$
$$N_{A_i}P(\{N_A\},\{N_B\},\{N_C\};t) +$$
$$(N_{A_j}+1)P(...,N_{A_i}-1,N_{A_j}+1,...,\{N_B\},\{N_C\};t) -$$
$$N_{A_j}P(\{N_A\},\{N_B\},\{N_C\};t)\big) +$$
$$\bar{\zeta}_B \sum_{\langle ij\rangle} \big((N_{B_i}+1)P(\{N_A\},...,N_{B_i}+1,N_{B_j}-1,...,\{N_C\};t) -$$
$$N_{B_i}P(\{N_A\},\{N_B\},\{N_C\};t) +$$
$$(N_{B_j}+1)P(\{N_A\},...,N_{B_i}-1,N_{B_j}+1,...,\{N_C\};t) -$$
$$N_{B_j}P(\{N_A\},\{N_B\},\{N_C\};t)\big)+$$

$$\bar{\zeta}_C \sum_{\langle ij \rangle} \big((N_{C_i}+1) P(\{N_A\},\{N_B\},...,N_{C_i}+1,N_{C_j}-1,...;t) - N_{C_i} P(\{N_A\},\{N_B\},\{N_C\};t) + (N_{C_j}+1) P(\{N_A\},\{N_B\},...,N_{C_i}-1,N_{C_j}+1,...;t) - N_{C_j} P(\{N_A\},\{N_B\},\{N_C\};t) \big),$$

(5.42)

where $\{N_X\} := \{N_{X_1}, N_{X_2}, N_{X_3}, ...N_{X_{i_{max}}}\}$, with i_{max} the maximum number of lattice sites i, is the set denoting the number of particles of type X at lattice site i and $P(\{N_A\},\{N_B\},\{N_C\};t)$ the probability distribution for the total number of particles. The Poisson initial condition on each lattice site reads

$$P(\{N_A\},\{N_B\},\{N_C\};t=0) = e^{-\bar{n}_A(0)-\bar{n}_B(0)-\bar{n}_C(0)} \prod_i \frac{\bar{n}_A(0)^{N_{A_i}} \bar{n}_B(0)^{N_{B_i}} \bar{n}_C(0)^{N_{C_i}}}{N_{A_i}! N_{B_i}! N_{C_i}!}, \tag{5.43}$$

with the initial average occupation numbers per lattice site $\bar{n}_A(0)$ $\bar{n}_B(0)$ and $\bar{n}_C(0)$ for the A, B and C particles, respectively. The master equation (5.42) is equivalent to the Schrödinger-like equation

$$\frac{\mathrm{d}}{\mathrm{d}t}|\Psi(t)\rangle = -\mathtt{H}[\overset{+}{\mathtt{a}}_{A_i}, \overset{-}{\mathtt{a}}_{A_j}, \overset{+}{\mathtt{a}}_{B_k}, \overset{-}{\mathtt{a}}_{B_l}, \overset{+}{\mathtt{a}}_{C_m}, \overset{-}{\mathtt{a}}_{C_n}]|\Psi(t)\rangle, \tag{5.44}$$

with the many-body wave function

$$|\Psi(t)\rangle := \sum_{\{N_A\},\{N_B\},\{N_C\}} P(\{N_A\},\{N_B\},\{N_C\};t) \prod_i (\overset{+}{\mathtt{a}}_{A_i})^{N_{A_i}} (\overset{+}{\mathtt{a}}_{B_i})^{N_{B_i}} (\overset{+}{\mathtt{a}}_{C_i})^{N_{C_i}} |\{0\}\rangle, \tag{5.45}$$

and the Hamiltonian-like operator

$$\mathtt{H}[\overset{+}{\mathtt{a}}_{A_i}, \overset{-}{\mathtt{a}}_{A_j}, \overset{+}{\mathtt{a}}_{B_k}, \overset{-}{\mathtt{a}}_{B_l}, \overset{+}{\mathtt{a}}_{C_m}, \overset{-}{\mathtt{a}}_{C_n}] = \sum_{M\in\{A,B,C\}} \sum_i (\overset{+}{\mathtt{a}}_{M_i} - \mathtt{1}_i)(\bar{\iota}_M \mathtt{1}_i - \bar{\lambda}_M \overset{-}{\mathtt{a}}_{M_i}) - \frac{\bar{\kappa}_{AB}}{V} \sum_i \big(\overset{+}{\mathtt{a}}_{C_i} - \overset{+}{\mathtt{a}}_{A_i} \overset{+}{\mathtt{a}}_{B_i} \big) \overset{-}{\mathtt{a}}_{A_i} \overset{-}{\mathtt{a}}_{B_i} + \sum_{M\in\{A,B,C\}} \bar{\zeta}_M \sum_{\langle ij \rangle} (\overset{+}{\mathtt{a}}_{M_i} - \overset{+}{\mathtt{a}}_{M_j})(\overset{-}{\mathtt{a}}_{M_i} - \overset{-}{\mathtt{a}}_{M_j}). \tag{5.46}$$

The expectation values of operators $\mathtt{O}(t)$ are obtained via

$$\langle \mathtt{O}(t) \rangle = \frac{\int \prod_i \mathrm{D}\psi_i \mathrm{D}\psi_i^* O(\{\bar{\psi}\}) \exp\Big(-S(\{\tilde{\psi}\},\{\psi\})\Big)}{\int \prod_i \mathrm{D}\psi_i \mathrm{D}\psi_i^* \exp\Big(-S(\{\tilde{\psi}\},\{\psi\})\Big)}. \tag{5.47}$$

The Doi-shifted action $\tilde{S}$ for the chemical reaction $A+B \longrightarrow C$ in the continuum limit is given by

$$\begin{aligned}\tilde{S}[\psi_A,\tilde{\psi}_A,\psi_B,\tilde{\psi}_B,\psi_C,\tilde{\psi}_C] := \int \mathrm{d}^D x \Big(& - n_A(0) + n_A(0)(\tilde{\psi}_A(\mathbf{x},0) - n_A(0)) - \\ & n_B(0) + n_B(0)(\tilde{\psi}_B(\mathbf{x},0) - n_B(0)) - \\ & n_C(0) + n_C(0)(\tilde{\psi}_C(\mathbf{x},0) - n_C(0)) + \\ & \int_0^{t_T} dt \big(\tilde{\psi}_A(\mathbf{x},t) \frac{\partial \psi_A(\mathbf{x},t)}{\partial t} + \tilde{\psi}_B(\mathbf{x},t) \frac{\partial \psi_B(\mathbf{x},t)}{\partial t} + \\ & \tilde{\psi}_C(\mathbf{x},t) \frac{\partial \psi_C(\mathbf{x},t)}{\partial t} + \\ & \tilde{H}[\psi_A(\mathbf{x},t),\tilde{\psi}_A(\mathbf{x},t),\psi_B(\mathbf{x},t),\tilde{\psi}_B(\mathbf{x},t),\psi_C(\mathbf{x},t),\tilde{\psi}_C(\mathbf{x},t)] \Big),\end{aligned} \tag{5.48}$$

with the Doi-shifted Hamiltonian $\tilde{H}$ in the continuum limit

$$\begin{aligned}&\tilde{H}[\psi_A(\mathbf{x},t),\tilde{\psi}_A(\mathbf{x},t),\psi_B(\mathbf{x},t),\tilde{\psi}_B(\mathbf{x},t),\psi_C(\mathbf{x},t),\tilde{\psi}_C(\mathbf{x},t)] = \\ &\quad - \tilde{\psi}_A(\mathbf{x},t)(\iota_A - \lambda_A \psi_A(\mathbf{x},t)) - \tilde{\psi}_B(\mathbf{x},t)(\iota_B - \lambda_B \psi_B(\mathbf{x},t)) - \\ &\quad \tilde{\psi}_C(\mathbf{x},t)(\iota_C - \lambda_C \psi_C(\mathbf{x},t)) + \\ &\quad \kappa_{AB} \psi_A(\mathbf{x},t)\psi_B(\mathbf{x},t)\big(\tilde{\psi}_A(\mathbf{x},t)\tilde{\psi}_B(\mathbf{x},t) + \tilde{\psi}_A(\mathbf{x},t) + \tilde{\psi}_B(\mathbf{x},t) - \tilde{\psi}_C(\mathbf{x},t)\big) - \\ &\quad \tilde{\psi}_A(\mathbf{x},t)\zeta_A \Delta\psi_A(\mathbf{x},t) - \tilde{\psi}_B(\mathbf{x},t)\zeta_B \Delta\psi_B(\mathbf{x},t) - \tilde{\psi}_C(\mathbf{x},t)\zeta_C \Delta\psi_C(\mathbf{x},t).\end{aligned} \tag{5.49}$$

In order to be able to proceed we untangle the pseudo-quadratic term $\tilde{\psi}_A(\mathbf{x},t)\tilde{\psi}_B(\mathbf{x},t)$ that appears in the above expression (5.49) according to a Gaussian integral transformation. An n-dimensional Gaussian transformation with linear term reads

$$\int \mathrm{D}^n \mathbf{e} \exp\left(-\mathbf{e}^T \mathbf{A} \mathbf{e} + \mathbf{b}^T \mathbf{e}\right) = \sqrt{\frac{\pi^n}{|\det \mathbf{A}|}} \exp\left(\frac{1}{4}\mathbf{b}^T \mathbf{A}^{-1} \mathbf{b}\right), \tag{5.50}$$

where $\mathbf{A}$ is a symmetric $n \times n$ matrix and $\mathbf{b}$ and $\mathbf{e}$ are two n-dimensional vectors with functional dependence. From the form of the action integral (5.48) together with (5.49) it follows that

$$\kappa_{AB}\psi_A(\mathbf{x},t)\psi_B(\mathbf{x},t)\tilde{\psi}_A(\mathbf{x},t)\tilde{\psi}_B(\mathbf{x},t) \stackrel{!}{=} \frac{1}{4}\frac{a_4a_1 - 2a_2b_1b_2 + a_1b_2^2}{\mid a_1a_4 - a_2^2 \mid}, \tag{5.51}$$

with

$$\mathbf{A} = \begin{pmatrix} a_1 & a_2 \\ a_3 & a_4 \end{pmatrix} \tag{5.52}$$

We choose $a_1 = a_4 = 0$ and $a_2 = 1$. In addition, we have

$$4\kappa_{AB}\psi_A(\mathbf{x},t)\psi_B(\mathbf{x},t)\tilde{\psi}_A(\mathbf{x},t)\tilde{\psi}_B(\mathbf{x},t) \stackrel{!}{=} -2b_1b_2, \tag{5.53}$$

from which it follows that

$$\begin{aligned} b_1 &= \mathrm{i}\sqrt{2\kappa_{AB}\psi_A(\mathbf{x},t)\psi_B(\mathbf{x},t)}\tilde{\psi}_A(\mathbf{x},t), \\ b_2 &= \mathrm{i}\sqrt{2\kappa_{AB}\psi_A(\mathbf{x},t)\psi_B(\mathbf{x},t)}\tilde{\psi}_B(\mathbf{x},t). \end{aligned} \tag{5.54}$$

Furthermore, we have

$$-2e_1e_2 \stackrel{!}{=} -\frac{1}{2}\eta_A(\mathbf{x},t)\eta_B(\mathbf{x},t), \tag{5.55}$$

which leads to

$$\begin{aligned} e_1 &= \frac{\eta_A(\mathbf{x},t)}{2}, \\ e_2 &= \frac{\eta_B(\mathbf{x},t)}{2}. \end{aligned} \tag{5.56}$$

The pseudo-quadratic term in the Doi-shifted Hamiltonian (5.49)

$$e^{-\kappa_{AB}\int\int \tilde{\psi}_A(\mathbf{x},t)\tilde{\psi}_B(\mathbf{x},t)\psi_A(\mathbf{x},t)\psi_B(\mathbf{x},t)\mathrm{d}^Dx\mathrm{d}t}, \tag{5.57}$$

can be replaced by a term proportional to

$$\int \mathrm{D}\eta\ \mathcal{P}[\eta]e^{\mathrm{i}\sqrt{2\kappa_{AB}}\int\int\left(\tilde{\psi}_A(\mathbf{x},t)\psi_A(\mathbf{x},t)\eta_A(\mathbf{x},t)+\tilde{\psi}_B(\mathbf{x},t)\psi_B(\mathbf{x},t)\eta_B(\mathbf{x},t)\right)\mathrm{d}^Dx\mathrm{d}t}, \tag{5.58}$$

with the Gaussian probability distribution

$$\mathcal{P}[\eta] = e^{-\frac{1}{2}\int\int\eta_A(\mathbf{x},t)\eta_B(\mathbf{x},t)\mathrm{d}^Dx\mathrm{d}t}. \tag{5.59}$$

The above procedure leads to a Doi-shifted action $\tilde{S}$ being linear in $\tilde{\psi}_A$ and $\tilde{\psi}_B$. Thus, one can integrate out over $\tilde{\psi}_A(\mathbf{x},t)$, $\tilde{\psi}_B(\mathbf{x},t)$ and $\tilde{\psi}_C(\mathbf{x},t)$ in (5.47). One obtains

$$\begin{aligned}\langle \mathtt{O}[\psi_A,\psi_B,\psi_C]\rangle \propto \int \mathrm{D}\psi_A\mathrm{D}\psi_B\mathrm{D}\psi_C\mathrm{D}\eta_A\mathrm{D}\eta_B\ \mathtt{O}[\psi_A,\psi_B,\psi_C]\times \\ \delta[\mathcal{F}_A]\delta[\mathcal{F}_B]\delta[\mathcal{F}_C]\delta[\mathcal{F}_{A_0}]\delta[\mathcal{F}_{B_0}]\delta[\mathcal{F}_{C_0}]P[\eta] \\ \propto \int \mathrm{D}\eta_A\mathrm{D}\eta_B\ \mathtt{O}[\bar{\psi}_A,\bar{\psi}_B,\bar{\psi}_C]P[\eta],\end{aligned} \tag{5.60}$$

where the fluctuating unknown functions $\bar{\psi}_A(\mathbf{x},t)$, $\bar{\psi}_B(\mathbf{x},t)$ and $\bar{\psi}_C(\mathbf{x},t)$ have to solve the following set of coupled nonlinear complex stochastic differential equations

$$\begin{aligned}\mathcal{F}_A[\bar{\psi}_A(\mathbf{x},t),\mathbf{x},t] \equiv -\frac{\partial\bar{\psi}_A(\mathbf{x},t)}{\partial t}+\zeta_A\Delta\bar{\psi}_A(\mathbf{x},t)-\kappa_{AB}\bar{\psi}_A(\mathbf{x},t)\bar{\psi}_B(\mathbf{x},t)- \\ \lambda_A\bar{\psi}_A(\mathbf{x},t)+\iota_A+\mathrm{i}\sqrt{\frac{\kappa_{AB}\bar{\psi}_A(\mathbf{x},t)\bar{\psi}_B(\mathbf{x},t)}{2}}\eta_A(\mathbf{x},t)=0,\end{aligned} \tag{5.61}$$

$$\begin{aligned}\mathcal{F}_B[\bar{\psi}_B(\mathbf{x},t),\mathbf{x},t] \equiv -\frac{\partial\bar{\psi}_B(\mathbf{x},t)}{\partial t}+\zeta_B\Delta\bar{\psi}_B(\mathbf{x},t)-\kappa_{AB}\bar{\psi}_A(\mathbf{x},t)\bar{\psi}_B(\mathbf{x},t)- \\ \lambda_B\bar{\psi}_B(\mathbf{x},t)+\iota_B+\mathrm{i}\sqrt{\frac{\kappa_{AB}\bar{\psi}_A(\mathbf{x},t)\bar{\psi}_B(\mathbf{x},t)}{2}}\eta_B(\mathbf{x},t)=0,\end{aligned} \tag{5.62}$$

$$\begin{aligned}\mathcal{F}_C[\bar{\psi}_C(\mathbf{x},t),\mathbf{x},t] \equiv -\frac{\partial\bar{\psi}_C(\mathbf{x},t)}{\partial t}+\zeta_C\Delta\bar{\psi}_C(\mathbf{x},t)+\kappa_{AB}\bar{\psi}_A(\mathbf{x},t)\bar{\psi}_B(\mathbf{x},t)- \\ \lambda_C\bar{\psi}_C(\mathbf{x},t)+\iota_C=0,\end{aligned} \tag{5.63}$$

$$\mathcal{F}_{A_0}[\bar{\psi}_A(\mathbf{x},0),\mathbf{x},0] \equiv \bar{\psi}_A(\mathbf{x},0)-n_A(0)=0, \tag{5.64}$$

$$\mathcal{F}_{B_0}[\bar{\psi}_B(\mathbf{x},0),\mathbf{x},0] \equiv \bar{\psi}_B(\mathbf{x},0)-n_B(0)=0, \tag{5.65}$$

$$\mathcal{F}_{C_0}[\bar{\psi}_C(\mathbf{x},0),\mathbf{x},0] \equiv \bar{\psi}_C(\mathbf{x},0)-n_C(0)=0. \tag{5.66}$$

In the literature, the stochastic noises $\eta_A(\mathbf{x},t)$ and $\eta_B(\mathbf{x},t)$ are often referred to as "complex white Gaussian noises". This terminology needs further explanation. We have that

$$\eta_A(\mathbf{x},t)=\frac{1}{\sqrt{2}}\Big(\Re\big(\eta(\mathbf{x},t)\big)+\mathrm{i}\Im\big(\eta(\mathbf{x},t)\big)\Big), \tag{5.67}$$

$$\eta_B(\mathbf{x},t)=\frac{1}{\sqrt{2}}\Big(\Re\big(\eta(\mathbf{x},t)\big)-\mathrm{i}\Im\big(\eta(\mathbf{x},t)\big)\Big), \tag{5.68}$$

where $\Re\big(\eta(\mathbf{x},t)\big)$ and $\Im\big(\eta(\mathbf{x},t)\big)$ are real Gaussian noises. Equations (5.67) and (5.68) indicate that one noise is the complex conjugate of the other. The stochastic noises $\eta_A(\mathbf{x},t)$ and $\eta_B(\mathbf{x},t)$ have vanishing mean value, vanishing auto-correlations but non-zero cross-correlations

$$
\begin{aligned}
\langle\eta_A(\mathbf{x},t)\rangle_{\mathcal{P}[\eta]} &= \left\langle \frac{1}{\sqrt{2}}\Big(\Re\big(\eta(\mathbf{x},t)\big) + \mathrm{i}\Im\big(\eta(\mathbf{x},t)\big)\Big)\right\rangle_{\mathcal{P}[\eta]} = 0\\
\langle\eta_B(\mathbf{x},t)\rangle_{\mathcal{P}[\eta]} &= \left\langle \frac{1}{\sqrt{2}}\Big(\Re\big(\eta(\mathbf{x},t)\big) - \mathrm{i}\Im\big(\eta(\mathbf{x},t)\big)\Big)\right\rangle_{\mathcal{P}[\eta]} = 0,\\
\langle\eta_A(\mathbf{x},t)\eta_A(\mathbf{x}',t')\rangle_{\mathcal{P}[\eta]} &= \frac{1}{2}\big(\langle\Re\big(\eta(\mathbf{x},t)\big)\Re\big(\eta(\mathbf{x}',t')\big)\rangle_{\mathcal{P}[\eta]} + \langle\mathrm{i}\Re\big(\eta(\mathbf{x},t)\big)\Im\big(\eta(\mathbf{x}',t')\big)\rangle_{\mathcal{P}[\eta]} +\\
&\quad \langle\mathrm{i}\Im\big(\eta(\mathbf{x},t)\big)\Re\big(\eta(\mathbf{x}',t')\big)\rangle_{\mathcal{P}[\eta]} - \langle\Im\big(\eta(\mathbf{x},t)\big)\Im\big(\eta(\mathbf{x},t)\big)\rangle_{\mathcal{P}[\eta]}\big) = 0\\
\langle\eta_B(\mathbf{x},t)\eta_B(\mathbf{x}',t')\rangle_{\mathcal{P}[\eta]} &= \frac{1}{2}\big(\langle\Re\big(\eta(\mathbf{x},t)\big)\Re\big(\eta(\mathbf{x}',t')\big)\rangle_{\mathcal{P}[\eta]} - \langle\mathrm{i}\Re\big(\eta(\mathbf{x},t)\big)\Im\big(\eta(\mathbf{x}',t')\big)\rangle_{\mathcal{P}[\eta]} -\\
&\quad \langle\mathrm{i}\Im\big(\eta(\mathbf{x},t)\big)\Re\big(\eta(\mathbf{x}',t')\big)\rangle_{\mathcal{P}[\eta]} - \langle\Im\big(\eta(\mathbf{x},t)\big)\Im\big(\eta(\mathbf{x},t)\big)\rangle_{\mathcal{P}[\eta]}\big) = 0,\\
\langle\eta_A(\mathbf{x},t)\eta_B(\mathbf{x}',t')\rangle_{\mathcal{P}[\eta]} &= \frac{1}{2}\big(\langle\Re\big(\eta(\mathbf{x},t)\big)\Re\big(\eta(\mathbf{x}',t')\big)\rangle_{\mathcal{P}[\eta]} - \langle\mathrm{i}\Re\big(\eta(\mathbf{x},t)\big)\Im\big(\eta(\mathbf{x}',t')\big)\rangle_{\mathcal{P}[\eta]} +\\
&\quad \langle\mathrm{i}\Im\big(\eta(\mathbf{x},t)\big)\Re\big(\eta(\mathbf{x}',t')\big)\rangle_{\mathcal{P}[\eta]} + \langle\Im\big(\eta(\mathbf{x},t)\big)\Im\big(\eta(\mathbf{x},t)\big)\rangle_{\mathcal{P}[\eta]}\big)\\
&\quad = \delta^{(D)}(\mathbf{x}-\mathbf{x}')\delta(t-t'),\\
\langle\eta_B(\mathbf{x},t)\eta_A(\mathbf{x}',t')\rangle_{\mathcal{P}[\eta]} &= \frac{1}{2}\big(\langle\Re\big(\eta(\mathbf{x},t)\big)\Re\big(\eta(\mathbf{x}',t')\big)\rangle_{\mathcal{P}[\eta]} + \langle\mathrm{i}\Re\big(\eta(\mathbf{x},t)\big)\Im\big(\eta(\mathbf{x}',t')\big)\rangle_{\mathcal{P}[\eta]} -\\
&\quad \langle\mathrm{i}\Im\big(\eta(\mathbf{x},t)\big)\Re\big(\eta(\mathbf{x}',t')\big)\rangle_{\mathcal{P}[\eta]} + \langle\Im\big(\eta(\mathbf{x},t)\big)\Im\big(\eta(\mathbf{x},t)\big)\rangle_{\mathcal{P}[\eta]}\big)\\
&\quad = \delta^{(D)}(\mathbf{x}-\mathbf{x}')\delta(t-t'). \qquad (5.69)
\end{aligned}
$$

In the Doi-Peliti formalism the average particle density for molecules of species A, B and C, respectively, involved in the heterogeneous chemical reaction $A+B\to C$, can be calculated by choosing the operator $\mathtt{O}[\bar{\psi}_A,\bar{\psi}_B,\bar{\psi}_C]$ in equation (5.60) to be the fluctuating unknown function itself

$$
\langle\bar{\psi}_X(\mathbf{x},t)\rangle = \frac{\int \mathrm{D}\eta_A\mathrm{D}\eta_B\bar{\psi}_X(\mathbf{x},t)\mathcal{P}[\eta(t)]}{\int \mathrm{D}\eta_A\mathrm{D}\eta_B\mathcal{P}[\eta(t)]}, \quad X\in\{A,B,C\}. \qquad (5.70)
$$

Let us now continue with a more complex situation, namely chemical reaction networks.

5.2 Hydrogen-Oxygen Network

In this section we consider the simple reaction network of the following chemical reactions:

$$
\begin{aligned}
H + H &\longrightarrow H_2 \\
H + O &\longrightarrow OH \\
H + OH &\longrightarrow H_2O \\
O + O &\longrightarrow O_2
\end{aligned}
$$

Although photodestruction in the reverse chemical reactions $H_2O \rightarrow H + OH$ and $OH \rightarrow H + O$ is known to play a role we will not concern ourselves with the reverse chemical reactions. The above chemical reaction network is of specific interest to molecule production in interstellar space.

5.2.1 The Mean-Field Dynamical Model

The evolution of the average density of reactants and reaction products $\langle \mathrm{n}(\mathbf{x}, t)\rangle$ on a grain surface in the mean-field model is governed by the following set of coupled non-linear first order ordinary differential equations:

$$
\begin{aligned}
\frac{\partial\langle \mathrm{n}_H(\mathbf{x},t)\rangle}{\partial t} &= \zeta_H \Delta\langle \mathrm{n}_H(\mathbf{x},t)\rangle + \iota_H - \lambda_H\langle \mathrm{n}_H(\mathbf{x},t)\rangle - 2\kappa_{HH}\langle \mathrm{n}_H(\mathbf{x},t)\rangle^2 - \\
&\quad \kappa_{OH}\langle \mathrm{n}_H(\mathbf{x},t)\rangle\langle \mathrm{n}_O(\mathbf{x},t)\rangle - \kappa_{HOH}\langle \mathrm{n}_H(\mathbf{x},t)\rangle\langle \mathrm{n}_{OH}(\mathbf{x},t)\rangle, \\
\frac{\partial\langle \mathrm{n}_O(\mathbf{x},t)\rangle}{\partial t} &= \zeta_O \Delta\langle \mathrm{n}_O(\mathbf{x},t)\rangle + \iota_O - \lambda_O\langle \mathrm{n}_O(\mathbf{x},t)\rangle - \kappa_{OH}\langle \mathrm{n}_H(\mathbf{x},t)\rangle\langle \mathrm{n}_O(\mathbf{x},t)\rangle - \\
&\quad 2\kappa_{OO}\langle \mathrm{n}_O(\mathbf{x},t)\rangle^2 \\
\frac{\partial\langle n_{OH}(\mathbf{x},t)\rangle}{\partial t} &= \zeta_{OH} \Delta\langle \mathrm{n}_{OH}(\mathbf{x},t)\rangle + \iota_{OH} - \lambda_{OH}\langle \mathrm{n}_{OH}(\mathbf{x},t)\rangle - \\
&\quad \kappa_{HOH}\langle \mathrm{n}_H(\mathbf{x},t)\rangle\langle \mathrm{n}_{OH}(\mathbf{x},t)\rangle + \mu_{OH}\kappa_{OH}\langle \mathrm{n}_H(\mathbf{x},t)\rangle\langle \mathrm{n}_O(\mathbf{x},t)\rangle \\
\frac{\partial\langle \mathrm{n}_{H_2}(\mathbf{x},t)\rangle}{\partial t} &= \zeta_{H_2} \Delta\langle \mathrm{n}_{H_2}(\mathbf{x},t)\rangle + \iota_{H_2} - \lambda_{H_2}\langle \mathrm{n}_{H_2}(\mathbf{x},t)\rangle + \mu_{HH}\kappa_{HH}\langle \mathrm{n}_H(\mathbf{x},t)\rangle^2, \\
\frac{\partial\langle \mathrm{n}_{O_2}(\mathbf{x},t)\rangle}{\partial t} &= \zeta_{O_2} \Delta\langle \mathrm{n}_{O_2}(\mathbf{x},t)\rangle + \iota_{O_2} - \lambda_{O_2}\langle \mathrm{n}_{O_2}(\mathbf{x},t)\rangle + \mu_{OO}\kappa_{OO}\langle \mathrm{n}_O(\mathbf{x},t)\rangle^2, \\
\frac{\partial\langle \mathrm{n}_{H_2O}(\mathbf{x},t)\rangle}{\partial t} &= \zeta_{H_2O} \Delta\langle \mathrm{n}_{H_2O}(\mathbf{x},t)\rangle + \iota_{H_2O} - \lambda_{H_2O}\langle \mathrm{n}_{H_2O}(\mathbf{x},t)\rangle + \\
&\quad \mu_{H_2O}\kappa_{HOH}\langle \mathrm{n}_H(\mathbf{x},t)\rangle\langle \mathrm{n}_{OH}(\mathbf{x},t)\rangle,
\end{aligned}
\tag{5.71}
$$

where the constants μ give the fraction of reaction products that are not released into the gas-phase upon formation but rather stay on the surface of the grain. As we will see in the following paragraphs, again, the above set of evolution equations resembles —in its form— the stochastic constraint equations in the Doi-Peliti formalism.

5.2.2 The Stochastic Dynamical Model

We define $\mathfrak{N}$ as the set of the molecule numbers of all chemical species

$$\mathfrak{N} := \{\{N_H\}, \{N_O\}, \{N_{H_2}\}, \{N_{OH}\}, \{N_{H_2O}\}, \{N_{O_2}\}\}, \tag{5.72}$$

and $\{N_X\} := \{N_{X,1}, N_{X,2}, N_{X,3}, ..., N_{X,i_{max}}\}$ with i_{max} the maximal number of lattice sites. The symbol $P(\mathfrak{N}) := P(\mathfrak{N}; t)$ defines the probability to find a certain number of X particles at lattice site i, $N_{X,i}$. The master equation for the hydrogen-oxygen network in the single spatial site model reads

$$\begin{aligned}
\frac{\mathrm{d}P(\mathfrak{N})}{\mathrm{d}t} = &\sum_i \sum_{X\in[H,O,OH,H_2,O_2,H_2O]} \bar{\iota}_X \big(P(...N_{X,i}-1,...,\mathfrak{N}-\{N_X\}) - P(\mathfrak{N})\big) + \\
&\sum_i \sum_{X\in[H,O,OH,H_2,O_2,H_2O]} \bar{\lambda}_X \big((N_{X,i}+1)P(...N_{X,i}+1,...,\mathfrak{N}-\{N_X\}) - \\
&\qquad N_{X,i}P(\mathfrak{N})\big) - \\
&\sum_i \sum_{X\in[H,O]} \bar{\kappa}_{XX} \big(N_{X,i}(N_{X,i}-1)P(\mathfrak{N}) - \\
&(N_{X,i}+2)(N_{X,i}+1)P(...N_{X,i}+2,...,N_{XX,i}-1,...,\mathfrak{N}-\{N_X\}-\{N_{XX,i}\})\big) - \\
&\sum_i \sum_{X\in[OH,O]} \bar{\kappa}_{HX} \big(N_{H,i}N_{X,i}P(\mathfrak{N}) - \\
&(N_{H,i}+1)(N_{X,i}+1)\times \\
&\times P(...N_{H,i}+1,...,N_{X,i}+1,...,N_{HX,i}-1,...,\mathfrak{N}-\{N_H\}-\{N_X\}-\{N_{HX,i}\})\big) + \\
&\sum_{X\in[H,O,OH,H_2,O_2,H_2O]} \bar{\zeta}_X \sum_{\langle ij\rangle} \big((N_{X,i}+1)P(...,N_{X,i}+1,N_{X,j}-1,...\mathfrak{N}-\{N_X\}) - \\
&\qquad N_{X,i}P(\mathfrak{N}) + \\
&(N_{X,j}+1)P(...,N_{X,i}-1,N_{X,j}+1,...\mathfrak{N}-\{N_X\};t) - N_{X,j}P(\mathfrak{N})\big)
\end{aligned} \tag{5.73}$$

To my knowledge this is the first time that this particular master equation has been explicitly worked out and employed in the Doi-Peliti formalism. If one attempted to include reverse chemical reactions in the model, for example $H_2O \rightarrow H + O$, one would have to add the following terms on the right-hand-side of the above master equation

$$\bar{\varsigma}_{H_2O} \sum_i \Big((N_{H_2O} + 1) \times \\ \times P(..., N_{O,i} - 1, ..., N_{OH,i} - 1, ..., N_{H_2O} + 1, ...\mathfrak{N} - \{N_O\}\{N_{OH}\} - \{N_{H_2O}\}) - \\ N_{H_2O} P(\mathfrak{N}) \Big), \tag{5.74}$$

with $\bar{\varsigma}_{H_2O}$ the separation rate coefficient. Again, the initial conditions correspond to Poissonian distributions at each lattice site. We proceed with the master equation (5.73) and identify the Hamiltonian-like operator in the equivalent Schrödinger-like equation according to the Second Quantised Representation. The Hamiltonian-like operator reads

$$\begin{aligned} \mathtt{H}[\overset{+}{\mathtt{a}}, \bar{\mathtt{a}}] = & \sum_i \sum_{X \in [H,O,OH,H_2,O_2,H_2O]} (\overset{+}{\mathtt{a}}_{X,i} - 1_i)(\bar{j}_X 1_i - \bar{\lambda}_X \, \bar{\mathtt{a}}_{X,i}) - \\ & \sum_i \sum_{X \in [H,O]} \bar{\kappa}_{XX} (\overset{+2}{\mathtt{a}}_{X,i} \bar{\mathtt{a}}^2_{X,i} - \overset{+}{\mathtt{a}}_{XX,i} \bar{\mathtt{a}}^2_{X,i}) - \\ & \sum_i \sum_{X \in [OH,O]} \bar{\kappa}_{HX} (\overset{+}{\mathtt{a}}_{H,i} \overset{+}{\mathtt{a}}_{X,i} \bar{\mathtt{a}}_{H,i} \bar{\mathtt{a}}_{X,i} - \overset{+}{\mathtt{a}}_{HX,i} \bar{\mathtt{a}}_{H,i} \bar{\mathtt{a}} \, X, i) + \\ & \sum_{X \in [H,O,OH,H_2,O_2,H_2O]} \bar{\zeta}_X \sum_{\langle ij \rangle} (\overset{+}{\mathtt{a}}_{X,i} - \overset{+}{\mathtt{a}}_{X,j})(\bar{\mathtt{a}}_{X,i} - \bar{\mathtt{a}}_{X,j}). \end{aligned} \tag{5.75}$$

The field-shifted action integral in the Coherent State Representation is derived according to the procedures introduced in the Chapter 2 and, for the hydrogen-oxygen chemical reaction network, takes the following form

$$\begin{aligned} \tilde{S} = \int \mathrm{d}^D x \Big(& \sum_{X \in [H,O,OH,H_2,O_2,H_2O]} (-n_X(0) + n_X(0)(\tilde{\psi}_X(\mathbf{x}, 0) - n_X(0))) + \\ & \int \mathrm{d}t \big(\sum_{X \in [H,O,OH,H_2,O_2,H_2O]} \tilde{\psi}_X(\mathbf{x}, t) \frac{\partial \psi_X(\mathbf{x}, t)}{\partial t} + \tilde{H}[\psi_Y(\mathbf{x}, t), \tilde{\psi}_Y(\mathbf{x}, t)] \big) \Big), \end{aligned} \tag{5.76}$$

with the Doi shifted Hamiltonian

$$\tilde{H}[\psi_Y(\mathbf{x},t),\tilde{\psi}_Y(\mathbf{x},t)] = \sum_{X\in[H,O,OH,H_2,O_2,H_2O]} -\tilde{\psi}_X(\mathbf{x},t)(j_X - \lambda_X\psi_X(\mathbf{x},t)) +$$
$$\sum_{X\in[O,H]} \kappa_{XX}(2\tilde{\psi}_X(\mathbf{x},t) + \tilde{\psi}_X^2(\mathbf{x},t) - \tilde{\psi}_{XX}(\mathbf{x},t))\psi_X^2(\mathbf{x},t) +$$
$$\sum_{X\in[OH,O]} \kappa_{HX}(\tilde{\psi}_H(\mathbf{x},t)\tilde{\psi}_X(\mathbf{x},t) + \tilde{\psi}_H(\mathbf{x},t) + \tilde{\psi}_X(\mathbf{x},t) - \tilde{\psi}_{HX}(\mathbf{x},t))\psi_H(\mathbf{x},t)\psi_X(\mathbf{x},t) -$$
$$\sum_{X\in[H,O,OH,H_2,O_2,H_2O]} \tilde{\psi}_X(\mathbf{x},t)\zeta_X\Delta\psi_X(\mathbf{x},t). \tag{5.77}$$

Since there appear pseudo-quadratic terms in the above shifted Hamiltonian we have to resort to the Reverse Standard Field Theory Representation of a Langevin-type stochastic differential equation. We employ the Gaussian transformation as described below

$$\int \mathrm{D}^n\mathbf{e}\exp\big(-\mathbf{e}^T\mathbf{A}\mathbf{e}+\mathbf{b}^T\mathbf{e}\big) = \sqrt{\frac{\pi^n}{|\det\mathbf{A}|}}\exp\left(\frac{1}{4}\mathbf{b}^T\mathbf{A}^{-1}\mathbf{b}\right). \tag{5.78}$$

For the particular reaction network under consideration the vectors $\mathbf{e}$ and $\mathbf{b}$ are 6-dimensional vectors and the matrix $\mathbf{A}$ is 6×6 dimensional. Their respective entries are

$$\mathbf{b} = \begin{pmatrix} \mathrm{i}2\sqrt{\kappa_{HH}}\tilde{\psi}_H(\mathbf{x},t)\psi_H(\mathbf{x},t) \\ \mathrm{i}2\sqrt{\kappa_{OO}}\tilde{\psi}_O(\mathbf{x},t)\psi_O(\mathbf{x},t) \\ \mathrm{i}\sqrt{2\kappa_{HO}\psi_H(\mathbf{x},t)\psi_O(\mathbf{x},t)}\tilde{\psi}_H(\mathbf{x},t) \\ \mathrm{i}\sqrt{2\kappa_{HO}\psi_H(\mathbf{x},t)\psi_O(\mathbf{x},t)}\tilde{\psi}_O(\mathbf{x},t) \\ \mathrm{i}\sqrt{2\kappa_{HOH}\psi_H(\mathbf{x},t)\psi_{OH}(\mathbf{x},t)}\tilde{\psi}_H(\mathbf{x},t) \\ \mathrm{i}\sqrt{2\kappa_{HOH}\psi_H(\mathbf{x},t)\psi_{OH}(\mathbf{x},t)}\tilde{\psi}_{OH}(\mathbf{x},t) \end{pmatrix}, \tag{5.79}$$

$$\mathbf{e} = \begin{pmatrix} \frac{\eta_{H,1}(\mathbf{x},t)}{\sqrt{2}} \\ \frac{\eta_{O,1}(\mathbf{x},t)}{\sqrt{2}} \\ \frac{\eta_{H,2}(\mathbf{x},t)}{2} \\ \frac{\eta_{O,2}(\mathbf{x},t)}{2} \\ \frac{\eta_{H,3}(\mathbf{x},t)}{2} \\ \frac{\eta_{OH}(\mathbf{x},t)}{2} \end{pmatrix}, \quad \mathbf{A} = \begin{pmatrix} 1&0&0&0&0&0 \\ 0&1&0&0&0&0 \\ 0&0&0&1&0&0 \\ 0&0&1&0&0&0 \\ 0&0&0&0&0&1 \\ 0&0&0&0&1&0 \end{pmatrix}, \tag{5.80}$$

with $\eta_{H_1}(\mathbf{x},t)$ and $\eta_{O_1}(\mathbf{x},t)$ real Gaussian noises and the other noises

$$\eta_{H,2} := \frac{1}{\sqrt{2}}\Big(\Re(\eta_{H,2}(\mathbf{x},t)) + \mathrm{i}\Im(\eta_{H,2}(\mathbf{x},t))\Big) = \eta_{O,2}^*(\mathbf{x},t),$$
$$\eta_{H,3} := \frac{1}{\sqrt{2}}\Big(\Re(\eta_{H,3}(\mathbf{x},t)) + \mathrm{i}\Im(\eta_{H,3}(\mathbf{x},t))\Big) = \eta_{OH}^*(\mathbf{x},t). \tag{5.81}$$

where $\Re(\eta_{H,2}(\mathbf{x},t))$, $\Im(\eta_{H,2}(\mathbf{x},t))$, $\Re(\eta_{H,3}(\mathbf{x},t))$ and $\Im(\eta_{H,3}(\mathbf{x},t))$ are real Gaussian noises, that is,

$$\begin{aligned}
&\langle\eta_{H,1}(\mathbf{x},t)\rangle_{\mathcal{P}[\eta(\mathbf{x},t)]} = \langle\eta_{H,2}(\mathbf{x},t)\rangle_{\mathcal{P}[\eta(\mathbf{x},t)]} = \langle\eta_{H,3}(\mathbf{x},t)\rangle_{\mathcal{P}[\eta(\mathbf{x},t)]} \\
&\qquad = \langle\eta_{O,1}(\mathbf{x},t)\rangle_{\mathcal{P}[\eta(\mathbf{x},t)]} = \langle\eta_{O,1}(\mathbf{x},t)\rangle_{\mathcal{P}[\eta(\mathbf{x},t)]} = \langle\eta_{OH}(\mathbf{x},t)\rangle_{\mathcal{P}[\eta(\mathbf{x},t)]} = 0, \\
&\langle\eta_{H,1}(\mathbf{x},t)\eta_{H,1}(\mathbf{x}',t')\rangle_{\mathcal{P}[\eta(\mathbf{x},t)]} = \langle\eta_{O,1}(\mathbf{x},t)\eta_{O,1}(\mathbf{x}',t')\rangle_{\mathcal{P}[\eta(\mathbf{x},t)]} \\
&\qquad = \langle\eta_{H,2}(\mathbf{x},t)\eta_{O,2}(\mathbf{x}',t')\rangle_{\mathcal{P}[\eta(\mathbf{x},t)]} = \langle\eta_{H,3}(\mathbf{x},t)\eta_{OH}(\mathbf{x}',t')\rangle_{\mathcal{P}[\eta(\mathbf{x},t)]} = \delta(\mathbf{x}-\mathbf{x}')\delta(t-t'),
\end{aligned} \tag{5.82}$$

and all other cross correlations are zero.

The average density of the chemical species X on the grain surface is given by

$$\langle\psi_X(\mathbf{x},t)\rangle = \frac{\int \mathrm{D}\eta\bar{\psi}_X(\mathbf{x},t)\mathcal{P}[\eta(\mathbf{x},t)]}{\int \mathrm{D}\eta\mathcal{P}[\eta(\mathbf{x},t)]}, \tag{5.83}$$

where $X \in [H, O, H_2, O_2, OH, H_2O]$ and the measure is the following

$$\mathrm{D}\eta := \mathrm{D}\eta_{H,1}\mathrm{D}\eta_{H,2}\mathrm{D}\eta_{H,3}\mathrm{D}\eta_{O,1}\mathrm{D}\eta_{O,2}\mathrm{D}\eta_{OH}. \tag{5.84}$$

The probability distribution $\mathcal{P}[\eta(\mathbf{x},t)]$ reads

$$\begin{aligned}
\mathcal{P}[\eta(\mathbf{x},t)] := \exp\Bigg(-\frac{1}{2}\int\int \big(&\eta_{H,1}^2(\mathbf{x},t) + \eta_{O,1}^2(\mathbf{x},t) + \\
&\eta_{H,2}(\mathbf{x},t)\eta_{O,2}(\mathbf{x},t) + \eta_{H,3}(\mathbf{x},t)\eta_{OH}(\mathbf{x},t)\big)\,\mathrm{d}^D x\mathrm{d}t\Big).
\end{aligned} \tag{5.85}$$

The unknown fields $\bar{\psi}_X(\mathbf{x},t)$ have to satisfy the stochastic constraint equations for the hydrogen-oxygen chemical reaction network:

$$\begin{aligned}\frac{\partial\bar{\psi}_H(\mathbf{x},t)}{\partial t} &= \zeta_H\Delta\bar{\psi}_H(\mathbf{x},t) + j_H - \lambda_H\bar{\psi}_H(\mathbf{x},t) - 2\kappa_{HH}\bar{\psi}_H^2(\mathbf{x},t) - \\ &\quad \kappa_{OH}\bar{\psi}_H(\mathbf{x},t)\bar{\psi}_O(\mathbf{x},t) - \kappa_{HOH}\bar{\psi}_H(\mathbf{x},t)\bar{\psi}_{OH}(\mathbf{x},t) + \\ &\quad \mathrm{i}\left(\sqrt{2\kappa_{HH}}\bar{\psi}_H(\mathbf{x},t)\eta_{H,1}(\mathbf{x},t) + \sqrt{\frac{\kappa_{OH}\bar{\psi}_H(\mathbf{x},t)\bar{\psi}_O(\mathbf{x},t)}{2}}\eta_{H,2}(\mathbf{x},t) + \right. \\ &\quad \left.\sqrt{\frac{\kappa_{HOH}\bar{\psi}_H(\mathbf{x},t)\bar{\psi}_{OH}(\mathbf{x},t)}{2}}\eta_{H,3}(\mathbf{x},t)\right),\end{aligned} \tag{5.86}$$

$$\begin{aligned}\frac{\partial\bar{\psi}_O(\mathbf{x},t)}{\partial t} &= \zeta_O\Delta\bar{\psi}_O(\mathbf{x},t) + j_O - \lambda_O\bar{\psi}_O(\mathbf{x},t) - \kappa_{OH}\bar{\psi}_H(\mathbf{x},t)\bar{\psi}_O(\mathbf{x},t) - 2\kappa_{OO}\bar{\psi}_O^2(\mathbf{x},t) + \\ &\quad \mathrm{i}\left(\sqrt{2\kappa_{OO}}\bar{\psi}_O(\mathbf{x},t)\eta_{O,1}(\mathbf{x},t) + \sqrt{\frac{\kappa_{OH}\bar{\psi}_H(\mathbf{x},t)\bar{\psi}_O(\mathbf{x},t)}{2}}\eta_{O,2}(\mathbf{x},t)\right),\end{aligned}$$

$$\begin{aligned}\frac{\partial\bar{\psi}_{OH}(\mathbf{x},t)}{\partial t} &= \zeta_{OH}\Delta\bar{\psi}_{OH}(\mathbf{x},t) + j_{OH} - \lambda_{OH}\bar{\psi}_{OH}(\mathbf{x},t) - \kappa_{HOH}\bar{\psi}_H(\mathbf{x},t)\bar{\psi}_{OH}(\mathbf{x},t) + \\ &\quad \mu_{OH}\kappa_{OH}\bar{\psi}_H(\mathbf{x},t)\bar{\psi}_O(\mathbf{x},t) + \mathrm{i}\sqrt{\frac{\kappa_{HOH}\bar{\psi}_H(\mathbf{x},t)\bar{\psi}_O(\mathbf{x},t)}{2}}\eta_{OH}(\mathbf{x},t),\end{aligned} \tag{5.87}$$

$$\frac{\partial\bar{\psi}_{H_2}(\mathbf{x},t)}{\partial t} = \zeta_{H_2}\Delta\bar{\psi}_{H_2}(\mathbf{x},t) + j_{H_2} - \lambda_{H_2}\bar{\psi}_{H_2}(\mathbf{x},t) + \mu_{HH}\kappa_{HH}\bar{\psi}_H^2(\mathbf{x},t), \tag{5.88}$$

$$\frac{\partial\bar{\psi}_{O_2}(\mathbf{x},t)}{\partial t} = \zeta_{O_2}\Delta\bar{\psi}_{O_2}(\mathbf{x},t) + j_{O_2} - \lambda_{O_2}\bar{\psi}_{O_2}(\mathbf{x},t) + \mu_{OO}\kappa_{OO}\bar{\psi}_O^2(\mathbf{x},t), \tag{5.89}$$

$$\begin{aligned}\frac{\partial\bar{\psi}_{H_2O}(\mathbf{x},t)}{\partial t} &= \zeta_{H_2O}\Delta\bar{\psi}_{H_2O}(\mathbf{x},t) + j_{H_2O} - \lambda_{H_2O}\bar{\psi}_{H_2O}(\mathbf{x},t) + \\ &\quad \mu_{H_2O}\kappa_{HOH}\bar{\psi}_H(\mathbf{x},t)\bar{\psi}_{OH}(\mathbf{x},t),\end{aligned} \tag{5.90}$$

where the constants μ indicate that only a fraction of the chemical reaction products will stay on the surface of the grain. Furthermore, we have the additional constraints that the inital populations of the chemical species X have to coincide with the inital values of the unknown fluctuating fields $\bar{\psi}_X(\mathbf{x},0)$ for each X.

5.3 Conclusions and Outlook

General theory of ordinary differential equations states that for any simple fixed point —that means that there is no zero eigenvalue for the linearised system— of a system of nonlinear differential equations the phase space portrait close to the fixed point remains qualitatively the same as for the linearised form of the equations provided

the fixed point is not a centre —see, for example, [28]. As we have encountered in the previous analysis non-simple fixed points will occur under certain conditions. In such cases, small effective changes in eigenvalues alter the evolution and result in altered phase portraits.

Under certain circumstances, the steady state solution of the system of mean-field evolution equations for the heterogeneous chemical reaction of type $A + B \longrightarrow C$, equations (5.2), (5.3) and (5.4), can be an unstable fixed point. This leads to the conclusion that, in practice, it is not possible to choose the initial conditions in numerical calculations in a way such that the late-time value of the evolution equations reaches the steady state value.

In analogy to the numerical investigations for the heterogeneous chemical reaction of type $A + A \longrightarrow C$ it is reasonable to start analysing the set of equations arising from the consideration of a chemical reaction network in the single-spatial site model and take values for the rate coefficients according to the M1 and M2 data. Since the mean-field rate equations do not form a stable system under all circumstances it is not clear whether the corresponding stochastic constraint equations will exhibit difficulties for particular choices of parameters. Special attention should be paid to the stability and convergence of the numerical evaluation of the constraints. Furthermore, under interstellar conditions, the rate coefficients for the various species involved in the heterogeneous chemical reactions can differ significantly in the order of magnitude. Thus, one is faced with a situation involving stochastic differential equations that are stiff.

Chapter 6

Heterogeneous Nucleation of Aerosols

This chapter is concerned with nucleation processes that take place on pre-existing particles that are assumed to be spherically symmetric. We study the formation of clusters on the seed and consider the Fletcher theory and the Becker-Döring theory where distinct choices of the rate coefficients in the evolution equations lead to qualitatively different behaviour in the development of the mean cluster concentrations on the surface of the seed particle. In the mean-field framework, we confront the theoretical predictions for the nucleation current with experimental observations and comment on the limitations of the methods. We proceed to develop a stochastic dynamical framework on the lines of calculations undertaken in the previous chapters. Nucleation is a fluctuation-driven phenomenon: each cluster has to overcome a free energy barrier if it is to grow into a droplet, and furthermore, local fluctuations in cluster populations can be instrumental in driving such a sensitive process forward. An analogy to a chemical reaction network can be made —cfr. Chapter 5— when one formulates the process of cluster formation as a nucleation ladder:

$$
\begin{aligned}
&monomer + monomer \leftrightarrows dimer \\
&monomer + dimer \leftrightarrows trimer \\
&monomer + trimer \leftrightarrows tetramer \\
&\vdots \\
&momomer + (\mathtt{i}_{max} - 1) - mer \leftrightarrows (\mathtt{i}_{max}) - mer.
\end{aligned}
$$

Monomers are independent molecules and `i`-mers are clusters of higher orders that consist of `i` molecules. We use this analogy to implement the same techniques on

heterogeneous nucleation processes as introduced to treat surface chemistry in small systems and derive an alternative stochastic framework according to the Doi-Peliti formalism to replace the traditional mean-field evolution equations, namely, the Becker-Döring rate equations (6.16).

We concentrate our investigations on one-component systems. The pre-existing particles or surfaces are assumed to be electrically neutral and insoluble to the nucleating fluid, i.e. we exclude the exchange of molecules between the surface of the seed and the vapour phase. Under normal circumstances it is safe to assume that there are many more monomers than clusters of higher orders in the vapour phase. Therefore, we only consider the gain of monomers to a cluster. In addition, we also assume that only monomers can be broken apart from a cluster of higher order. In the sequel, if not otherwise stated, evolution equations of any kind are solved assuming zero initial conditions. For *cluster size* we understand the order of the cluster $\mathtt{i}$, that is (in terms of the Classical Nucleation Theory), the number of monomers in a cluster, and not the radius of a cluster $r(\mathtt{i})$.

6.1 Mean-Field Heterogeneous Nucleation Theory

In this section, we present the Standard Nucleation Theory, the Fletcher Theory, and the Becker-Döring Model in the mean-field framework and develop the means to include the evolution of clusters according to diffusion processes on the surface of the seed particle in addition to the evolution of clusters due to the attachment of molecules to the cluster directly from the vapour phase. We compute the mean cluster populations and the nucleation current making several distinct assumptions on the form of the rate coefficients. Furthermore, we summarise the results of a specific experiment investigating heterogeneous nucleation on small seed particles and compare the theoretical predictions of the most realistic model for the rate coefficients with the experimental data with and without modifications of one of the input parameters, namely, the surface tension between the vapour and the liquid phase, that is the surface tension at the gas-cluster interface.

6.1.1 Fletcher Theory

In the standard heterogeneous nucleation theory, a critical cluster is formed on a pre-existing surface —the seed particle. If the seed particles are assumed to be spherically symmetric a critical cluster takes the form of a cap-shaped part of a

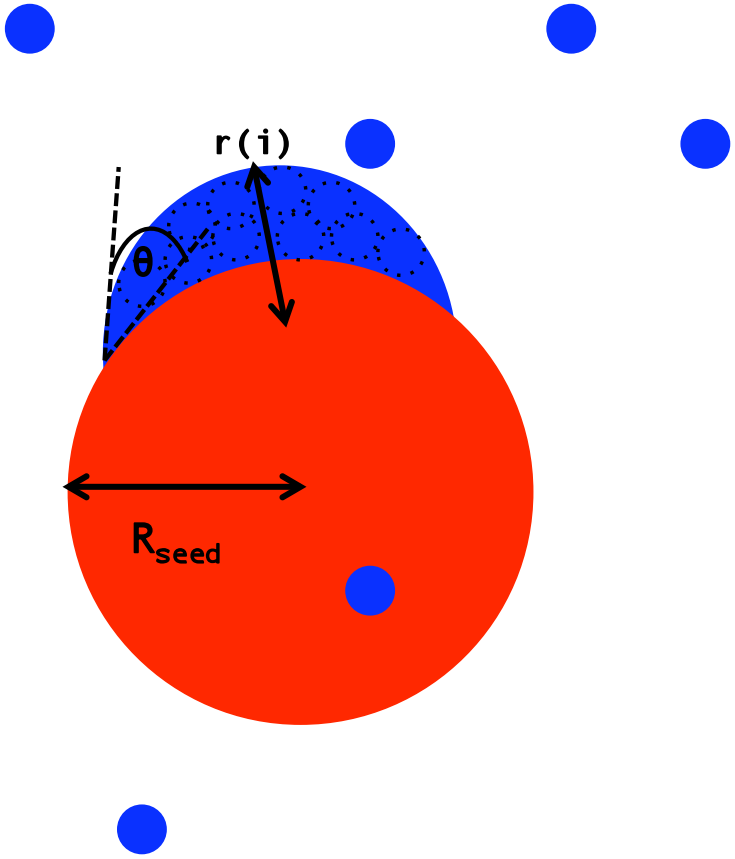

Figure 6.1: Cluster formation in classical heterogeneous nucleation theory. On a pre-existing seed particle — indicated by the red sphere with a radius of R_{seed}— monomers —illustrated by the blue spheres— can form clusters with radii $r(\mathtt{i})$ that are attached to the surface of the seed with a contact angle θ. The symbol $\mathtt{i}$ gives the number of monomers forming a cluster.

sphere attached to the curved surface of the seed —see Figure 6.1. There are several drawbacks of the *Fletcher model*. Foremost, the physical properties of a microscopic entity are assumed to be the same as the ones of a macroscopic quantity —the *capillarity approximation*. The assumption of a continuum model of the geometry is a bad approximation especially for small cluster sizes. Another limitation of the Classical Nucleation Theory is that there are no interactions of particles around the considered nuclei included in the model. Furthermore, the contact angle, that is the angle between the tangents to the solid surface (seed particle) and the liquid surface (cluster) and the surface tensions between the contact interfaces are taken to be constant for all clusters regardless of their sizes. Keeping these limitations in mind, we continue with our calculations in the Fletcher model.

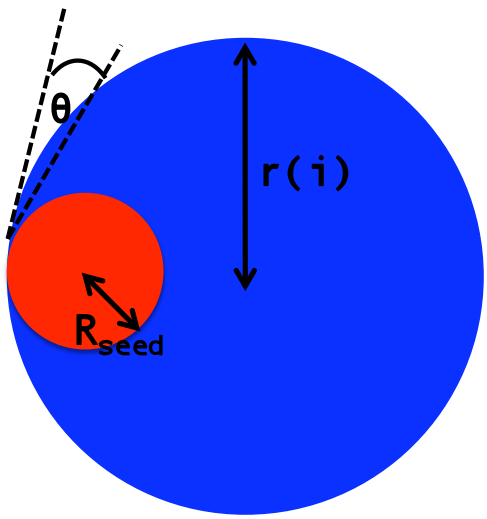

Figure 6.2: Completely wetted seed surface. The surface of the seed particle (red sphere) with radius R_{seed} is completely wetted by a cluster (blue sphere) with radius $r(\mathtt{i})$ and with a contact angle θ. In contrast to a monolayer, this is an asymmetric configuration.

We define the *contact angle* θ as the angle between the tangent to the pre-existing surface and the tangent to the cluster surface at the intersection point of the two surfaces —see Figure 6.1. The contact angle can be related to the surface tension between liquid (cluster) and solid (seed), $\sigma_{l,s}$ [Nm^{-1}], the surface tension between vapour (surrounding gas phase) and liquid (cluster), $\sigma_{v,l}$ [Nm^{-1}], and the surface tension between vapour (surrounding gas phase) and solid (seed), $\sigma_{v,s}$ [Nm^{-1}]. This relation is contained in *Young's Equation*:

$$\cos\theta = \frac{\sigma_{v,s} - \sigma_{l,s}}{\sigma_{v,l}}. \tag{6.1}$$

The nucleation current in the Fletcher model, $\mathcal{J}_{Fletcher}$, —see [18]—, is the rate at which critical clusters are formed per unit surface area of the seed particles. Its form stems from an *Arrhenius Ansatz* and reads

$$\mathcal{J}_{Fletcher} = K^* \exp\left(-\frac{\triangle G^*}{kT}\right) \quad [\mathrm{m}^{-2}\mathrm{s}^{-1}]. \tag{6.2}$$

The symbol $\triangle G^*$ [$\mathrm{m}^2\mathrm{kgs}^{-2}$] denotes the *formation free energy* or *nucleation barrier* of the critical cluster, T [K] is the temperature of the surface of the seed and k

$[\mathrm{m^2 kgs^{-2} K^{-1}}]$ the Boltzmann constant. The factor K^* is a kinetic pre-factor and is obtained via

$$K^* = Z^* \mathrm{g}^{dv}_{\mathtt{i}^*_{Fletcher}} \langle C_{mon,ads} \rangle \quad [\mathrm{m^{-2} s^{-1}}], \tag{6.3}$$

where Z^* is the *Zeldovich non-equilibrium factor* for heterogeneous nucleation processes, $\mathrm{g}^{dv}_{\mathtt{i}^*_{Fletcher}}$ the growth rate of the critical cluster $[\mathrm{s^{-1}}]$ and $\langle C_{mon,ads} \rangle$ $[\mathrm{m^{-2}}]$ the mean concentration of the surface-adsorbed monomers. The latter two expressions will be determined later on. The Zeldovich factor is defined as

$$Z^* := \sqrt{-\frac{1}{2\pi kT} \left(\frac{\partial^2 \triangle G(\mathtt{i})}{\partial \mathtt{i}^2} \right) \Bigg|_{\mathtt{i}=\mathtt{i}^*}} \quad [1], \tag{6.4}$$

where $\triangle G(\mathtt{i})$ is the formation free energy of a cluster of size $\mathtt{i}$. The Zeldovich factor can be calculated in the following way

$$\begin{aligned}
&Z^* := Z^*_{hom} f(r^*_{Fletcher}, R_{seed}, \theta), \\
&Z^*_{hom} := \frac{v_l \sqrt{\sigma_{v,l}}}{2\pi r^{*2}_{Fletcher} \sqrt{kT}}, \\
&f(r^*_{Fletcher}, R_{seed}, \theta) := 2 \left(2 + \frac{(1 - X\cos\theta)(2 - 4X\cos\theta - ((\cos\theta)^2 - 3)X^2))}{(1 - 2X\cos\theta + X^2)^{\frac{3}{2}}} \right)^{-\frac{1}{2}},
\end{aligned} \tag{6.5}$$

with v_l $[\mathrm{m^3}]$ the volume of a single molecule in the liquid phase and $\sigma_{v,l}$ the surface tension of the vapour-liquid interface and $X := R_{seed}(r^*_{Fletcher})^{-1}$. The factor $f(r^*_{Fletcher}, R_{seed}, \theta)$ takes into account the special geometry of a seed particle with radius R_{seed}. The Zeldovich factor for heterogeneous nucleation processes reduces to the one for homogeneous nucleation processes if either $\cos\theta = -1$ or $R_{seed}(r^*_{Fletcher})^{-1} = 0$. The Fletcher critical cluster radius is given by

$$r^*_{Fletcher} := \frac{2 v_l \sigma_{v,l}}{kT \ln(S)} \quad [\mathrm{m}], \tag{6.6}$$

where $S > 1$ [1] stands for the vapour phase saturation ratio defined as the fraction of the vapour pressure relative to the saturated vapour pressure. The above equation is also known as the *Kelvin equation* in homogeneous nucleation theory. The form of the radius of the heterogeneous critical cluster and of the radius of the homogeneous critical cluster coincide at the same temperature and vapour concentration since, at the critical cluster size $\mathtt{i}^*_{Fletcher}$, the liquid under the curved surface of the droplet (cluster) is in equilibrium with the vapour phase and the chemical potentials in all phases are

equal in equilibrium. In the Fletcher theory, the mean concentration of the adsorbed monomers on the surface of the pre-existing particle can be estimated via

$$\langle C_{mon,ads} \rangle \approx \frac{\mathrm{j}}{\mathrm{l}} \quad [\mathrm{m}^{-2}]. \tag{6.7}$$

where j $[\mathrm{m}^{-2}\mathrm{s}^{-1}]$ is the *source rate coefficient*, that is, the mean rate with which monomers are adsorbed onto the surface of the seed, and l $[\mathrm{s}^{-1}]$ the *evaporation rate coefficient*, that is, the mean rate with which monomers are evaporated from the surface of the seed. The growth rate of the critical cluster in the Fletcher theory, $\mathrm{g}^{dv}_{\mathtt{i}^*_{Fletcher}}$, is

$$\mathrm{g}^{dv}_{\mathtt{i}^*_{Fletcher}} = \mathrm{j} 2\pi r^{*2}_{Fletcher} \left(1 - \cos\left(\Psi\left(r^*_{Fletcher}, R_{seed}, \theta\right)\right)\right) \quad [\mathrm{s}^{-1}], \tag{6.8}$$

where the cosine in terms of the contact angle θ, and the radii r and R_{seed} reads

$$\cos\Psi[r, R_{seed}, \theta] = \frac{R_{seed}\cos\theta - r}{\sqrt{r^2 + R^2_{seed} - 2rR_{seed}\cos\theta}}. \tag{6.9}$$

The formation free energy of the critical cluster is given by

$$\triangle G(r^*_{Fletcher}) = \triangle G_{hom}(r^*_{Fletcher}) g(r^*_{Fletcher}, R_{seed}, \theta), \tag{6.10}$$

with

$$\begin{aligned}
&\triangle G_{hom}(r^*_{Fletcher}) = \frac{4\pi\sigma_{v,l} r^{*2}_{Fletcher}}{3}, \\
&g(r^*_{Fletcher}, R_{seed}, \theta) = \frac{1}{2}\left(1 + \left(\frac{1 - X\cos\theta}{\sqrt{1 + X^2 - 2X\cos\theta}}\right)^3 + \right. \\
&\quad X^3\left(2 - 3\frac{X - \cos\theta}{\sqrt{1 + X^2 - 2X\cos\theta}} + \left(\frac{X - \cos\theta}{\sqrt{1 + X^2 - 2X\cos\theta}}\right)^3\right) + \\
&\quad \left. 3X^2\cos\theta\left(\frac{X - \cos\theta}{\sqrt{1 + X^2 - 2X\cos\theta}} - 1\right)\right).
\end{aligned} \tag{6.11}$$

The existence of a foreign particle favours nucleation in the sense that the thermodynamic barrier, that is, the increase in the free energy of a system due to the formation of a cluster, decreases in value compared to a homogeneous nucleation —see the above equations and Figure 6.3. Alternatively, the formation free energy can be expressed as

$$\triangle G(r^*_{Fletcher}) = -\mathtt{i}^*_{Fletcher} \ln(S) kT + \sigma_{v,l} A_{v,l}(r^*_{Fletcher}) - \cos\theta\sigma_{v,l} A_{l,s}(r^*_{Fletcher}), \tag{6.12}$$

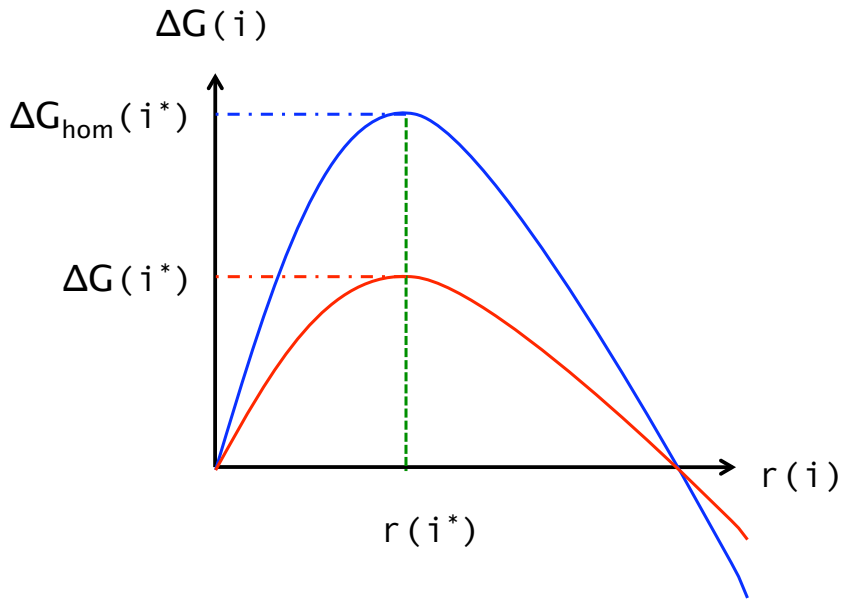

Figure 6.3: The dependence of the formation free energy $\triangle G(\mathtt{i})$ on the radius of the cluster of order $\mathtt{i}$. Although the nucleation barrier for homogeneous nucleation is greater than for heterogeneous nucleation, at the critical cluster size $\mathtt{i}^*$, both nucleation barriers —for homogeneous nucleation $\triangle G_{hom}(\mathtt{i})$ and for heterogeneous nucleation $\triangle G(\mathtt{i}^*)$— have a maximum.

with $\mathtt{i}^*_{Fletcher}$ the heterogeneous critical cluster size in Fletcher theory,

$$
\begin{aligned}
&\mathtt{i}^*_{Fletcher} = \mathtt{i}^*_{Fletcher;hom} h(r^*_{Fletcher}, R_{seed}, \theta), \\
&\mathtt{i}^*_{Fletcher;hom} := \frac{4\pi r^{*3}_{Fletcher}}{3v_l}, \\
&h(r^*_{Fletcher}, R_{seed}, \theta) := \\
&\quad \frac{1}{4}\left(2 + 3\frac{1 - X\cos\theta}{\sqrt{1 + X^2 - 2X\cos\theta}} - \left(\frac{1 - X\cos\theta}{\sqrt{1 + X^2 - 2X\cos\theta}}\right)^3\right) - \\
&\quad \frac{1}{4}\left(X^3\left(2 - 3\frac{X - \cos\theta}{\sqrt{1 + X^2 - 2X\cos\theta}} + \left(\frac{X - \cos\theta}{\sqrt{1 + X^2 - 2X\cos\theta}}\right)^3\right)\right).
\end{aligned}
\tag{6.13}
$$

The symbols $A_{v,l}(r^*_{Fletcher})$ and $A_{l,s}(r^*_{Fletcher})$ denote the area at the vapour-liquid interface, that is, the contact area between the gas-phase and the critical cluster, and the area at the liquid-solid interface, that is, the contact area between the critical cluster and the surface of the grain particle, respectively. Since the composition and the radius of the heterogeneous critical cluster are the same as that of the homogeneous critical

cluster at the same temperature and vapour concentrations, the number of molecules in a homogeneous critical cluster at the same conditions is greater than the number of molecules in a heterogeneous critical cluster —cfr. the above equations (6.13). Nevertheless, the maximum of $\triangle G_{hom}(r^*_{Fletcher})$ and $\triangle G(r^*_{Fletcher})$ appears at the same value of the radius $r^*_{Fletcher}$.

6.1.2 Becker-Döring Theory

In the Becker-Döring theory for heterogeneous nucleation processes, we distinguish between two different growth and decay processes —see Figure 6.4. In the direct vapour deposition mechanism, gas molecules can attach themselves to an existing cluster on the surface of the seed particle and can be evaporated from the cluster back into the surrounding gas phase. In the surface diffusion mechanism, clusters grow when molecules that are adsorbed onto the surface of the seed diffuse over the particle surface and eventually collide with another cluster and build up clusters of higher order. In the same fashion, molecules can be released from clusters and diffuse on the surface of the seed. In the sequel, superscripts "*dv*" indicate processes taking place according to the direct vapour deposition mechanism, superindices "*sd*" denote processes in the surface diffusion mechanism. The dynamics of nucleation are normally developed within a framework of embryo population dynamics, where the numbers of embryos of a given size in the system evolve according to particular embryonic growth and decay processes. The *Becker-Döring rate equations* [2] model the processes of gain and loss of molecules from clusters as chemical reactions without memory (*Markov processes*). In the sequel, we assume that clusters larger than $\mathtt{i}_{max}$ do not decay, that is, $\mathrm{d}^{dv}_{\mathtt{i}_{max}+1} = \mathrm{d}^{sd}_{\mathtt{i}_{max}+1} \equiv 0$. The evolution equations for the mean concentrations $\langle C_{\mathtt{i}}(t)\rangle$ [m^{-2}] of clusters of order $\mathtt{i}$ read

$$\begin{aligned}\frac{\mathrm{d}}{\mathrm{d}t}\langle C_{\mathtt{i}}(t)\rangle = \left(\mathrm{g}^{dv}_{\mathtt{i}-1} + \mathrm{g}^{sd}_{\mathtt{i}-1}(t)\right)\langle C_{\mathtt{i}-1}(t)\rangle - \left(\mathrm{d}^{dv}_{\mathtt{i}} + \mathrm{d}^{sd}_{\mathtt{i}}\right)\langle C_{\mathtt{i}}(t)\rangle - \\ \left(\mathrm{g}^{dv}_{\mathtt{i}} + \mathrm{g}^{sd}_{\mathtt{i}}(t)\right)\langle C_{\mathtt{i}}(t)\rangle + \left(\mathrm{d}^{dv}_{\mathtt{i}+1} + \mathrm{d}^{sd}_{\mathtt{i}+1}\right)\langle C_{\mathtt{i}+1}(t)\rangle,\end{aligned} \tag{6.14}$$

with the index $\mathtt{i} \in [2, ..., \mathtt{i}_{max}]$ and where g^{dv} [s^{-1}] is the growth rate coefficient in the direct vapour deposition mechanism, $\mathrm{g}^{sd}(t)$ [s^{-1}] the growth rate coefficient in the surface diffusion mechanism, d^{dv} [s^{-1}] the decay rate coefficient in the direct vapour deposition mechanism and d^{sd} [s^{-1}] the decay rate coefficient in the surface diffusion mechanism. For the dynamics of the mean concentration of monomers in the mean-field

framework, the equation of motion is given by

$$\frac{\mathrm{d}}{\mathrm{d}t}\langle C_1(t)\rangle = \mathrm{j} - \mathrm{l}\langle C_1(t)\rangle + \mathrm{d}_2^{dv}\langle C_2(t)\rangle - \mathrm{g}_1^{dv}\langle C_1(t)\rangle - \mathrm{g}_1^{sd}(t)\langle C_1(t)\rangle + \mathrm{d}_2^{sd}\langle C_2(t)\rangle - \sum_{\mathtt{i}=1}^{\mathtt{i}_{max}} \left(\mathrm{g}_{\mathtt{i}}^{sd}(t)\langle C_{\mathtt{i}}(t)\rangle - \mathrm{d}_{\mathtt{i}+1}^{sd}\langle C_{\mathtt{i}+1}(t)\rangle\right). \tag{6.15}$$

The factor of 2 in the surface diffusion terms $\mathrm{g}_1^{sd}(t)\langle C_1(t)\rangle$ and $\mathrm{d}_2^{sd}\langle C_2(t)\rangle$ in equation (6.15) arises from the fact that in the surface diffusion approach two monomers collide in order to form a dimer. However, in the direct vapour deposition approach a molecule from the gas phase lands on top of a monomer residing on the surface of the seed hence the coefficient of unity for the terms $\mathrm{g}_1^{dv}\langle C_1(t)\rangle$ and $\mathrm{d}_2^{dv}\langle C_2(t)\rangle$. The maximum size of clusters, $\mathtt{i}_{max}$, and hence the maximum number of equations, has to be chosen to be large enough to exceed the order of the critical cluster $\mathtt{i}^*$ comfortably. Since growth is more probable than decay for clusters above the critical size, the choice of a cluster sink boundary condition at $\mathtt{i}_{max} \gg \mathtt{i}^*$ is physically acceptable. The above mentioned processes are visualised in the schematic 6.5. As an alternative, it is also possible to formulate the Becker-Döring rate equations (6.14) and (6.15) for populations $\langle M_{\mathtt{i}}(t)\rangle$ [1] rather than for concentrations $\langle C_{\mathtt{i}}(t)\rangle$ [m^{-2}]. Consequently, we have

$$\begin{aligned}
\frac{\mathrm{d}}{\mathrm{d}t}\langle M_1(t)\rangle &= \mathrm{J} - \mathrm{L}\langle M_1(t)\rangle + \mathrm{D}_2^{dv}\langle M_2(t)\rangle - \mathrm{G}_1^{dv}\langle M_1(t)\rangle - \\
&\qquad \mathrm{G}_1^{sd}(t)\langle M_1(t)\rangle + \mathrm{D}_2^{sd}\langle M_2(t)\rangle - \sum_{\mathtt{j}=1}^{\mathtt{i}_{max}} \left(\mathrm{G}_{\mathtt{j}}^{sd}(t)\langle M_{\mathtt{j}}(t)\rangle - \mathrm{D}_{\mathtt{j}+1}^{sd}\langle M_{\mathtt{j}+1}(t)\rangle\right) \\
\frac{\mathrm{d}}{\mathrm{d}t}\langle M_{\mathtt{i}}(t)\rangle &= \left(\mathrm{G}_{\mathtt{i}-1}^{dv} + \mathrm{G}_{\mathtt{i}-1}^{sd}(t)\right)\langle M_{\mathtt{i}-1}(t)\rangle - \left(\mathrm{D}_{\mathtt{i}}^{dv} + \mathrm{D}_{\mathtt{i}}^{sd}\right)\langle M_{\mathtt{i}}(t)\rangle - \\
&\qquad \left(\mathrm{G}_{\mathtt{i}}^{dv} + \mathrm{G}_{\mathtt{i}}^{sd}(t)\right)\langle M_{\mathtt{i}}(t)\rangle + \left(\mathrm{D}_{\mathtt{i}+1}^{dv} + \mathrm{D}_{\mathtt{i}+1}^{sd}\right)\langle M_{\mathtt{i}+1}(t)\rangle,
\end{aligned} \tag{6.16}$$

where the index $\mathtt{i}$ in the second of the above equations runs from two until the maximum number of $\mathtt{i}$-mers. The rate coefficients now read

$$\begin{aligned}
&\mathrm{g}_{\mathtt{i}}^{sd}(t) := \mathrm{g}_{\mathtt{i}}^{\prime sd}\langle C_1(t)\rangle \quad [\mathrm{s}^{-1}],\\
&\mathrm{G}_{\mathtt{i}}^{sd}(t) := \mathrm{G}_{\mathtt{i}}^{\prime sd}\langle M_1(t)\rangle \quad [\mathrm{s}^{-1}], \quad \text{with: } \mathrm{G}_{\mathtt{i}}^{\prime sd} = \frac{\mathrm{g}_{\mathtt{i}}^{\prime sd}}{4\pi R_{seed}^2} \quad [\mathrm{s}^{-1}],\\
&\mathrm{J} = \mathrm{j}4\pi R_{seed}^2 \quad [\mathrm{s}^{-1}],\\
&\mathrm{l} = \mathrm{L} \quad [\mathrm{s}^{-1}],\\
&\mathrm{d}_{\mathtt{i}}^{dv} = \mathrm{D}_{\mathtt{i}}^{dv} \quad [\mathrm{s}^{-1}], \quad \text{and} \quad \mathrm{d}_{\mathtt{i}}^{sd} = \mathrm{D}_{\mathtt{i}}^{sd} \quad [\mathrm{s}^{-1}],\\
&\mathrm{g}_{\mathtt{i}}^{dv} = \mathrm{G}_{\mathtt{i}}^{dv} \quad [\mathrm{s}^{-1}].
\end{aligned} \tag{6.17}$$

The next step is to derive explicit expressions for the above rate coefficients, namely the source rate J or j, the evaporation rate L or l, the growth rates $\mathrm{G}_{\mathtt{i}}$ or $\mathrm{g}_{\mathtt{i}}$ and the decay rates $\mathrm{D}_{\mathtt{i}}$ or $\mathrm{d}_{\mathtt{i}}$ in the direct vapour deposition mechanism and in the surface diffusion mechanism.

Rate Coefficients: Power Law Model

The following investigations are based on the determination of the free parameters of the equations (6.14) and (6.15) as introduced in [3], namely the rate J at which monomers attach themselves onto the surface of the seed particle, the rate L at which monomers evaporate from the surface of the seed particle, the rate $\mathrm{D}_{\mathtt{i}}$ at which monomers are lost from a cluster of size $\mathtt{i} \geq 2$ and the rate $\mathrm{G}_{\mathtt{i}}^{\prime}$ at which monomers attach themselves onto a cluster of size $\mathtt{i} \geq 2$. In [3] the direct vapour deposition mechanism was ignored, hence

$$\begin{aligned}
&\mathrm{G}_{\mathtt{i}}^{dv} = \mathrm{D}_{\mathtt{i}}^{dv} \equiv 0,\\
&\mathrm{G}_{\mathtt{i}}^{\prime} := \mathrm{G}_{\mathtt{i}}^{\prime sd}, \quad \text{and} \quad \mathrm{D}_{\mathtt{i}} := \mathrm{D}_{\mathtt{i}}^{sd},
\end{aligned}$$

for all orders $\mathtt{i}$. Let us summarise the assumptions of the model for the rate coefficients in the Becker-Döring theory presented in [3].

Definition. *We define a dimensionless* size parameter χ *which is proportional to the surface area of the seed particle.*

Assumptions.

- *We assume that* $\chi \stackrel{!}{=} 1$ *gives the system with a nominal mean monomer population of unity.*

- *We assume that the evaporation rates* L *and* $D_{\mathtt{i}}$ *are independent of the surface area of the seed particle and hence independent of the size parameter.*

- *Furthermore, we assume that*

$$J(\chi) = J_0 \chi \quad [s^{-1}], \tag{6.18}$$

with

$$J_0 := J(\chi)|_{\chi=1} \quad [s^{-1}]. \tag{6.19}$$

Considering the dynamics in absence of any dimer production we obtain that $\langle M_1 \rangle \sim JL^{-1}$*, from which it follows that* $L = J_0$*. Therefore, we have*

$$J(\chi) = L\chi. \tag{6.20}$$

- *The growth rates* $G'_{\mathtt{i}}$ *are assumed to be independent of the cluster size that is*

$$G'_{\mathtt{i}} \equiv G' \quad [s^{-1}] \quad \forall \mathtt{i}. \tag{6.21}$$

We define

$$G'_0 := G'(\chi)|_{\chi=1}. \tag{6.22}$$

We assume that

$$G'(\chi) = G'_0 \chi^{-1}. \tag{6.23}$$

From

$$G_{\mathtt{i}}(\chi; t) = G'_{\mathtt{i}}(\chi) \langle M_1(t) \rangle \tag{6.24}$$

and together with the assumption that $G_0 \stackrel{!}{=} 1$ *we conclude that*

$$G(\chi; t) = \chi^{-1} \langle M_1(t) \rangle \quad [s^{-1}]. \tag{6.25}$$

- *Let* $\mathtt{i}^*$ *be the critical size of a cluster. From the assumption* $D_{\mathtt{i}^*} = G'_{\mathtt{i}^*} \langle M_1 \rangle$ *it follows that*

$$D_{\mathtt{i}^*} = 1 \quad \forall \chi. \tag{6.26}$$

We choose

$$D_{\mathtt{i}} = \left(\frac{\mathtt{i}^*}{\mathtt{i}} \right)^c, \tag{6.27}$$

where c is a constant to be freely determined.

For clusters of size $\mathtt{i} < \mathtt{i}^*$ the probability of a decay process is high whereas for clusters of size $\mathtt{i} > \mathtt{i}^*$ the probability of growth is high. This is illustrated in Figure 6.6 and Figure 6.8. To the left of the intersection point between the graphs of the growth rates $G'_{\mathtt{i}}$ and the decay rates $D_{\mathtt{i}}$ the probability for loss of monomers from the cluster is higher than to the right of the intersection point, i.e. the probability for growth of a cluster is higher on the right of the intersection point than it is to the left of the intersection point. For greater values of the critical cluster size $\mathtt{i}^*$ the intersection point shifts further to the right. For greater values of the constant c the curve of the loss rate coefficient $\mathrm{D}_{\mathtt{i}}$ gets steeper.

The mean-field evolution equations (6.16) with the particular choice of the rate coefficients take the form

$$\begin{aligned}
\frac{\mathrm{d}}{\mathrm{d}t}\langle M_1(t)\rangle &= \mathrm{L}\left(\chi - \langle M_1(t)\rangle\right) - 2\left(\frac{\langle M_1(t)\rangle^2}{\chi} - \left(\frac{\mathtt{i}^*}{2}\right)^c \langle M_2(t)\rangle\right) - \\
&\qquad \sum_{\mathtt{j}=2}^{\mathtt{i}_{max}-1}\left(\frac{\langle M_1(t)\rangle\langle M_{\mathtt{j}}(t)\rangle}{\chi} - \left(\frac{\mathtt{i}^*}{\mathtt{j}+1}\right)^c \langle M_{\mathtt{j}+1}(t)\rangle\right) - \frac{\langle M_1(t)\rangle\langle M_{\mathtt{i}_{max}}(t)\rangle}{\chi}, \\
\frac{\mathrm{d}}{\mathrm{d}t}\langle M_{\mathtt{i}}(t)\rangle &= \frac{\langle M_1(t)\rangle\langle M_{\mathtt{i}-1}(t)\rangle - \langle M_1(t)\rangle\langle M_{\mathtt{i}}(t)\rangle}{\chi} + \\
&\qquad \left(\frac{\mathtt{i}^*}{\mathtt{i}+1}\right)^c \langle M_{\mathtt{i}+1}(t)\rangle - \left(\frac{\mathtt{i}^*}{\mathtt{i}}\right)^c \langle M_{\mathtt{i}}(t)\rangle, \\
\frac{\mathrm{d}}{\mathrm{d}t}\langle M_{\mathtt{i}_{max}}(t)\rangle &= \frac{\langle M_1(t)\rangle\langle M_{\mathtt{i}_{max}-1}(t)\rangle - \langle M_1(t)\rangle\langle M_{\mathtt{i}_{max}}(t)\rangle}{\chi} - \\
&\qquad \left(\frac{\mathtt{i}^*}{\mathtt{i}_{max}}\right)^c \langle M_{\mathtt{i}_{max}}(t)\rangle.
\end{aligned} \tag{6.28}$$

In [3] the model constants were chosen such that $\mathtt{i}^* = 2$ and $c = 2$, and the maximum order of $\mathtt{i}$-mers was taken to be 4. We proceed by performing a stability analysis for a system of four mean-field evolution equations. The above equations (6.28) for

$\mathtt{i}_{max} = 4$, $\mathtt{i}^* = 2$ and $c = 2$ reduce to

$$\begin{aligned}
\frac{\mathrm{d}}{\mathrm{d}t}\langle M_1(t)\rangle &= \mathrm{L}(\chi - \langle M_1(t)\rangle) - \frac{2\langle M_1(t)\rangle^2 + \langle M_1(t)\rangle\langle M_2(t)\rangle}{\chi} - \\
&\quad - \frac{\langle M_1(t)\rangle\langle M_3(t)\rangle + \langle M_1(t)\rangle M_4(t)\rangle}{\chi} + \frac{4\langle M_3(t)\rangle}{9} + \frac{\langle M_4(t)\rangle}{4} + 2\langle M_2(t)\rangle, \\
\frac{\mathrm{d}}{\mathrm{d}t}\langle M_2(t)\rangle &= \frac{\langle M_1(t)\rangle^2 - \langle M_1(t)\rangle\langle M_2(t)\rangle}{\chi} + \frac{4\langle M_3(t)\rangle}{9} - \langle M_2(t)\rangle, \\
\frac{\mathrm{d}}{\mathrm{d}t}\langle M_3(t)\rangle &= \frac{\langle M_1(t)\rangle\langle M_2(t)\rangle - \langle M_1(t)\rangle\langle M_3(t)\rangle}{\chi} + \frac{\langle M_4(t)\rangle}{4} - \frac{4\langle M_3(t)\rangle}{9}, \\
\frac{\mathrm{d}}{\mathrm{d}t}\langle M_4(t)\rangle &= \frac{\langle M_1(t)\rangle\langle M_3(t)\rangle - \langle M_1(t)\rangle\langle M_4(t)\rangle}{\chi} - \frac{\langle M_4(t)\rangle}{4}.
\end{aligned} \tag{6.29}$$

In analogy to the analysis undertaken in Chapter 5, we solve the stationary mean-field equations arising from (6.29). We undertake numerical investigations in `MAPLE 11` for $\mathrm{L} = 100\mathrm{s}^{-1}$ and $\chi = \{10^3, 10^2, 10^1, 10^0, 10^{-1}, 10^{-2}, 10^{-3}\}$ and for $\mathrm{L} = 1\mathrm{s}^{-1}$ and $\chi = \{10^3, 10^2, 10^1, 10^0, 10^{-1}, 10^{-2}, 10^{-3}\}$. We obtain five steady state solutions for each order of $\mathtt{i}$-mer but in each case only one of these steady state solutions is real and positive which is a necessary condition for a physically meaningful solution to the stationary equations. These strictly positive steady state solutions $\mathring{\mathbf{m}} := (\mathring{M}_1, \mathring{M}_2, \mathring{M}_3, \mathring{M}_4)^T$ are given in Tables 6.1 and 6.2. The linearised mean-field evolution equations take the form

$$\frac{\mathrm{d}}{\mathrm{d}t}\mathbf{v}(t) = \mathbf{J}\big|_{\mathring{\mathbf{m}}}\mathbf{v}(t) + \mathbf{w}, \tag{6.30}$$

where

$$\begin{aligned}
\mathbf{v}(t) &:= \mathbf{m}(t) - \mathring{\mathbf{m}}, \\
\mathbf{J}\big|_{\mathring{\mathbf{m}}} &:= \begin{pmatrix}
-\mathrm{L} - \frac{4\mathring{M}_1 + \mathring{M}_2 + \mathring{M}_3 + \mathring{M}_4}{\chi} & 2 - \frac{\mathring{M}_1}{\chi} & \frac{4}{9} - \frac{\mathring{M}_1}{\chi} & \frac{1}{4} - \frac{\mathring{M}_1}{\chi} \\
\frac{2\mathring{M}_1 - \mathring{M}_2}{\chi} & -1 - \frac{\mathring{M}_1}{\chi} & \frac{4}{9} & 0 \\
\frac{\mathring{M}_2 - \mathring{M}_3}{\chi} & \frac{\mathring{M}_1}{\chi} & -\frac{\mathring{M}_1}{\chi} - \frac{4}{9} & \frac{1}{4} \\
\frac{\mathring{M}_3 - \mathring{M}_4}{\chi} & 0 & \frac{\mathring{M}_1}{\chi} & -\frac{\mathring{M}_1}{\chi} - \frac{1}{4}
\end{pmatrix}, \\
\mathbf{w} &:= \begin{pmatrix}
\mathrm{L}(\chi - \mathring{M}_1) - \frac{2\mathring{M}_1(\mathring{M}_1 + \mathring{M}_2 + \mathring{M}_3 + \mathring{M}_4)}{\chi} + \frac{4\mathring{M}_3}{9} + \frac{\mathring{M}_4}{4} + 2\mathring{M}_2 \\
\frac{\mathring{M}_1(\mathring{M}_1 - \mathring{M}_2)}{\chi} + \frac{4\mathring{M}_3}{9} - \mathring{M}_2 \\
\frac{\mathring{M}_1(\mathring{M}_2 - \mathring{M}_3)}{\chi} + \frac{\mathring{M}_4}{4} - \frac{4\mathring{M}_3}{9} \\
\frac{\mathring{M}_1(\mathring{M}_3 - \mathring{M}_4)}{\chi} - \frac{\mathring{M}_4}{4}
\end{pmatrix}.
\end{aligned} \tag{6.31}$$

We shift the constant vector $\mathbf{w}$ in order to obtain a system of equations that are homogeneous in $\mathbf{v}(t)$. The eigenvalues of the Jacobian matrix $\mathbf{J}\big|_{\mathring{\mathbf{m}}}$ which are calculated in MAPLE 11 are real and negative for the above mentioned choices of L and χ.

Therefore, in contrast to the heterogeneous chemical reaction of type $A+B \longrightarrow C$, the strictly positive steady state solution is a stable node[1]. The numerical calculation of solutions to the mean-field evolution equations for an order of four $\mathtt{i}$-mers —equation (6.29)— for $\mathrm{L} = 100\mathrm{s}^{-1}$ and $\chi = \{10^3, 10^2, 10^1, 10^0, 10^{-1}, 10^{-2}, 10^{-3}\}$ as well as for $\mathrm{L} = 1\mathrm{s}^{-1}$ and $\chi = \{10^3, 10^2, 10^1, 10^0, 10^{-1}, 10^{-2}, 10^{-3}\}$ was undertaken in a programme written in the computer language C. As expected the mean-field equilibrium values for late times and the mean-field steady state values coincide.

In a next step, we analyse under which conditions the power law model for the rate coefficients fulfills the convergence behaviour that one expects from physical considerations. For all orders of $\mathtt{i}$-mers it should hold —for the steady state solution $\langle M_{\mathtt{i}} \rangle^{ss}$ as well as for the dynamical solution $\langle M_{\mathtt{i}}(t_\infty) \rangle$ at late times t_∞, that is, the time when equilibrium has been reached — that

$$\begin{aligned} \lim_{\mathtt{i}_{max} \to \infty} \langle M_{\mathtt{i}}(\mathtt{i}_{max}) \rangle^{ss} &= \langle \bar{M}_{\mathtt{i}} \rangle^{ss} \equiv \text{constant} \quad \forall \mathtt{i}, \\ \lim_{\mathtt{i}_{max} \to \infty} \langle M_{\mathtt{i}}(\mathtt{i}_{max}; t_\infty) \rangle &= \langle \bar{M}_{\mathtt{i}}(t_\infty) \rangle \equiv \text{constant} \quad \forall \mathtt{i}, \end{aligned} \tag{6.32}$$

and

$$\begin{aligned} \lim_{\mathtt{i} \to \mathtt{i}_{max}} \langle M_{\mathtt{i}} \rangle^{ss} &= \langle M_{\mathtt{i}_{max}} \rangle^{ss}, \\ \lim_{\mathtt{i} \to \mathtt{i}_{max}} \langle M_{\mathtt{i}}(t_\infty) \rangle &= \langle M_{\mathtt{i}_{max}}(t_\infty) \rangle. \end{aligned} \tag{6.33}$$

We solve the Becker-Döring rate equations with the rate coefficients according to the assumptions mentioned in 6.1.2 —see equations (6.28)— for $\mathrm{J} = 1000\mathrm{s}^{-1}$ and $\mathrm{L} = 100\mathrm{s}^{-1}$ as well as for $\mathrm{J} = 10\mathrm{s}^{-1}$ and $\mathrm{L} = 1\mathrm{s}^{-1}$ and for the following three choices of model parameters:

- Model 1: $\mathrm{G}' = 0.1\mathrm{s}^{-1}$, $\mathrm{D}_i = \left(\frac{\mathtt{i}^*}{\mathtt{i}}\right)^c$ where $c = 2$ and $\mathtt{i}^* = 2$;
- Model 2: $\mathrm{G}' = 0.1\mathrm{s}^{-1}$, $\mathrm{D}_i = \left(\frac{\mathtt{i}^*}{\mathtt{i}}\right)^c$ where $c = 5$ and $\mathtt{i}^* = 2$;
- Model 3: $\mathrm{G}' = 0.1\mathrm{s}^{-1}$, $\mathrm{D}_i = \left(\frac{\mathtt{i}^*}{\mathtt{i}}\right)^c$ where $c = 2$ and $\mathtt{i}^* = 10$.

[1]It is important to note that one cannot conclude stability for the stochastic evolution equations from the system of mean-field evolution equations even when the deterministic part of the stochastic equations is identical to the mean-field evolution equations as it was the case for the heterogeneous chemical reactions. The addition of a stochastic noise term to a deterministic ordinary differential equation can stabilise an unstable system. Similarly, the addition of a noise term can destabilise a stable system of ordinary differential equations. Since the solutions to the mean-field evolution equations and the solutions according to the Doi-Peliti formalism have to coincide in the deterministic regime we can at least test the stability of the stochastic constraint equations in the deterministic regime by comparison.

For Model 1 and Model 2 we repeat the numerical computations for a maximum order of $\mathtt{i}$-mers $\mathtt{i}_{max} \in [5, 10, 15, 20, 25, 30]$ whereas for Model 3 we repeat the numerical computations for a maximum order of $\mathtt{i}$-mers $\mathtt{i}_{max} \in [15, 20, 25, 30]$. We list the mean late-time $\mathtt{i}$-mers populations $\langle M_{\mathtt{i}}(t_\infty)\rangle$ in Tables E.1, E.2, E.3, E.4, E.5, E.6, E.7, E.8, E.9, E.10, E.11, E.12 in the appendix and visualise the results of our findings in the following Figures: in Figures 6.10, 6.12, and 6.14 we plot the dependence of the mean late-time monomer population on the maximum order of $\mathtt{i}$-mers for Model 1, Model 2 and Model 3, respectively. Figures 6.11, 6.13, and 6.15 show the dependence of the mean late-time cluster populations on the order of $\mathtt{i}$-mers for a maximum order of $\mathtt{i}_{max} = 30$ for Model 1, Model 2 and Model 3, respectively. The convergence behaviour according to (6.32) is represented in Figures 6.10, 6.12, and 6.14 and the convergence behaviour according to (6.33) is reflected in Figures 6.11, 6.13, and 6.15. For Model 1 and Model 2, the convergence with regards to (6.32) is slow whereas for Model 3 we observe only a marginally small change in the dependence on the maximum number of $\mathtt{i}$-mers. It seems that this particular convergence behaviour depends on the choice of the value of the critical cluster employed in the expression of the decay rate. The convergence behaviour according to (6.33) is well reflected in Figure 6.15 although there is an indistinguishable difference in the mean late-time cluster populations for a choice of $\mathrm{J} = 1000\mathrm{s}^{-1}$ compared to the mean late-time cluster populations with $\mathrm{J} = 1\mathrm{s}^{-1}$. The respective changes in the value of the mean late-time cluster populations for Model 1 and Model 2 are large for smaller cluster sizes and almost negligible for larger cluster sizes.

Furthermore, we investigate the consequences of the choice of model parameters regarding the nucleation current. The *dynamical nucleation current* or *dynamical nucleation rate* in the Becker-Döring model is defined as

$$\mathcal{J}_{BD,dyn}(t_\infty) \equiv \frac{\mathrm{d}}{\mathrm{d}t}\langle M_{\mathtt{i}_{max+1}}(t)\rangle\Big|_{t_\infty} = \left(\left(\mathrm{G}^{dv}_{\mathtt{i}_{max}} + \mathrm{G}'^{sd}_{\mathtt{i}_{max}}\langle M_1(t)\rangle\right)\langle M_{\mathtt{i}_{max}}(t)\rangle\right)\Big|_{t_\infty}, \tag{6.34}$$

where it is assumed that clusters of order $\mathtt{i}_{max}$ do not decay, that is $\mathrm{D}^{dv}_{\mathtt{i}_{max}+\mathtt{m}} = \mathrm{D}^{dv}_{\mathtt{i}_{max}+\mathtt{m}} \equiv 0$ for all $\mathtt{m} \in \mathbb{N}$. The dynamical nucleation current for Model 1, Model 2 —where $\mathtt{i}_{max} \in [5, 10, 15, 20, 25, 30]$— and Model 3 —where $\mathtt{i}_{max} \in [15, 20, 25, 30]$— are listed in Tables 6.3, 6.4, 6.5. One observes that in Model 1 and Model 2 the difference in percentage, $\triangle$, between the nucleation current computed for $\mathtt{i}_{max} \equiv \mathtt{k}$ and the nucleation current computed for $\mathtt{i}_{max} \equiv \mathtt{k} + 5$ for the same model constants is much greater for $\mathrm{L} = 1\mathrm{s}^{-1}$ than for $\mathrm{L} = 100\mathrm{s}^{-1}$. Although the difference between $\mathcal{J}_{BD,dyn}(\mathrm{L} = 100\mathrm{s}^{-1})$ and $\mathcal{J}_{BD,dyn}(\mathrm{L} = 1\mathrm{s}^{-1})$ is great for Model 1 and Model 2 this is

not the case for Model 3. A convergence of the nucleation rate with regards to the maximum order of i-mers is evident for Model 1 and Model 2 for any choice of rate coefficients whereas for Model 3 the convergence is insignificant. The difference between the nucleation currents in Model 1 and Model 2 for fixed rate coefficients is rather small whereas the difference in the nucleation currents between Model 1 and Model 3 as well as Model 2 and Model 3 is large. The qualitative behaviour of the models with regards to the nucleation current depends, again, on the size of the critical cluster.

Rate Coefficients: Fletcher Theory

The particular form of the rate coefficients which we consider in this part of the thesis stems from the Fletcher theory and can be determined from the kinetic gas theory. The rate coefficient j, the *source rate*, gives the monomer flux per unit area and unit time. It takes the form

$$\mathrm{j} = \frac{pS}{\sqrt{2\pi m k T}} \quad [\mathrm{s}^{-1}\mathrm{m}^{-2}], \tag{6.35}$$

where p is the saturation vapour pressure ($[\mathrm{Nm}^{-2}]$), S is the vapour phase saturation ratio, m is the molecular mass of a gas molecule ([kg]), k the Boltzmann constant ($[\mathrm{m}^2\mathrm{kgs}^{-2}\mathrm{K}^{-1}]$) and T the temperature ([K]). The evaporation rate l determines the process of evaporation of molecules back into the vapour phase and is given by

$$\mathrm{l} = \nu \exp\left(-\frac{L}{kT}\right) \quad [\mathrm{s}^{-1}], \tag{6.36}$$

where ν is the vibration frequency ($[\mathrm{s}^{-1}]$) and L the latent heat per molecule ([Nm]). The symbol $\mathrm{g}_{\mathtt{i}}^{dv}$ denotes the growth rate in the direct vapour deposition mechanism ($[\mathrm{s}^{-1}]$) for a cluster of size i, the symbol $\mathrm{d}_{\mathtt{i}+1}^{dv}$ the decay rate by direct emission of a monomer to the vapour phase ($[\mathrm{s}^{-1}]$) for a cluster of size $\mathtt{i}+1$. In order to employ a more realistic model for the rate coefficients one has to assign a radius $r(\mathtt{i})$ to each cluster of any order i. The form of the radius $r(\mathtt{i})$ is derived from the assumption that the volume of the cap-shaped liquid phase V_{cap} is equal to the total volume of all molecules in the cluster combined

$$V_{cap} \stackrel{!}{=} \mathtt{i} v_l. \tag{6.37}$$

where v_l denotes the volume of a single molecule in the liquid phase and i is the number of monomers in the cluster. We are aware of the error that arises from the *packaging problem*, that is, the over-estimation of the volume of the cluster, but in the Fletcher theory this is neglected. For a planar seed particle without boundaries, the volume of

the cap is simply

$$V_{cap} = \frac{\pi}{3} r^3 (2 - 3\cos\theta + \cos^3\theta). \tag{6.38}$$

One can determine the radius $r(\mathtt{i})$ of an $\mathtt{i}$-mer employing the approximation for the volume of the cluster (6.37) and solve for $r(\mathtt{i})$

$$r(\mathtt{i}) = \sqrt[3]{\frac{3\mathtt{i}v_l}{\pi(2 - 3\cos(\theta) + \cos(\theta)^3)}}. \tag{6.39}$$

Special cases for different values of the contact angle are summarised in Table 6.6. For the computation of the rate coefficients it is important to know the form of the surface areas of the contact interfaces which, for a planar seed, are given by

$$\begin{aligned} A_{v,l} &= 2\pi r^2 (1 - \cos\theta), \\ A_{l,s} &= \pi r^2 \sin^2\theta. \end{aligned} \tag{6.40}$$

In the case of a spherically symmetric seed particle, the volume of the cluster (in fact, the cap of the spherically symmetric cluster attached to the surface of the seed) can be obtained via

$$\begin{aligned} V_{cap} = \frac{\pi}{3} r^3 \left(2 - 3\cos\Psi[r, R_{seed}, \theta] + \cos^3\Psi[r, R_{seed}, \theta]\right) - \\ \frac{\pi}{3} R_{seed}^3 \left(2 - 3\cos\phi[r, R_{seed}, \theta] + \cos^3\phi[r, R_{seed}, \theta]\right). \end{aligned} \tag{6.41}$$

The cosines can be expressed in terms of the contact angle θ, and the radii r and R_{seed},

$$\begin{aligned} \cos\Psi[r, R_{seed}, \theta] &= \frac{R_{seed}\cos\theta - r}{\sqrt{r^2 + R_{seed}^2 - 2rR_{seed}\cos\theta}}, \\ \cos\phi[r, R_{seed}, \theta] &= \frac{R_{seed} - r\cos\theta}{\sqrt{r^2 + R_{seed}^2 - 2rR_{seed}\cos\theta}}. \end{aligned} \tag{6.42}$$

The homogeneous case corresponds to $R_{seed} = 0$ or $\theta = \pi$. Note that

$$r^*_{Fletcher} = r(\mathtt{i}^*_{Fletcher}). \tag{6.43}$$

Unfortunately, it is not possible to give an explicit expression for $r(\mathtt{i})$ on these terms. However, combining equations (6.41) and (6.37) one can numerically determine the value of the radius of the cluster, $r(\mathtt{i}) := r(\mathtt{i}, v_l, R_{seed}, \theta)$, which depends on the number of monomers in the cluster $\mathtt{i}$, on the volume of the monomer in the liquid phase v_l, on the radius of the seed R_{seed} and on the contact angle θ. We calculate the growth rate

in the direct vapour deposition mechanism in the following way:

$$\mathrm{g}_{\mathtt{i}}^{dv} = \mathrm{j} A_{v,l}(r(\mathtt{i})) \quad [\mathrm{s}^{-1}], \tag{6.44}$$

where the cap area at the vapour-liquid interface is given by

$$A_{v,l}(r(\mathtt{i})) = 2\pi r(\mathtt{i})^2 \left(1 - \cos\left(\Psi(r(\mathtt{i}), R_{seed}, \theta)\right)\right) \quad [\mathrm{m}^2]. \tag{6.45}$$

The loss rate in the direct vapour deposition mechanism is determined via the expression

$$\mathrm{d}_{\mathtt{i}+1}^{dv} = \left(\mathrm{g}_{\mathtt{i}}^{dv} \exp\left(\frac{\triangle G_{\mathtt{i}+1} - \triangle G_{\mathtt{i}}}{kT}\right)\right)\Bigg|_{S=1} \quad [\mathrm{s}^{-1}], \tag{6.46}$$

where the formation free energy of a cluster of order $\mathtt{i}$ takes the form

$$\triangle G_{\mathtt{i}} = \sigma_{v,l}\left(A_{v,l}(r(\mathtt{i})) - A_{l,s}(r(\mathtt{i}))\cos\theta\right) - \mathtt{i}kT\ln(S) \quad [\mathrm{Nm}], \tag{6.47}$$

with the cap area at the liquid-solid interface

$$A_{l,s}(r(\mathtt{i})) = 2\pi R_{seed}^2 \left(1 - \cos\left(\Phi(r(\mathtt{i}), R_{seed}, \theta)\right)\right) \quad [\mathrm{m}^2], \tag{6.48}$$

and with $\sigma_{v,l}$ the surface tension of the vapour-liquid interface ($[\mathrm{Nm}^{-1}]$). We base equation (6.46) on the requirement of detailed balance in the saturated equilibrium between vapour and liquid phase, that is when the saturation ratio is taken to be equal to one. The derivation of the rate coefficients in the surface diffusion mechanism follows that of the rate coefficients in the direct vapour deposition mechanism except that the growth rate coefficient in the surface diffusion mechanism depends on the unknown mean adsorbed monomer concentration, namely,

$$\mathrm{g}_{\mathtt{i}}^{sd}(t) = \mathrm{g}_{\mathtt{i}}^{\prime sd}\langle C_1(t)\rangle \quad [\mathrm{s}^{-1}], \tag{6.49}$$

where the constant factor $\mathrm{g}_{\mathtt{i}}^{\prime sd}$ is determined by the number of molecules in a circular region around the cluster, times the vibration frequency leading to jumps, times an exponential function containing the activation energy for surface diffusion:

$$\mathrm{g}_{\mathtt{i}}^{\prime sd} = 2\pi R_{seed}\delta \sin\left(\Phi(r(\mathtt{i}), R_{seed}, \theta)\right)\nu \exp\left(-\frac{E}{kT}\right) \quad [\mathrm{m}^2\mathrm{s}^{-1}], \tag{6.50}$$

where δ is the average jumping distance ([m]), and E is the energy of the surface diffusion process ([Nm]) [63]. The decay rate in the surface diffusion mechanism can

be obtained via

$$\mathrm{d}_{\mathtt{i}+1}^{sd} = \left(\frac{\mathrm{g}_{\mathtt{i}}^{\prime sd}\mathrm{j}}{\mathrm{l}} \exp\left(\frac{\triangle G_{\mathtt{i}+1} - \triangle G_{\mathtt{i}}}{kT} \right) \right) \Bigg|_{S=1} \quad [\mathrm{s}^{-1}], \tag{6.51}$$

which is again derived from a detailed balance argument. The form of the rate coefficients as derived above can be inserted into the Becker-Döring rate equations (6.14) and (6.15) which are then solved numerically. Alternatively, one can consider the stationary Becker-Döring equations for the steady state mean concentration of the i-mers, $\langle C_{\mathtt{i}} \rangle^{ss}$,

$$\begin{aligned} 0 = {} & \mathrm{j} - \mathrm{l}\langle C_1 \rangle^{ss} + \mathrm{d}_2^{dv}\langle C_2 \rangle^{ss} - \mathrm{g}_1^{dv}\langle C_1 \rangle^{ss} - \\ & \mathrm{g}_1^{sd}(t)\langle C_1 \rangle^{ss} + \mathrm{d}_2^{sd}\langle C_2 \rangle^{ss} - \sum_{\mathtt{j}=1}^{\mathtt{i}_{max}} \left(\mathrm{g}_{\mathtt{j}}^{sd}(t)\langle C_{\mathtt{j}} \rangle^{ss} - \mathrm{d}_{\mathtt{j}+1}^{sd}\langle C_{\mathtt{j}+1} \rangle^{ss} \right) \\ 0 = {} & \left(\mathrm{g}_{\mathtt{i}-1}^{dv} + \mathrm{g}_{\mathtt{i}-1}^{sd}(t) \right) \langle C_{\mathtt{i}-1} \rangle^{ss} - \left(\mathrm{d}_{\mathtt{i}}^{dv} + \mathrm{d}_{\mathtt{i}}^{sd} \right) \langle C_{\mathtt{i}} \rangle^{ss} - \\ & \left(\mathrm{g}_{\mathtt{i}}^{dv} + \mathrm{g}_{\mathtt{i}}^{sd}(t) \right) \langle C_{\mathtt{i}} \rangle^{ss} + \left(\mathrm{d}_{\mathtt{i}+1}^{dv} + \mathrm{d}_{\mathtt{i}+1}^{sd} \right) \langle C_{\mathtt{i}+1} \rangle^{ss}. \end{aligned} \tag{6.52}$$

The above equations can be solved subject to the boundary conditions $\langle C_1 \rangle^{ss} = \langle C_1 \rangle^{kin} \equiv \textit{constant}$ and $\langle C_{\mathtt{i}_{max}+1} \rangle^{ss} = 0$. The resulting steady flux of clusters in size space was calculated by Becker and Döring [2] to be equal to

$$\mathcal{J}_{BD,kin}(\langle C_1 \rangle^{kin}) = \frac{(\mathrm{g}_1^{dv} + \mathrm{g}_1^{\prime sd}\langle C_1 \rangle^{kin})\langle C_1 \rangle^{kin}}{1 + \sum_{\mathtt{j}=2}^{\mathtt{i}_{max}} \prod_{\mathtt{i}=2}^{\mathtt{j}} \frac{\mathrm{d}_{\mathtt{i}}^{dv} + \mathrm{d}_{\mathtt{i}}^{sd}}{\mathrm{g}_{\mathtt{i}}^{dv} + \mathrm{g}_{\mathtt{i}}^{\prime sd}\langle C_1 \rangle^{kin}}}. \tag{6.53}$$

The mean monomer concentration can, again, be estimated via

$$\langle C_1 \rangle^{kin} \approx \mathrm{j}\mathrm{l}^{-1}. \tag{6.54}$$

The above expression (6.53) may be referred to as the *kinetic Becker-Döring nucleation current*. We explicitly note that $\mathcal{J}_{BD,kin}$ is a function of a specified monomer concentration.

From the condition

$$\frac{\mathrm{d}}{\mathrm{d}t}\langle C_{\mathtt{i}}(t) \rangle = 0 \quad \forall \mathtt{i} \in \{1, \mathtt{i}_{max}\}, \tag{6.55}$$

where the mean concentrations $\langle C_{\mathtt{i}}(t) \rangle$ are understood to be the ones employed in (6.14) and (6.15) we derive an expression for the dynamical nucleation current in the

Becker-Döring model equivalent to the form (6.34), namely,

$$\mathcal{J}_{BD,dyn}(t_\infty) = \left(\left(\mathrm{g}_{\mathtt{i}}^{dv} + \mathrm{g}_{\mathtt{i}}^{'sd} \langle C_1(t) \rangle \right) \langle C_{\mathtt{i}}(t) \rangle - \left(\mathrm{d}_{\mathtt{i}+1}^{dv} + \mathrm{d}_{\mathtt{i}+1}^{sd} \right) \langle C_{\mathtt{i}+1}(t) \rangle \right) \Big|_{t_\infty} . \quad (6.56)$$

The full Becker-Döring equations are in fact non-linear equations for the cluster concentrations, and the steady state solution referred to above is obtained in terms of a given monomer concentration. In a system undergoing heterogeneous nucleation, the monomers are in fact a participating species with a freely variable population. Therefore $\langle C_1 \rangle^{kin}$ will, in general, differ from jl^{-1}. To allow for this, we could solve the equations iteratively, using the steady state Becker-Döring solution, or alternatively, simply perform a numerical solution of the time-dependent non-linear differential equations, and identify an equilibrium at late times. The largest cluster size under consideration must satisfy $\mathtt{i}_{max} > \mathtt{i}^*$, and one therefore has to solve $\mathtt{i}_{max}$ equations for the unknown $\mathtt{i}$-mer concentrations $\langle C_{\mathtt{i}}(t) \rangle$. Having done this, we obtain the dynamical Becker-Döring nucleation current. Notice that the difference between $\mathcal{J}_{BD,dyn}$ and $\mathcal{J}_{BD,kin}$ corresponds to the difference between a self-consistent, and an estimated monomer concentration, respectively. One should expect, however, to find that $\mathcal{J}_{BD,kin}(\langle C_1(t_\infty) \rangle) = \mathcal{J}_{BD,dyn}(t_\infty)$. In a next step we employ the model of the rate coefficients according to Fletcher theory in order to compare the theoretical predictions with experimental results in terms of the different expressions for the nucleation current.

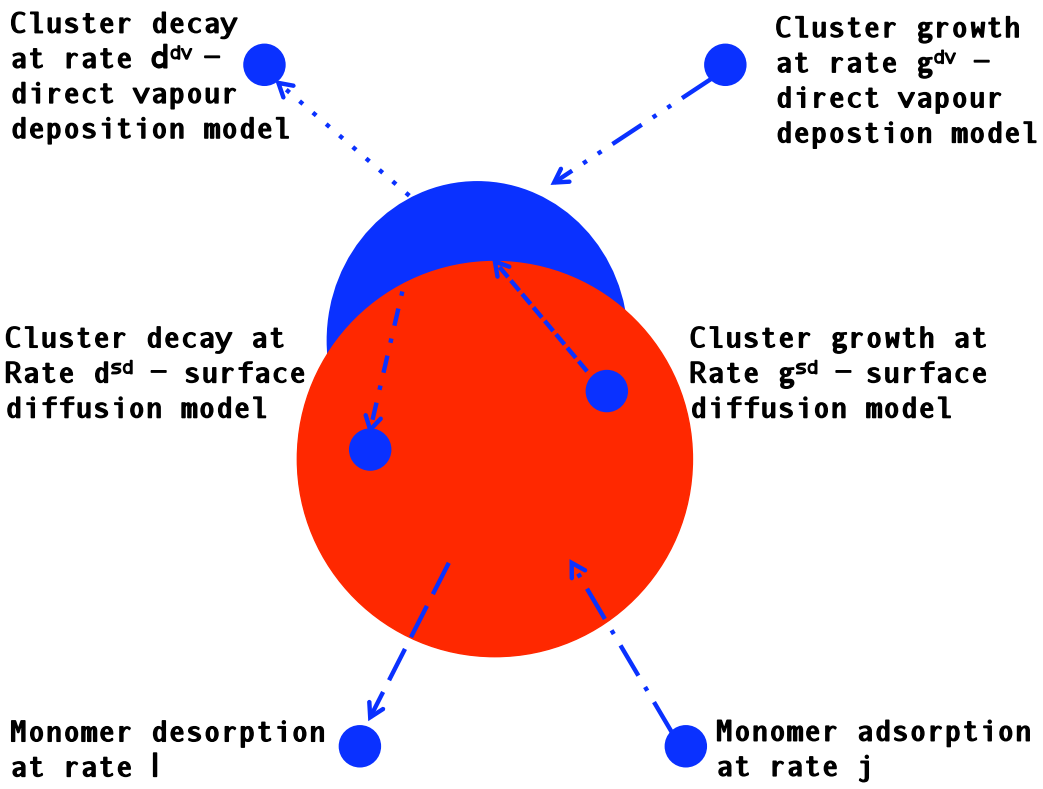

Figure 6.4: Becker-Döring model. Monomers are attached to the surface of the seed particle (red sphere) with an adsorption rate j and are evaporated into the surrounding gas phase with a desorption rate l. In the direct vapour deposition mechanism, clusters (blue sphere) are growing due to the gain of monomers from the gas phase with a growth rate g^{dv} and are decaying due to the loss of monomers from the clusters into the surrounding gas phase with a loss rate d^{dv}. In the surface diffusion mechanism, clusters are growing due to the attachment of monomers that are diffusing on the surface of the grain with a growth rate g^{sd} and are decaying due to the loss of monomers from the cluster onto the surface of the seed with a decay rate d^{sd}.

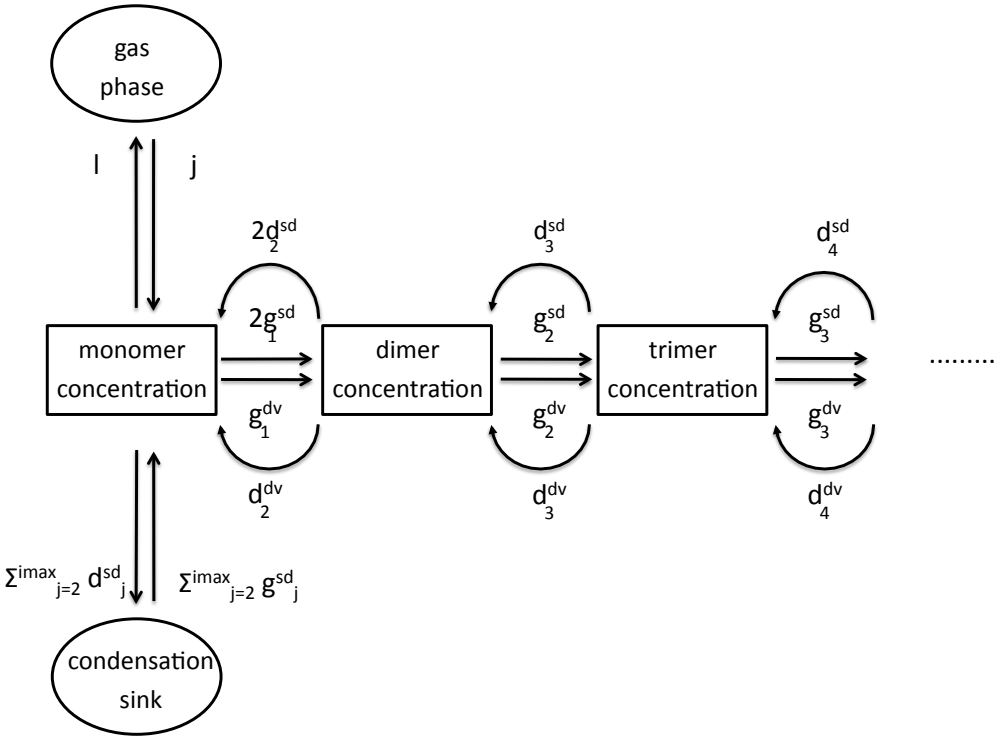

Figure 6.5: Schematic of the Becker-Döring model. Clusters are formed due to the gain and loss of monomers in the direct vapour deposition mechanism with growth rate g^{dv} and decay rate d^{dv} and in the surface diffusion mechanism with growth rate g^{sd} and decay rate d^{sd}. Monomers are gained from the gas-phase at a rate j and lost to the gas-phase at a rate l.

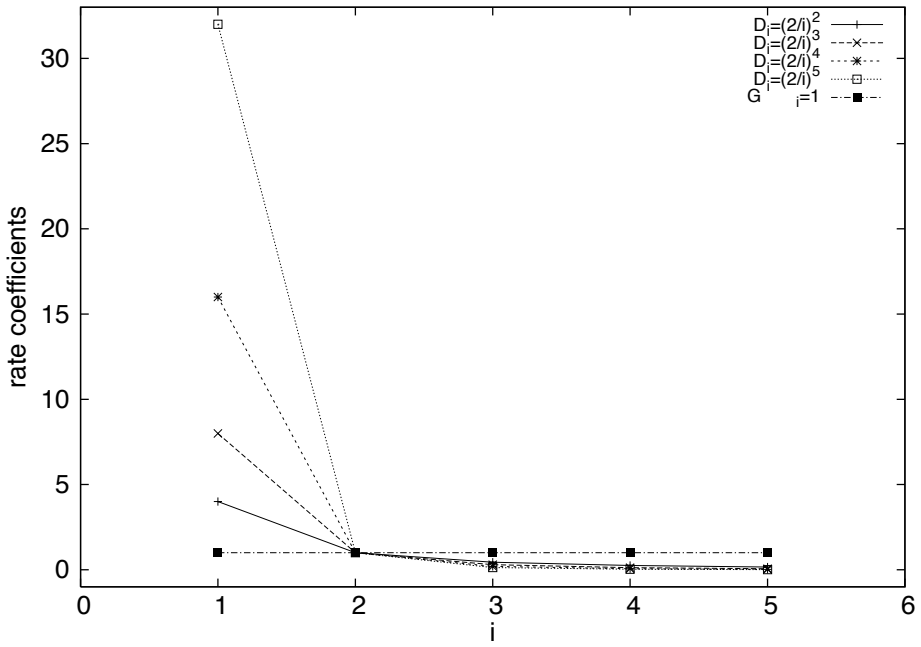

Figure 6.6: This graph shows the dependence of the growth and loss rate coefficients on the order $\mathtt{i}$ of $\mathtt{i}$-mers for $G'(\chi) \equiv \chi^{-1} = 1$, $D_\mathtt{i} = \left(\frac{2}{\mathtt{i}}\right)^c$ for fixed critical cluster size $\mathtt{i}^* = 2$. The lines are are a guide to the eye.

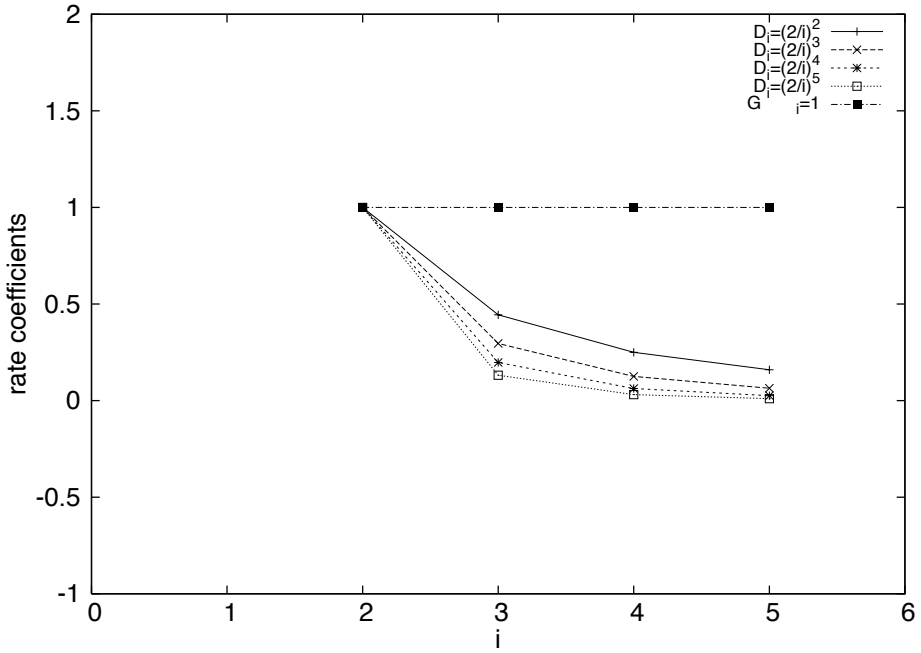

Figure 6.7: This graph is a zoom of 6.6. The lines are are a guide to the eye.

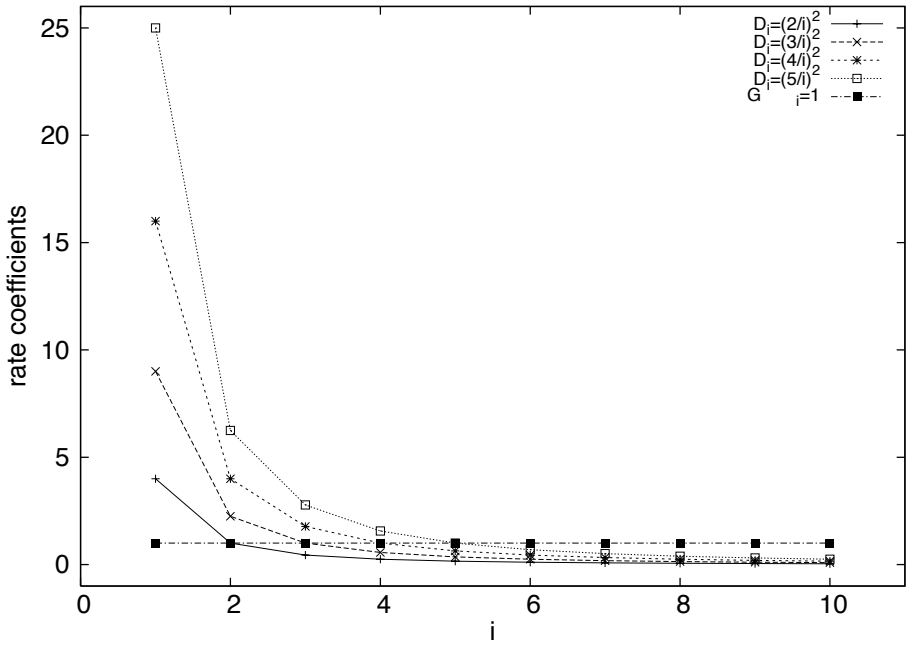

Figure 6.8: This graph shows the dependence of the growth and loss rate coefficients on the order i of i-mers for $G'(\chi) = \chi^{-1} = 1$, $D_i = \left(\frac{i^*}{i}\right)^2$ and for fixed constant $c = 2$. The lines are are a guide to the eye.

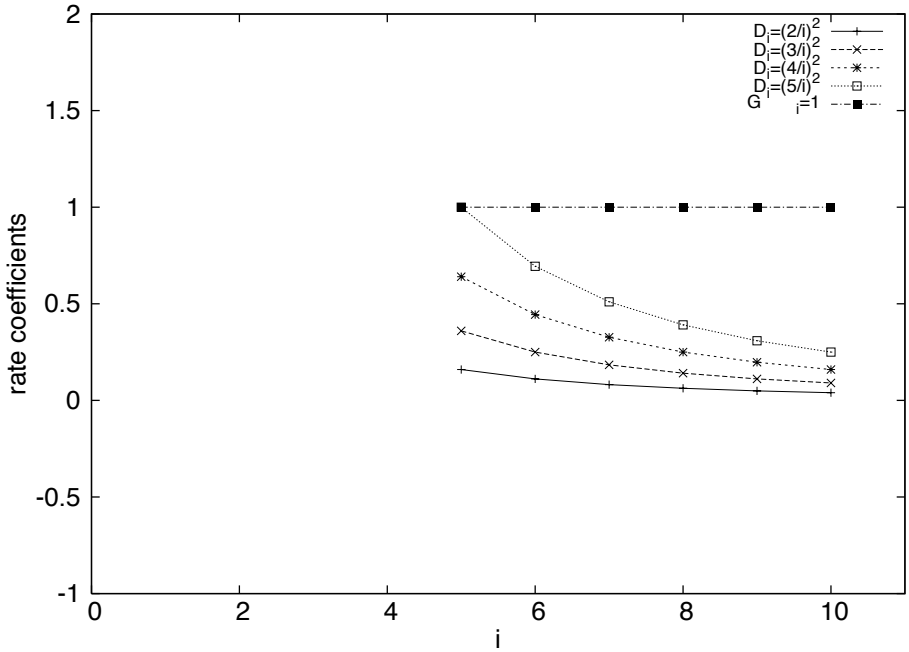

Figure 6.9: This graph is a zoom of 6.8. The lines are are a guide to the eye.

χ	$\mathring{M}_1$	$\mathring{M}_2$	$\mathring{M}_3$	$\mathring{M}_4$
10^3	9.8146×10^2	5.9247×10^2	4.7404×10^2	3.7780×10^2
10^2	9.8146×10^1	5.9247×10^1	4.7404×10^1	3.7780×10^1
10^1	9.8146×10^0	5.9247×10^0	4.7404×10^0	3.7780×10^0
10^0	9.8146×10^{-1}	5.9247×10^{-1}	4.7404×10^{-1}	3.7780×10^{-1}
10^{-1}	9.8146×10^{-2}	5.9247×10^{-2}	4.7404×10^{-2}	3.7780×10^{-2}
10^{-2}	9.8146×10^{-3}	5.9247×10^{-3}	4.7404×10^{-3}	3.7780×10^{-3}
10^{-3}	9.8146×10^{-4}	5.9247×10^{-4}	4.7404×10^{-4}	3.7780×10^{-4}

Table 6.1: Strictly positive steady state values for monomers, dimers, trimers and tetramers for L = 100s^{-1} used as fixed points in the stability analysis for the power law model.

χ	$\mathring{M}_1$	$\mathring{M}_2$	$\mathring{M}_3$	$\mathring{M}_4$
10^3	5.9763×10^2	2.7669×10^2	1.9098×10^2	1.3466×10^2
10^2	5.9763×10^1	2.7669×10^1	1.9098×10^1	1.3466×10^1
10^1	5.9763×10^0	2.7669×10^0	1.9098×10^0	1.3466×10^0
10^0	5.9763×10^{-1}	2.7669×10^{-1}	1.9098×10^{-1}	1.3466×10^{-1}
10^{-1}	5.9763×10^{-2}	2.7669×10^{-2}	1.9098×10^{-2}	1.3466×10^{-2}
10^{-2}	5.9763×10^{-3}	2.7669×10^{-3}	1.9098×10^{-3}	1.3466×10^{-3}
10^{-3}	5.9763×10^{-4}	2.7669×10^{-4}	1.9098×10^{-4}	1.3466×10^{-4}

Table 6.2: Strictly positive steady state values for monomers, dimers, trimers and tetramers for L = 1s^{-1} used as fixed points in the stability analysis for the power law model.

$\mathtt{i}_{max}$	$\mathcal{J}_{BD,dyn}(c=2)$ $[\mathrm{s}^{-1}]$	$\triangle$ in %	$\mathcal{J}_{BD,dyn}(c=5)$ $[\mathrm{s}^{-1}]$	$\triangle$ in %
5	3.64466		4.36925	
10	3.46729	5.12	4.14573	5.39
15	3.31253	4.67	3.94876	4.99
20	3.17386	4.37	3.77347	4.65
25	3.04869	4.11	3.61616	4.35
30	2.93496	3.88	3.47396	4.09

Table 6.3: Mean-field nucleation rate $\mathcal{J}_{BD,dyn}$ according to the Becker-Döring rate equations for the model parameters $\mathrm{G}' = 0.1\mathrm{s}^{-1}$, $\mathrm{D}_i = \left(\frac{\mathtt{i}^*}{i}\right)^c \mathrm{s}^{-1}$, $\mathrm{J} = 1000\mathrm{s}^{-1}$ and $\mathrm{L} = 100\mathrm{s}^{-1}$ and for fixed critical cluster size $\mathtt{i}^* = 2$. The symbol $\triangle$ denotes the difference in percent in the nucleation currents as defined in the main text.

$\mathtt{i}_{max}$	$\mathcal{J}_{BD,dyn}(c=2)$ $[\mathrm{s}^{-1}]$	$\triangle$ in %	$\mathcal{J}_{BD,dyn}(c=5)$ $[\mathrm{s}^{-1}]$	$\triangle$ in %
5	7.01426×10^{-1}		7.96141×10^{-1}	
10	4.45478×10^{-1}	57.45	5.0358×10^{-1}	58.10
15	3.31166×10^{-1}	34.52	3.73061×10^{-1}	34.99
20	2.65218×10^{-1}	24.87	2.98056×10^{-1}	25.16
25	2.21978×10^{-1}	19.48	2.49009×10^{-1}	19.70
30	1.91307×10^{-1}	16.03	2.14287×10^{-1}	16.20

Table 6.4: Mean-field nucleation rate $\mathcal{J}_{BD,dyn}$ according to the Becker-Döring rate equations for the model parameters $\mathrm{G}' = 0.1\mathrm{s}^{-1}$, $\mathrm{D}_i = \left(\frac{\mathtt{i}^*}{i}\right)^c \mathrm{s}^{-1}$, $\mathrm{J} = 10\mathrm{s}^{-1}$ and $\mathrm{L} = 1\mathrm{s}^{-1}$ and for fixed critical cluster size $\mathtt{i}^* = 2$. The symbol $\triangle$ denotes the difference in percent in the nucleation currents as defined in the main text.

$\mathtt{i}_{max}$	$\mathcal{J}_{BD,dyn}(J=1000\mathrm{s}^{-1})$ $[\mathrm{s}^{-1}]$	$\mathcal{J}_{BD,dyn}(J=10\mathrm{s}^{-1})$ $[\mathrm{s}^{-1}]$
15	2.31387×10^{-5}	2.31296×10^{-5}
20	2.29579×10^{-5}	2.29461×10^{-5}
25	2.29576×10^{-5}	2.2943×10^{-5}
30	2.29576×10^{-5}	2.29402×10^{-5}

Table 6.5: Mean-field nucleation rate $\mathcal{J}_{BD,dyn}$ according to the Becker-Döring rate equations for the model parameters $\mathrm{G}' = 0.1\mathrm{s}^{-1}$, $\mathrm{D}_i = \left(\frac{\mathtt{i}^*}{i}\right)^c \mathrm{s}^{-1}$ for fixed constant $c = 2$ and a critical cluster size $\mathtt{i}^* = 10$ and, in the case of $\mathcal{J}_{BD,dyn}(J = 1000\mathrm{s}^{-1})$ $[\mathrm{s}^{-1}]$, with $\mathrm{J} = 1000\mathrm{s}^{-1}$ and $\mathrm{L} = 100\mathrm{s}^{-1}$ and, in the case of $\mathcal{J}_{BD,dyn}(J = 10\mathrm{s}^{-1})$ $[\mathrm{s}^{-1}]$ with $\mathrm{J} = 10\mathrm{s}^{-1}$ and $\mathrm{L} = 1\mathrm{s}^{-1}$.

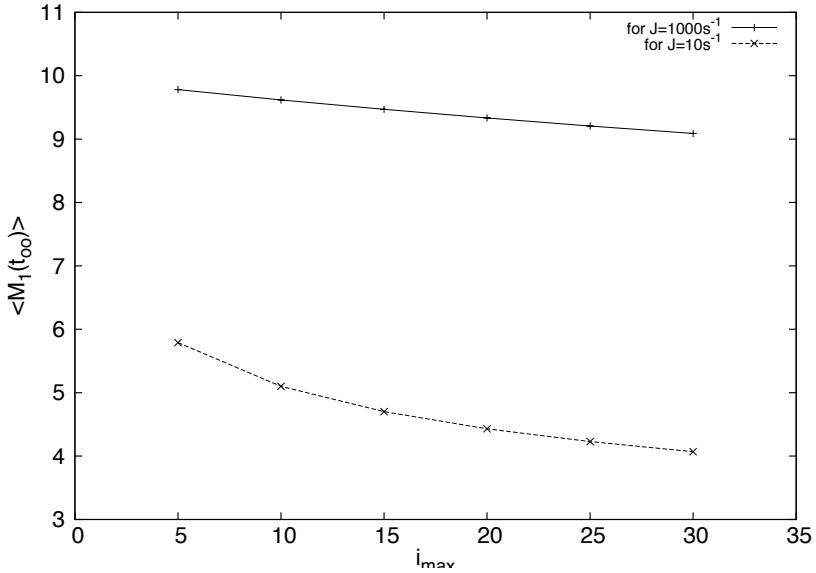

Figure 6.10: Dependence of the mean late-time monomer population according to the mean-field framework on the maximum order of i-mers with the model parameters $G' = 0.1s^{-1}$, $D_i = \left(\frac{i^*}{i}\right)^c$ where $c = 2$ and $i^* = 2$ and for $J = 1000s^{-1}$ and $L = 100s^{-1}$ as well as for $J = 10s^{-1}$ and $L = 1s^{-1}$. The lines are are a guide to the eye.

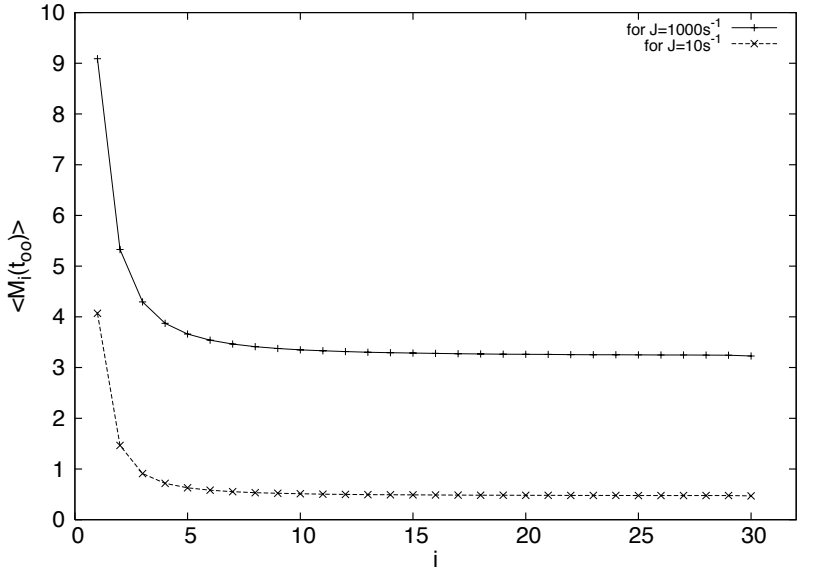

Figure 6.11: Dependence of the mean late-time cluster populations according to the mean-field framework on the order of i-mers with the model parameters $G' = 0.1s^{-1}$, $D_i = \left(\frac{i^*}{i}\right)^c$ where $c = 2$ and $i^* = 2$ and for $J = 1000s^{-1}$ and $L = 100s^{-1}$ as well as for $J = 10s^{-1}$ and $L = 1s^{-1}$. The maximum order of i-mers was chosen to be 30. The lines are are a guide to the eye.

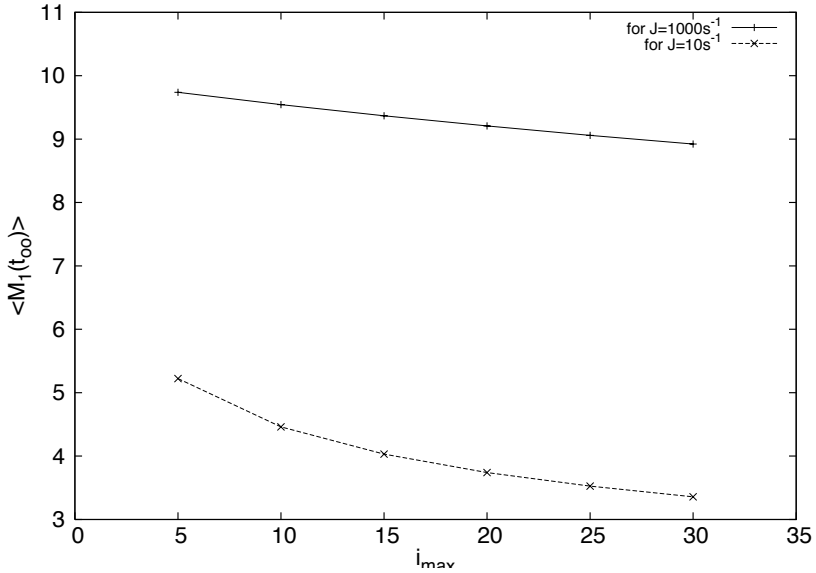

Figure 6.12: Dependence of the mean late-time monomer population according to the mean-field framework on the maximum order of i-mers with the model parameters $G' = 0.1s^{-1}$, $D_i = \left(\frac{i^*}{i}\right)^c$ where $c = 5$ and $i^* = 2$ and for $J = 1000s^{-1}$ and $L = 100s^{-1}$ as well as for $J = 10s^{-1}$ and $L = 1s^{-1}$. The lines are are a guide to the eye.

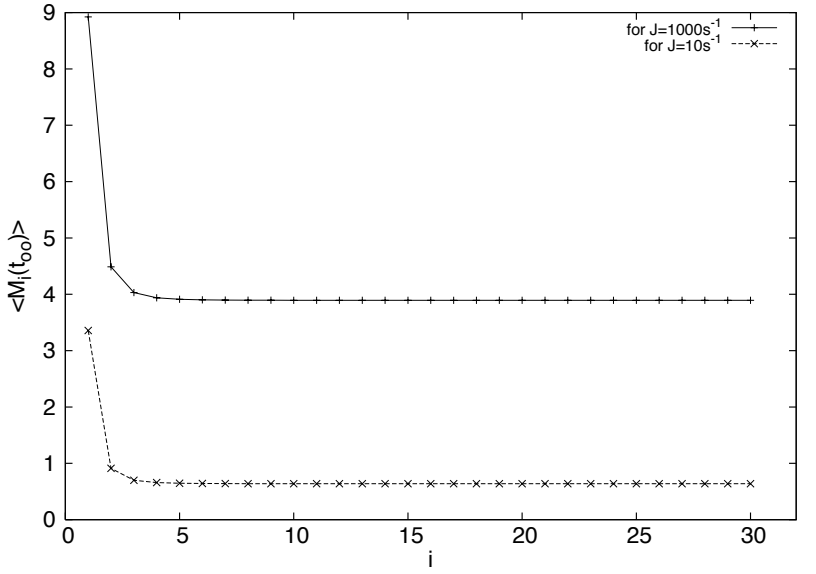

Figure 6.13: Dependence of the mean late-time cluster populations according to the mean-field framework on the order of i-mers with the model parameters $G' = 0.1s^{-1}$, $D_i = \left(\frac{i^*}{i}\right)^c$ where $c = 5$ and $i^* = 2$ and for $J = 1000s^{-1}$ and $L = 100s^{-1}$ as well as for $J = 10s^{-1}$ and $L = 1s^{-1}$. The maximum order of i-mers was chosen to be 30. The lines are are a guide to the eye.

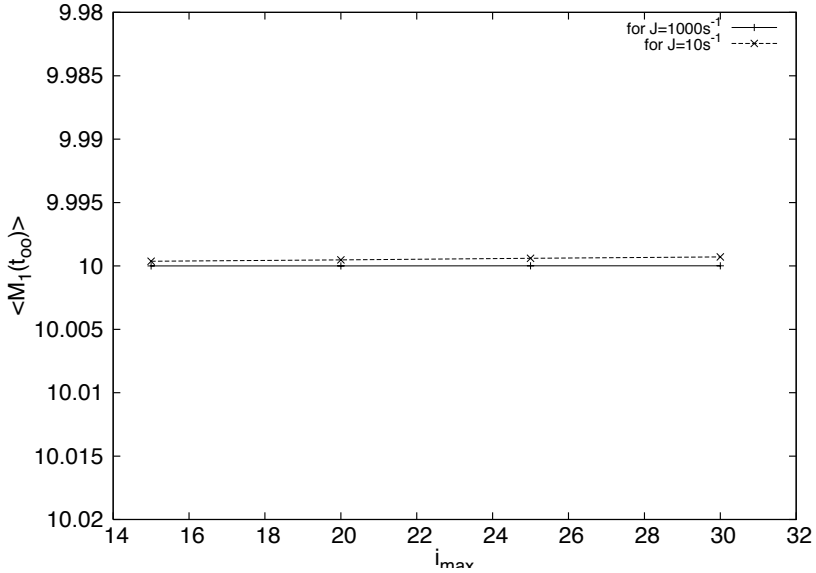

Figure 6.14: Dependence of the mean late-time monomer population according to the mean-field framework on the maximum order of i-mers with the model parameters $G' = 0.1\text{s}^{-1}$, $D_i = \left(\frac{\mathtt{i}^*}{\mathtt{i}}\right)^c$ where $c = 2$ and $\mathtt{i}^* = 10$ and for $J = 1000\text{s}^{-1}$ and $L = 100\text{s}^{-1}$ as well as for $J = 10\text{s}^{-1}$ and $L = 1\text{s}^{-1}$. The lines are are a guide to the eye.

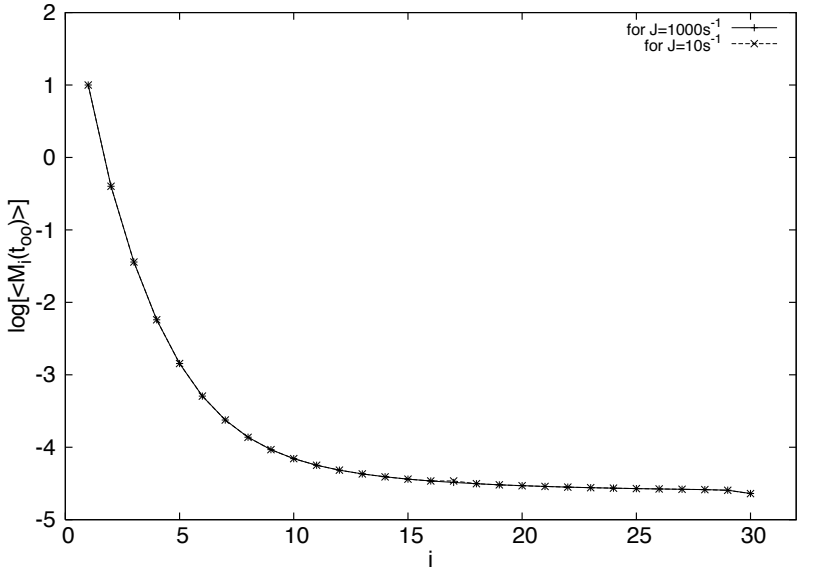

Figure 6.15: Dependence of the mean late-time cluster populations according to the mean-field framework on the order of i-mers with the model parameters $G' = 0.1\text{s}^{-1}$, $D_i = \left(\frac{\mathtt{i}^*}{\mathtt{i}}\right)^c$ where $c = 2$ and $\mathtt{i}^* = 10$ and for $J = 1000\text{s}^{-1}$ and $L = 100\text{s}^{-1}$ as well as for $J = 10\text{s}^{-1}$ and $L = 1\text{s}^{-1}$. The maximum order of i-mers was chosen to be 30. The lines are are a guide to the eye.

θ	$r(\mathtt{i})$	$A_{v,l}$	$A_{l,s}$
0°	∞	undefined	∞
90°	$\sqrt[3]{\frac{3\mathtt{i}v_l}{2\pi}}$	$2\pi r(\mathtt{i})^2$	$\pi r(\mathtt{i})^2$
180°	$\sqrt[3]{\frac{3\mathtt{i}v_l}{4\pi}}$	$4\pi r(\mathtt{i})^2$	0
270°	$\sqrt[3]{\frac{3\mathtt{i}v_l}{2\pi}}$	$2\pi r(\mathtt{i})^2$	$\pi r(\mathtt{i})^2$
360°	∞	undefined	undefined

Table 6.6: List of the values of the radii of i-clusters, $r(\mathtt{i})$, of the vapour-liquid surface areas $A_{v,l}$ and of the liquid-solid surface areas $A_{l,s}$ for special choices of the contact angle θ for a planar seed particle without boundaries.

6.1.3 Comparison with Experimental Data

In the following, we compare the theoretical predictions according to the Fletcher and Becker-Döring framework to data obtained in an experiment undertaken at the University of Vienna. The results of the experiment which was completed in collaboration with the University of Helsinki were published in [67]. Organic vapour, namely n-propanol, condensed on molecular ions as well as on charged and uncharged inorganic nanoparticles, namely tungsten oxide (WOx) particles. The activation of the pre-existing seed particles was triggered by heterogeneous nucleation. Vapour supersaturation was achieved by adiabatic expansion in a thermostated expansion chamber of a Size Analyzing Nuclei Counter (SANC). Droplet growth was observed by the Contact Angle Mie Scattering detection method (CAMS). For each vapour saturation ratio S the fraction of activated particles relative to the total number concentration was determined, and was used to create a nucleation-activation probability curve depending on the vapour supersaturation ratio for seed diameters ranging from 0.9nm to 4nm. The smaller the size of the seed the higher was the vapour supersaturation needed for the activation of the particles. Each nucleation-activation probability curve can be used to extract the corresponding onset saturation ratio, which is the vapour saturation ratio where 50% of particles of a specific size are activated. Accordingly, one can plot the onset saturation ratio as a function of the seed particle mobility diameter and compare the experimental data to the theoretical prediction within the Fletcher framework.

We concentrate on the data representing the neutral tungsten oxide seed particles[2]. In Table 6.7 we give the values of the parameters used in the calculations according to the experimental set-up. The small contact angle indicates that the seed particle was

[2]Note that one has to be careful concerning the monodispersion of the particles.

totally wettable to the vapour phase —see Figure 6.2. It has been claimed [67] that the Fletcher theory predicts the observed onset activations for neutral particles accidingly well — see Table 6.9. We would like to reconsider this statement in terms of the nucleation current. This proposed reconsideration is driven by the observation that the standard Fletcher theory based on the capillarity approximation leads to disparities between the value of the critical cluster size obtained from theoretical considerations compared to the experimental estimation.

The First Heterogeneous Nucleation Theorem [64] together with the nucleation-activation probability curve provides the means to determine the number of molecules in the nucleating cluster. Since the First Heterogeneous Nucleation Theorem is derived from general statistical mechanical considerations, this calculation is independent of the model used to describe the cluster. If one knows the dependence of the nucleation rate on the saturation ratio at constant temperature, the first nucleation theorem gives a method for determining the difference in the number of molecules if there is a cluster in the critical volume in the liquid phase compared to the same volume being filled with vapour, that is one can determine $\mathtt{i}^*$.

The number of molecules in the critical cluster as obtained in this fashion will, in the sequel, be called the *experimental critical cluster size*. In the particular experiment presented in [67] the experimental critical cluster size $\mathtt{i}^*_{exp}$ was between twenty and twenty-five. If one calculates the critical cluster size as predicted by the Fletcher theory, $\mathtt{i}^*_{Fletcher}$ —cfr. equation (6.13)—, one finds higher values as the experimental data imply —see Table 6.9.

The quantity that is most often measured in experiments is the *nucleation probability*, P_{nucl}, that is, the probability with which one critical cluster forms on the surface of a seed particle in a chosen time period, the experimental *activation time* t_{exp}. For the calculations we assumed[3] that $t_{exp} = 10^{-3}$s. The nucleation probability is defined as

$$P_{nucl} := 1 - \exp\left(-4\pi \mathcal{J}_{exp} R^2_{seed} t_{exp}\right). \tag{6.57}$$

From equation (6.57) one can determine the nucleation rate, expressed per unit area of the seed particle surface and per unit time, taking $P_{nucl} = 0.5$ so that

$$\mathcal{J}_{exp} := -\frac{ln(0.5)}{4\pi R^2_{seed} t_{exp}} \quad [\mathrm{m}^{-2}\mathrm{s}^{-1}]. \tag{6.58}$$

[3]Dr Paul Winkler: private communication

The temperature chosen in the experiment was $T = 275$K. A detailed list of the experimental quantities and their specific values are given in Table 6.7 and Table 6.8. The *onset saturation ratio*, that is, the saturation ratio at which half of the particles of a certain size are activated, was found to be $S\,|_{P_{nucl}=0.5}= 2.62$ for neutral WO_x clusters with a radius of $R_{seed} = 1 \times 10^{-9}$m. For neutral WO_x seeds with radius $R_{seed} = 2 \times 10^{-9}$m the saturation ratio at $P_{nucl} = 0.5$ was $S = 1.574$. The molecular volume in the liquid phase calculates as $v_l = m\rho^{-1}$ where m is the molecular mass and ρ the liquid density. Since the seed particle was totally wettable, the contact angle θ was taken to be $\theta \approx 0.3°$. Note that the assumption of a constant contact angle made in the Fletcher theory is more justified for clusters of sizes $\mathtt{i} > \mathtt{i}^*$ than for clusters of smaller sizes.

Comparison of the Fletcher nucleation current, and the kinetic Becker-Döring nucleation current with experimental data

The Fletcher critical cluster size and onset supersaturation (6.43) are calculated for two particular sizes of seed particles —see Table 6.9— and compared with experimental data. The radius of the experimental critical cluster $r(\mathtt{i} = \mathtt{i}^*_{exp})$ is obtained using the experimental critical cluster size $\mathtt{i}^*_{exp}$ which is inserted into equation (6.41). The disparity between model and experimental critical cluster sizes is large, even though the onset supersaturations are in reasonable agreement.
Calculations of the nucleation current according to the Fletcher theory and the kinetic Becker-Döring model can be found in Table 6.10. For a seed radius of value $R_{seed} = 1$nm we choose the largest cluster size to be $\mathtt{i}_{max} = 135$ and for a seed radius of value $R_{seed} = 2$nm we assume $\mathtt{i}_{max} = 820$. We observe that the agreement between the experimental nucleation current $\mathcal{J}_{exp}$ —equation (6.58)— and the Fletcher nucleation current $\mathcal{J}_{Fletcher}$ —equation (6.2)— is better for a smaller seed radius than for the bigger seed particle. The Fletcher nucleation current $\mathcal{J}_{Fletcher}$ and the kinetic Becker-Döring nucleation rate in the steady state

$$\mathcal{J}^{dv}_{BD,kin}(\langle C^{dv}_1\rangle^{kin}) = \frac{\mathrm{g}^{dv}_1\langle C^{dv}_1\rangle^{kin}}{1+\sum_{\mathtt{j}=2}^{\mathtt{i}_{max}}\prod_{\mathtt{i}=2}^{\mathtt{j}}\frac{\mathrm{d}^{dv}_{\mathtt{i}}}{\mathrm{g}^{dv}_{\mathtt{i}}}}, \tag{6.59}$$

are of the same order of magnitude. Clearly, neither is an acceptable description of the data for both seed radii. We shall now attempt to address this by modifying the capillarity approximation.

The heterogeneous nucleation current for the modified direct vapour deposition mechanism

In order to remove the disparity between the experimental and theoretical critical cluster size we modify parameters such that the critical cluster size as predicted by Fletcher theory, $\mathtt{i}^*_{Fletcher}$ —see equation (6.13)—, coincides with the experimental critical cluster size $\mathtt{i}^*_{exp}$:

$$\mathtt{i}^*_{Fletcher} = \mathtt{i}^*_{exp} = 25. \tag{6.60}$$

The simplest way to proceed is to alter the surface tension between the vapour phase and the droplet which we will call the *effective surface tension* σ_{eff} and which is given in Table 6.11. As a consequence of imposing the condition $\mathtt{i}^*_{Fletcher} = \mathtt{i}^*_{exp}$ we have $r(\mathtt{i} = \mathtt{i}^*_{exp}) = r(\mathtt{i} = \mathtt{i}^*_{Fletcher}) = r^*_{Fletcher}$ where $r^*_{Fletcher}$ is given by equation (6.6). All other physical and experimental parameters are unchanged. We recalculate the nucleation currents for the various models used in the last subsection with the assumed value $\mathtt{i}_{max} = 30$ and summarise the results in Table 6.12. The Becker-Döring equations are solved with zero initial conditions. Now the modified Fletcher theory overpredicts the nucleation current —compare with Table 6.10— yet the result for the bigger seed particle is closer to the experimental nucleation current than in the unmodified theory.

The difference —as given in Table 6.10— in the values of the kinetic nucleation current $\mathcal{J}^{dv}_{BD,kin}(\langle C^{dv}_1\rangle^{kin})$ for the direct vapour deposition mechanism —see equation (6.59)— and the dynamical nucleation current for the direct vapour deposition mechanism

$$\mathcal{J}^{dv}_{BD,dyn}(t_\infty) = \mathrm{g}^{dv}_{\mathtt{i}_{max}} \langle C^{dv}_{\mathtt{i}_{max}}(t)\rangle \Big|_{t_\infty}, \tag{6.61}$$

arises due to the estimation of the monomer concentration by the ratio jl^{-1} —see equation (6.54). This can be illustrated by considering the ratio

$$F(R_{seed}) := \frac{\mathcal{J}^{dv}_{BD,kin}(\langle C^{dv}_1\rangle^{kin})}{\mathcal{J}^{dv}_{BD,kin}(\langle C^{dv}_1(t_\infty)\rangle)} = \frac{\langle C^{dv}_1\rangle^{kin}}{\langle C^{dv}_1(t_\infty)\rangle}. \tag{6.62}$$

We have $F(R_{seed} = 1\mathrm{nm}) = 1.16 \times 10^4$ and $F(R_{seed} = 2\mathrm{nm}) = 8.86 \times 10^4$. If one recalculates the nucleation rate $\mathcal{J}^{dv}_{BD,kin}$ taking the late-time value of the mean monomer concentration $\langle C^{dv}_1(t_\infty)\rangle$ according to the solution of the dynamical Becker-Döring rate equations (6.14) —with $\mathrm{g}'^{sd}_{\mathtt{i}} = \mathrm{d}^{sd}_{\mathtt{i}} \equiv 0$— instead of using the estimation for the mean

monomer concentration in the steady state (6.54), one finds that

$$\mathcal{J}^{dv}_{BD,kin}[\langle C^{dv}_1(t_\infty)\rangle] = \mathcal{J}^{dv}_{BD,dyn}(t_\infty), \tag{6.63}$$

as expected. The Fletcher nucleation current $\mathcal{J}_{Fletcher}$ clearly overestimates the true nucleation current in the same way as the kinetic Becker-Döring nucleation rate $\mathcal{J}^{dv}_{BD,kin}$, and for the same reason, namely the overestimation of the monomer concentration. Using $\mathcal{J}^{dv}_{BD,dyn}$ the disparity with respect to experimental data is reduced, and the correct tendency for a change in seed radius is obtained.

The heterogeneous nucleation current for the combined modified direct vapour deposition mechanism and surface diffusion mechanism

Due to the difference of several orders of magnitude between the constant growth rate coefficients $\mathrm{g}^{'sd}_{\mathtt{i}}$ and the decay rate coefficients $\mathrm{d}^{sd}_{\mathtt{i}}$, problems in the numerical evaluation of the evolution equations (6.14) and (6.15) arise. In order to avoid these numerical difficulties we employ an estimate of the mean monomer concentration in the combined modified direct vapour deposition mechanism and surface diffusion mechanism at late times to solve the Becker-Döring rate equations (6.14) and (6.15) iteratively in the following way. The iteration for the mean monomer concentration $\langle C^{sd,dv}_1(t_\infty)\rangle$ at late times t_∞ is performed according to

$$[\langle C^{sd,dv}_1(t_\infty)\rangle^{m+1}]_{in} = \left([\langle C^{sd,dv}_1(t_\infty)\rangle^{m}]_{out}[\langle C^{sd,dv}_1(t_\infty)\rangle^{m}]_{in}\right)^{\frac{1}{2}}, \tag{6.64}$$

where $[\langle C^{sd,dv}_1(t_\infty)\rangle^{m}]_{in}$ is the input value and $[\langle C^{sd,dv}_1(t_\infty)\rangle^{m}]_{out}$ the output value in the m-th iteration step. The above estimate for the mean monomer concentration at late times is inserted into the expression for the rate coefficients

$$\mathrm{g}^{sd}_{\mathtt{i}} = \mathrm{g}^{'sd}_{\mathtt{i}}[\langle C^{sd,dv}_1(t_\infty)\rangle^{m}]_{in}, \tag{6.65}$$

and the system of Becker-Döring rate equations (6.14) and (6.15) is solved. In the zeroth iteration step the mean monomer concentration at late times is estimated to be

$$[\langle C^{sd,dv}_1(t_\infty)\rangle^{0}]_{in} = \mathrm{jl}^{-1}. \tag{6.66}$$

The iteration procedure is terminated when

$$\frac{[\langle C^{sd,dv}_1(t_\infty)\rangle^{m}]_{out}}{[\langle C^{sd,dv}_1(t_\infty)\rangle^{m}]_{in}} \approx 1. \tag{6.67}$$

In our calculations, this point is reached when $m = 4$ at which

$$[\langle C_1^{sd,dv}(t_\infty)\rangle^m]_{out}\left([\langle C_1^{sd,dv}(t_\infty)\rangle^m]_{in}\right)^{-1} = 1 \pm \mathcal{O}(10^{-4}). \tag{6.68}$$

The nucleation current from the full Becker-Döring rate equations for both the surface diffusion and the direct vapour deposition mechanisms can be obtained using the expression (6.34). In Table 6.14 we compare the dynamical Becker-Döring nucleation current as computed for the direct vapour deposition mechanism, $\mathcal{J}_{BD,dyn}^{dv}$, according to equation (6.34) where $\mathrm{g}_{\mathtt{i}_{max}}^{\prime sd} \equiv 0$ with the dynamical Becker-Döring nucleation current as computed for both mechanisms, $\mathcal{J}_{BD,dyn}^{sd,dv}$, according to equation (6.34) where $\mathrm{g}_{\mathtt{i}_{max}}^{\prime sd} \neq 0$. One observes that the nucleation current that was calculated taking both the direct vapour deposition and the surface diffusion mechanism into account is generally an order of magnitude less than the nucleation current that results from the consideration of the direct vapour deposition mechanism only. This is a slightly unexpected result but might be understood by considering that the inclusion of surface diffusion allows both the additional growth, but also additional decay of adsorbed clusters. The additional decay can potentially reduce the nucleation rate since the wider kinetic scheme reduces the concentration of clusters on the surface:

$$\frac{\langle C_{\mathtt{i}}^{dv}(t_\infty; R_{seed} = 1\mathrm{nm})\rangle}{\langle C_{\mathtt{i}}^{sd,dv}(t_\infty; R_{seed} = 1\mathrm{nm})\rangle} > \frac{\langle C_{\mathtt{i}}^{dv}(t_\infty; R_{seed} = 2\mathrm{nm})\rangle}{\langle C_{\mathtt{i}}^{sd,dv}(t_\infty; R_{seed} = 2\mathrm{nm})\rangle} > 1 \quad \forall \mathtt{i} \in [1, \mathtt{i}_{max}], \tag{6.69}$$

which can be seen in Figures 6.16 and 6.17. In Figure 6.16 the dependence of the mean cluster concentrations on the order of i-mers for a seed particle with radius $R_{seed} = 1\mathrm{nm}$ is plotted for the direct vapour deposition mechanism as well as for the combined direct vapour deposition mechanism and surface diffusion mechanism. Figure 6.17 shows the same quantities for a seed particle with radius $R_{seed} = 2\mathrm{nm}$. The plots in 6.16 and 6.17 can be confronted with the curves in Figures 6.11, 6.13, and 6.15 where the dependence of the mean late-time cluster concentrations on the order of i-mers was depicted graphically for a power law model of the decay rate coefficient. The convergence behaviour of the mean late-time cluster concentration in the limit (6.33) according to the modified rate coefficients model is followed nicely as indicated by the curves in Figures 6.16 and 6.17 and, in a sense, more accurately than in Figures 6.11, 6.13, and 6.15. Examples of values of specific mean late-time cluster concentrations are given in Table 6.13.

It can be concluded from the relatively small change in the nucleation current that surface diffusion processes do not play an essential role, at least for the het-

erogeneous nucleation conditions studied in the experiments. A reason for this may be the observation that the linear dimension of a single molecule is of the same order of magnitude as the radius of the seed particle and that very quickly after a heterogeneous nucleus has started to grow, there is little seed surface left for additional adsorbed monomers to diffuse on.

liquid density[1]	ρ [kgm^{-3}]	$1047.94 - 0.835978T$
saturation vapour pressure[1]	p [Nm^{-2}]	$133.322 \times 10^{31.52-\frac{3.46}{T}\times 10^3 - 7.52\times \log T - 4.29\times 10^{-11}T + 1.3T^2\times 10^{-7}}$
surface tension[1]	$\sigma_{v,l}$ [Nm^{-1}]	$(25.26 - 0.0777(T - 273.15)) \times 10^{-3}$
molecular mass[1]	m [kg]	1.0054×10^{-25}
latent heat[1]	L [Nm]	$60.11(\frac{1.1840\times 10^6 - 1.285T\times 10^3}{6.022}) \times 10^{-26}$
vibration frequency[1]	ν [s^{-1}]	8.8495575×10^{11}
average jump distance[2]	δ [m]	10^{-10}
activation energy for surface diffusion[2]	E [Nm]	$\frac{L}{10}$

Table 6.7: Table of experimental data. Data indicated by index 1 are taken from [67] and index 2 from [41].

constants in SI units	$R_{seed} = 1$nm	$R_{seed} = 2$nm
θ	5.24×10^{-3}	
p	535.96	
$S\mid_{P=0.5}$	2.62	1.67
m	1×10^{-25}	
k	1.38×10^{-23}	
T	275	
ν	8.85×10^{11}	
L	8.29×10^{-20}	
δ	1×10^{-10}	
E	8.29×10^{-21}	
σ	2.5×10^{-2}	
j	2.87×10^{25}	1.83×10^{25}
l	290.57	

Table 6.8: List of values for constants as implied by the experimental set-up (Winkler et al, 2008) and theoretical estimates (Määttänen et al, 2007) and (Seki & Hasegawa, 1983).

[SI units]	$R_{seed} = 1$nm	$R_{seed} = 2$nm
S_{exp}	2.62	1.67
$S_{Fletcher}$	2.71	1.87
$\mathtt{i}^*_{exp}$	25	25
$\mathtt{i}^*_{Fletcher}$	130	814
$r(\mathtt{i} = \mathtt{i}^*_{exp})$	1.2×10^{-9}	2.06×10^{-9}
$r(\mathtt{i} = \mathtt{i}^*_{Fletcher})$	1.69×10^{-9}	3.17×10^{-9}

Table 6.9: List of calculated quantities: the experimental onset saturation ratio S_{exp}, the onset saturation ratio as obtained from Fletcher theory $S_{Fletcher}$, the experimental critical cluster size $\mathtt{i}^*_{exp}$, the size of the critical cluster as given by Fletcher theory $\mathtt{i}^*_{Fletcher}$, the radius of a cluster evaluated for the experimental critical cluster size $r(\mathtt{i} = \mathtt{i}^*_{exp})$, the radius of a cluster evaluated for the size of the critical cluster as given by Fletcher theory $r(\mathtt{i} = \mathtt{i}^*_{Fletcher})$ —equivalent to the Fletcher radius $r^*_{Fletcher}$— for two particular radii of the seed particle R_{seed}.

nucleation rate [$\mathrm{m}^{-2}\mathrm{s}^{-1}$]	$R_{seed} = 1$nm	$R_{seed} = 2$nm
$\mathcal{J}_{exp}$	5.52×10^{19}	1.38×10^{19}
$\mathcal{J}_{Fletcher}$	6.32×10^{17}	3.61×10^{-8}
$\mathcal{J}^{dv}_{BD,kin}(\langle C^{dv}_1\rangle^{kin})$	2.0×10^{18}	9.05×10^{-8}

Table 6.10: List of the calculated nucleation currents in the various models: the experimental nucleation current $\mathcal{J}_{exp}$, the Fletcher nucleation current $\mathcal{J}_{Fletcher}$, the kinetic Becker-Döring nucleation rate $\mathcal{J}^{dv}_{BD,kin}(\langle C^{dv}_1\rangle^{kin})$ for two particular radii of the seed particle R_{seed}.

[SI units]	$R_{seed} = 1$nm	$R_{seed} = 2$nm
σ_{exp}	2.51×10^{-2}	$2.51\times10-2$
σ_{eff}	1.79×10^{-2}	1.63×10^{-2}
$\mathtt{i}^*_{exp} = \mathtt{i}^*_{Fletcher}$	25	25
$r(\mathtt{i} = \mathtt{i}^*_{exp}) = r(\mathtt{i} = \mathtt{i}^*_{Fletcher}) = r^*_{Fletcher}$	1.2×10^{-9}	2.06×10^{-9}
S_{exp}	2.62	1.67
$S_{Fletcher}$	1.94	1.47

Table 6.11: List of calculated quantities in the modified model: the experimental surface tension σ_{exp}, the effective surface tension σ_{eff}; the experimental critical cluster size $\mathtt{i}^*_{exp}$; the size of the critical cluster as given by Fletcher theory $\mathtt{i}^*_{Fletcher}$, the radius of a cluster evaluated for the experimental critical cluster size $r(\mathtt{i}^*_{exp})$, the radius of a cluster evaluated for the order of the critical cluster as given by Fletcher theory $r(\mathtt{i} = \mathtt{i}^*_{Fletcher})$, and the Fletcher radius $r^*_{Fletcher}$ for two particular radii of the seed particle R_{seed}; the experimental onset saturation ratio S_{exp}, and the onset saturation ratio as obtained from Fletcher theory $S_{Fletcher}$,

nucleation rate [$m^{-2}s^{-1}$]	$R_{seed} = 1$nm	$R_{seed} = 2$nm
$\mathcal{J}_{exp}$	5.52×10^{19}	1.38×10^{19}
$\mathcal{J}_{Fletcher}$	1.79×10^{29}	4.81×10^{29}
$\mathcal{J}^{dv}_{BD,kin}(\langle C_1^{dv}\rangle^{kin})$	3.32×10^{29}	1.62×10^{30}
$\mathcal{J}^{dv}_{BD,dyn}(t_\infty)$	2.87×10^{25}	1.83×10^{25}
$\mathcal{J}^{dv}_{BD,kin}(\langle C_1^{dv}(t_\infty)\rangle)$	2.87×10^{25}	1.83×10^{25}

Table 6.12: List of the calculated nucleation currents in the various modified models: the experimental nucleation current $\mathcal{J}_{exp}$, the Fletcher nucleation current $\mathcal{J}_{Fletcher}$, the kinetic Becker-Döring nucleation rate $\mathcal{J}^{dv}_{BD,kin}(\langle C_1^{dv}\rangle^{kin})$, the nucleation rate at late times as derived from the dynamical Becker-Döring rate equations $\mathcal{J}^{dv}_{BD,dyn}(t_\infty)$, and the kinetic Becker-Döring nucleation current obtained with the late-time mean monomer concentration as calculated from the dynamical Becker-Döring rate equations $\mathcal{J}^{dv}_{BD,kin}(\langle C_1^{dv}(t_\infty)\rangle)$, for two particular radii of the seed particle R_{seed}.

concentrations [m^{-2}]	$R_{seed} = 1$nm	$R_{seed} = 2$nm
$\langle C_1^{dv}(t_\infty)\rangle$	7.1×10^{17}	8.51×10^{18}
$\langle C_1^{sd,dv}(t_\infty)\rangle$	2.21×10^{16}	2.08×10^{17}
$\langle C_{25}^{dv}(t_\infty)\rangle$	1.12×10^{17}	3.15×10^{17}
$\langle C_{25}^{sd,dv}(t_\infty)\rangle$	4.85×10^{15}	9.73×10^{15}
$\langle C_{30}^{dv}(t_\infty)\rangle$	1.87×10^{16}	5.22×10^{16}
$\langle C_{30}^{sd,dv}(t_\infty)\rangle$	8.28×10^{14}	1.68×10^{15}

Table 6.13: Late-time mean cluster concentrations in the mean-field framework computed employing the modified parameters according to the direct vapour deposition mechanism $\langle C_1^{dv}(t_\infty)\rangle$ and according to the combined direct vapour deposition mechanism and surface diffusion mechanism $\langle C_1^{sd,dv}(t_\infty)\rangle$ for two different values of the radius of the seed particle R_{seed}.

nucleation rate [$m^{-2}s^{-1}$]	$R_{seed} = 1$nm	$R_{seed} = 2$nm
$\mathcal{J}^{dv}_{BD,dyn}(t_\infty)$	2.87×10^{25}	1.83×10^{25}
$\mathcal{J}^{sd,dv}_{BD,dyn}((t_\infty)$	1.52×10^{24}	1.16×10^{24}

Table 6.14: List of the calculated nucleation currents in the modified models as derived from the dynamical Becker-Döring rate equations in the direct vapour deposition mechanism, $\mathcal{J}^{dv}_{BD,dyn}(t_\infty)$, and $\mathcal{J}^{sd,dv}_{BD,dyn}(t_\infty)$ as derived from the dynamical Becker-Döring rate equations for the combined mechanism (direct vapour deposition and surface diffusion mechanism) for two particular radii of the seed particle R_{seed}.

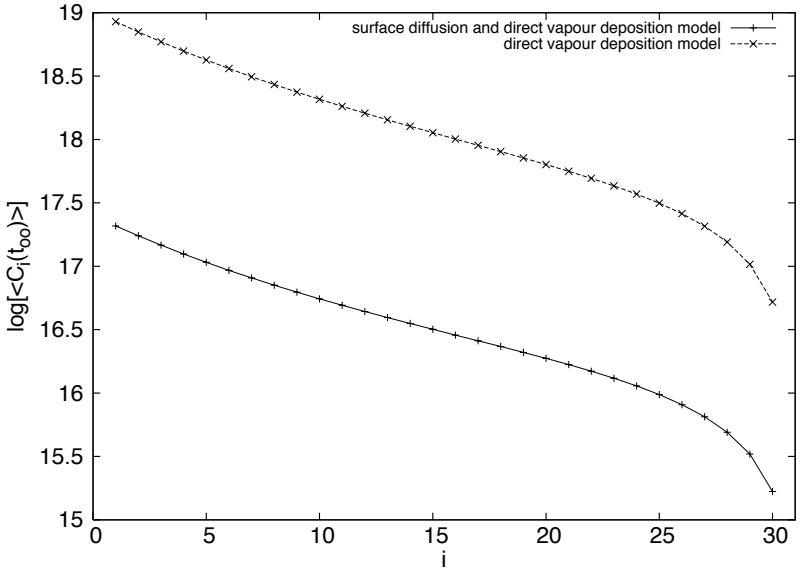

Figure 6.16: Dependence of the mean late-time cluster concentrations on the order of `i`-mers with regards to the mean-field framework for the modified model parameters according to the direct vapour deposition mechanism and according to the combined surface diffusion and direct vapour deposition mechanism. The maximum order of `i`-mers was chosen to be 30. The lines are a guide to the eye.

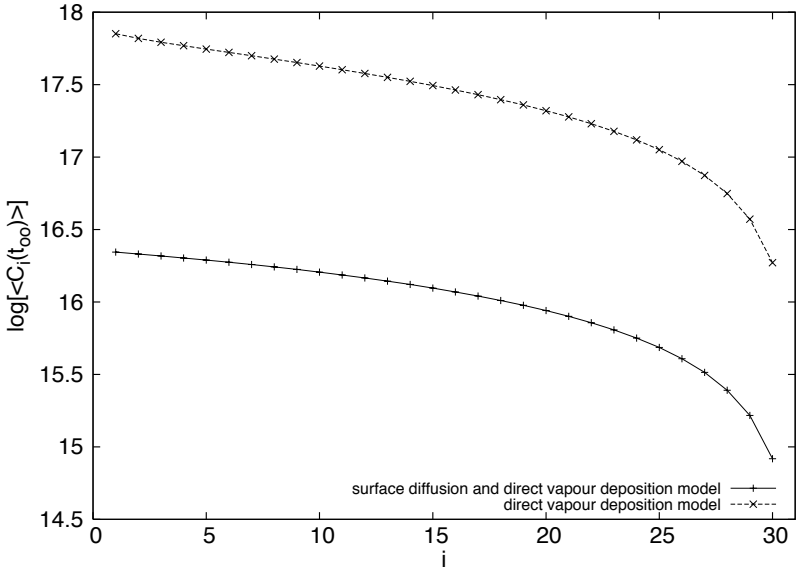

Figure 6.17: Dependence of the mean late-time cluster concentrations on the order of `i`-mers with regards to the mean-field framework for the modified model parameters according to the direct vapour deposition mechanism and according to the combined surface diffusion and direct vapour deposition mechanism. The maximum order of `i`-mers was chosen to be 30. The lines are a guide to the eye.

6.2 Stochastic Theory

The Becker-Döring birth and death equations (6.16) are *inter alia* based on the assumption that cluster growth processes take place at a rate which is proportional to the product of the mean concentrations of clusters. This assumption is justified as long as the cluster populations are large. However, if populations are small fluctuations and correlations are important. In order to develop a model beyond the mean-field approach, that is the Becker-Döring rate equations (6.16), we consider the evolution of the probability distribution $W(\{M\};t)$ —where $\{M\} := \{M_1, M_2, M_3, ..., M_{\mathtt{i}_{max}-1}, M_{\mathtt{i}_{max}}\}$— of the system containing $M_{\mathtt{i}}$ i-mers at time t. In [3] a master equation for the nucleation based on the surface diffusion mechanism was presented, namely,

$$\begin{aligned}
\frac{\mathrm{d}W(\{M\};t)}{\mathrm{d}t} &= \mathrm{J}W(M_1-1,...;t) - \mathrm{J}W(\{M\};t) + \\
&\mathrm{L}(M_1+1)W(M_1+1,...;t) - \mathrm{L}M_1W(\{M\};t) + \\
&\mathrm{G}_1'(M_1+2)(M_1+1)W(M_1+2,M_2-1,...;t) - \mathrm{G}_1'M_1(M_1-1)W(\{M\};t) + \\
&\sum_{\mathtt{i}=2}^{\mathtt{i}_{max}-1} \mathrm{G}_{\mathtt{i}}'(M_1+1)(M_{\mathtt{i}+1})W(M_1+1,...,M_{\mathtt{i}}+1,M_{\mathtt{i}+1}-1,...;t) + \\
&\mathrm{G}_{\mathtt{i}_{max}}'(M_1+1)(M_{\mathtt{i}_{max}}+1)W(M_1+1,...,M_{\mathtt{i}_{max}}+1;t) - \\
&\sum_{\mathtt{i}=2}^{\mathtt{i}_{max}} \mathrm{G}_i'M_1M_{\mathtt{i}}W(\{M\};t) + \\
&\mathrm{D}_2(M_2+1)W(M_1-2,M_2+1,...;t) - \mathrm{D}_2M_2W(\{M\};t) + \\
&\sum_{\mathtt{i}=3}^{\mathtt{i}_{max}} \mathrm{D}_{\mathtt{i}}(M_{\mathtt{i}}+1)W(M_1-1,...,M_{\mathtt{i}-1}-1,M_{\mathtt{i}}+1,...;t) - \\
&\sum_{\mathtt{i}=3}^{\mathtt{i}_{max}} \mathrm{D}_{\mathtt{i}}M_{\mathtt{i}}W(\{M\};t). \qquad (6.70)
\end{aligned}$$

In the same way as we have assumed for the traditional Becker-Döring equations (6.16), in the above master equation, one ignores the gain and loss of dimers, trimers, etc. and rather considers the gain and loss of monomers only. The processes of growth under consideration are:
(a) $1 + (\mathtt{i}-1) \rightarrow \mathtt{i}$: monomer attachment to a cluster of size $\mathtt{i}-1$ from the surface of the seed with rate coefficient $\mathrm{G}_{\mathtt{i}-1}'$;
(b) $1 + \mathtt{i} \rightarrow (\mathtt{i}+1)$: monomer attachment to a cluster of size $\mathtt{i}$ from the surface of the

seed with rate coefficient $G'_{\mathtt{i}}$.
The decay processes under considerations are:
(c) $\mathtt{i} \to (\mathtt{i}-1)+1$: monomer loss from a cluster of size $\mathtt{i}$ onto the surface of the seed with rate coefficient $D_{\mathtt{i}}$;
(d) $(\mathtt{i}+1) \to \mathtt{i}+1$: monomer loss from a cluster of size $\mathtt{i}+1$ onto the surface of the seed with rate coefficient $D_{\mathtt{i}+1}$.
In addition, one has the following processes:
(e) the adsorption of monomers from the surrounding gas-phase onto the surface of the pre-existing particle with rate coefficient J;
(f) the evaporation of monomers from the surface of the seed into the surrounding gas-phase with rate coefficient L.

In [3] deviations from the mean-field behaviour were observed in the numerical calculations for the nucleation current for a certain region in the parameter space of the power law model for the rate coefficients with the particular choice $c = 2$ and $\mathtt{i}^* = 2$ which we have called Model 1 earlier. Yet, for numerical reasons the maximum order of $\mathtt{i}$-mers was very small, namely $\mathtt{i}_{max} = 4$. Concerning the deviations in the results of the master equation approach compared to the results of the mean-field Becker-Döring rate equations our aim is to provide the full dynamical stochastic model which could be extended to higher orders of $\mathtt{i}$-mers without too much cost of computational effort.

We extend the master equation (6.70) presented in [3] by formulating a master equation that comprises both the surface diffusion mechanism as well as the direct vapour deposition mechanism and derive the system of stochastic differential constraint equations and the path integral average in the Doi-Peliti formalism according to the techniques presented in Chapter 2 and Chapter 5.

The full master equation replacing the set of Becker-Döring rate equations reads

$$
\begin{aligned}
\frac{\mathrm{d}W(\{M\};t)}{\mathrm{d}t} = {} & \mathrm{J}W(M_1-1,...;t) - \mathrm{J}W(\{M\};t) + \\
& \mathrm{L}(M_1+1)W(M_1+1,...;t) - \mathrm{L}M_1W(\{M\};t) + \\
& \sum_{\mathtt{i}=1}^{\mathtt{i}_{max}-1} \mathrm{G}_{\mathtt{i}}^{dv}(M_{\mathtt{i}}+1)W(...,M_{\mathtt{i}}+1,M_{\mathtt{i}+1}-1,...;t) + \\
& \mathrm{G}_{\mathtt{i}_{max}}^{dv}(M_{\mathtt{i}_{max}}+1)W(...,M_{\mathtt{i}_{max}}+1;t) - \\
& \sum_{\mathtt{i}=1}^{\mathtt{i}_{max}} \mathrm{G}_{\mathtt{i}}^{dv}M_{\mathtt{i}}W(\{M\};t) + \\
& \mathrm{G}_1^{\prime sd}(M_1+2)(M_1+1)W(M_1+2,M_2-1,...;t) - \mathrm{G}_1^{\prime sd}M_1(M_1-1)W(\{M\};t) + \\
& \sum_{\mathtt{i}=2}^{\mathtt{i}_{max}-1} \mathrm{G}_{\mathtt{i}}^{\prime sd}(M_1+1)(M_{\mathtt{i}}+1)W(M_1+1,...,M_{\mathtt{i}}+1,M_{\mathtt{i}+1}-1,...;t) + \\
& \mathrm{G}_{\mathtt{i}_{max}}^{\prime sd}(M_1+1)(M_{\mathtt{i}_{max}}+1)W(M_1+1,...,M_{\mathtt{i}_{max}}+1;t) - \\
& \sum_{\mathtt{i}=2}^{\mathtt{i}_{max}} \mathrm{G}_{\mathtt{i}}^{\prime sd}M_1M_{\mathtt{i}}W(\{M\};t) + \\
& \mathrm{D}_2^{sd}(M_2+1)W(M_1-2,M_2+1,...;t) - \mathrm{D}_2^{sd}M_2W(\{M\};t) + \\
& \sum_{\mathtt{i}=3}^{\mathtt{i}_{max}} \mathrm{D}_{\mathtt{i}}^{sd}(M_{\mathtt{i}}+1)W(M_1-1,...,M_{\mathtt{i}-1}-1,M_{\mathtt{i}}+1,...;t) - \\
& \sum_{\mathtt{i}=3}^{\mathtt{i}_{max}} \mathrm{D}_{\mathtt{i}}^{sd}M_{\mathtt{i}}W(\{M\};t) + \\
& \mathrm{D}_2^{dv}(M_2+1)W(M_1-1,M_2+1,...;t) - \mathrm{D}_2^{dv}M_2W(\{M\};t) + \\
& \sum_{\mathtt{i}=3}^{\mathtt{i}_{max}} \mathrm{D}_{\mathtt{i}}^{dv}(M_{\mathtt{i}}+1)W(...,M_{\mathtt{i}-1}-1,M_{\mathtt{i}}+1,...;t) - \\
& \sum_{\mathtt{i}=3}^{\mathtt{i}_{max}} \mathrm{D}_{\mathtt{i}}^{dv}M_{\mathtt{i}}W(\{M\};t).
\end{aligned}
\tag{6.71}
$$

The terms indicated in yellow colour in the above equation (6.71) describe the change in the monomer population due to monomers that are gained from the surrounding gas-phase of the seed particle. The terms highlighted in green colour give the change in the monomer population due to the monomers that are evaporated from the surface of the seed particle into the surrounding gas-phase of the grain. The subsequent terms

shown in blue colour specify the aggregation of an i-mer on the surface of the grain particle with a monomer gained from the surrounding gas-phase of the seed. The terms pictured in cyan colour detail the association of an i-mer and a monomer that are both diffusing on the surface of the grain. The following terms in equation (6.71) characterise the situation where an i-mer splits into an $(\mathtt{i}-1)$-mer and one monomer. Either only the $(\mathtt{i}-1)$-cluster stays on the surface of the seed particle and the monomer escapes into the surrounding gas-phase of the grain (red colour) or both resulting clusters stay on the surface (magenta colour). The inital condition of the probability distribution $W(\{M\};t)$ reads

$$W(\{M\};t\equiv 0)=\exp\left(-\sum_{\mathtt{i}=1}^{\mathtt{i}_{max}}\bar{M}_{\mathtt{i}}(0)\right)\left(\prod_{M_{\mathtt{i}}}M_{\mathtt{i}}!\right)^{-1}\bar{M}_1(0)^{M_1}\times\ldots\times\bar{M}_{\mathtt{i}_{max}}(0)^{M_{\mathtt{i}_{max}}}, \tag{6.72}$$

where $\bar{M}_{\mathtt{i}}(0)$ is the initial mean number of i-mers. Note that, in contrast to the studies concerning heterogeneous chemical reactions, in this part of the thesis we consider a single lattice point from the start. Following the mathematical techniques of the Doi-Peliti formalism and in analogy to past procedures we reformulate the master equation (6.70) as a Schrödinger-like equation

$$\begin{aligned}\frac{\mathrm{d}}{\mathrm{d}t}|\Psi\rangle_{HN}=\Bigg(&(\overset{+}{\mathtt{a}}_1-1)(\mathrm{J}-\mathrm{L}\,\overset{-}{\mathtt{a}}_1)+\\&\sum_{\mathtt{i}=1}^{\mathtt{i}_{max}-1}\mathrm{G}_{\mathtt{i}}^{dv}\,\overset{-}{\mathtt{a}}_{\mathtt{i}}\overset{+}{\mathtt{a}}_{\mathtt{i}+1}+\mathrm{G}_{\mathtt{i}_{max}}^{dv}\,\overset{-}{\mathtt{a}}_{\mathtt{i}_{max}}-\sum_{\mathtt{i}=1}^{\mathtt{i}_{max}}\mathrm{G}_{\mathtt{i}}^{dv}\,\overset{+}{\mathtt{a}}_{\mathtt{i}}\overset{-}{\mathtt{a}}_{\mathtt{i}}+\\&\mathrm{G}_1^{\prime sd}\left((\overset{-}{\mathtt{a}}_1)^2\,\overset{+}{\mathtt{a}}_2-(\overset{+}{\mathtt{a}}_1)^2(\overset{-}{\mathtt{a}}_1)^2\right)+\sum_{\mathtt{i}=2}^{\mathtt{i}_{max}-1}\mathrm{G}_{\mathtt{i}}^{\prime sd}\,\overset{-}{\mathtt{a}}_1\overset{-}{\mathtt{a}}_{\mathtt{i}}\overset{+}{\mathtt{a}}_{\mathtt{i}+1}+\\&\mathrm{G}_{\mathtt{i}_{max}}^{\prime sd}\,\overset{-}{\mathtt{a}}_1\overset{-}{\mathtt{a}}_{\mathtt{i}_{max}}-\sum_{\mathtt{i}=2}^{\mathtt{i}_{max}}\mathrm{G}_{\mathtt{i}}^{\prime sd}\,\overset{+}{\mathtt{a}}_1\overset{-}{\mathtt{a}}_1\overset{+}{\mathtt{a}}_{\mathtt{i}}\overset{-}{\mathtt{a}}_{\mathtt{i}}\\&\sum_{\mathtt{i}=2}^{\mathtt{i}_{max}}\mathrm{D}_{\mathtt{i}}^{sd}\,\overset{+}{\mathtt{a}}_1\overset{+}{\mathtt{a}}_{\mathtt{i}-1}\overset{-}{\mathtt{a}}_{\mathtt{i}}+\sum_{\mathtt{i}=2}^{\mathtt{i}_{max}}\mathrm{D}_{\mathtt{i}}^{dv}\,\overset{+}{\mathtt{a}}_{\mathtt{i}-1}\overset{-}{\mathtt{a}}_{\mathtt{i}}-\\&\sum_{\mathtt{i}=2}^{\mathtt{i}_{max}}\left(\mathrm{D}_{\mathtt{i}}^{dv}+\mathrm{D}_{\mathtt{i}}^{sd}\right)\overset{+}{\mathtt{a}}_{\mathtt{i}}\overset{-}{\mathtt{a}}_{\mathtt{i}}\Bigg)|\Psi\rangle_{HN},\end{aligned} \tag{6.73}$$

where $|\Psi\rangle_{HN}$ is the many-body wave function which is defined as

$$|\Psi\rangle_{HN}:=\sum_{\{M_{\mathtt{i}}\}}\left(\prod_{\mathtt{i}=1}^{\mathtt{i}_{max}}\overset{+}{\mathtt{a}}_{\mathtt{i}}^{M_{\mathtt{i}}}\right)W(\{M\};t)|0\rangle, \tag{6.74}$$

with $\overset{+}{\mathtt{a}}$ denoting the creation operator and $\bar{\mathtt{a}}$ denoting the corresponding annihilation operator. The summation is taken over all orders of $\mathtt{i}$-mers up to the maximum order of unstable configurations. The Hamiltonian in the coherent state representation $H_{HN}[\{\varphi(t)\},\{\varphi^*(t)\}]$ —cfr. (2.37)— reads

$$
\begin{aligned}
-H_{HN}[\{\varphi(t)\},\{\varphi^*(t)\}] = \\
&(\varphi_1^*(t)-1)(\mathrm{J}-\mathrm{L}\varphi_1(t)) + \\
&\sum_{\mathtt{i}=1}^{\mathtt{i}_{max}-1} \mathrm{G}_{\mathtt{i}}^{dv}\varphi_{\mathtt{i}}(t)\varphi_{\mathtt{i}+1}^*(t) + \mathrm{G}_{\mathtt{i}_{max}}^{dv}\varphi_{\mathtt{i}_{max}}(t) - \sum_{\mathtt{i}=1}^{\mathtt{i}_{max}} \mathrm{G}_{\mathtt{i}}^{dv}\varphi_{\mathtt{i}}^*(t)\varphi_{\mathtt{i}}(t) + \\
&\mathrm{G}_1^{\prime sd}(\varphi_1^2(t)\varphi_2^*(t) - (\varphi_1^{*2}(t)\varphi_1^2(t)) + \sum_{\mathtt{i}=2}^{\mathtt{i}_{max}-1} \mathrm{G}_{\mathtt{i}}^{\prime sd}\varphi_1(t)\varphi_{\mathtt{i}}(t)\varphi_{\mathtt{i}+1}^*(t) + \\
&\mathrm{G}_{\mathtt{i}_{max}}^{\prime sd}\varphi_1(t)\varphi_{\mathtt{i}_{max}}(t) - \sum_{\mathtt{i}=2}^{\mathtt{i}_{max}} \mathrm{G}_{\mathtt{i}}^{\prime sd}\varphi_1^*(t)\varphi_1(t)\varphi_{\mathtt{i}}^*(t)\varphi_{\mathtt{i}}(t) + \\
&\sum_{\mathtt{i}=2}^{\mathtt{i}_{max}} \mathrm{D}_{\mathtt{i}}^{dv}\varphi_{\mathtt{i}-1}^*(t)\varphi_{\mathtt{i}}(t) + \sum_{\mathtt{i}=2}^{\mathtt{i}_{max}} \mathrm{D}_{\mathtt{i}}^{sd}\varphi_1^*(t)\varphi_{\mathtt{i}-1}^*(t)\varphi_{\mathtt{i}}(t) - \\
&\sum_{\mathtt{i}=2}^{\mathtt{i}_{max}} \left(\mathrm{D}_{\mathtt{i}}^{sd}+\mathrm{D}_{\mathtt{i}}^{dv}\right)\varphi_{\mathtt{i}}^*(t)\varphi_{\mathtt{i}}(t),
\end{aligned}
\tag{6.75}
$$

with $\varphi(t)$ the eigenvalue function of a coherent state vector which is a right eigenstate of the annihilation operator and $\varphi^*(t)$ the complex conjugate of $\varphi(t)$. The Doi-shifted action $\tilde{S}_{HN}[\{\varphi(t)\},\{\tilde{\varphi}(t)\}]$, that is, the action with the following substitution $\varphi_{\mathtt{i}}^*(t) \to \tilde{\varphi}_{\mathtt{i}}(t)+1$ for all orders $\mathtt{i}$ of the $\mathtt{i}$-mers is given by

$$
\tilde{S}_{HN}[\{\varphi(t)\},\{\tilde{\varphi}(t)\}] = \int_0^{t_T} \mathrm{d}t \left(\sum_{\mathtt{i}=1}^{\mathtt{i}_{max}} \tilde{\varphi}_{\mathtt{i}}(t)\frac{\mathrm{d}}{\mathrm{d}t}\varphi_{\mathtt{i}}(t) + \tilde{H}_{HN}[\{\varphi(t)\},\{\tilde{\varphi}(t)\}] \right) + \tilde{S}_0,
\tag{6.76}
$$

with $\tilde{S}_0$ the part of the action incorporating the initial conditions, namely,

$$
\tilde{S}_0 := -\sum_{\mathtt{i}=1}^{\mathtt{i}_{max}} \left(\bar{M}_{\mathtt{i}}(0) + \bar{M}_{\mathtt{i}}(0)\left(\tilde{\varphi}_{\mathtt{i}}(0) - \bar{M}_{\mathtt{i}}(0)\right)\right).
\tag{6.77}
$$

After some rearranging of the terms, the Doi-shifted Hamiltonian $\tilde{H}_{HN}[\{\varphi(t)\},\{\tilde{\varphi}(t)\}]$

takes the form

$$
\begin{aligned}
-\tilde{H}_{HN}[\{\varphi(t)\},\{\tilde{\varphi}(t)\}] = \tilde{\varphi}_1(t)(\mathrm{J}-\mathrm{L}\varphi_1(t)) + \\
\sum_{\mathtt{i}=1}^{\mathtt{i}_{max}-1} (\tilde{\varphi}_{\mathtt{i}+1}(t)-\tilde{\varphi}_{\mathtt{i}}(t))\left(\mathrm{G}_{\mathtt{i}}^{dv}\varphi_{\mathtt{i}}(t)-\mathrm{D}_{\mathtt{i}+1}^{dv}\varphi_{\mathtt{i}+1}(t)\right) - \\
\mathrm{G}_{\mathtt{i}_{max}}^{dv}\varphi_{\mathtt{i}_{max}}(t)\tilde{\varphi}_{\mathtt{i}_{max}}(t) + \\
\sum_{\mathtt{i}=1}^{\mathtt{i}_{max}-1} (\tilde{\varphi}_{\mathtt{i}+1}(t)-\tilde{\varphi}_1(t)\tilde{\varphi}_{\mathtt{i}}(t)-\tilde{\varphi}_1(t)-\tilde{\varphi}_{\mathtt{i}}(t))\left(\mathrm{G}_{\mathtt{i}}^{\prime sd}\varphi_1(t)\varphi_{\mathtt{i}}(t)-\right. \\
\left.\mathrm{D}_{\mathtt{i}+1}^{sd}\varphi_{\mathtt{i}+1}(t)\right) - \\
\mathrm{G}_{\mathtt{i}_{max}}^{\prime sd}\varphi_1(t)\varphi_{\mathtt{i}_{max}}(t)\left(\tilde{\varphi}_1(t)\tilde{\varphi}_{\mathtt{i}_{max}}(t)+\tilde{\varphi}_1(t)+\tilde{\varphi}_{\mathtt{i}_{max}}(t)\right). \qquad (6.78)
\end{aligned}
$$

We want to disentangle the terms in the Doi-shifted Hamiltonian (6.78) that are pseudo-quadratic in the Doi-shifted complex conjugates of the eigenvalue functions, namely,

$$
-\tilde{\varphi}_1(t)\left(\varphi_1(t)\sum_{\mathtt{i}=1}^{\mathtt{i}_{max}}\mathrm{G}_{\mathtt{i}}^{\prime sd}\tilde{\varphi}_{\mathtt{i}}(t)\varphi_{\mathtt{i}}(t)-\sum_{\mathtt{i}=1}^{\mathtt{i}_{max}}\mathrm{D}_{\mathtt{i}+1}^{sd}\tilde{\varphi}_{\mathtt{i}}(t)\varphi_{\mathtt{i}+1}(t)\right). \qquad (6.79)
$$

Therefore, in analogy to Chapter 5 where we considered the hydrogen-oxygen reaction network, we make use of the Gaussian transformation

$$
\int \mathrm{D}^n\mathbf{e}\exp\left(-\mathbf{e}^T\mathbf{A}\mathbf{e}+\mathbf{b}^T\mathbf{e}\right) = \sqrt{\frac{\pi^n}{|\det\mathbf{A}|}}\exp\left(\frac{1}{4}\mathbf{b}^T\mathbf{A}^{-1}\mathbf{b}\right), \qquad (6.80)
$$

where $\mathbf{A}$ is a symmetric $(\mathtt{i}_{max}\times\mathtt{i}_{max})$ matrix and $\mathbf{b}$ and $\mathbf{e}$ are two $\mathtt{i}_{max}$-dimensional vectors. The entries of the two vectors $\mathbf{b}$ and $\mathbf{e}$ and the matrix $\mathbf{A}$ read as follows:

$$
\mathbf{A} = \begin{pmatrix}
1 & 0 & 0 & 0 & 0 & 0 & \cdots & 0 \\
0 & 0 & 1 & 0 & 0 & 0 & \cdots & 0 \\
0 & 1 & 0 & 0 & 0 & 0 & \cdots & 0 \\
0 & 0 & 0 & 0 & 1 & 0 & \cdots & 0 \\
0 & 0 & 0 & 1 & 0 & 0 & \cdots & 0 \\
\vdots & \vdots & \vdots & \vdots & \vdots & \vdots & \vdots & \vdots
\end{pmatrix}, \qquad (6.81)
$$

$$\mathbf{b} = \begin{pmatrix} \mathrm{i}2\alpha_1(t)\tilde{\varphi}_1(t) \\ \mathrm{i}\sqrt{2}\alpha_2(t)\tilde{\varphi}_2(t) \\ \mathrm{i}\sqrt{2}\alpha_2(t)\tilde{\varphi}_1(t) \\ \mathrm{i}\sqrt{2}\alpha_3(t)\tilde{\varphi}_3(t) \\ \mathrm{i}\sqrt{2}\alpha_3(t)\tilde{\varphi}_1(t) \\ \vdots \\ \mathrm{i}\sqrt{2}\alpha_{\mathtt{i}_{max}-1}(t)\tilde{\varphi}_{\mathtt{i}_{max}-1}(t) \\ \mathrm{i}\sqrt{2}\alpha_{\mathtt{i}_{max}-1}(t)\tilde{\varphi}_1(t) \\ \mathrm{i}\sqrt{2}\alpha_{\mathtt{i}_{max}}(t)\tilde{\varphi}_{\mathtt{i}_{max}}(t) \\ \mathrm{i}\sqrt{2}\alpha_{\mathtt{i}_{max}}(t)\tilde{\varphi}_1(t) \end{pmatrix}, \quad \mathbf{e} = \begin{pmatrix} \frac{\eta_{1,1}(t)}{\sqrt{2}} \\ \frac{\eta_2(t)}{2} \\ \frac{\eta_{1,2}(t)}{2} \\ \frac{\eta_3(t)}{2} \\ \frac{\eta_{1,3}(t)}{2} \\ \vdots \\ \frac{\eta_{\mathtt{i}_{max}-1}(t)}{2} \\ \frac{\eta_{1,\mathtt{i}_{max}-1}(t)}{2} \\ \frac{\eta_{\mathtt{i}_{max}}(t)}{2} \\ \frac{\eta_{1,\mathtt{i}_{max}}(t)}{2} \end{pmatrix}, \tag{6.82}$$

where we defined

$$\alpha_{\mathtt{i}}(t) := \alpha_{\mathtt{i}}[\varphi_{\mathtt{j}}(t)] = \sqrt{\mathrm{G}'^{sd}_{\mathtt{i}}\varphi_1(t)\varphi_{\mathtt{i}}(t) - \mathrm{D}^{sd}_{\mathtt{i}+1}\varphi_{\mathtt{i}+1}(t)}, \tag{6.83}$$

with $\mathrm{D}^{dv}_{\mathtt{i}_{max}+1} = \mathrm{D}^{sd}_{\mathtt{i}_{max}+1} \equiv 0$. The noise $\eta_{1,1}(t)$ is a real white Gaussian noise whereas the other noises are defined as

$$\eta_{1,\mathtt{j}}(t) := \frac{1}{\sqrt{2}}\left(\Re(\eta_{1,\mathtt{j}}(t)) + \mathrm{i}\Im(\eta_{1,\mathtt{j}}(t))\right) = \eta^*_{\mathtt{j}}(t) \quad \mathtt{j} \in [2, \mathtt{i}_{max}], \tag{6.84}$$

with $\Re(\eta_{1,\mathtt{j}}(t))$ and $\Im(\eta_{1,\mathtt{j}}(t))$ being real white Gaussian noises. Accordingly, the auto-correlations and cross-correlations read

$$\begin{aligned} &\langle \eta_{1,\mathtt{k}}(t)\rangle_{\mathcal{P}[\eta]} = \langle \eta_{\mathtt{j}}(t)\rangle_{\mathcal{P}[\eta]} = 0, \\ &\langle \eta_{1,1}(t)\eta_{1,1}(t')\rangle_{\mathcal{P}[\eta]} = \langle \eta_{1,\mathtt{j}}(t)\eta_{\mathtt{j}}(t')\rangle_{\mathcal{P}[\eta]} = \delta(t-t'), \end{aligned} \tag{6.85}$$

where $\mathtt{j} \in [2, \mathtt{i}_{max}]$ and $\mathtt{k} \in [1, \mathtt{i}_{max}]$ and with $\mathcal{P}[\eta]$ the Gaussian probability distribution

$$\mathcal{P}[\eta] := \exp\left(-\frac{1}{2}\int \mathrm{d}t \left(\eta^2_{1,1}(t) + \sum_{\mathtt{j}=2}^{\mathtt{i}_{max}} \eta_{1,\mathtt{j}}(t)\eta_{\mathtt{j}}(t)\right)\right). \tag{6.86}$$

All other cross-correlations are vanishing.

According to the Doi-Peliti formalism, the expectation values are computed via the path integral average:

$$\langle \mathtt{O}(t)\rangle = \frac{\int \mathrm{D}\eta O[\bar{\varphi}_{\mathtt{i}}(t)]\mathcal{P}[\eta(t)]}{\int \mathrm{D}\eta \mathcal{P}[\eta(t)]}, \tag{6.87}$$

where the measure $\mathrm{D}\eta$ is given by

$$\mathrm{D}\eta := \mathrm{D}\eta_{1,1} \prod_{\mathtt{j}=2}^{\mathtt{i}_{max}} \mathrm{D}\eta_{1,\mathtt{j}} \mathrm{D}\eta_{\mathtt{j}}. \tag{6.88}$$

The unknown fields $\bar{\varphi}_{\mathtt{i}}(t)$ are solutions to the following constraint equations

$$\begin{aligned} \mathrm{d}\bar{\varphi}_1(t) = \left(\mathrm{J} - \mathrm{L}\bar{\varphi}_1(t) - \sum_{\mathtt{i}=1}^{\mathtt{i}_{max}} \alpha_{\mathtt{i}}^2[\bar{\varphi}_{\mathtt{k}}(t)] - \alpha_1^2[\bar{\varphi}_{\mathtt{k}}(t)] - \mathrm{G}_1^{dv}\bar{\varphi}_1(t) + \mathrm{D}_2^{dv}\bar{\varphi}_2(t) \right) \mathrm{d}t + \\ \mathrm{i}\sqrt{2}\alpha_1[\bar{\varphi}_{\mathtt{k}}(t)]\mathrm{d}W_{1,1} + \frac{\mathrm{i}}{\sqrt{2}} \sum_{\mathtt{j}=2}^{\mathtt{i}_{max}} \alpha_{\mathtt{j}}[\bar{\varphi}_{\mathtt{k}}(t)]\mathrm{d}W_{1,\mathtt{j}}, \end{aligned} \tag{6.89}$$

and for $\mathtt{j} \in [2, \mathtt{i}_{max}]$

$$\begin{aligned} \mathrm{d}\bar{\varphi}_{\mathtt{j}}(t) = \big(\mathrm{G}_{\mathtt{j}-1}^{dv}\bar{\varphi}_{\mathtt{j}-1}(t) - \mathrm{G}_{\mathtt{j}}^{dv}\bar{\varphi}_{\mathtt{j}}(t) - \mathrm{D}_{\mathtt{j}}^{dv}\bar{\varphi}_{\mathtt{j}}(t) + \mathrm{D}_{\mathtt{j}+1}^{dv}\bar{\varphi}_{\mathtt{j}+1}(t) + \\ \alpha_{\mathtt{j}-1}^2[\bar{\varphi}_{\mathtt{k}}(t)] - \alpha_{\mathtt{j}}^2[\bar{\varphi}_{\mathtt{k}}(t)] \big) \mathrm{d}t + \frac{\mathrm{i}}{\sqrt{2}} \alpha_{\mathtt{j}}[\bar{\varphi}_{\mathtt{k}}(t)]\mathrm{d}W_{\mathtt{j}}. \end{aligned} \tag{6.90}$$

The above set of constraint equations consists of $\mathtt{i}_{max}$ coupled ordinary stochastic differential equations. The symbols $\mathrm{d}W_{1,\mathtt{j}}$ and $\mathrm{d}W_{\mathtt{j}}$ are the Wiener increments corresponding to the Gaussian noises. Furthermore, we have for $\mathtt{i} \in [1, \mathtt{i}_{max}]$ that

$$\bar{\varphi}_{\mathtt{i}}(0) \equiv \bar{M}_{\mathtt{i}}(0), \tag{6.91}$$

where $\bar{M}_{\mathtt{i}}(0)$ is the value of the mean initial $\mathtt{i}$-mer population.

In the following paragraphs we will consider processes according to the surface diffusion mechanism only, hence $\mathrm{G}_{\mathtt{i}}^{dv} \equiv 0$, $\mathrm{D}_{\mathtt{i}}^{dv} \equiv 0$, $\mathrm{G}_{\mathtt{i}}^{\prime sd} \equiv \mathrm{G}_{\mathtt{i}}^{\prime}$ and $\mathrm{D}_{\mathtt{i}}^{sd} \equiv \mathrm{D}_{\mathtt{i}}$ In contrast to the nucleation current obtained from the dynamical mean-field theory

$$\mathcal{J}_{BD,dyn}(t_\infty) = \begin{cases} (\mathrm{G}_{\mathtt{i}}^{\prime}\langle M_1(t)\rangle\langle M_{\mathtt{i}}(t)\rangle - \mathrm{D}_{\mathtt{i}+1}\langle M_{\mathtt{i}+1}(t)\rangle) \Big|_{t=t_\infty} & : \quad \mathtt{i} \in [1, \mathtt{i}_{max}-1] \\ \mathrm{G}_{\mathtt{i}_{max}}^{\prime}\langle M_1(t)\rangle\langle M_{\mathtt{i}_{max}}(t)\rangle \Big|_{t=t_\infty} & : \quad \mathtt{i} = \mathtt{i}_{max}, \end{cases} \tag{6.92}$$

the nucleation current derived in the dynamical stochastic theory reads

$$\mathcal{J}_{DP}(t_\infty) = \begin{cases} (\mathrm{G}'_{\mathtt{i}}\langle\varphi_1(t)(\varphi_{\mathtt{i}}(t)-1)\rangle - \mathrm{D}_{\mathtt{i}+1}\langle\varphi_{\mathtt{i}+1}(t)\rangle)\Big|_{t=t_\infty} & : \quad \mathtt{i}=1 \\ (\mathrm{G}'_{\mathtt{i}}\langle\varphi_1(t)\varphi_{\mathtt{i}}(t)\rangle - \mathrm{D}_{\mathtt{i}+1}\langle\varphi_{\mathtt{i}+1}(t)\rangle)\Big|_{t=t_\infty} & : \quad \mathtt{i}\in[2,\mathtt{i}_{max}-1] \\ \mathrm{G}'_{\mathtt{i}_{max}}\langle\varphi_1(t)\varphi_{\mathtt{i}_{max}}(t)\rangle\Big|_{t=t_\infty} & : \quad \mathtt{i}=\mathtt{i}_{max}. \end{cases} \tag{6.93}$$

Note that in the expression for $\mathcal{J}_{BD,dyn}(t_\infty)$, equation (6.92), we have the product of averages whereas in the expression for $\mathcal{J}_{DP}(t_\infty)$, equation (6.93), we have the average of products. Furthermore, in the formula for the stochastic nucleation current, equation (6.93), we account for the fact that having a single monomer on the surface of the seed can not give rise to a nucleation current. In the Doi-Peliti formalism the stochastic average is determined by the path integral expression (6.87). This path integral average will be used to compute the mean i-mer populations $\langle\varphi_{\mathtt{i}}(t)\rangle$ in the dynamical stochastic framework —cfr. (6.89), (6.90) and (6.87)— as well as the stochastic nucleation current $\mathcal{J}_{DP}(t_\infty)$ —cfr. (6.93).

6.3 Comparison between Mean-Field and Stochastic Model

6.3.1 Constant Rate Coefficients

For convenience, we choose the source rate to be equal to the evaporation rate, $\mathrm{J} = \mathrm{L} \equiv \textit{constant}$, and the growth rate to be equal to the loss rate, $\mathrm{G}' = \mathrm{D} \equiv \textit{constant}$. The growth rate and decay rate coefficients are chosen to be equal to $\mathrm{G}' = \mathrm{D} = 10\mathrm{s}^{-1}$ in the sequel. When deriving the i-mer population according to the mean-field Becker-Döring rate equations —equations (6.16)— as well as according to the Doi-Peliti formalism —equations (6.89), (6.90) and (6.87)— we see that the tendency indicated in (6.32) is confirmed in Figure 6.18 where we plot the mean late-time cluster populations $\langle M_{\mathtt{i}}(t_\infty)\rangle$ according to the mean-field theory and the mean stochastic late-time cluster populations $\langle\varphi_{\mathtt{i}}(t_\infty)\rangle$ against the cluster order i for specific values of the maximum order of the clusters, namely, $\mathtt{i}_{max} \in [2,4,6,8,10]$. There is no noticeable difference between the values of $\langle M_{\mathtt{i}}(t_\infty)\rangle$ and $\langle\varphi_{\mathtt{i}}(t_\infty)\rangle$. Furthermore, one observes that, for fixed i, the values of the mean late-time cluster population of the same order i are greater for a larger number of unstable clusters in the systems, that is, for fixed i we

find

$$\langle M_{\mathtt{i}}(t_\infty)\rangle\Big|_{\mathtt{i}_{max}=\mathtt{k}} > \langle M_{\mathtt{i}}(t_\infty)\rangle\Big|_{\mathtt{i}_{max}=\mathtt{m}}, \tag{6.94}$$

where $\mathtt{k} > \mathtt{m}$. Furthermore, the convergence behaviour (6.33) is verified in Figures 6.19, 6.20, 6.21, 6.22 which show the dependence on the order of clusters $\mathtt{i}$ of the mean late-time cluster populations as derived from the Becker-Döring rate equations, $\langle M_{\mathtt{i}}(t_\infty)\rangle$, and —except for Figure 6.22— of the mean late-time cluster populations as given by the Doi-Peliti formalism, $\langle \varphi_{\mathtt{i}}(t_\infty)\rangle$, for the specific values of the rate coefficients $\mathrm{J} = \mathrm{L} \in [1000\mathrm{s}^{-1}, 100\mathrm{s}^{-1}, 10\mathrm{s}^{-1}, 1\mathrm{s}^{-1}]$ with a maximum number of unstable clusters $\mathtt{i}_{max} = 2$ —Figure 6.19—, $\mathtt{i}_{max} = 4$ —Figure 6.20—, $\mathtt{i}_{max} = 6$ —Figure 6.21—, and $\mathtt{i}_{max} = 8$ —Figure 6.22. Figure 6.22 demonstrates linear behaviour of the mean late-time cluster population with regards to the order of clusters for large values of the source rate coefficient and of the evaporation rate coefficient, whereas for small values of the rate coefficients this is no longer the case. Nevertheless, for decreasing values of J and L the mean late-time cluster populations decrease for all orders $\mathtt{i}$. Unfortunately, due to the larger number of the non-linear coupled stochastic differential equations (6.89) and (6.90), instabilities occur during the numerical evaluation of the constraint equations. Therefore, it is not possible for the particular choice of $\mathtt{i}_{max}$ to determine a meaningful value for the mean late-time cluster populations according to the Doi-Peliti formalism. Although in Figures 6.19, 6.20, 6.21 we give the path integral average $\langle \varphi_{\mathtt{i}}(t_\infty)\rangle$, the same instabilities force us to take the average for the larger number of $\mathtt{i}_{max}$ over only 100 realisations of the noises which is a crude estimate for the true value of the mean late-time cluster population. Even for such a small number of generated paths it takes several attempts to compute the path integral average with a configuration where no extreme spike occurs in the evolution that distorts the calculations. Despite the errors that arise in the value of the stochastic mean late-time cluster populations due to the small number of solutions to the stochastic constraints that are employed in the path integral average, it is clear from all three Figures 6.19, 6.20, 6.21 that for $\mathrm{J} = \mathrm{L} \in [1000\mathrm{s}^{-1}, 100\mathrm{s}^{-1}]$ the stochastic results and the mean-field results coincide. However, for $\mathrm{J} = \mathrm{L} \in [10\mathrm{s}^{-1}, 1\mathrm{s}^{-1}]$ one observes a deviation from the solutions to the traditional Becker-Döring rate equations: the stochastic mean late-time cluster populations are greater than their mean-field counterparts for each order of cluster $\mathtt{i}$ and for all maximum numbers of unstable cluster $\mathtt{i}_{max}$ under consideration.

For a large source rate coefficient and a large evaporation rate coefficient, that is, for $\mathrm{J} = \mathrm{L} = 1000\mathrm{s}^{-1}$, we notice only a small change in the mean late-time monomer population with regards to a change in the maximum order of clusters in

both frameworks as illustrated in Figure 6.23. For a choice of $\mathrm{J} = \mathrm{L} = 100\mathrm{s}^{-1}$, the mean late-time monomer population increases for increasing value of $\mathtt{i}_{max}$ in both frameworks. In general, the mean late-time monomer population which is given by solving the Becker-Döring rate equations increases for increasing value of the source rate. In Figure 6.24 we observe the same overall behaviour —the increase in the mean late-time monomer population for increasing value of $\mathtt{i}_{max}$— however, the stochastic mean late-time monomer populations for $\mathrm{J} = \mathrm{L} = 10\mathrm{s}^{-1}$ and $\mathrm{J} = \mathrm{L} = 1\mathrm{s}^{-1}$ agree and are greater than the respective mean-field solutions.

In Figure 6.25 we plot the mean late-time monomer population according to the mean-field framework and to the stochastic framework versus the logarithm of the source rate for different maximum orders of $\mathtt{i}$-mer populations, $\mathtt{i}_{max} \in [2, 4, 6]$. After the threshold of the stochastic regime is reached —which is independent of the maximum order of unstable clusters— the decrease in $\langle \varphi_{\mathtt{i}}(t_\infty) \rangle$ with regards to a decreasing source rate slows down compared to the decrease in $\langle M_{\mathtt{i}}(t_\infty) \rangle$.

As a result of our calculations of the mean late-time cluster populations we identified the deterministic regime for values of $\mathrm{J} = \mathrm{L} \in [1000\mathrm{s}^{-1}, 100\mathrm{s}^{-1}]$ and the stochastic regime for values of $\mathrm{J} = \mathrm{L} \in [10\mathrm{s}^{-1}, 1\mathrm{s}^{-1}]$. Although the mean late-time cluster populations for $\mathrm{J} = \mathrm{L} = 100\mathrm{s}^{-1}$ as derived from the Becker-Döring rate equations and the mean late-time cluster populations for $\mathrm{J} = \mathrm{L} = 100\mathrm{s}^{-1}$ as computed by the Doi-Peliti formalism give the same values, this is not true for the nucleation current. For $\mathrm{J} = \mathrm{L} = 1000\mathrm{s}^{-1}$ the stochastic nucleation rate

$$\mathcal{J}_{DP}(t_\infty) := \frac{\int \mathrm{D}\eta \mathrm{G}'_{\mathtt{i}_{max}} \bar{\varphi}_1(t) \bar{\varphi}_{\mathtt{i}_{max}}(t) \mathcal{P}[\eta(t)]}{\int \mathrm{D}\eta \mathcal{P}[\eta(t)]}, \tag{6.95}$$

where the probability distribution is given by (6.86) and the fields $\bar{\varphi}_1(t)$ and $\bar{\varphi}_{\mathtt{i}_{max}}(t)$ are solutions to (6.89) and (6.90) and the mean-field nucleation rate $\mathcal{J}_{BD,dyn}(t_\infty)$ —cfr. equation (6.34)— coincide —see Table 6.15— whereas for $\mathrm{J} = \mathrm{L} = 100\mathrm{s}^{-1}$ there is a slight deviation. At the threshold between the deterministic regime and the stochastic regime, the value of the stochastic nucleation current seems to be slightly smaller than the value of the mean-field nucleation current. In general, the nucleation rate decreases with increasing maximum order of clusters $\mathtt{i}_{max}$ for fixed rate coefficients which can be seen in Figure 6.26 where the rate coefficients were chosen to be $\mathrm{J} = \mathrm{L} \in [1000\mathrm{s}^{-1}, 100\mathrm{s}^{-1}]$. Furthermore, the nucleation rate computed with $\mathrm{J} = \mathrm{L} = 1000\mathrm{s}^{-1}$ is greater than the nucleation rate with $\mathrm{J} = \mathrm{L} = 100\mathrm{s}^{-1}$ —see Table 6.15.
Since the spikes in the fluctuating solutions to the constraint equations go quadratically

into the computation of the stochastic nucleation current one can have a situation in which it is reasonable to determine a mean population according to the Doi-Peliti formalism yet one might not be able to allocate a value to the nucleation current as illustrated in Figures 6.27 and 6.28. Figure 6.27 shows the evolution of the stochastic mean monomer population for a source rate of $\mathrm{J} = \mathrm{L} = 10\mathrm{s}^{-1}$ with $\mathtt{i}_{max} = 4$ averaged over 100 realisations of the noises. Although the number of paths employed in the path integral average is small it is clear that the solution fluctuates around a specific steady state which can be visually estimated. However, due to the extreme spikes in the evolution of the respective stochastic nucleation current —presented in Figure 6.28— it is not even possible to estimate a certain value. The more paths are generated to be employed in the path integral average the more likely it is to produce a path with an extreme spike that can even drive the evolution to explosion. A rigorous method to stabilise the evolution for any choice of parameters is not apparently available.

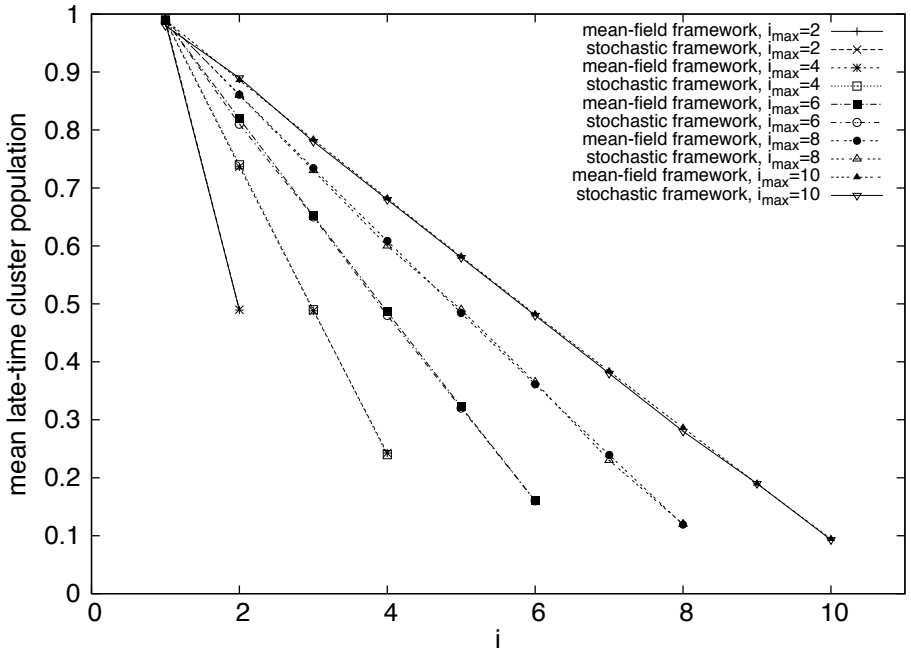

Figure 6.18: Mean late-time cluster populations according to the mean-field theory $\langle M_{\mathtt{i}}(t_\infty)\rangle$ and according to the stochastic theory $\langle \varphi_{\mathtt{i}}(t_\infty)\rangle$ for a maximum number of Becker-Döring equations of $\mathtt{i}_{max} \in [2, 4, 6, 8, 10]$ for the following choice of rate coefficients: $\mathrm{G}' = \mathrm{D} = 10\mathrm{s}^{-1}$ and $\mathrm{J} = \mathrm{L} = 1000\mathrm{s}^{-1}$. The lines are a guide to the eye.

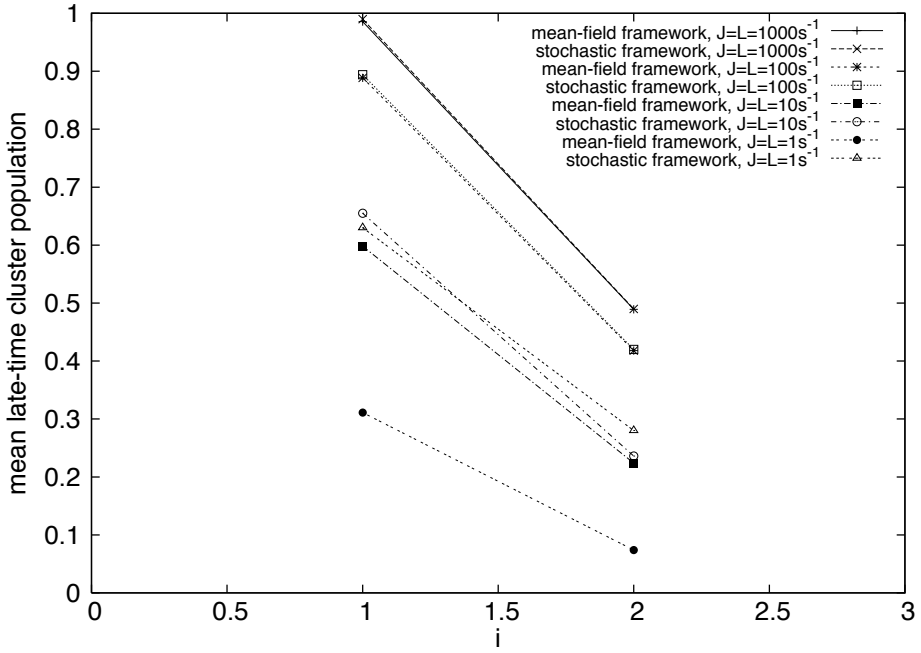

Figure 6.19: Mean late-time cluster populations according to the mean-field theory $\langle M_{\mathtt{i}}(t_\infty)\rangle$ and according to the stochastic theory $\langle \varphi_{\mathtt{i}}(t_\infty)\rangle$ for a maximum number of Becker-Döring equations of $\mathtt{i}_{max} = 2$ for the following choice of rate coefficients: $\mathrm{G}' = \mathrm{D} = 10\mathrm{s}^{-1}$ and $\mathrm{J} = \mathrm{L} \in [1000\mathrm{s}^{-1}, 100\mathrm{s}^{-1}, 10\mathrm{s}^{-1}, 1\mathrm{s}^{-1}]$. The lines are a guide to the eye.

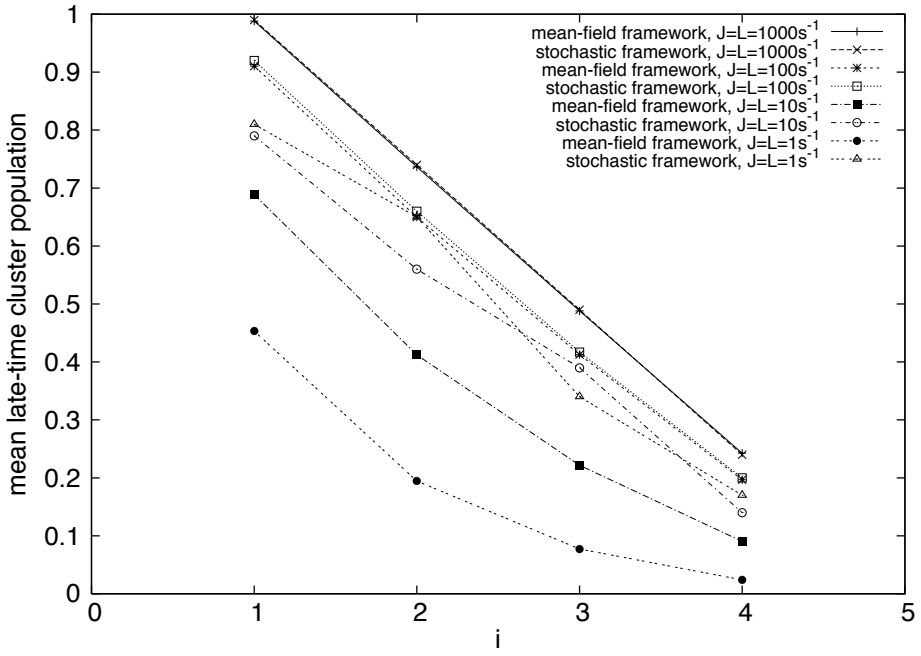

Figure 6.20: Mean late-time cluster populations according to the mean-field theory $\langle M_{\mathtt{i}}(t_\infty)\rangle$ and according to the stochastic theory $\langle \varphi_{\mathtt{i}}(t_\infty)\rangle$ for a maximum number of Becker-Döring equations of $\mathtt{i}_{max} = 4$ for the following choice of rate coefficients: $\mathrm{G}' = \mathrm{D} = 10\mathrm{s}^{-1}$ and $\mathrm{J} = \mathrm{L} \in [1000\mathrm{s}^{-1}, 100\mathrm{s}^{-1}, 10\mathrm{s}^{-1}, 1\mathrm{s}^{-1}]$. The lines are a guide to the eye.

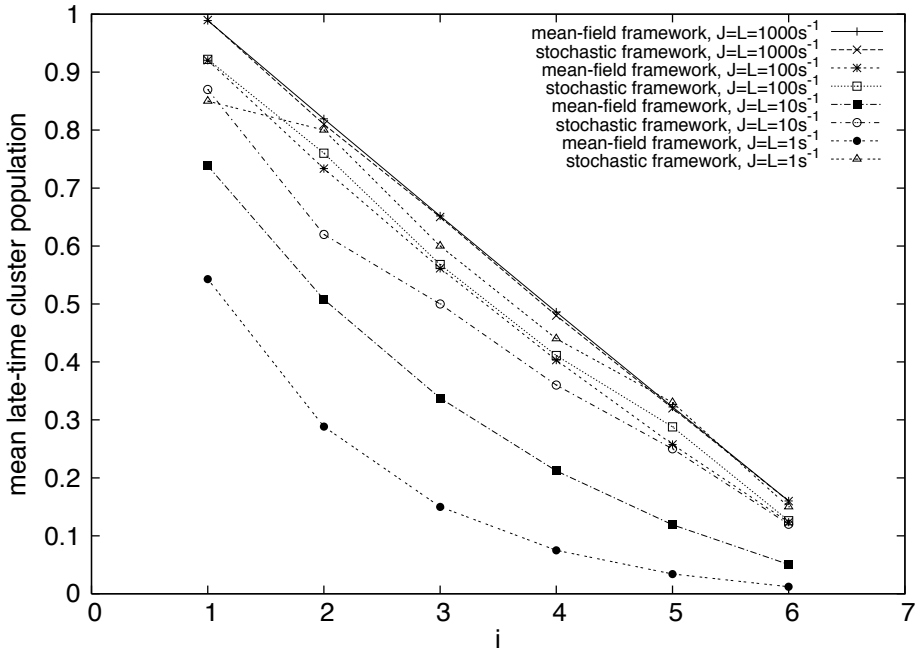

Figure 6.21: Mean late-time cluster populations according to the mean-field theory $\langle M_{\mathtt{i}}(t_\infty)\rangle$ and according to the stochastic theory $\langle \varphi_{\mathtt{i}}(t_\infty)\rangle$ for a maximum number of Becker-Döring equations of $\mathtt{i}_{max} = 6$ for the following choice of rate coefficients: $\mathrm{G}' = \mathrm{D} = 10\mathrm{s}^{-1}$ and $\mathrm{J} = \mathrm{L} \in [1000\mathrm{s}^{-1}, 100\mathrm{s}^{-1}, 10\mathrm{s}^{-1}, 1\mathrm{s}^{-1}]$. The lines are a guide to the eye.

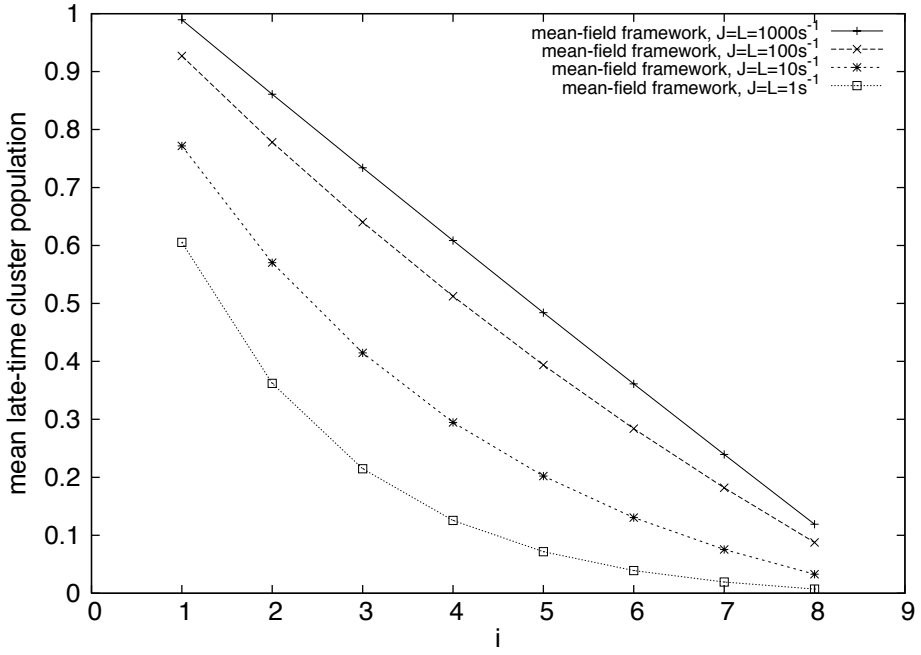

Figure 6.22: Mean late-time cluster populations according to the mean-field theory $\langle M_{\mathtt{i}}(t_\infty)\rangle$ for a maximum number of Becker-Döring equations of $\mathtt{i}_{max} = 8$ for the following choice of rate coefficients: $\mathrm{G}' = \mathrm{D} = 10\mathrm{s}^{-1}$ and $\mathrm{J} = \mathrm{L} \in [1000\mathrm{s}^{-1}, 100\mathrm{s}^{-1}, 10\mathrm{s}^{-1}, 1\mathrm{s}^{-1}]$. The lines are a guide to the eye.

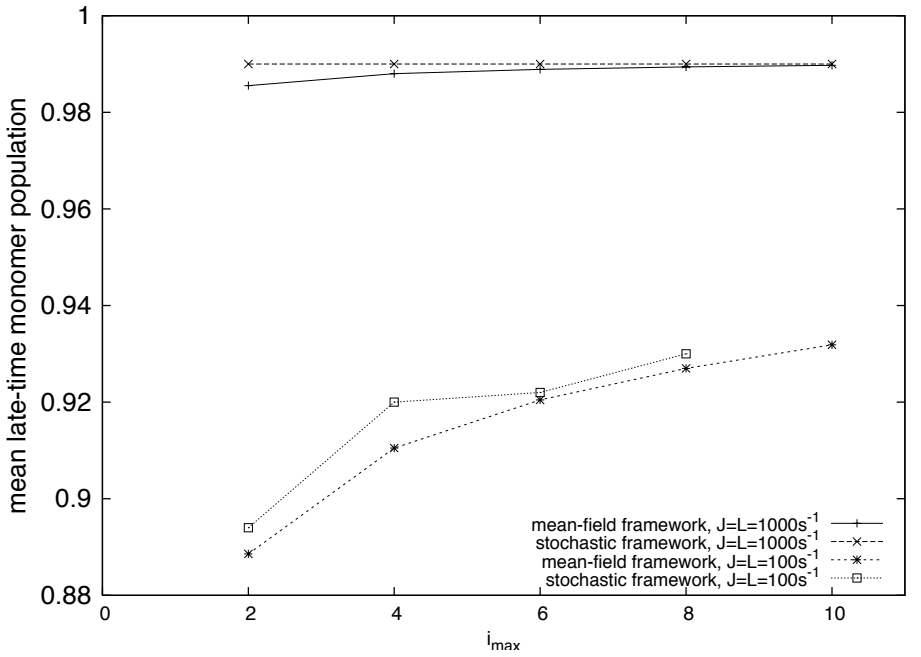

Figure 6.23: Dependence of the mean late-time cluster populations according to the mean-field theory $\langle M_{\mathtt{i}}(t_\infty)\rangle$ and of the mean late-time cluster populations according to the stochastic theory $\langle \varphi_{\mathtt{i}}(t_\infty)\rangle$ on the maximum order of $\mathtt{i}$-mers, $\mathtt{i}_{max}$, for the following choice of rate coefficients: $\mathrm{G}' = \mathrm{D} = 10\mathrm{s}^{-1}$ and $\mathrm{J} = \mathrm{L} \in [1000\mathrm{s}^{-1}, 100\mathrm{s}^{-1}]$. The lines are a guide to the eye.

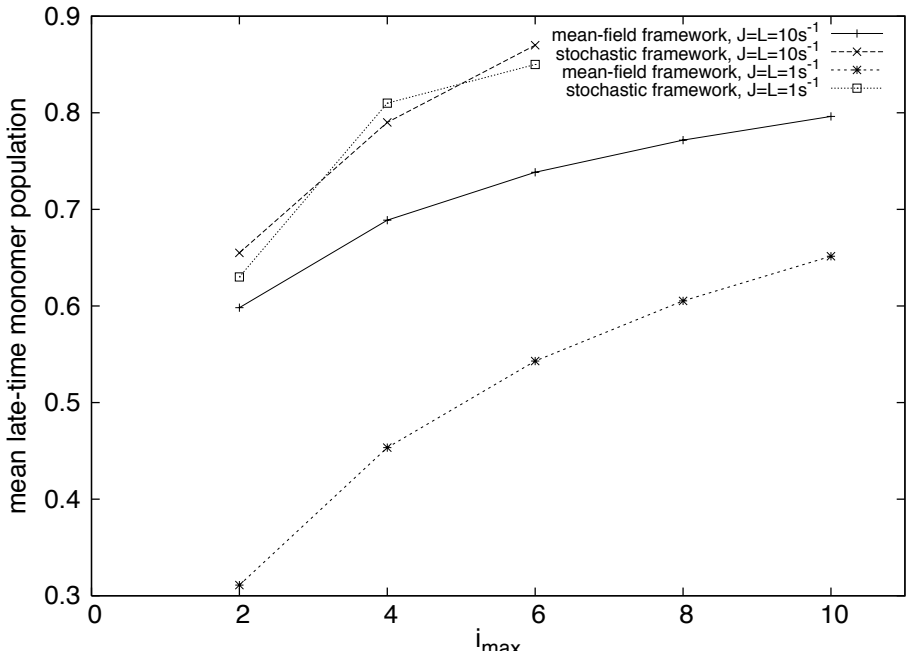

Figure 6.24: Dependence of the mean late-time cluster populations according to the mean-field theory $\langle M_{\mathtt{i}}(t_\infty)\rangle$ and of the mean late-time cluster populations according to the stochastic theory $\langle \varphi_{\mathtt{i}}(t_\infty)\rangle$ on the maximum order of i-mers, $\mathtt{i}_{max}$, for the following choice of rate coefficients: $\mathrm{G}' = \mathrm{D} = 10\mathrm{s}^{-1}$ and $\mathrm{J} = \mathrm{L} \in [10\mathrm{s}^{-1}, 1\mathrm{s}^{-1}]$. The lines are a guide to the eye.

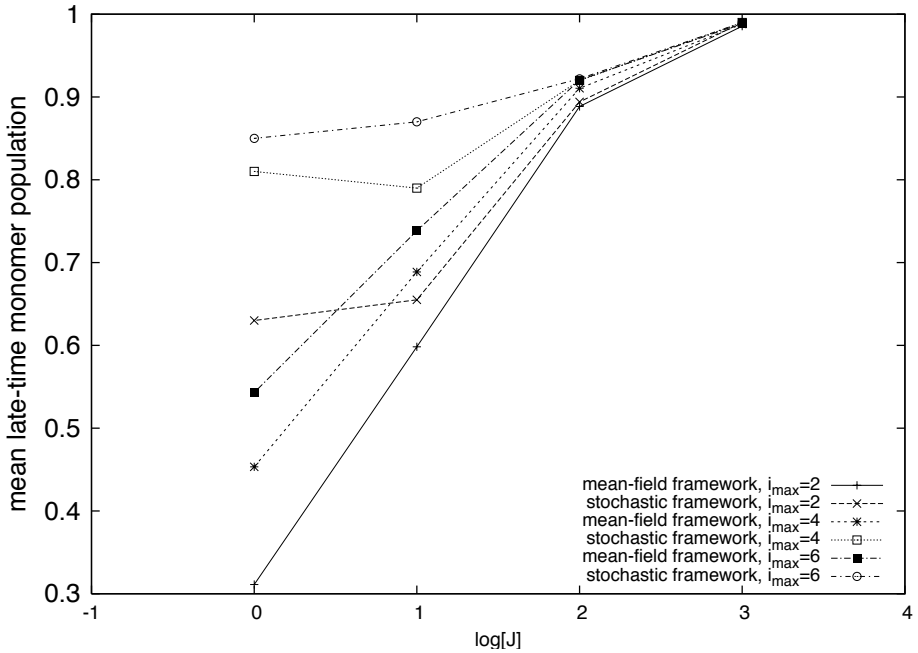

Figure 6.25: Dependence of the mean late-time monomer populations according to the mean-field theory $\langle M_{\mathtt{i}}(t_\infty)\rangle$ and of the mean late-time cluster populations according to the stochastic theory $\langle \varphi_{\mathtt{i}}(t_\infty)\rangle$ on the rate coefficients $\mathrm{J} = \mathrm{L} \in [1000\mathrm{s}^{-1}, 100\mathrm{s}^{-1}, 10\mathrm{s}^{-1}, 1\mathrm{s}^{-1}]$ and for $\mathrm{G}' = \mathrm{D} = 10\mathrm{s}^{-1}$ and $\mathtt{i}_{max} \in [2, 4, 6]$. The lines are a guide to the eye.

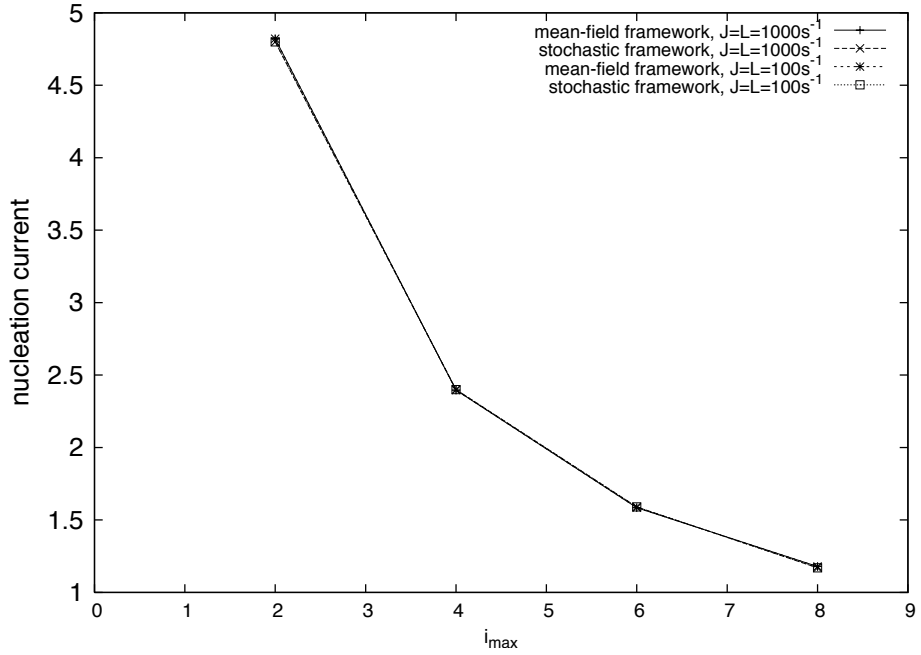

Figure 6.26: Dependence of the nucleation current according to the mean-field theory $\mathcal{J}_{BD,dyn}(t_\infty)$ and of the nucleation current according to the stochastic theory $\mathcal{J}_{DP}(t_\infty)$ on the maximum order of i-mers, $\mathtt{i}_{max}$, for the following choice of rate coefficients: $\mathrm{G}' = \mathrm{D} = 10\mathrm{s}^{-1}$ and $\mathrm{J} = \mathrm{L} \in [1000\mathrm{s}^{-1}, 100\mathrm{s}^{-1}]$. The lines are a guide to the eye.

$\mathtt{i}_{max}$	$\mathcal{J}_{BD,dyn}(t_\infty)$ $\mathrm{J} = \mathrm{L} = 1000\mathrm{s}^{-1}$	$\mathcal{J}_{DP}(t_\infty)$ $\mathrm{J} = \mathrm{L} = 1000\mathrm{s}^{-1}$	$\mathcal{J}_{BD,dyn}(t_\infty)$ $\mathrm{J} = \mathrm{L} = 100\mathrm{s}^{-1}$	$\mathcal{J}_{DP}(t_\infty)$ $\mathrm{J} = \mathrm{L} = 100\mathrm{s}^{-1}$
2	4.82104	4.8	3.71473	3.55
4	2.3965	2.4	1.79056	1.7
6	1.58476	1.59	1.1363	1.1
8	1.17845	1.17	0.811414	0.79

Table 6.15: Dependence of the nucleation current according to the mean-field theory $\mathcal{J}_{BD,dyn}(t_\infty)$ and of the nucleation current according to the stochastic theory $\mathcal{J}_{DP}(t_\infty)$ on the maximum order of i-mers, $\mathtt{i}_{max}$, for the following choice of rate coefficients: $\mathrm{G}' = \mathrm{D} = 10\mathrm{s}^{-1}$ and $\mathrm{J} = \mathrm{L} \in [1000\mathrm{s}^{-1}, 100\mathrm{s}^{-1}]$.

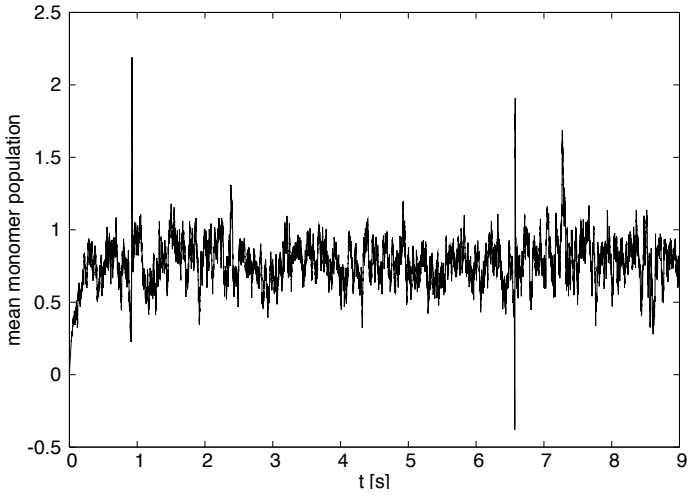

Figure 6.27: The mean late-time monomer population according to the stochastic theory $\langle M_1(t_\infty)\rangle$ for a maximum order of $\mathtt{i}_{max} = 4$ averaged over 100 realisations of the noises and for the following choice of rate coefficients: $\mathrm{G}' = \mathrm{D} = 10\mathrm{s}^{-1}$ and $\mathrm{J} = \mathrm{L} = 10\mathrm{s}^{-1}$.

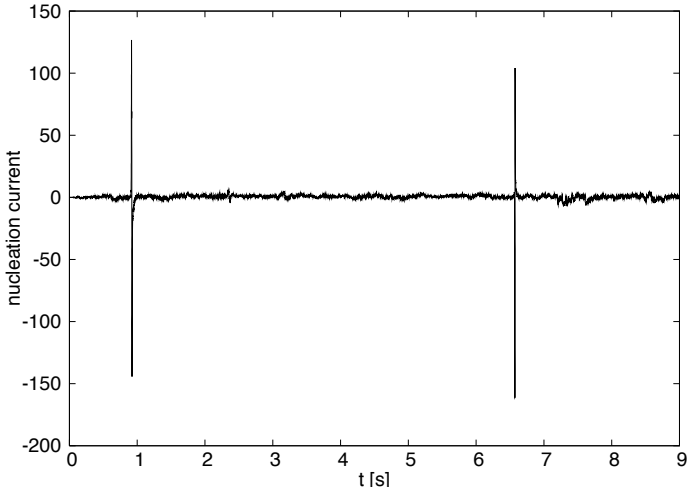

Figure 6.28: The nucleation current according to the stochastic theory $\mathcal{J}_{DP}(t_\infty)$ for a maximum order of $\mathtt{i}_{max} = 4$ averaged over 100 realisations of the noises and for the following choice of rate coefficients: $\mathrm{G}' = \mathrm{D} = 10\mathrm{s}^{-1}$ and $\mathrm{J} = \mathrm{L} = 10\mathrm{s}^{-1}$.

6.4 Conclusions and Outlook

In this chapter, we have analysed in some detail the influence of the form of the rate coefficients on the mean cluster concentrations and, in the same way, on the nucleation currents in the Becker-Döring model. The particular choice of the decay coefficients in the direct vapour deposition mechanism and in the surface diffusion mechanism based on the Fletcher theory was characterised by arguments arising from considerations of detailed balance. At this point it is important to emphasize that this is still only an estimate of the true physical properties of the system in accordance with the following statement taken from [55]:

"One of the most debated points in the nucleation theory is the method of determination of the emission coefficients. These coefficients are specified commonly by deriving the so-called equilibrium or constraint equilibrium distributions with respect to cluster sizes and applying the principles of detailed balancing to thermodynamic non-equilibirum states....Such an approach is, however, highly questionable...In application to thermodynamic non-equilibrium states such distributions are artificial constructs; they are not realized in nature. Moreover, the principle of detailed balancing holds for equilibrium but not for non-equilibrium states.".

In addition, a more detailed analysis of the dependence of the value of the nucleation current on the maximum order of clusters in the Becker-Döring theory with a choice of rate coefficients according to the Fletcher theory might give valuable insight into the accuracy of the model.

As we have observed from our own calculations —where we compared the theoretical nucleation currents obtained from the Fletcher theory and the Becker-Döring theory to the respective values determined in experiments—, in order to obtain a more realistic value of the true nucleation current it is necessary, even in deterministic systems, to modify the form of the rate coefficients and approach a microscopic statistical-mechanical treatment of the physical processes. The same line of argument was pointed out in [54]:

"It follows as one of the consequences of the preceding analysis that the clusters of critical sizes have properties that are widely different, in general from the properties of the newly evolving macroscopic phases. By this reason, also the properties of sub- and supercritical clusters will depend, in general, both on supersaturation and cluster size. In order to develop, consequently, an appropriate description of the course of the phase transitions, one has to develop a method to establish the dependence of composition of clusters of arbitrary sizes on mentioned parameters. The change in the composition of the clusters in dependence of their sizes leads to a size-dependence of

almost all thermodynamic... and kinetic parameters... determining the course of the phase transition... Note that this size dependence is connected with changes of the bulk properties of the clusters.".

Furthermore, more attention needs to be paid on the numerical implemention of the constraint equations in the Doi-Peliti formalism. We have seen that for the simple assumption of constant rate coefficients, stability issues arise in the numerical evaluation of the stochastic differential equations already for a very small maximum order of `i`-mers, that is, for a small set of coupled constraint equations. Therefore, a stochastic treatment of physically realistic situations as presented in the preceding section —where we studied the traditional Becker-Döring rate equations by employing the Fletcher model in order to derive expressions for the rate coefficients— is, for the time-being, not possible. Further analytical as well as further numerical investigations are needed to be able to extend the formalism to configurations of interest to researchers working in the experimental sciences.

Chapter 7

Concluding Remarks

The main focus of this thesis was, besides some deterministic investigations concerning several models for heterogeneous nucleation processes, to provide a stochastic framework that allows for the inclusion of statistical fluctuations in classical, many-body systems which is of great importance for systems with low densities.
The particular systems analysed in this thesis were single chemical reactions in interstellar surface chemistry, complex networks of heterogeneous chemical reactions and heterogeneous nucleation processes in aerosol science.
In order to take into account statistical fluctuations in the description of the time evolution of the populations in the above systems we employed mathematical techniques based on ideas from Quantum Field Theory. The comparison of the late-time results of the Doi-Peliti formalism with the explicit steady state solution employed to determine the mean numbers of chemical species involved in heterogeneous binary chemical reactions led to a revision of the well-known solutions to the stationary master equation with interesting new insights into the validity of the steady state solutions. Furthermore —for specific choices of the model parameters traditionally used in astrochemistry— it was possible to identify a threshold between the deterministic regime, where the solutions to the mean-field evolution equations and the results of the dynamical stochastic methods coincide, and the stochastic regime, where one observes significant deviations from the predictions of the mean-field theory. The extension of the numerical exploitation of the Doi-Peliti formalism to higher space dimensions was found to be fruitful and further projects in this direction seem promising. A generalisation of the methods to more complex systems as chemical reaction networks or heterogeneous nucleation processes was carried out. However, open problems remain in the numerical evaluation of the evolution equations of the complex, fluctuating variables. Concerning the determination of the mean-field nucleation currents in nucleation theory several models for heterogeneous nucleation processes were presented

and compared with experimental data. The various theoretical predictions and the experimental observations were found to be in bad agreement.

The main challenges in possible extensions and improvements of the work presented in this thesis are the following:

Stability Analysis for Stochastic Differential Equations

The set of coupled, non-linear stochastic partial differential equations with multiplicative noise that arise as constraint equations in the procedure of evaluating the path integral average which makes it possible to determine expectation values such as the mean particle density of certain chemical species or the nucleation rate of aerosols are at the heart of the Doi-Peliti formalism. Due to their complex nature, especially when considering realistic chemical reaction networks or the nucleation ladder for a large number of unstable clusters, there are hardly any rigorous results available to study the stability of the equations analytically in the sense of methods of dynamical systems. Such rigorous mathematical results are essential for making the outcome of numerical endeavours more reliable. As we have seen in Chapter 3, the analysis of the time-independent solutions to the master equation provide strong support for the correctness of the numerical results. However, the occasional occurrence of paths that exhibit extreme spikes needs further attention if the Doi-Peliti formalism is ever to be employed for complex classical many-body systems. Besides these obvious drawbacks the hope remains that stochastic frameworks such as the Doi-Peliti formalism can successfully bridge the gap between the macroscopic and the microscopic characteristics, between high and low densities, between the deterministic regime and the stochastic regime.

Models for Rate Coefficients

Another great challenge is to find models that describe the properties of microscopic entities such as the characteristics of clusters in nucleation processes more accurately. The form of the rate coefficients in both the surface chemical reaction processes as well as the heterogeneous nucleation processes, might be understood more as estimates than as a correct description of the physical properties of the system. This is a task that is relevant for experimental and theoretical physicists to the same extent. The lack of experimental data limits the possibilities to analyse the predicitions of a specific model critically. More collaborations between scientists working on the development of the various theories and researchers designing and conducting experiments are highly

desirable.

Appendix A

List of Equations

Arrhenius Equation

The Arrhenius equation gives the dependence of the rate constant R of chemical reactions on the temperature T and activation energy E

$$R(T, E) = A(T) \exp^{-\frac{E}{kT}}, \tag{A.1}$$

with k the Boltzmann constant, and A a pre-factor that, in general, has only a weak dependence on the temperature compared to the exponent. It can be understood in the following way: R is the number of collisions which result in a reaction per second, A is the total number of collisions per second that lead to a reaction or not. The exponent gives the probability that any given collision will result in a reaction.

Fokker-Planck Equation

The Fokker-Planck equation is an approximate description for any *Markov process* whose individual jumps are small. The Fokker-Planck equation is also known by the names of the *generalised diffusion equation*, *Smoluchowski equation*, or *second Kolgomorov equation*. It is a special type of a master equation and can be written as

$$\frac{\partial P(y,t)}{\partial t} = -\frac{\partial (A(y)P(y,t))}{\partial y} + \frac{1}{2}\frac{\partial^2 (B(y)P(y,t))}{\partial y^2}. \tag{A.2}$$

The range of y is continous $(-\infty, \infty)$. The terms $A(y)$ and $B(y)$ are differentiable real functions where $B(y) > 0$. The term $A(y)$ is called *transport term*, *convection term* or *drift term*. The term $B(y)$ is called *diffusion* or *fluctuation term*. The Fokker-Planck equation gives definite expressions for higher moments.

Langevin Equation

The Langevin equation is a special type of a stochastic differential equation:

$$\frac{dv(t)}{dt} = -\gamma v(t) + L(t), \tag{A.3}$$

where $L(t)$ is independent of $v(t)$ and rapidly varying in time. This stochastic variable is determined via the average over an ensemble of many systems in the following way

$$\begin{aligned} &\langle L(t)\rangle = 0, \\ &\langle L(t)L(t')\rangle = \Gamma\delta(t-t'). \end{aligned} \tag{A.4}$$

The first term in the Langevin equation is the damping average force term. The Langevin equation defines $v(t)$ as a stochastic process provided that an initial condition is added. It gives a treatment of Brownian motion. The Fokker-Planck equation gives the same values for the first and second moments of v as the Langevin equation. But the two equations are not really equivalent because their higher moments do not agree. In contrast to the Fokker-Planck equation the Langevin equation does not specify higher moments. One needs an additional condition such as imposing a Gaussian white noise.

Markov Process

A Markov process is a stochastic process such that for any set of n successive times $t_1 < t_2 < ... < t_n$

$$P(y_n, t_n|y_{n-1}, t_{n-1}; ...; y_1, t_1) = P(y_n, t_n|y_{n-1}, t_{n-1}), \tag{A.5}$$

where P is the conditional probability density at t_n, that is the probability density for y to take the value y_n at time t_n given that its value at t_{n-1} is y_{n-1}. The conditional probability density at time t_n is not affected by any knowledge of the values at earlier times.

Master equation

A master equation

$$\frac{\partial P(y,t)}{\partial t} = \int \Big(T_{y\to y'} P(y',t) - T_{y'\to y} P(y,t) \Big) dy', \tag{A.6}$$

where $T_{y\to y'}\Delta t$ is the probability for a transition during a short time Δt, is a differential version of the *Chapman-Kolgomorov equation*. The *Chapman-Kolgomorov equation* or

Smoluchowski equation is defined as

$$P(y_3, t_3|y_1, t_1) = \int_{-\infty}^{\infty} P(y_3, t_3|y_2, t_2)P(y_2, t_2|y_1, t_1)dy_2, \tag{A.7}$$

and gives the transitional densities of a Markov sequence. This identity must be obeyed by the transition probability of any Markov process. Note that time ordering is essential.

The master equation is valid for the transition probability of any stationary Markov process. The first term in (A.6) gives the gain due to transitions from states y' whereas the second term describes the loss due to transitions into states y'. We have used the discrete version of the master equation in this thesis:

$$\frac{dP(m;t)}{dt} = \sum_n T_{n\to m}P(n;t) - \sum_n T_{m\to n}P(m;t), \tag{A.8}$$

where $T_{n\to m}$ represents the *transition amplitude* or *propagator* from a *microstate* n to a microstate m and $P(m;t)$ is the *probability* to find the system in state m.

Poisson Distribution

The Poisson distribution is a discrete probability distribution where events occur at a known average rate and independently of the time since the last event

$$P(a, b) = \frac{a^b e^{-a}}{b!}, \tag{A.9}$$

where $a \in \mathbb{R}^+$ is the expected number of occurences that occur during a given time interval and b is the number of occurences of an event (success in trial). This can be applied to systems with a large number of possible events, each of which is rare.

Verhulst Equation

The deterministic Verhulst equation reads

$$\frac{dP(t)}{dt} = rP(t)\left(1 - \frac{P(t)}{K}\right), \tag{A.10}$$

with $P(t)$ the population at time t, r the growth rate and K the carrying capacity. The solution of the Verhulst equation is given by

$$P(t) = \frac{KP(0)e^{rt}}{K + P(0)\big(e^{rt} - 1\big)}. \tag{A.11}$$

The limit of the solution for late times is

$$\lim_{t\to\infty} P(t) = K. \tag{A.12}$$

White Gaussian Noise

White Noise:
A continuous time random process is a white noise process if and only if its mean function is zero for all times and the autocorrelation function is the Dirac delta function times a finite constant.
Gaussian Noise:
A Gaussian noise is a statistical noise that has a probability density function of a Gaussian distribution, that is, the values that the noise can take are Gaussian-distributed. A *Gaussian Distribution* or *Normal Distribution* is a family of continuous probability distributions defined by the mean μ and variance σ^2, $\sigma > 0$. The probability density function reads

$$P(y) = \left(\sigma\sqrt{2\pi}\right)^{-1} e^{\frac{-(y-\mu)^2}{2\sigma^2}} \tag{A.13}$$

The *Central Limit Theorem* states that the mean of any set of variates with any distribution having a finite mean and variance tends to the normal distribution, that is, data which are influenced by many small and unrelated random effects are approximately normally distributed.

Wiener Process

A Wiener process is a continuous time stochastic process $W(t)$ characterised by the following properties:

$$W(0) = 0 \tag{A.14}$$

$$W(t) - W(s) \text{ is Gaussian} \tag{A.15}$$

$$\text{increments for non-overlapping time intervals are independent} \tag{A.16}$$

Appendix B

Continued Fractions of Bessel functions

In [5] the authors stated that the continued fractions formula of the reduced form of the non-vanishing off-diagonal elements of the matrix $\mathbf{M}''$ —see equation (30) in [5]— in the inifinite limit could be expressed in the continued expression expansion of the ratio of two modified Bessel functions of the first kind, namely

$$\begin{aligned}
\frac{I_\nu(z)}{I_{\nu-1}(z)} &= \frac{z}{2\nu}\left(1 - \frac{I_{\nu+1}(z)}{I_{\nu-1}(z)}\right) \\
&= \frac{z}{2\nu}\left(1 + \frac{I_{\nu+1}(z)}{I_\nu(z)}\frac{z}{2\nu}\right)^{-1} \\
&= \left(\frac{2\nu}{z} + \cfrac{1}{\cfrac{2(\nu+1)}{z} + \cfrac{1}{\cfrac{2(\nu+2)}{z} + \cfrac{1}{\cfrac{2(\nu+3)}{z} + \ldots}}}\right)^{-1},
\end{aligned} \tag{B.1}$$

where $\nu := \frac{L_A}{K_{AA}} + N$ and $z := 2\sqrt{\frac{J_A}{K_{AA}}}$. In the above calculation we have used the following relation twice:

$$I_{\nu-1}(z) - I_{\nu+1}(z) = \frac{2\nu}{z} I_\nu(z). \tag{B.2}$$

On the other hand, one can derive in an analogous manner:

$$\begin{aligned}\frac{I_\nu(z)}{I_{\nu+1}(z)} &= -\frac{z}{2\nu}\left(1-\frac{I_{\nu-1}(z)}{I_{\nu+1}(z)}\right)\\ &= -\frac{z}{2\nu}\left(1-\frac{I_{\nu-1}(z)}{I_\nu(z)}\frac{z}{2\nu}\right)^{-1}\\ &= -\left(\frac{2\nu}{z}+\cfrac{1}{\cfrac{2(\nu-1)}{z}+\cfrac{1}{\cfrac{2(\nu-2)}{z}+\cfrac{1}{\cfrac{2(\nu-3)}{z}+\ldots}}}\right)^{-1}. \end{aligned} \tag{B.3}$$

Since (B.2) is valid for all $\nu \in \mathbb{C}$ one can perform the following substitution $\nu \to -\nu$ so that

$$\begin{aligned}\frac{I_{-\nu}(z)}{I_{-\nu+1}(z)} &= \\ &= -\left(\frac{2(-\nu)}{z}+\cfrac{1}{\cfrac{2(-\nu-1)}{z}+\cfrac{1}{\cfrac{2(-\nu-2)}{z}+\cfrac{1}{\cfrac{2(-\nu-3)}{z}+\ldots}}}\right)^{-1}\end{aligned} \tag{B.4}$$

The above continued fractions expansion is equivalent to the continued fractions expansion (B.1) so that we have

$$\frac{I_\nu(z)}{I_{\nu-1}(z)} = \frac{I_{-\nu}(z)}{I_{-\nu+1}(z)}. \tag{B.5}$$

The above equivalence means that it is possible to express the continued fractions formula of the reduced form of the non-vanishing off-diagonal elements of the matrix $\mathbf{M}''$ in infinite limit by either of the two ratios of the modified Bessel functions of the first kind. Therefore, the full solution of the stationary master equation is a superposition of two Bessel functions as derived by methods of generating functions.

Appendix C

Numerical Schemes

In this part of the appendix we illustrate the various numerical schemes that we employed to numerically evaluate the constraint equations (3.199) and (3.200) to the path integral (2.64) in Chapter 3. In the following we refer to the following definitions:

$$
\begin{aligned}
&X_n := \Phi(t_n) \text{ in discretised time } \ t_n, \\
&\triangle_n := t_{n+1} - t_n, \\
&\triangle W_n := W_{t_{n+1}} - W_{t_n} \\
&\frac{\delta}{\delta[\mathfrak{f}(x)]}\mathfrak{F}[\mathfrak{f}(x)] : \ \text{functional derivative}
\end{aligned}
$$

with $n = 0, .., N$.

Family of implicit Euler methods

A family of implicit Euler methods is given by

$$
\begin{aligned}
&X_{n+1} = X_n + \Big(\alpha\hat{a}[X_{n+1}] + (1-\alpha)\hat{a}[X_n]\Big)\triangle_n + \Big(\beta b[X_{n+1}] + (1-\beta)b[X_n]\Big)\triangle W_n, \\
&\hat{a}[X_n] = a[X_n] - \beta b[X_n]\frac{\delta b[X_n]}{\delta X_n}.
\end{aligned}
$$

The impliciteness parameters are $\alpha, \beta \in [0, 1]$.

Simplified weak Taylor scheme, order 2.0

The simplified order 2.0 weak Taylor scheme is defined as follows

$$X_{n+1} = X_n + a[X_n]\triangle + b[X_n]\triangle W_n + \frac{1}{2}b[X_n]\frac{\delta b[X_n]}{\delta X_n}\big((\triangle W_n)^2 - \triangle_n\big)$$
$$+ \frac{1}{2}\left(\frac{\delta a[X_n]}{\delta X_n}b[X_n] + a[X_n]\frac{\delta b[X_n]}{\delta X_n} + \frac{1}{2}\frac{\delta^2 b[X_n]}{\delta X_n^2}b^2[X_n]\right)\triangle W_n\triangle_n$$
$$+ \frac{1}{2}\left(a[X_n]\frac{\delta a[X_n]}{\delta X_n} + \frac{1}{2}\frac{\delta^2 a[X_n]}{\delta X_n^2}a^2[X_n]\right)\triangle_n^2.$$

Family of Predictor-corrector methods, order 1.0

The family of predictor-corrector methods of order 1.0 with predictor are presented by

$$X_{n+1} = X_n + \left(\alpha\hat{a}[\hat{X}_{n+1}] + (1-\alpha)\hat{a}[X_n]\right)\triangle_n + \left(\beta b[\hat{X}_{n+1}] + (1-\beta)b[X_n]\right)\triangle W_n,$$
$$\hat{a}[X_n] = a[X_n] - \beta b[X_n]\frac{\delta b[X_n]}{\delta X_n},$$

and the predictor

$$\hat{X}_{n+1} = X_n + a[X_n]\triangle + b[X_n]\triangle W_n,$$

where $\alpha, \beta \in [0, 1]$.

Implicit strong Runge-Kutta method, order 1.0

The general formula for the implicit order 1.0 strong Runge-Kutta scheme is given by

$$X_{n+1} = X_n + a[X_{n+1}]\triangle + b[X_n]\triangle W_n + \frac{1}{2\sqrt{\triangle_n}}\big(b[\hat{X}_n] - b[X_n]\big)\big((\triangle W_n)^2 - \triangle_n\big),$$
$$\hat{X}_n = X_n + \alpha\triangle_n + b[X_n]\sqrt{\triangle_n},$$

where the parameter $\alpha \in [0, 1]$.

Appendix D

Binary Recombination of type $A + A \rightarrow A$ In The Single Spatial Site Model

D.1 Mean Field Model For Vanishing Source Rate

The mean-field equation describing the evolution of the average population of molecules of type A, $\langle N_A(t)\rangle$ for vanishing source rate and for positive L_A and positive K_{AA}

$$\frac{\mathrm{d}\langle N_A(t)\rangle}{\mathrm{d}t} = -K_{AA}\langle N_A(t)\rangle^2 - L_A\langle N_A(t)\rangle, \tag{D.1}$$

is solved by

$$\langle N_A(t)\rangle = \frac{\langle N_A(0)\rangle L_A}{L_A \exp\left(L_A t\right) + K_{AA}\langle N_A(0)\rangle(\exp\left(L_A t\right) - 1)}. \tag{D.2}$$

In the mean-field framework, the late time limit of the average molecule population approaches zero.

D.2 Stochastic Model For Vanishing Source Rate

In a stochastic framework, equation (D.1) can be replaced by the following master equation for a single lattice site:

$$\frac{\mathrm{d}P(N_A;t)}{\mathrm{d}t} = L_A(N_A+1)P(N_A+1;t) - L_A N_A P(N_A;t) + \\ K_{AA}(N_A+1)N_A P(N_A+1;t) - K_{AA}N_A(N_A-1)P(N_A;t), \tag{D.3}$$

for $N_A \geq 1$. Following the procedure of the Doi-Peliti formalism one derives the stochastic constraint equation:

$$\frac{\mathrm{d}\Phi_A(t)}{\mathrm{d}t} = -K_{AA}\Phi_A^2(t) - L_A\Phi_A(t) + \mathrm{i}\sqrt{2K_{AA}}\Phi_A(t)\eta(t) \tag{D.4}$$

with:

$$\langle \eta(t) \rangle = 0 \\ \langle \eta(t)\eta(t') \rangle = \delta(t-t') \tag{D.5}$$

for the eigenvalue functions of the coherent state vectors, $\Phi_A(t)$. The exact solution to equation (D.4), whose path integral average gives the mean number of A molecules on the surface of the grain particle, reads:

$$\Phi_A(t) = \frac{\Phi_A(0)e^{(K_{AA}-L_A)t+\mathrm{i}\sqrt{2K_{AA}}W(t)}}{1+K_{AA}\Phi_A(0)\int_0^t e^{(K_{AA}-L_A)s+\mathrm{i}\sqrt{2K_{AA}}W(s)}\mathrm{d}s} \tag{D.6}$$

The modulus of the exact solution to the stochastic equation (D.4) has a lower bound as can be seen from the following calculation:

$$\begin{aligned} |\Phi_A(t)| &= \left| \Phi_A(0)\frac{e^{(K_{AA}-L_A)t}e^{\mathrm{i}\sqrt{2K_{AA}}W(t)}}{1+K_{AA}\Phi_A(0)\int_0^t e^{(K_{AA}-L_A)s}e^{\mathrm{i}\sqrt{2K_{AA}}W(s)}\mathrm{d}s} \right| \\ &= \left| \Phi_A(0)\frac{e^{(K_{AA}-L_A)t}}{1+K_{AA}\Phi_A(0)\int_0^t e^{(K_{AA}-L_A)s}e^{\mathrm{i}\sqrt{2K_{AA}}W(s)}\mathrm{d}s} \right| \\ &\geq |\Phi_A(0)| \frac{e^{(K_{AA}-L_A)t}}{1+\frac{K_{AA}|\Phi(0)|\left(e^{(K_{AA}-L_A)t}-1\right)}{K_{AA}-L_A}}, \end{aligned} \tag{D.7}$$

with $\left|e^{\mathrm{i}\sqrt{2K_{AA}}W(s)}\right| = 1$ and

$$\left|1 + K_{AA}\Phi_A(0)\int_0^t e^{(K_{AA}-L_A)s}e^{\mathrm{i}\sqrt{2K_{AA}}W(s)}\mathrm{d}s\right| \leq 1 + K_{AA}\left|\Phi_A(0)\int_0^t e^{(K_{AA}-L_A)s}e^{\mathrm{i}\sqrt{2K_{AA}}W(s)}\mathrm{d}s\right|. \tag{D.8}$$

The late-time behaviour of the modulus can be obtained by means of the rule of L'Hôspital and is given by

$$\lim_{t\to\infty} \mid \Phi_A(t) \mid \geq 1 - \frac{L_A}{K_{AA}}. \tag{D.9}$$

From the numerical calculations it can be seen that the bound $1 - \frac{L_A}{K_{AA}}$ corresponds to the late-time value $\langle\Phi_A(t_\infty)\rangle$ for an appropriate choice of L_A and K_{AA}, for example, values that comply with the M1 data. Indeed, one can observe from the numerical implementation that the late-time behaviour of the solution $\langle\Phi_A(t)\rangle$ is independent of the initial condition $\Phi_A(0)$ which can also be seen from the exact solution (D.6).

Appendix E

Heterogenous Nucleation: Tables

In this part of the appendix, we list the mean late-time i-mer populations derived from the traditional Becker-Döring rate equations where the rate coefficients were taken according to the power law model.

	$c = 2$, $\mathtt{i}^* = 2$	$c = 5$, $\mathtt{i}^* = 2$
$\langle M_1(t_\infty)\rangle$	9.78132	9.73785
$\langle M_2(t_\infty)\rangle$	5.92276	5.11332
$\langle M_3(t_\infty)\rangle$	4.8343	4.63237
$\langle M_4(t_\infty)\rangle$	4.33566	4.53405
$\langle M_5(t_\infty)\rangle$	3.72615	4.48687

Table E.1: Mean-field late-time i-mer populations for $\mathrm{G}' = 0.1\mathrm{s}^{-1}$, $\mathrm{D}_i = \left(\frac{\mathtt{i}^*}{i}\right)^c \mathrm{s}^{-1}$, $\mathrm{J} = 1000\mathrm{s}^{-1}$ and $\mathrm{L} = 100\mathrm{s}^{-1}$ and with $\mathtt{i}_{max} = 5$.

	$c = 2$, $\mathtt{i}^* = 2$	$c = 10$, $\mathtt{i}^* = 2$
$\langle M_1(t_\infty)\rangle$	5.79144	5.22315
$\langle M_2(t_\infty)\rangle$	2.65265	1.93199
$\langle M_3(t_\infty)\rangle$	1.8784	1.61724
$\langle M_4(t_\infty)\rangle$	1.54574	1.55414
$\langle M_5(t_\infty)\rangle$	1.21114	1.52425

Table E.2: Mean-field late-time $\mathtt{i}$-mer populations for $\mathrm{G}' = 0.1\mathrm{s}^{-1}$, $\mathrm{D}_i = \left(\frac{\mathtt{i}^*}{i}\right)^c \mathrm{s}^{-1}$, $\mathrm{J} = 10\mathrm{s}^{-1}$ and $\mathrm{L} = 1\mathrm{s}^{-1}$ and with $\mathtt{i}_{max} = 5$.

	$c = 2$, $\mathtt{i}^* = 2$	$c = 5$, $\mathtt{i}^* = 2$
$\langle M_1(t_\infty)\rangle$	9.6186	9.54397
$\langle M_2(t_\infty)\rangle$	5.78445	4.96301
$\langle M_3(t_\infty)\rangle$	4.7172	4.48758
$\langle M_4(t_\infty)\rangle$	4.27997	4.39062
$\langle M_5(t_\infty)\rangle$	4.05895	4.36258
$\langle M_6(t_\infty)\rangle$	3.93166	4.35249
$\langle M_7(t_\infty)\rangle$	3.85154	4.34826
$\langle M_8(t_\infty)\rangle$	3.79755	4.34628
$\langle M_9(t_\infty)\rangle$	3.75469	4.34527
$\langle M_{10}(t_\infty)\rangle$	3.60478	4.34382

Table E.3: Mean-field late-time $\mathtt{i}$-mer populations for $\mathrm{G}' = 0.1\mathrm{s}^{-1}$, $\mathrm{D}_i = \left(\frac{\mathtt{i}^*}{i}\right)^c \mathrm{s}^{-1}$, $\mathrm{J} = 1000\mathrm{s}^{-1}$ and $\mathrm{L} = 100\mathrm{s}^{-1}$ and with $\mathtt{i}_{max} = 2$.

	$c = 2$, $\mathtt{i}^* = 2$	$c = 5$, $\mathtt{i}^* = 2$
$\langle M_1(t_\infty)\rangle$	5.09974	4.46062
$\langle M_2(t_\infty)\rangle$	2.15525	1.48613
$\langle M_3(t_\infty)\rangle$	1.4707	1.20987
$\langle M_4(t_\infty)\rangle$	1.21816	1.1551
$\langle M_5(t_\infty)\rangle$	1.09844	1.13941
$\langle M_6(t_\infty)\rangle$	1.03229	1.13378
$\langle M_7(t_\infty)\rangle$	9.91768×10^{-1}	1.13142
$\langle M_8(t_\infty)\rangle$	9.64754×10^{-1}	1.13032
$\langle M_9(t_\infty)\rangle$	9.42048×10^{-1}	1.12976
$\langle M_{10}(t_\infty)\rangle$	8.73532×10^{-1}	1.12895

Table E.4: Mean-field late-time $\mathtt{i}$-mer populations for $\mathrm{G}' = 0.1\mathrm{s}^{-1}$, $\mathrm{D}_i = \left(\frac{\mathtt{i}^*}{i}\right)^c \mathrm{s}^{-1}$, $\mathrm{J} = 10\mathrm{s}^{-1}$ and $\mathrm{L} = 1\mathrm{s}^{-1}$ and with $\mathtt{i}_{max} = 2$.

	$c = 2$,$\mathtt{i}^* = 2$	$c = 5$, $\mathtt{i}^* = 2$	$c = 2$, $\mathtt{i}^* = 10$
$\langle M_1(t_\infty)\rangle$	9.46999	9.3682	10^1
$\langle M_2(t_\infty)\rangle$	5.65555	4.82755	3.99999×10^{-1}
$\langle M_3(t_\infty)\rangle$	4.59736	4.35722	3.59978×10^{-2}
$\langle M_4(t_\infty)\rangle$	4.16465	4.26134	5.75594×10^{-3}
$\langle M_5(t_\infty)\rangle$	3.94617	4.23362	1.4332×10^{-3}
$\langle M_6(t_\infty)\rangle$	3.82043	4.22364	5.07622×10^{-4}
$\langle M_7(t_\infty)\rangle$	3.74134	4.21946	2.37397×10^{-4}
$\langle M_8(t_\infty)\rangle$	3.68831	4.21751	1.37125×10^{-4}
$\langle M_9(t_\infty)\rangle$	3.65098	4.21651	$9.2329\mathrm{e}\times10^{-5}$
$\langle M_{10}(t_\infty)\rangle$	3.6237	4.21596	6.91902×10^{-5}
$\langle M_{11}(t_\infty)\rangle$	3.60315	4.21565	5.57223×10^{-5}
$\langle M_{12}(t_\infty)\rangle$	3.58727	4.21546	4.69204×10^{-5}
$\langle M_{13}(t_\infty)\rangle$	3.57472	4.21534	4.0191×10^{-5}
$\langle M_{14}(t_\infty)\rangle$	3.56359	4.21526	3.34226×10^{-5}
$\langle M_{15}(t_\infty)\rangle$	3.49792	4.21507	2.31387×10^{-5}

Table E.5: Mean-field late-time i-mer populations for $\mathrm{G}' = 0.1\mathrm{s}^{-1}$, $\mathrm{D}_i = \left(\frac{\mathtt{i}^*}{i}\right)^c \mathrm{s}^{-1}$, $\mathrm{J} = 1000\mathrm{s}^{-1}$ and $\mathrm{L} = 100\mathrm{s}^{-1}$ and with $\mathtt{i}_{max} = 15$.

	$c = 2$, $\mathtt{i}^* = 2$	$c = 10$, $\mathtt{i}^* = 2$	$c = 2$, $\mathtt{i}^* = 10$
$\langle M_1(t_\infty)\rangle$	4.70135	4.03102	9.99963
$\langle M_2(t_\infty)\rangle$	1.8791	1.25185	3.99969×10^{-1}
$\langle M_3(t_\infty)\rangle$	1.2426	9.99063×10^{-1}	3.59938×10^{-2}
$\langle M_4(t_\infty)\rangle$	1.01209	9.49226×10^{-1}	5.7551×10^{-3}
$\langle M_5(t_\infty)\rangle$	9.04075×10^{-1}	9.34968×10^{-1}	1.43294×10^{-3}
$\langle M_6(t_\infty)\rangle$	8.44841×10^{-1}	9.29857×10^{-1}	5.07512×10^{-4}
$\langle M_7(t_\infty)\rangle$	8.08786×10^{-1}	9.2772×10^{-1}	2.37338×10^{-4}
$\langle M_8(t_\infty)\rangle$	7.85162×10^{-1}	9.2672×10^{-1}	1.37088×10^{-4}
$\langle M_9(t_\infty)\rangle$	7.68815×10^{-1}	9.2621×10^{-1}	9.23021×10^{-5}
$\langle M_{10}(t_\infty)\rangle$	7.57017×10^{-1}	9.25931×10^{-1}	6.91691×10^{-5}
$\langle M_{11}(t_\infty)\rangle$	7.48215×10^{-1}	9.2577×10^{-1}	5.57047×10^{-5}
$\langle M_{12}(t_\infty)\rangle$	7.41467×10^{-1}	9.25673×10^{-1}	4.69051×10^{-5}
$\langle M_{13}(t_\infty)\rangle$	7.3614×10^{-1}	9.25612×10^{-1}	4.01776×10^{-5}
$\langle M_{14}(t_\infty)\rangle$	7.31043×10^{-1}	9.25572×10^{-1}	3.34111×10^{-5}
$\langle M_{15}(t_\infty)\rangle$	7.04406×10^{-1}	9.25475×10^{-1}	2.31305×10^{-5}

Table E.6: Mean-field late-time i-mer populations for $\mathrm{G}' = 0.1\mathrm{s}^{-1}$, $\mathrm{D}_i = \left(\frac{\mathtt{i}^*}{i}\right)^c \mathrm{s}^{-1}$, $\mathrm{J} = 10\mathrm{s}^{-1}$ and $\mathrm{L} = 1\mathrm{s}^{-1}$ and with $\mathtt{i}_{max} = 15$.

	$c=2$, $\mathtt{i}^*=2$	$c=5$, $\mathtt{i}^*=2$	$c=2$, $\mathtt{i}^*=10$
$\langle M_1(t_\infty)\rangle$	9.33349	9.20757	10^1
$\langle M_2(t_\infty)\rangle$	5.53754	4.70447	3.99999×10^{-1}
$\langle M_3(t_\infty)\rangle$	4.48782	4.23887	3.59978×10^{-2}
$\langle M_4(t_\infty)\rangle$	4.05934	4.14401	5.75597×10^{-3}
$\langle M_5(t_\infty)\rangle$	3.84324	4.11658	1.43325×10^{-3}
$\langle M_6(t_\infty)\rangle$	3.71895	4.10671	5.07706×10^{-4}
$\langle M_7(t_\infty)\rangle$	3.64081	4.10257	2.37526×10^{-4}
$\langle M_8(t_\infty)\rangle$	3.58842	4.10064	1.37324×10^{-4}
$\langle M_9(t_\infty)\rangle$	3.55157	4.09965	9.26363×10^{-5}
$\langle M_{10}(t_\infty)\rangle$	3.52463	4.09911	6.96784×10^{-5}
$\langle M_{11}(t_\infty)\rangle$	3.50434	4.0988	5.65318×10^{-5}
$\langle M_{12}(t_\infty)\rangle$	3.48867	4.09861	4.83464×10^{-5}
$\langle M_{13}(t_\infty)\rangle$	3.47631	4.09849	4.29066×10^{-5}
$\langle M_{14}(t_\infty)\rangle$	3.46638	4.09841	3.90994×10^{-5}
$\langle M_{15}(t_\infty)\rangle$	3.4583	4.09836	3.63183×10^{-5}
$\langle M_{16}(t_\infty)\rangle$	3.45162	4.09832	3.42026×10^{-5}
$\langle M_{17}(t_\infty)\rangle$	3.44603	4.0983	3.24972×10^{-5}
$\langle M_{18}(t_\infty)\rangle$	3.44132	4.09828	3.09073×10^{-5}
$\langle M_{19}(t_\infty)\rangle$	3.43695	4.09827	2.86974×10^{-5}
$\langle M_{20}(t_\infty)\rangle$	3.40051	4.09822	2.29579×10^{-5}

Table E.7: Mean-field late-time i-mer populations for $\mathrm{G}' = 0.1\mathrm{s}^{-1}$, $\mathrm{D}_i = \left(\frac{\mathtt{i}^*}{i}\right)^c \mathrm{s}^{-1}$, $\mathrm{J} = 1000\mathrm{s}^{-1}$ and $\mathrm{L} = 100\mathrm{s}^{-1}$ and with $\mathtt{i}_{max} = 20$.

	$c=2$, $\mathtt{i}^*=2$	$c=10$, $\mathtt{i}^*=2$	$c=2$, $\mathtt{i}^*=10$
$\langle M_1(t_\infty)\rangle$	4.43042	3.74083	9.99952
$\langle M_2(t_\infty)\rangle$	1.69764	1.10133	3.99961×10^{-1}
$\langle M_3(t_\infty)\rangle$	1.09554	8.65165×10^{-1}	3.59926×10^{-2}
$\langle M_4(t_\infty)\rangle$	8.8061×10^{-1}	8.18815×10^{-1}	5.75487×10^{-3}
$\langle M_5(t_\infty)\rangle$	7.80804×10^{-1}	8.05573×10^{-1}	1.43291×10^{-3}
$\langle M_6(t_\infty)\rangle$	7.26395×10^{-1}	8.0083×10^{-1}	5.07563×10^{-4}
$\langle M_7(t_\infty)\rangle$	6.9341×10^{-1}	7.98847×10^{-1}	2.3745×10^{-4}
$\langle M_8(t_\infty)\rangle$	6.71859×10^{-1}	7.97919×10^{-1}	1.37275×10^{-4}
$\langle M_9(t_\infty)\rangle$	6.56978×10^{-1}	7.97446×10^{-1}	9.26014×10^{-5}
$\langle M_{10}(t_\infty)\rangle$	6.46255×10^{-1}	7.97187×10^{-1}	6.96508×10^{-5}
$\langle M_{11}(t_\infty)\rangle$	6.38265×10^{-1}	7.97038×10^{-1}	5.65086×10^{-5}
$\langle M_{12}(t_\infty)\rangle$	6.32146×10^{-1}	7.96947×10^{-1}	4.83261×10^{-5}
$\langle M_{13}(t_\infty)\rangle$	6.27352×10^{-1}	7.9689×10^{-1}	4.28882×10^{-5}
$\langle M_{14}(t_\infty)\rangle$	6.23526×10^{-1}	7.96853×10^{-1}	3.90824×10^{-5}
$\langle M_{15}(t_\infty)\rangle$	6.20421×10^{-1}	7.96829×10^{-1}	3.63023×10^{-5}
$\langle M_{16}(t_\infty)\rangle$	6.17866×10^{-1}	7.96812×10^{-1}	3.41874×10^{-5}
$\langle M_{17}(t_\infty)\rangle$	6.15738×10^{-1}	7.968×10^{-1}	3.24827×10^{-5}
$\langle M_{18}(t_\infty)\rangle$	6.1394×10^{-1}	7.96791×10^{-1}	3.08934×10^{-5}
$\langle M_{19}(t_\infty)\rangle$	6.12142×10^{-1}	7.96785×10^{-1}	2.86843×10^{-5}
$\langle M_{20}(t_\infty)\rangle$	5.9863×10^{-1}	7.96764×10^{-1}	2.29472×10^{-5}

Table E.8: Mean-field late-time $\mathtt{i}$-mer populations for $\mathrm{G}' = 0.1\mathrm{s}^{-1}$, $\mathrm{D}_i = \left(\frac{\mathtt{i}^*}{i}\right)^c \mathrm{s}^{-1}$, $\mathrm{J} = 10\mathrm{s}^{-1}$ and $\mathrm{L} = 1\mathrm{s}^{-1}$ and with $\mathtt{i}_{max} = 20$.

	$c=2$, $\mathtt{i}^*=2$	$c=5$, $\mathtt{i}^*=2$	$c=2$, $\mathtt{i}^*=10$
$\langle M_1(t_\infty)\rangle$	9.20734	9.0598	9.99999
$\langle M_2(t_\infty)\rangle$	5.42882	4.59184	3.99999×10^{-1}
$\langle M_3(t_\infty)\rangle$	4.38708	4.13067	3.59978×10^{-2}
$\langle M_4(t_\infty)\rangle$	3.96258	4.03675	5.75597×10^{-3}
$\langle M_5(t_\infty)\rangle$	3.7487	4.0096	1.43325×10^{-3}
$\langle M_6(t_\infty)\rangle$	3.62576	3.99983	5.07706×10^{-4}
$\langle M_7(t_\infty)\rangle$	3.54851	3.99574	2.37526×10^{-4}
$\langle M_8(t_\infty)\rangle$	3.49674	3.99382	1.37324×10^{-4}
$\langle M_9(t_\infty)\rangle$	3.46032	3.99284	9.26367×10^{-5}
$\langle M_{10}(t_\infty)\rangle$	3.43371	3.99231	6.9679×10^{-5}
$\langle M_{11}(t_\infty)\rangle$	3.41367	3.992	5.65329×10^{-5}
$\langle M_{12}(t_\infty)\rangle$	3.39819	3.99181	4.83483×10^{-5}
$\langle M_{13}(t_\infty)\rangle$	3.38598	3.99169	4.29103×10^{-5}
$\langle M_{14}(t_\infty)\rangle$	3.37618	3.99162	3.91073×10^{-5}
$\langle M_{15}(t_\infty)\rangle$	3.3682	3.99157	3.63367×10^{-5}
$\langle M_{16}(t_\infty)\rangle$	3.3616	3.99153	3.42504×10^{-5}
$\langle M_{17}(t_\infty)\rangle$	3.35609	3.99151	3.26363×10^{-5}
$\langle M_{18}(t_\infty)\rangle$	3.35143	3.99149	3.13588×10^{-5}
$\langle M_{19}(t_\infty)\rangle$	3.34747	3.99148	3.03284×10^{-5}
$\langle M_{20}(t_\infty)\rangle$	3.34406	3.99147	2.94833×10^{-5}
$\langle M_{21}(t_\infty)\rangle$	3.34112	3.99146	2.87782×10^{-5}
$\langle M_{22}(t_\infty)\rangle$	3.33855	3.99145	2.81714×10^{-5}
$\langle M_{23}(t_\infty)\rangle$	3.3363	3.99145	2.7581×10^{-5}
$\langle M_{24}(t_\infty)\rangle$	3.33417	3.99145	2.66308×10^{-5}
$\langle M_{25}(t_\infty)\rangle$	3.31115	3.99143	2.29576×10^{-5}

Table E.9: Mean-field late-time i-mer populations for $\mathrm{G}' = 0.1\mathrm{s}^{-1}$, $\mathrm{D}_i = \left(\frac{\mathtt{i}^*}{i}\right)^c \mathrm{s}^{-1}$, $\mathrm{J} = 1000\mathrm{s}^{-1}$ and $\mathrm{L} = 100\mathrm{s}^{-1}$ and with $\mathtt{i}_{max} = 25$.

	$c=2$, $\mathtt{i}^*=2$	$c=10$, $\mathtt{i}^*=2$	$c=2$, $\mathtt{i}^*=10$
$\langle M_1(t_\infty)\rangle$	4.22855	3.52578	9.9994
$\langle M_2(t_\infty)\rangle$	1.56609	9.94102×10^{-1}	3.99951×10^{-1}
$\langle M_3(t_\infty)\rangle$	9.90559×10^{-1}	7.70688×10^{-1}	3.59914×10^{-2}
$\langle M_4(t_\infty)\rangle$	7.87536×10^{-1}	7.27004×10^{-1}	5.75461×10^{-3}
$\langle M_5(t_\infty)\rangle$	6.93964×10^{-1}	7.14539×10^{-1}	1.43283×10^{-3}
$\langle M_6(t_\infty)\rangle$	6.43204×10^{-1}	7.10076×10^{-1}	5.07529×10^{-4}
$\langle M_7(t_\infty)\rangle$	6.12534×10^{-1}	7.08211×10^{-1}	2.37432×10^{-4}
$\langle M_8(t_\infty)\rangle$	5.92543×10^{-1}	7.07338×10^{-1}	1.37264×10^{-4}
$\langle M_9(t_\infty)\rangle$	5.78763×10^{-1}	7.06893×10^{-1}	9.25934×10^{-5}
$\langle M_{10}(t_\infty)\rangle$	5.68847×10^{-1}	7.0665×10^{-1}	6.96448×10^{-5}
$\langle M_{11}(t_\infty)\rangle$	5.61465×10^{-1}	7.06509×10^{-1}	5.65042×10^{-5}
$\langle M_{12}(t_\infty)\rangle$	5.55816×10^{-1}	7.06424×10^{-1}	4.83232×10^{-5}
$\langle M_{13}(t_\infty)\rangle$	5.51394×10^{-1}	7.06371×10^{-1}	4.28875×10^{-5}
$\langle M_{14}(t_\infty)\rangle$	5.47865×10^{-1}	7.06336×10^{-1}	3.90862×10^{-5}
$\langle M_{15}(t_\infty)\rangle$	5.45003×10^{-1}	7.06313×10^{-1}	3.63169×10^{-5}
$\langle M_{16}(t_\infty)\rangle$	5.42649×10^{-1}	7.06297×10^{-1}	3.42317×10^{-5}
$\langle M_{17}(t_\infty)\rangle$	5.40689×10^{-1}	7.06285×10^{-1}	3.26183×10^{-5}
$\langle M_{18}(t_\infty)\rangle$	5.39039×10^{-1}	7.06277×10^{-1}	3.13415×10^{-5}
$\langle M_{19}(t_\infty)\rangle$	5.37637×10^{-1}	7.06271×10^{-1}	3.03115×10^{-5}
$\langle M_{20}(t_\infty)\rangle$	5.36435×10^{-1}	7.06267×10^{-1}	2.94668×10^{-5}
$\langle M_{21}(t_\infty)\rangle$	5.35397×10^{-1}	7.06264×10^{-1}	2.8762×10^{-5}
$\langle M_{22}(t_\infty)\rangle$	5.34494×10^{-1}	7.06261×10^{-1}	2.81556×10^{-5}
$\langle M_{23}(t_\infty)\rangle$	5.33703×10^{-1}	7.0626×10^{-1}	2.75655×10^{-5}
$\langle M_{24}(t_\infty)\rangle$	5.32896×10^{-1}	7.06258×10^{-1}	2.66157×10^{-5}
$\langle M_{25}(t_\infty)\rangle$	5.24951×10^{-1}	7.06251×10^{-1}	2.29444×10^{-5}

Table E.10: Mean-field late-time $\mathtt{i}$-mer populations for $\mathrm{G}' = 0.1\mathrm{s}^{-1}$, $\mathrm{D}_i = \left(\frac{\mathtt{i}^*}{i}\right)^c \mathrm{s}^{-1}$, $\mathrm{J} = 10\mathrm{s}^{-1}$ and $\mathrm{L} = 1\mathrm{s}^{-1}$ and with $\mathtt{i}_{max} = 25$.

	$c = 2$, $\mathtt{i}^* = 2$	$c = 5$, $\mathtt{i}^* = 2$	$c = 2$, $\mathtt{i}^* = 10$
$\langle M_1(t_\infty)\rangle$	9.09016	8.92307	9.99999
$\langle M_2(t_\infty)\rangle$	5.32815	4.48816	3.99999×10^{-1}
$\langle M_3(t_\infty)\rangle$	4.29393	4.03116	3.59978×10^{-2}
$\langle M_4(t_\infty)\rangle$	3.87318	3.93812	5.75597×10^{-3}
$\langle M_5(t_\infty)\rangle$	3.66139	3.91123	1.43325×10^{-3}
$\langle M_6(t_\infty)\rangle$	3.53974	3.90155	5.07705×10^{-4}
$\langle M_7(t_\infty)\rangle$	3.46332	3.8975	2.37526×10^{-4}
$\langle M_8(t_\infty)\rangle$	3.41213	3.8956	1.37324×10^{-4}
$\langle M_9(t_\infty)\rangle$	3.37612	3.89463	9.26366×10^{-5}
$\langle M_{10}(t_\infty)\rangle$	3.34982	3.8941	6.9679×10^{-5}
$\langle M_{11}(t_\infty)\rangle$	3.33001	3.8938	5.65328×10^{-5}
$\langle M_{12}(t_\infty)\rangle$	3.31471	3.89361	4.83483×10^{-5}
$\langle M_{13}(t_\infty)\rangle$	3.30265	3.8935	4.29103×10^{-5}
$\langle M_{14}(t_\infty)\rangle$	3.29297	3.89342	3.91072×10^{-5}
$\langle M_{15}(t_\infty)\rangle$	3.28508	3.89337	3.63367×10^{-5}
$\langle M_{16}(t_\infty)\rangle$	3.27856	3.89334	3.42504×10^{-5}
$\langle M_{17}(t_\infty)\rangle$	3.27311	3.89331	3.26363×10^{-5}
$\langle M_{18}(t_\infty)\rangle$	3.26851	3.89329	3.13589×10^{-5}
$\langle M_{19}(t_\infty)\rangle$	3.2646	3.89328	3.03286×10^{-5}
$\langle M_{20}(t_\infty)\rangle$	3.26123	3.89327	2.94842×10^{-5}
$\langle M_{21}(t_\infty)\rangle$	3.25832	3.89327	2.87824×10^{-5}
$\langle M_{22}(t_\infty)\rangle$	3.25578	3.89326	2.8192×10^{-5}
$\langle M_{23}(t_\infty)\rangle$	3.25356	3.89326	2.76901×10^{-5}
$\langle M_{24}(t_\infty)\rangle$	3.2516	3.89325	2.72595×10^{-5}
$\langle M_{25}(t_\infty)\rangle$	3.24986	3.89325	2.68868×10^{-5}
$\langle M_{26}(t_\infty)\rangle$	3.24832	3.89325	2.65615×10^{-5}
$\langle M_{27}(t_\infty)\rangle$	3.24694	3.89325	2.62727×10^{-5}
$\langle M_{28}(t_\infty)\rangle$	3.24569	3.89324	2.59907×10^{-5}
$\langle M_{29}(t_\infty)\rangle$	3.2445	3.89324	2.55084×10^{-5}
$\langle M_{30}(t_\infty)\rangle$	3.22872	3.89324	2.29576×10^{-5}

Table E.11: Mean-field late-time $\mathtt{i}$-mer populations for $\mathrm{G}' = 0.1\mathrm{s}^{-1}$, $\mathrm{D}_i = \left(\frac{\mathtt{i}^*}{i}\right)^c \mathrm{s}^{-1}$, $\mathrm{J} = 1000\mathrm{s}^{-1}$ and $\mathrm{L} = 100\mathrm{s}^{-1}$ and with $\mathtt{i}_{max} = 30$.

	$c = 2$, $\mathtt{i}^* = 2$	$c = 10$, $\mathtt{i}^* = 2$	$c = 2$, $\mathtt{i}^* = 10$
$\langle M_1(t_\infty)\rangle$	4.06949	3.3571	9.99929
$\langle M_2(t_\infty)\rangle$	1.46476	9.12725×10^{-1}	3.99942×10^{-1}
$\langle M_3(t_\infty)\rangle$	9.10748×10^{-1}	6.99563×10^{-1}	3.59902×10^{-2}
$\langle M_4(t_\infty)\rangle$	7.17282×10^{-1}	6.58021×10^{-1}	5.75435×10^{-3}
$\langle M_5(t_\infty)\rangle$	6.28688×10^{-1}	6.4618×10^{-1}	1.43275×10^{-3}
$\langle M_6(t_\infty)\rangle$	5.8083×10^{-1}	6.41941×10^{-1}	5.07495×10^{-4}
$\langle M_7(t_\infty)\rangle$	5.51998×10^{-1}	6.4017×10^{-1}	2.37414×10^{-4}
$\langle M_8(t_\infty)\rangle$	5.33243×10^{-1}	6.39342×10^{-1}	1.37252×10^{-4}
$\langle M_9(t_\infty)\rangle$	5.20334×10^{-1}	6.38919×10^{-1}	9.2585×10^{-5}
$\langle M_{10}(t_\infty)\rangle$	5.11055×10^{-1}	6.38688×10^{-1}	6.96382×10^{-5}
$\langle M_{11}(t_\infty)\rangle$	5.04154×10^{-1}	6.38555×10^{-1}	5.64986×10^{-5}
$\langle M_{12}(t_\infty)\rangle$	4.98876×10^{-1}	6.38474×10^{-1}	4.83183×10^{-5}
$\langle M_{13}(t_\infty)\rangle$	4.94747×10^{-1}	6.38424×10^{-1}	4.28831×10^{-5}
$\langle M_{14}(t_\infty)\rangle$	4.91454×10^{-1}	6.3839×10^{-1}	3.90821×10^{-5}
$\langle M_{15}(t_\infty)\rangle$	4.88784×10^{-1}	6.38368×10^{-1}	3.63131×10^{-5}
$\langle M_{16}(t_\infty)\rangle$	4.86588×10^{-1}	6.38353×10^{-1}	3.4228×10^{-5}
$\langle M_{17}(t_\infty)\rangle$	4.84761×10^{-1}	6.38342×10^{-1}	3.26148×10^{-5}
$\langle M_{18}(t_\infty)\rangle$	4.83222×10^{-1}	6.38335×10^{-1}	3.13381×10^{-5}
$\langle M_{19}(t_\infty)\rangle$	4.81916×10^{-1}	6.38329×10^{-1}	3.03085×10^{-5}
$\langle M_{20}(t_\infty)\rangle$	4.80796×10^{-1}	6.38325×10^{-1}	2.94646×10^{-5}
$\langle M_{21}(t_\infty)\rangle$	4.79828×10^{-1}	6.38322×10^{-1}	2.87631×10^{-5}
$\langle M_{22}(t_\infty)\rangle$	4.78987×10^{-1}	6.38319×10^{-1}	2.81731×10^{-5}
$\langle M_{23}(t_\infty)\rangle$	4.78251×10^{-1}	6.38318×10^{-1}	2.76715×10^{-5}
$\langle M_{24}(t_\infty)\rangle$	4.77603×10^{-1}	6.38316×10^{-1}	2.72411×10^{-5}
$\langle M_{25}(t_\infty)\rangle$	4.7703×10^{-1}	6.38315×10^{-1}	2.68687×10^{-5}
$\langle M_{26}(t_\infty)\rangle$	4.7652×10^{-1}	6.38314×10^{-1}	2.65436×10^{-5}
$\langle M_{27}(t_\infty)\rangle$	4.76064×10^{-1}	6.38313×10^{-1}	2.6255×10^{-5}
$\langle M_{28}(t_\infty)\rangle$	4.75655×10^{-1}	6.38313×10^{-1}	2.59731×10^{-5}
$\langle M_{29}(t_\infty)\rangle$	4.75235×10^{-1}	6.38312×10^{-1}	2.54911×10^{-5}
$\langle M_{30}(t_\infty)\rangle$	4.70101×10^{-1}	6.3831×10^{-1}	2.29418×10^{-5}

Table E.12: Mean-field late-time $\mathtt{i}$-mer populations for $\mathrm{G}' = 0.1\mathrm{s}^{-1}$, $\mathrm{D}_i = \left(\frac{\mathtt{i}^*}{i}\right)^c \mathrm{s}^{-1}$, $\mathrm{J} = 10\mathrm{s}^{-1}$ and $\mathrm{L} = 1\mathrm{s}^{-1}$ and with $\mathtt{i}_{max} = 30$.

Appendix F

List of Symbols

Vectors are given by small letters in bold font, as in $\mathbf{e}$, matrices by capital letters in bold font, as in $\mathbf{E}$, and operators in the following font, as in $\mathtt{E}$. The symbol * denotes both, the complex conjugate of a function, and the value of a function at the critical cluster size in nucleation theory. The particular meaning will be clear from the context.

$|\{0\}\rangle$: vacuum state

$\langle . \rangle$: expectation value

$\langle . \rangle_{SG}$: average in the Stochastic Gauge Theory

Δ: Laplace operator

$\frac{\delta}{\delta[.]}$: functional derivative

$\triangle_n$: time increments in the numerical evaluation

$\mathbf{A}$: symmetric matrix in the Gaussian integral transformation

$A_{v,l}$ [m^2]: area at the vapour-liquid interface in heterogeneous nucleation theory

$A_{l,s}$ [m^2]: area at the gas-phase and cluster interface in heterogeneous nucleation theory

$a[.]$: drift coefficient in a stochastic differential equation

$\overset{+}{\mathtt{a}}_i$: creation operator at lattice site i

$\overset{-}{\mathtt{a}}_i$: annihilation operator at lattice site i

$b[.]$: diffusion coefficient in a stochastic differential equation

$\mathbf{b}$: vector containing the entangled functions in the Gaussian integral transformation

$\mathcal{C}$ [m]: circumference of ring

$|\mathtt{C}_i\rangle$: coherent state vector at lattice site i

$\langle\mathtt{C}_i|$: dual of the coherent state vector at lattice site i

$|\{\mathtt{C}\}\rangle$: the direct product of all coherent state vectors

$\langle C_{\mathtt{x}}\rangle^{ss}$ [m^{-2}]: average concentration of $\mathtt{x}$-mers on the surface of a grain particle according to the stationary mean-field model

$\langle C_{\mathtt{x}}(t)\rangle$ [1]: average concentration of $\mathtt{x}$-mers on the surface of a grain particle according to the dynamical mean-field model

$\langle C_{mon,ads}\rangle$ [m^{-2}]: mean concentration of the surface-adsorbed monomers

$\langle C_1\rangle^{kin}$ [m^{-2}]: constant boundary condition for the solution of the stationary Becker-Döring rate equations estimating the mean concentration of the surface-adsorbed monomers

$\mathbb{C}$: set of complex numbers

c: constant exponent for the decay rate coefficient in the power law model

D: number of dimensions

$\mathrm{D}f$: measure in the space of paths

D^{dv} [s^{-1}]: decay rate coefficient in the direct vapour deposition mechanism employed in the determination of the mean cluster populations

D^{sd} [s^{-1}]: decay rate coefficient in the surface diffusion mechanism employed in the determination of the mean cluster populations

d_X [$\mathrm{m}^2\mathrm{s}^{-1}$]: diffusion rate coefficient for molecules of type X in the continuum limit in $D = 1$ space dimensions

d_1, d_2 [m]: grain diameter

$\mathrm{d}f$: measure on the real numbers

d^{dv} [s^{-1}]: decay rate coefficient in the direct vapour deposition mechanism employed in the determination of the mean cluster concentrations

d^{sd} [s^{-1}]: decay rate coefficient in the surface diffusion mechanism employed in the determination of the mean cluster concentrations

E [J]: energy barrier against the surface diffusion of monomers

E_d [J]: energy barrier against diffusion from one lattice site to another

E_e [J]: energy barrier against evaporation

$\mathbf{e}_i$: eigenvectors in the stability analysis of binary heterogeneous chemical processes according to the mean-field theory

$\mathbf{e}$: vector containing the auxiliary functions in the Gaussian integral transformation

$\mathcal{F}_\nu$: Fock space

$F(z)$: generating function in the stationary master equation approach

G_1, G_2: independent standard Gaussian random variables

$G(z)$: generating function candidate in the stationary master equation approach

G^{dv} [s^{-1}]: growth rate coefficient in the direct vapour deposition mechanism employed in the determination of the mean cluster populations

$\mathrm{G}^{sd}(t)$ [s^{-1}]: monomer-dependent growth rate coefficient in the surface diffusion mechanism employed in the determination of the mean cluster populations

G'^{sd} [s^{-1}]: constant growth rate coefficient in the surface diffusion mechanism employed in the determination of the mean cluster populations

$\triangle G_{hom}$ [J]: formation free energy of a cluster for homogeneous nucleation processes

$\triangle G$ [J]: formation free energy of a cluster for heterogeneous nucleation processes

g: stochastic variable with Gaussian distribution

g_A: amplitude gauge

g_P: phase gauge

g_S: step gauge

g^{dv} [s^{-1}]: growth rate coefficient in the direct vapour deposition mechanism employed in the determination of the mean cluster concentrations

$\mathrm{g}^{sd}(t)$ [s^{-1}]: monomer-dependent growth rate coefficient in the surface diffusion mechanism employed in the determination of the mean cluster concentrations

g'^{sd} [$\mathrm{m}^2\mathrm{s}^{-1}$]: constant growth rate coefficient in the surface diffusion mechanism employed in the determination of the mean cluster concentrations

$\mathrm{g}^{dv}_{\mathtt{i}^*_{Fletcher}}$ [s^{-1}]: growth rate of the Fletcher critical cluster

$\mathcal{H}$: Hilbert space

$\mathtt{H}$: quasi-Hamiltonian operator

H: quasi-Hamiltionan function

$\tilde{H}$: Doi-shifted quasi-Hamiltonian function

$I_\nu(z)$: modified Bessel function of the first kind

$\Im(f)$: imaginary part of f

i: corresponds to $\sqrt{-1}$

$\mathtt{i}$: number of molecules in a cluster

$\mathtt{i}^*$: number of molecules in a critical cluster for heterogeneous nucleation processes

$\mathtt{i}_{max}$: number of molecules in the largest unstable cluster in heterogeneous nucleation processes

$\mathtt{i}^*_{exp}$: experimentally determined number of molecules in the critical cluster for heterogeneous nucleation processes

$\mathtt{i}^*_{Fletcher}$: number of molecules in a Fletcher critical cluster for heterogeneous nucleation processes

$\mathtt{i}^*_{Fletcher;hom}$: number of molecules in a Fletcher critical cluster for heterogeneous nucleation processes

J_X [s^{-1}]: source rate coefficient for molecules of type X in the continuum limit in $D = 0$ space dimensions

$\mathfrak{J}$ [$\mathrm{s}^{-1}\mathrm{m}^{-3}$]: flux of gas-phase species

J [s^{-1}]: mean source rate coefficient for monomer attachment in heterogeneous nucleation processes employed in the determination of the mean cluster populations

$\mathcal{J}_{Fletcher}$ [$\mathrm{m}^{-2}\mathrm{s}^{-1}$]: nucleation current in the Fletcher model

$\mathcal{J}_{exp}$ [$\mathrm{m}^{-2}\mathrm{s}^{-1}$]: experimental nucleation current

$\mathcal{J}_{BD,kin}$ [$\mathrm{m}^{-2}\mathrm{s}^{-1}$]: kinetic nucleation current in the Becker-Döring model

$\mathcal{J}_{BD,dyn}$ [s^{-1}]: dynamical nucleation current in the Becker-Döring model

$\mathcal{J}_{DP}$ [s^{-1}]: stochastic nucleation current according to the Doi-Peliti formalism

j_X [$\mathrm{m}^{-1}\mathrm{s}^{-1}$]: source rate coefficient for molecules of type X in the continuum limit in $D = 1$ space dimensions

j [$\mathrm{m}^{-2}\mathrm{s}^{-1}$]: mean source rate coefficient for monomer attachment in heterogeneous nucleation processes employed in the determination of the mean cluster concentrations

K_{XY} [s^{-1}]: reaction rate coefficient for the recombination of molecules of type X and Y in the continuum limit in $D = 0$ space dimensions

K^* [$\mathrm{m}^{-2}\mathrm{s}^{-1}$]: kinetic pre-factor

k_{XY} [$\mathrm{m}^{1}\mathrm{s}^{-1}$]: reaction rate coefficient for the recombination of molecules of type X and Y in the continuum limit in $D = 1$ space dimensions

L [Nm]: latent heat per molecule

L_X [s^{-1}]: evaporation rate coefficient for molecules of type X in the continuum limit in $D = 0$ space dimensions

L_X^{thd} [s^{-1}]: thermal desorption rate coefficient for molecules of type X in the continuum limit in $D = 0$ space dimensions

L_X^{crd} [s^{-1}]: cosmic ray desorption rate coefficient for molecules of type X in the continuum limit in $D = 0$ space dimensions

$\mathcal{L}$: lower bound of the late-time value of the modulus of the exact solution to the first stochastic constraint equation in one space dimension for zero source rate in the binary heterogeneous chemical reaction process

$\mathbb{L}$: lattice

L [s^{-1}]: mean evaporation rate coefficient for desorption of monomers in heterogeneous nucleation processes employed in the determination of the mean cluster populations

l: lattice constant in the discrete D-dimensional lattice

l_X [s^{-1}]: evaporation rate coefficient for molecules of type X in the continuum limit in $D = 1$ space dimensions

l_i: eigenvalues in the stability analysis of binary heterogeneous chemical processes according to the mean-field theory

ł [m]: tunnelling length

$\triangle l$ [m]: lattice constant in the discrete $D = 1$-dimensional lattice

l [s^{-1}]: mean evaporation rate coefficient for desorption of monomers in heterogeneous nucleation processes employed in the determination of the mean cluster concentrations

$\langle M_{\mathtt{x}} \rangle^{ss}$ [1]: average population of `x`-mers on the surface of a grain particle according to the stationary mean-field model

$\langle M_{\mathtt{x}}(t) \rangle$ [1]: average population of `x`-mers on the surface of a grain particle according to the dynamical mean-field model

$M_{\mathtt{i}}$: occupation number for clusters of order `i`

$\{M\}$: total number of clusters

$\bar{M}_{\mathtt{i}}(0)$ [1]: initial mean number of clusters of order `i`

$\mathring{M}_{\mathtt{i}}$: steady state solutions for clusters of order $\mathtt{i}$ in the stability analysis of heterogeneous nucleation processes according to the mean-field theory

m [kg]: mass of the gas-phase adsorbate

N: number of numerical grid points

N_i: occupation number with multi-index i denoting the location in the lattice

N_S [per monolayer]: number of lattice sites

$\{N_X\}$: total number of adsorbed molecules of chemical species type X

$\mathring{N}_X$: steady state solutions for chemical species of type X in the stability analysis of binary heterogeneous chemical processes according to the mean-field theory

$|N_i\rangle$: state vector at lattice site i

$\langle N_X(t)\rangle$ [1]: average population of molecules of type X on the surface of a grain particle for $D = 0$ space dimensions according to the dynamical mean-field model

$\langle N_X\rangle^{ss}$ [1]: average population of molecules of type X on the surface of a grain particle for $D = 0$ space dimensions according to the stationary mean-field model

$\langle \mathcal{N}_X\rangle^{ss}$ [1]: average population of molecules of type X on the surface of a grain particle in $D = 0$ space time dimensions according to the stationary master equation

$\langle \mathcal{N}_X\rangle^{ss}_{lit}$ [1]: average population of molecules of type X on the surface of a grain particle in $D = 0$ space time dimensions according to the stationary master equation as presented in the standard literature

$\mathfrak{N}$: set of the molecule numbers of all chemical species involved in a binary reaction network

$\mathbb{N}$: set of natural numbers

$\langle n_X(x,t)\rangle$ [m^{-1}]: average density of molecules of type X on the surface of a grain particle for $D = 1$ space dimensions according to the dynamical mean-field model

$\bar{n}_X(0)$ [1]: mean initial occupation number per lattice site for a chemical species of type X

$n_X(0)$ [m^{-D}]: mean initial density of a chemical species of type X in the continuum limit for D space dimensions

n_X [m^{-3}]: gas phase concentration of the chemical species of type X

$\langle \mathrm{n}_X(\mathbf{x},t)\rangle$ [m^{-D}]: average density of molecules of type X on the surface of a grain particle for D space dimensions according to the dynamical mean-field model

$\mathtt{O}$: general observable operator

O: general observable function

$\mathcal{O}$: symbol for higher orders in a series expansion

P: probability distribution for the total number of adsorbed molecules

P_{even}: probability for an even number of particles

P_{odd}: probability for an odd number of particles

P_{nucl}: nucleation probability

P_X [s^{-1}]: production rate for the average number of molecules of chemical species of type X in the mean-field framework

$\mathcal{P}$: Gaussian probability distribution for the stochastic noises

$\mathcal{P}_X$ [s^{-1}]: production rate for the average number of molecules of chemical species of type X in the stochastic framework

$\langle\{\mathtt{P}\}|$: projection state

p [Nm^{-2}]: saturation vapour pressure

R [m]: radius of a spherically symmetric grain particle in astrochemistry

R_{seed} [m]: radius of a spherically symmetric grain particle in aerosol science

$\mathbb{R}$: set of real numbers

$\Re(f)$: real part of f

$r(\mathtt{i})$ [m]: radius of a cluster

$r^*_{Fletcher}$ [m]: Fletcher critical radius

$S[.]$: action functional

$\tilde{S}[.]$: Doi-shifted action functional

$\tilde{S}_0[.]$: Doi-shifted action functional containing the initial conditions

S_{exp} [1]: experimentally determined onset saturation ratio

$S_{Fletcher}$ [1]: onset saturation ratio obtained from Fletcher theory

S [1]: vapour phase saturation ratio

$\mathcal{S}$ [1]: sticking coefficient

s [m^{-2} monolayer^{-1}]: surface density of lattice sites

T [K]: temperature of the grain surface

T_{gas} [K]: temperature of the gas-phase

τ: time index labelling a time slice

$\triangle t$ [s]: time increment

t_E [s]: evaporation time

t_{exp} [s]: activation time of clusters in heterogeneous nucleation processes as determined in experiments

t_n: discretised time

$t_{transient}$ [s]: approximate time needed to reach equlibrium

t_S [s]: surface diffusion time

t_∞ [s]: time after equilibrium has been reached

U_1, U_2: independent uniformly distributed random variables

V_{cap} [m^3]: volume of the cap-shaped liquid phase in heterogeneous nucleation theory

v_X [ms^{-1}]: speed of the gas-phase species X

v_l [m^3]: volume of a single molecule in the liquid phase

$W(t)$ [$\mathrm{s}^{\frac{1}{2}}$]: Wiener process in $D = 0$ space dimensions

$W(.;t)$: probability distribution for cluster microstates

$\triangle W_n$ [$\mathrm{s}^{\frac{1}{2}}$]: Wiener increments in $D = 0$ space dimensions

$w(x,t)[\mathrm{m}^{\frac{1}{2}}\mathrm{s}^{\frac{1}{2}}]$: Wiener process in $D = 1$ space dimensions

$\triangle w_{t,x}$ [$\mathrm{m}^{\frac{1}{2}}\mathrm{s}^{\frac{1}{2}}$]: Wiener increments in $D = 1$ space dimensions

X: ratio between radius of seed and Fletcher critical radius

$X_{Y,n}$: unknown variables in discretised time for chemical species of type Y

$\triangle x$ [m]: separation between numerical grid points

Z_{hom} [1]: Zeldovich factor for homogeneous nucleation processes

Z [1]: Zeldovich factor for heterogeneous nucleation processes

α: implicitness parameter in numerical schemes

β: implicitness parameter in numerical schemes

γ: Gamma function

δ [m]: average jumping distance of monomers on the surface of the grain

δ_{ij}: Kronecker delta

$\delta(.)$: Dirac Delta distribution

$\delta[.]$: functional Dirac delta distribution

ζ_X [$\mathrm{m}^{2D}\mathrm{s}^{-1}$]: diffusion rate coefficient for molecules of type X in the continuum limit in D space dimensions

$\bar{\zeta}_X$: diffusion rate coefficient for molecules of type X on a discrete lattice

$\eta(t)$ [$\mathrm{s}^{-\frac{1}{2}}$]: stochastic noise in $D = 0$ space dimensions

$\eta(x,t)$ [$\mathrm{m}^{-\frac{1}{2}}\mathrm{s}^{-\frac{1}{2}}$]: stochastic noise in $D = 1$ space dimensions

$\eta(\mathbf{x},t)$ [$\mathrm{m}^{-\frac{D}{2}}\mathrm{s}^{-\frac{1}{2}}$]: stochastic noise in D space dimensions

$\Theta(.)$: Heaviside step function

$\Theta(.,.)$: coefficients in term of first order in the expansion of Bessel functions

for small perturbations of the index

θ: contact angle between the tangent to the surface of the seed and the tangent to the surface of the cluster

ι_X [$\mathrm{m}^{-D}\mathrm{s}^{-1}$]: source rate coefficient for molecules of type X in the continuum limit in D space dimensions

$\bar{\iota}_X$: source rate coefficient for molecules of type X on a discrete lattice

κ_{XY} [$\mathrm{m}^{D}\mathrm{s}^{-1}$]: reaction rate coefficient for the recombination of molecules of type X and Y in the continuum limit in D space dimensions

$\bar{\kappa}_{XY}$: reaction rate coefficient for the recombination of molecules of type X and Y on a discrete lattice

λ_X [s^{-1}]: evaporation rate coefficient for molecules of type X in the continuum limit in D space dimensions

$\bar{\lambda}_X$: evaporation rate coefficient for molecules of type X on a discrete lattice

μ: constant indicating the fraction of chemical species remaining on the pre-existing surface

ν [s^{-1}]: vibration frequency of monomers

ν_v [s^{-1}]: frequency of vibration of the adsorbed chemical species

ρ [kgm^{-3}]: liquid density

σ [m^2]: cross section of the spherically symmetric seed particle

σ_{eff} [Nm^{-1}]: effective surface tension between gas-phase and cluster

σ_{exp} [Nm^{-1}]: experimentally determined surface tension between gas-phase and cluster

$\sigma_{l,s}$ [Nm^{-1}]: surface tension between cluster and seed

$\sigma_{v,l}$ [Nm^{-1}]: surface tension between gas-phase and cluster

$\sigma_{v,s}$ [Nm^{-1}]: surface tension between gas-phase and seed

$\bar{\varsigma}_X$: separation rate coefficient of a chemical species of type X on a discrete lattice

Υ: Gauge variable

$\Phi(t)$ [1]: eigenvalue function of the coherent state vector in the continuum limit in $D = 0$ space dimensions according to the Doi-Peliti formalism

$\bar{\Phi}(t)$ [1]: solution to the stochastic constraint equations in the continuum limit in $D = 0$ space dimensions according to the Doi-Peliti formalism

$\hat{\Phi}(t)$ [1]: solution to the stochastic constraint equations in the continuum limit in $D = 0$ space dimensions according to the Stochastic Gauge Theory

$\langle \Phi(t) \rangle_Y$ [1]: average density of molecules of type X on the surface of a grain particle in the continuum limit in $D = 0$ space dimensions according to the path integral average for Y realisations of the noise in the Doi-Peliti formalism

$\langle \Phi_{\mathtt{x}}(t) \rangle_Y$ [1]: average population of $\mathtt{x}$-mers on the surface of a grain particle according to the path integral average for Y realisations of the noise in the Doi-Peliti formalism

$\phi(x,t)$ [m^{-1}]: eigenvalue function of the coherent state vector in the continuum limit in $D = 1$ space dimensions according to the Doi-Peliti formalism

$\bar{\phi}(x,t)$ [m^{-1}]: solution to the stochastic constraint equations in the continuum limit in $D = 1$ space dimensions according to the Doi-Peliti formalism

$\langle \phi(x,t) \rangle_Y$ [m^{-1}]: average density of molecules of type X on the surface of a grain particle in the continuum limit in $D = 1$ space dimensions according to the path integral average for Y realisations of the noise in the Doi-Peliti formalism

φ_i: eigenvalue function of the coherent state vector on a discrete lattice with lattice sites i according to the Doi-Peliti formalism

φ_i^*: complex conjugate of the eigenvalue function of the coherent state vector on a discrete lattice with lattice sites i according to the Doi-Peliti formalism

$\tilde{\varphi}_i$: Doi-shifted eigenvalue function of the complex conjugate of the coherent state vector on a discrete lattice with lattice sites i according to the Doi-Peliti formalism

$\bar{\varphi}(t)$ [1]: solution to the stochastic constraint equations in the continuum limit according to the Doi-Peliti formalism in $D = 0$ space dimensions according to the Doi-Peliti formalism

$\psi(\mathbf{x}, t)$ [m^{-D}]: eigenvalue function of the coherent state vector in the continuum limit in D space dimensions according to the Doi-Peliti formalism

$\bar{\psi}(\mathbf{x}, t)$ [m^{-D}]: solution to the stochastic constraint equations in the continuum limit in D space dimensions according to the Doi-Peliti formalism

$\tilde{\psi}(\mathbf{x}, t)$ [m^{-D}]: Doi-shifted complex conjugate of the eigenvalue function of the coherent state vector in the continuum limit in D space dimensions according to the Doi-Peliti formalism

$\langle \psi(\mathbf{x}, t) \rangle_Y$ [m^{-D}]: average density of molecules of type X on the surface of a grain particle in the continuum limit in D space dimensions according to the path integral average for Y realisations of the noise in the Doi-Peliti formalism

ξ: size parameter for the grain surface area

Boltzmann constant:
$k := 1.3806504(24) \times 10^{-23}$ JK^{-1}

Planck constant:
$h := 6.62606896(33) \times 10^{-34}$ Js

Bibliography

[1] B. Barzel & O. Biham, *Efficient Simulations of Interstellar Gas-Grain Chemistry Using Moment Equations*, The Astrophysical Journal **658**, L37–L40 (2007).

[2] R. Becker & W. Döring, *Kinetische Behandlung der Keimbildung in übersättigten Dämpfen*, Annalen der Physik (Leipzig) **24**, 719 (1935).

[3] J. S. Bhatt & I. J. Ford, *Kinetics of heterogeneous nucleation for low mean cluster populations*, Journal of Chemical Physics **118**(7), 3166–3176 (2002).

[4] O. Biham et al., *Master equation for hydrogen recombination on grain surfaces*, The Astrophysical Journal **553**, 595–603 (2001).

[5] O. Biham & A. Lipshtat, *Exact results for hydrogen recombination on dust grain surfaces*, Physical Review E **66**, 056103 (2002).

[6] J. P. Blaizot & H. Orland, *Coherent states: Applications in Physics and Mathematical Physics*, page 474, World Scientific, 1985.

[7] P. Caselli, T. I. Hasegawa, & E. Herbst, *A proposed modification of the rate equations for reactions on grain surfaces*, The Astrophysical Journal **495**, 309–316 (1998).

[8] Q. Chang, H. Cuppen, & E. Herbst, *Continuous-time random-walk simulation of H2 formation on interstellar grains*, Astronomy & Astrophysics **434**, 599–611 (2005).

[9] S. Charnley, *Stochastic Astrochemical Kinetics*, Astronomy & Astrophysics **509**, L121–L124 (1998).

[10] S. Charnley, *Stochastic Theory of Molecule Formation on Dust*, Astronomy & Astrophysics **562**, L99–L102 (2001).

[11] R. Courant & F. John, *Introduction to Calculus and Analysis I*, volume 1, Springer, 1999.

[12] L. Deloubriére et al., *Imaginary noise and parity conservation in the reaction* $A + A \leftrightarrow 0$, Physica A **308**, 135–147 (2002).

[13] O. Deloubrière, L. Frachebourg, H. Hilhorst, & K. Kithara, *Imaginary noise and parity conservation in the reaction* $A + A \rightleftharpoons 0$, Physica A **308**, 135–147 (2002).

[14] P. Deuar, *First-Principles Quantum Simulations of Many-Mode Open Interacting Bose Gases using Stochastic Gauge Methods*, PhD thesis, University of Queensland, 2004.

[15] M. Doi, *Second quantization representation for classical many-particle systems*, Journal of Physics A: Math. Gen. **9**(9), 1465–1477 (1976).

[16] M. Doi, *Stochastic theory of diffusion-controlled reaction*, Journal of Physics A: Math. Gen. **9**(9), 1479–1495 (1976).

[17] P. Drummond, *Gauge Poisson representations for birth/death master equations*, The European Physical Journal B **38**, 617–634 (2004).

[18] N. Fletcher, *Size Effect in Heterogeneous Nucleation*, Journal of Chemical Physics **29**(3), 572 (1958).

[19] T. Fließbach, *Statistische Physik: Lehrbuch zur Theoretischen Physik IV*, Spektrum, third edition, 1999.

[20] V. Fokin et al., *Nucleation Theory and Applications*, chapter Nucleation and Crystallization Kinetics in Silicate Glasses: Theory and Experiment, Wiley-VCH, 2005.

[21] J. Frenkel, *Kinetic Theory of Liquids*, Clarendon Press, Oxford, 1946.

[22] C. W. Gardiner, *Handbook of Stochastic Methods for Physics, Chemistry and the Natural Sciences*, Springer, third edition, 2004.

[23] R. Garrod et al., *Are gas-phase models of interstellar chemistry tenable? The case of methanol*, Faraday Discussions **133**, 51–62 (2006).

[24] J. Gibbs et al., *The Collected Works of J.Willard Gibbs*, volume 1, Longmans, Green and Co., 1928.

[25] A. Gilchrist, C. Gardiner, & P. Drummond, *Positive P representation: Application and validity*, Physical Review A **55**(4), 3014–3032 (1997).

[26] D. Gillespie, *A General Method for Numerically Simulating the Stochastic Time Evolution of Coupled Chemical Reactions*, Journal of Computational Physics **22**(4), 403–434 (1976).

[27] N. J. B. Green et al., *A stochastic approach to grain surface chemical kinetics*, Astronomy & Astrophysics **375**, 1111–1119 (2001).

[28] P. Hartman, *Ordinary Differential Equations*, SIAM, second edition, 2002.

[29] T. Hasegawa, E. Herbst, & C. Leung, *Models of gas-grain chemistry in dense interstellar clouds with complex organic molecules*, The Astrophysical Journal Supplement Series **82**(1), 167–195 (1992).

[30] E. Herbst, Q. Chang, & H. Cuppen, *Chemistry on Interstellar Grains*, Journal of Physics — Conference Series: Light, Dust and Chemical Evolution **6**, 18–35 (2005).

[31] E. Herbst & H. M. Cuppen, *Interstellar Chemistry Special Feature: Monte Carlo studies of surface chemistry and nonthermal desorption involving interstellar grains*, Proceedings of the National Academy of Sciences **103**, 12257–12262 (2006).

[32] E. Herbst & V. I. Shematovich, *New approaches to the modelling of surface chemistry on interstellar grains*, Astrophysics and Space Science **285**, 725–735 (2003).

[33] D. Hochberg, M.-P. Zorzano, & F. Morán, *Complex noise in diffusion-limited reactions of replicating and competing species*, Physical Review E **73**, 066109 (2006).

[34] M. Howard & J. Cardy, *Fluctuation effects and mulitscaling of the reaction-diffusion fron for* $A + B \longrightarrow \emptyset$, Journal of Physics A: Math.Gen. **28**, 3599–3621 (1995).

[35] N. Katz et al., *Molecular hydrogen formation on astrophysically relevant surfaces*, The Astrophysical Journal **522**, 305 (1999).

[36] W. Klemperer, *Interstellar Chemistry Special Feature: Interstellar Chemistry*, Proceedings of the National Academy of Sciences **103**, 12232–12234 (2006).

[37] P. E. Kloeden & E. Platen, *Numerical Solution of Stochastic Differential Equations*, Springer, 1992.

[38] K. Kondratyev et al., *Atmospheric Aerosol Properties - Formation, Processes and Impacts*, Springer, 2006.

[39] B. P. Lee, *Renormalization group calculation for the reaction* $kA \longrightarrow \emptyset$, Journal of Physics A: Math.Gen. **27**, 2633–2652 (1994).

[40] A. A. Lushnikov, J. S. Bhatt, & I. J. Ford, *Stochastic approach to chemical kinetics in ultrafine aerosols*, Journal of Aerosol Science **34**, 1117–1133 (2003).

[41] A. Määttänen et al., *Two-component heterogeneous nucleation kinetics and an application to Mars*, Journal of Chemical Physics **127**, 134710 (2007).

[42] C. McKee & J. Ostriker, *A Theory of the Interstellar Medium: Three Components Regulated by Supernova Explosions in an Inhomogeneous Substrate*, The Astrophysical Journal **218**, 148–169 (1977).

[43] N. Metropolis et al., *Equation of state calculations by fast computing machines*, Journal of Chemical Physics **21**(6), 1087–1092 (1953).

[44] K. Öberg et al., *Photodesorption of ices II.* H_2O *and* D_2O, The Astrophysical Journal **693**, 1209–1218 (2009).

[45] L. Peliti, *Path integral approach to birth-death processes on a lattice*, Journal de Physique **46**, 1469–1483 (1985).

[46] V. Pirronello et al., *Laboratory Synthesis of Molecular Hydrogen on Surfaces of Astrophysical Interest*, The Astrophysical Journal Letters **475**, L69 (1997).

[47] V. Pirronello et al., *Efficiency of molecular hydrogen formation on silicates*, The Astrophysical Journal Letters **483**, L131 (1997a).

[48] V. Pirronello et al., *Measurement of Molecular Hydrogen Formation on Carbonaceous Grains*, Astronomy & Astrophysics **344**, 681 (1999).

[49] W. H. Press et al., *Numerical Recipes in C —The Art of Scientific Computing*, Cambridge University Press, second edition, 1992.

[50] W. Raith, editor, *Bergmann& Schaefer — Lehrbuch der Experimentalphysik: Erde und Planeten*, volume 7, Walter de Gruyter, 2 edition, 2001.

[51] H. Reiss, *The Kinetics of Phase Transitions in Binary Systems*, Journal of Chemical Physics **18**(840) (1950).

[52] P.-A. Rey & M. Droz, *A renormalization group study of a class of reaction-diffusion models, with particles input*, Journal of Physics A: Math. Gen. **30**, 1101–1114 (1997).

[53] D. Ruffle & E. Herbst, *New models of interstellar gas-grain chemistry - I. Surface diffusion rates*, Monthly Notices of the Royal Astronomical Society **319**(3), 837–850 (2000).

[54] J. Schmelzer, *Nucleation Theory and Applications*, chapter Summary and Outlooks, Wiley-VCH, 2005.

[55] V. Slezov et al., *Nucleation Theory and Applications*, chapter A New Method of Determination of the Coefficients of Emission in Nucleation Theory, Wiley-VCH, 2005.

[56] T. Snow & B. McCall, *Diffuse Atomic and Molecular Clouds*, Annual Review of Astronomy and Astrophysics **44**, 367–414 (2006).

[57] T. Stantcheva, P. Caselli, & E. Herbst, *Modified rate equations revisited. A corrected treatment for diffusive reactions on grain surfaces*, Astronomy & Astrophysics **375**, 673–679 (2001).

[58] T. Stantcheva & E. Herbst, *Models of gas-grain chemistry in interstellar cloud cores with a stochastic approach to surface chemistry*, Astronomy & Astrophysics **423**, 241–251 (2004).

[59] T. Stantcheva, V. I. Shematovich, & E. Herbst, *On the master equation approach to diffusive grain-surface chemistry: The H, O, CO system*, Astronomy & Astrophysics **391**, 1069–1080 (2002).

[60] U. C. Taeuber, M. J. Howard, & B. Vollmayr-Lee, *Applications of field-theoretic renormalization group methods to reaction-diffusion problems*, Journal of Physics A: Math. Gen. **38**, R79–R131.

[61] D. Turnbull & J. Fisher, *Rate of Nucleation in Condensed Systems*, Journal of Chemical Physics **17**(71) (1949).

[62] N. Van Kampen, *Stochastic Processes in Physics and Chemistry*, North-Holland Physics Publishing, third edition, 1984.

[63] H. Vehkamäki, *Classical Nucleation Theory in Multicomponent Systems*, Springer, 2006.

[64] H. Vehkamäki et al., *Heterogeneous multicomponent nucleation theorems for the analysis of nanoclusters*, Journal of Chemical Physics **126**, 174707 (2007).

[65] M. Volmer, *Kinetik der Phasenbildung*, Steinkopff, Dresden und Leipzig, 1939.

[66] G. Watson, *A treatise on the theory of Bessel functions*, Cambridge University Press, second edition, 2006.

[67] P. Winkler et al., *Heterogeneous Nucleation Experiments Bridging the Scale from Molecular Ion Clusters to Nanoparticles*, Science **319**, 1374 (2008).